Monte Carlo modeling of targeted radionuclide therapy of micrometastases

Mario Enrique Alcocer Avila

université de BORDEAUX

THÈSE PRÉSENTÉE

POUR OBTENIR LE GRADE DE

DOCTEUR DE

L'UNIVERSITÉ DE BORDEAUX

ÉCOLE DOCTORALE SCIENCES PHYSIQUES ET DE L'INGÉNIEUR

ASTROPHYSIQUE, PLASMAS, NUCLÉAIRE

Par Mario Enrique ALCOCER ÁVILA

Monte Carlo modeling of targeted radionuclide therapy of micrometastases

Sous la direction de : Christophe CHAMPION
Co-directeur : Juan Manuel MONTI

Soutenue le 12 mars 2021

Membres du jury :

Mme. FARIZON, Bernadette	Directrice de Recherche au CNRS	Présidente du jury
M. POUGET, Jean-Pierre	Directeur de Recherche à l'INSERM	Rapporteur
M. GROETZ, Jean-Emmanuel	Maître de Conférences, Université de Franche-Comté	Rapporteur
M. HINDIÉ, Elif	Professeur, Université de Bordeaux	Examinateur
M. CHAMPION, Christophe	Professeur, Université de Bordeaux	Directeur de thèse
M. MONTI, Juan Manuel	Profesor Asistente, Universidad Nacional de Rosario	Co-directeur de thèse
M. QUINTO, Michele Arcangelo	Investigador Asistente, Instituto de Física Rosario	Invité

A mis padres

Acknowledgments

Mi primer agradecimiento es a mis padres, quienes siempre me han apoyado de forma incondicional en todos mis proyectos, aunque en ocasiones eso implique estar lejos de la familia. Han dado lo mejor de sí a sus hijos. Son extraordinarios, los amo.

I would like to express my profound gratitude to Prof. Christophe Champion, my PhD advisor, for his always pertinent remarks aiming to improve my work. I admire your dynamism and your love for physics. Your help was instrumental to find, in the middle of the pandemic, the funding required to successfully finish my PhD.

I am deeply indebted to Dr. Michele Arcangelo Quinto for his continuous guidance and support in the development of Monte Carlo simulations.

I am extremely grateful to Prof. Juan Manuel Monti and Prof. Roberto Daniel Rivarola for sharing their knowledge in the field of ion-atom collisions. I would like to thank you as well for all your help during my stay in Rosario.

I am also grateful to Prof. Elif Hindié for his invaluable insight into the topic of targeted radionuclide therapy and his suggestions during the revision of this thesis.

I would like to acknowledge the financial support provided by the Consejo Nacional de Ciencia y Tecnología (Conacyt, Mexico) and the Site de Recherche Intégrée sur le Cancer de Bordeaux, Bordeaux Recherche Intégrée en Oncologie (SIRIC BRIO).

I wish to thank all the people in the CELIA with whom I had the chance to interact during these years, especially my fellow PhD colleagues Erwan, Julien and Paul, for fruitful exchanges. Special thanks to the administrative staff, particularly Sonia and Céline, for their kindness and assistance in preparing missions and dealing with other procedures.

Finalmente, quiero agradecer profundamente a esas personas maravillosas que, a lo largo de estos años, me han brindado su cariño y apoyo moral cuando más lo he necesitado: Yuliana, Lesly, Andrea, María Fernanda, Jorge, José Ángel, Manolo.

« La science, mon garçon, est faite d'erreurs, mais d'erreurs qu'il est bon de commettre, car elles mènent peu à peu à la vérité. »

Jules Verne
(Voyage au centre de la Terre)

" A model is a lie that helps you see the truth."

Howard Skipper
(quoted in The Emperor of All Maladies: A Biography of Cancer, by Siddhartha Mukherjee)

Modélisation Monte Carlo en radiothérapie interne vectorisée de micrométastases

Résumé: La radiothérapie interne vectorisée (RIV) est une technique pour traiter le cancer dans laquelle des isotopes radioactifs sont couplés à des molécules vectrices capables de cibler spécifiquement les cellules tumorales pour les irradier. Le but de cette thèse est de fournir une description précise des dépôts d'énergie induits dans la matière biologique par les radionucléides émetteurs d'électrons Auger et de particules alpha les plus prometteurs actuellement pour la RIV, au moyen de simulations Monte Carlo de structure de traces. Dans le cadre de cette thèse, le code *TILDA-V* a été étendu et amélioré pour inclure le ralentissement complet des particules alpha dans l'eau. Des études de transport et de dosimétrie des rayonnements ont été réalisées pour valider dans leur ensemble les capacités de la version la plus récente de *TILDA-V* à simuler les interactions des protons, des particules alpha et des électrons avec la matière biologique. Les prédictions du code ont été largement comparées aux résultats obtenus avec d'autres outils numériques et aux données expérimentales disponibles, avec des résultats très satisfaisants. L'effet sur les simulations de la description du milieu biologique (l'eau par opposition à l'ADN) a également été analysé de façon détaillée. De plus, les différents radionucléides d'intérêt ont été évalués en calculant la dose absorbée à des cellules tumorales isolées et à un petit amas cellulaire représentant une micrométastase. Les résultats du présent travail seront précieux pour la communauté de médecine nucléaire pour comprendre les mérites relatifs des différents radionucléides et guider le choix du radionucléide le plus adapté pour armer une molécule vectrice, en tenant compte du contexte clinique en oncologie.

Mots-clés: radiothérapie interne vectorisée, simulation Monte Carlo, rayonnements ionisants, médecine nucléaire, dosimétrie des rayonnements ionisants, micrométastases.

Monte Carlo modeling of targeted radionuclide therapy of micrometastases

Abstract: Targeted radionuclide therapy (TRT) is a cancer treatment modality in which radioactive isotopes are coupled to tumor-specific carrier molecules for the selective irradiation of tumor cells. The aim of this thesis is to provide an accurate description of the pattern of energy deposit by some of the most promising Auger electron- and alpha particle-emitting radionuclides currently considered for TRT, by means of accurate Monte Carlo track structure (MCTS) simulations. As part of this doctoral work, the *TILDA-V* code was extended and improved to include the full slowing-down of alpha particles in water. Radiation transport and dosimetry studies were performed to validate as a whole the capabilities of the latest version of *TILDA-V* for simulating the interactions of protons, alpha particles and electrons with biological matter. The code was extensively benchmarked against other numerical tools and available experimental data with satisfactory results. The effect on the simulations of changing the description of the biological medium (water versus DNA) was analyzed in detail as well. Furthermore, the various radionuclides of interest were evaluated by computing the absorbed dose to isolated tumor cells and to a small cell cluster representing a micrometastasis. The results of the present work will be valuable to the community of nuclear medicine to understand the relative merits of various radionuclides and to guide the choice of the most adapted radionuclide to arm a targeting molecule, taking into account the clinical setting in oncology.

Keywords: targeted radionuclide therapy, Monte Carlo simulation, ionizing radiation, nuclear medicine, radiation dosimetry, micrometastases.

Unité de recherche:
Centre Lasers Intenses et Applications
UMR 5107 Université de Bordeaux - CNRS - CEA, 43 Rue Pierre Noailles 33400 Talence, France.

RÉSUMÉ SUBSTANTIEL

Contexte de la recherche

La radiothérapie est un composant indispensable dans le traitement du cancer. Dans de nombreuses situations, les radiothérapies conventionnelles telles que la radiothérapie externe et la curiethérapie peuvent donner des résultats satisfaisants lorsqu'elles sont utilisées en association avec la chirurgie et la chimiothérapie. Cependant, certains types de cancer, en particulier ceux qui développent des métastases, nécessitent de nouvelles stratégies de traitement pour contrôler et potentiellement guérir les tumeurs. Dans ce contexte, la radiothérapie interne vectorisée (RIV) qui utilise des radiopharmaceutiques est une approche avec des possibilités prometteuses. La RIV est une modalité de traitement du cancer qui couple un radionucléide à une molécule vectrice (par exemple un anticorps, un peptide, un oligonucléotide, etc.) capable de cibler les cellules tumorales ou le microenvironnement tumoral pour irradier la tumeur de façon spécifique, minimisant ainsi la dose au tissu sain. Le choix du radionucléide le plus approprié dépend de plusieurs facteurs, dont ses propriétés physiques (caractéristiques d'émission et demi-vie); les propriétés chimiques de l'élément, qui déterminent la faisabilité de la liaison à la molécule vectrice; la taille de la tumeur; et la distribution de la molécule vectrice dans les tumeurs.

Historiquement, la RIV a été introduite dans les années 1940 avec l'utilisation de l'iode-131 (^{131}I), un émetteur de particules β^-, pour le traitement du cancer de la thyroïde. Depuis lors, la plupart des applications en RIV ont utilisé ce radionucléide ainsi que d'autres émetteurs β^-, notamment l'yttrium-90 (^{90}Y) et le lutécium-177 (^{177}Lu), pour traiter d'autres types de tumeurs. Néanmoins, plus récemment il y a eu un grand intérêt pour étudier les avantages d'utiliser des émetteurs d'électrons Auger ou de particules α au lieu d'émetteurs β^- pour la RIV, surtout dans les étapes précoces des cancers métastatiques. En effet, il a été suggéré que les émetteurs Auger ou α pourraient être plus efficaces pour éradiquer les cellules tumorales isolées et les micrométastases.

Les simulations numériques basées sur la méthode Monte Carlo (MC) permettent de décrire la distribution des dépôts d'énergie induits dans les tumeurs par ces radionu-

cléides prometteurs. La méthode MC aide à résoudre des problèmes du monde réel au moyen d'échantillonnages sur des distributions de probabilité. Les codes MC conviennent à cette tâche car les interactions des rayonnements avec la matière sont des phénomènes intrinsèquement stochastiques. De plus, parmi les divers codes MC existants, seuls ceux appelés de « structure de trace » (MCST) suivent les particules simulées événement par événement, une approche qui est censé être précise même à l'échelle subcellulaire. Pour simuler correctement le transport de particules dans un milieu donné, les codes MCST nécessitent des sections efficaces différentielles et totales pour décrire les diverses interactions induites par les particules. La plupart du temps, ces sections efficaces sont obtenues à partir d'une combinaison de données expérimentales et de modèles théoriques. Il convient de noter qu'en fin de compte, l'efficacité et la fiabilité du code dépendront de l'exactitude et de l'exhaustivité de la base de données des sections efficaces d'interaction.

Dans cette thèse, nous avons étendu le code MCST *TILDA-V* pour simuler le transport de particules α dans un milieu biologique. Nous avons effectué une série de simulations pour valider le transport de toutes les particules incluses dans le code, à savoir des protons, des particules α et des électrons. Nous avons ensuite mené une série d'études dosimétriques dans le but de déterminer la distribution des dépôts d'énergie induits dans les tumeurs (y compris dans des cellules tumorales isolées et des micrométastases) par les émetteurs β^-, α et Auger les plus intéressants pour la RIV.

Méthodes

Le code *TILDA-V*

TILDA-V (**T**ransport d'**I**ons **L**ourds **D**ans l'**A**qua et **V**ivo) est un code MCST maison créé par Champion et ses collègues [1] pour simuler les interactions des ions dans des milieux biologiques. Le code est écrit en C++ et implémente le calcul parallèle avec OpenMP (Open Multi-Processing). *TILDA-V* était jusqu'ici limité au transport de protons, y compris des atomes d'hydrogène neutre. Dans le cadre de cette thèse, *TILDA-V* a été étendu pour simuler le ralentissement complet des particules α dans l'eau, en prenant en compte tous les états de charge de l'hélium (He^{2+}, He^{+} et He^{0}). De nouvelles routines ont également été mises en œuvre pour la dosimétrie des rayonnements dans des cellules tumorales isolées et des micrométastases.

Les simulations avec *TILDA-V* concernent uniquement l'étape physique des dépôts d'énergie induits par les rayonnements dans les cibles biologiques. Les simulations peuvent être effectuées dans l'eau et l'ADN pour des protons et des particules α avec des énergies cinétiques comprises entre 10 keV u^{-1} et 100 MeV u^{-1}. Les électrons secondaires sont suivis jusqu'à une coupure à basse énergie de 7.4 eV avec des routines initialement

développées pour le code EPOTRAN (**E**lectron and **PO**sitron **TRAN**sport) [2], et qui sont maintenant pleinement intégrées dans *TILDA-V*. La relaxation des atomes n'est modélisée que par l'émission d'électrons Auger. Le transport de photons n'est pas inclus dans *TILDA-V*. La principale différence entre *TILDA-V* et les autres codes MCST existants est que le premier repose en grande partie sur des sections efficaces multiplement différentielles et totales calculées *ab initio* dans le cadre d'un traitement quantique des interactions et en appliquant une description moléculaire de l'eau et de l'ADN. Les sections efficaces ont été calculées en considérant des molécules cibles isolées à l'état vapeur. Cette approche est valable car les effets liés à la phase du milieu ne sont pas censés être importants dans la gamme d'énergie considérée ici.

Concernant les processus physiques, *TILDA-V* prend en compte l'ionisation, l'excitation et la diffusion élastique pour les ions (protons et particules α) et les électrons. Pour les ions, les processus d'échange de charge (capture et perte d'électrons) sont également inclus dans le code (cf. tab. I.2). Les sections efficaces théoriques pour l'ionisation et la capture d'un électron par des protons ont été calculées avec la version *prior* de l'approximation d'onde distordue du continu avec état initial eikonale (continuum distorted wave - eikonal initial state, CDW-EIS en anglais) [3], une méthode perturbative au premier ordre en mécanique quantique. Le même modèle théorique a été utilisé pour obtenir les sections efficaces d'ionisation pour les atomes d'hydrogène neutre et pour tous les ions d'hélium (He^{2+}, He^{+} et He^{0}). Le modèle *prior* CDW-EIS a également été utilisé pour calculer les sections efficaces de capture électronique simple par He^{2+}. Notons que pour les ions d'hélium il est également possible d'utiliser dans *TILDA-V* un ensemble de sections efficaces semi-empiriques pour tous ces processus. Les sections efficaces pour tous les autres processus d'échange de charge pour les ions d'hélium ont été dérivées de l'approche semi-empirique développée par Uehara et Nikjoo [4]. En outre, le modèle semi-empirique bien connu de Miller et Green [5] a été utilisé pour calculer les sections efficaces de perte d'électron par les atomes d'hydrogène neutre et les sections efficaces d'excitation pour tous les ions. De plus, les sections efficaces de diffusion élastique pour les ions ont été obtenues à partir de calculs faits dans le cadre de la mécanique classique.

Pour les électrons, les sections efficaces d'ionisation ont été calculées avec deux méthodes: l'approximation de Born de l'onde distordue (distorted wave Born approximation, DWBA en anglais) [6] et le modèle relativiste de collision binaire de Bethe (relativistic binary-encounter-Bethe, RBEB en anglais) [7]. Les sections efficaces d'excitation électronique sont basées sur la méthode semi-empirique d'Olivero *et al.* [8]. D'autre part, les sections efficaces pour la diffusion élastique des électrons ont été calculées avec la théorie des ondes partielles [9].

En ce qui concerne l'ADN, les sections efficaces des processus d'ionisation et de capture d'un électron par des protons ont été calculées aussi avec le modèle *prior* CDW-EIS. Pour

le processus d'excitation électronique par impact de protons, les sections efficaces pour les différents composants de l'ADN ont été obtenues avec le modèle semi-empirique de Miller et Green à partir d'extrapolations basées sur des données expérimentales pour la thymine. Finalement, pour les processus de perte d'un électron et de diffusion élastique, on a appliqué une procédure de rééchelonnement simple (basée sur le nombre d'électrons de la cible) aux sections efficaces obtenues pour l'eau (cf. éqs. II.51 et II.69).

Calcul de paramètres physiques pour le transport des rayonnements

La validation d'un code MC pour le transport des rayonnement se fait généralement en calculant plusieurs grandeurs macroscopiques clés caractérisant les traces des particules incidentes dans le milieu d'intérêt. Des paramètres physiques utiles pour vérifier la fiabilité des simulations sont le pouvoir d'arrêt, le parcours (« range », en anglais) et la distribution radiale de la dose (c'est-à-dire autour du trajet de l'ion).

Pouvoir d'arrêt

Le pouvoir d'arrêt est la perte d'énergie moyenne par unité de longueur subie par les particules chargées lors de la traversée d'un matériau [10]. Le pouvoir d'arrêt total est constitué de trois contributions: le pouvoir d'arrêt électronique, résultant des collisions inélastiques du projectile avec les électrons de la cible; le pouvoir d'arrêt nucléaire, résultant de collisions entre le projectile et le noyau cible; et le pouvoir d'arrêt radiatif, dû au rayonnement de freinage (Bremsstrahlung). Pour les particules chargées et les énergies cinétiques considérées dans ce travail, seul le pouvoir d'arrêt électronique est pertinent. Le pouvoir d'arrêt a été obtenu en simulant un nombre de projectiles suffisamment grand pour réduire les fluctuations statistiques à un niveau raisonnable (généralement 10^6 projectiles). Pour les projectiles dont l'état de charge peut changer pendant le transport, comme les protons et les particules α, une simulation a été réalisée pour chaque état de charge. Les simulations ont été réalisées en mode stationnaire, c'est-à-dire que chaque projectile a été suivi jusqu'à ce qu'il subisse une interaction avec le milieu. Une simulation a été réalisée pour chaque énergie incidente (nous avons considéré 37 énergies incidentes sur une grille logarithmique couvrant toute la gamme d'énergie d'intérêt). Une somme sur la perte d'énergie et la distance parcourue par chaque projectile a été réalisée dans chaque simulation. Le pouvoir d'arrêt à une énergie incidente donnée a ensuite été calculée comme l'énergie totale perdue par les projectiles divisée par leur parcours total (cf. éq. III.7). Pour les ions, ce dernier calcul a fourni le pouvoir d'arrêt pour un état de charge donné. Donc le pouvoir d'arrêt total a été obtenu en considérant les fractions de charge à l'équilibre pour les ions d'hydrogène et d'hélium (cf. éqs. III.8 et V.4).

Parcours (range)

Le parcours (range) est la distance moyenne parcourue par une particule chargée avant de perdre toute son énergie et de s'arrêter dans un matériau. Dans le cas des électrons, qui suivent des trajectoires très tortueuses, il est parfois utile de calculer la pénétration (« penetration range », en anglais), définie comme la longueur du vecteur $|\mathbf{R_f} - \mathbf{R_i}|$ du point de départ ($\mathbf{R_i}$) à la position finale ($\mathbf{R_f}$) de l'électron après thermalisation [11]. Pour calculer le parcours des protons et des particules α dans *TILDA-V*, les simulations ont été effectuées dans un milieu semi-infini et les particules ont été transportées en mode « slowing-down » (ralentissement), c'est-à-dire que chaque particule primaire a été suivie jusqu'à ce que son énergie tombe en dessous de $10\,\mathrm{keV\,u^{-1}}$. Le range a ensuite été obtenu en additionnant les distances parcourues par toutes les particules primaires et en divisant par le nombre de projectiles simulés ($\geq 5 \times 10^4$). En raison de la coupure à basse énergie pour les ions, les valeurs de range calculées avec *TILDA-V* ont été corrigées pour compenser le parcours d'un ion de $10\,\mathrm{keV\,u^{-1}}$ dans l'eau. Par ailleurs, pour calculer la pénétration des électrons, les coordonnées de la position finale de chaque électron ont été enregistrées lors de la simulation. La distance entre le point de départ et la position finale a ensuite été déterminée pour chaque électron. La pénétration moyenne a été obtenue en additionnant toutes ces distances et en divisant le résultat par le nombre d'électrons simulés.

Distribution de dose radiale

La distribution de dose radiale est un autre paramètre de transport utile pour vérifier la validité d'un code MCST. Ce paramètre fournit des informations sur l'énergie déposée par les électrons secondaires autour de la trajectoire de l'ion primaire. La distribution de dose radiale pour les protons dans l'eau a été obtenue avec *TILDA-V* en simulant 10^6 protons en mode stationnaire, mais en activant le mode slowing-down pour les électrons secondaires. L'énergie déposée par chaque électron secondaire a été calculée dans des manchons cylindriques d'une épaisseur de 0.1 nm et centrées autour du trajet du proton. La hauteur des manchons cylindriques était égale à la distance moyenne parcourue par les protons. Vu que le volume de ces manchons cylindriques était connu, on a déterminé la dose absorbée en fonction de la distance radiale à la trajectoire du proton.

Calculs dosimétriques

Protons

Nous avons étudié l'irradiation d'une cellule tumorale isolée par des faisceaux de protons monoénergétiques. Le modèle cellulaire consistait en trois sphères concentriques

représentant les éléments principaux d'une cellule: le noyau, le cytoplasme et la membrane cellulaire. Dans cette étude, le rayon cellulaire, le rayon nucléaire et l'épaisseur de la membrane ont été fixés à $7\,\mu$m, $4\,\mu$m [12] et 10 nm [13], respectivement. Le cytoplasme et la membrane cellulaire ont été modélisés par de l'eau avec une masse volumique de $1.0\,\mathrm{g\,cm^{-3}}$. Pour étudier la variation de la dose déposée à l'intérieur du noyau cellulaire en fonction de sa composition, trois simulations différentes ont été réalisées pour chaque énergie incidente, en supposant que le noyau contenait: 1) de l'eau ($\rho = 1.0\,\mathrm{g\,cm^{-3}}$); 2) de l'eau avec la masse volumique rééchelonnée à $1.29\,\mathrm{g\,cm^{-3}}$ et 3) de l'ADN hydraté ($\rho = 1.29\,\mathrm{g\,cm^{-3}}$). La source de rayonnements a été modélisée comme des protons arrivant dans la cellule dans des directions aléatoires (cf. fig. III.12). On a calculé l'énergie déposée dans le noyau par toutes les particules primaires et secondaires et on a ensuite converti cette énergie en dose absorbée.

Radionucléides émetteurs β^- et Auger

En utilisant le code MCST EPOTRAN et son extension pour la dosimétrie, CELLDOSE [14–17], nous avons calculé les facteurs S (dose absorbée par unité d'activité cumulée) cellulaires de quelques émetteurs β^- (^{131}I, ^{90}Y, ^{177}Lu et ^{161}Tb), et ceux pour quelques émetteurs Auger (^{71}Ge, ^{103m}Rh, ^{119}Sb, ^{125}I, ^{161}Ho, ^{189m}Os, ^{193m}Pt et ^{195m}Pt). Pour calculer les facteurs S cellulaires dans CELLDOSE, nous avons utilisé le même modèle cellulaire décrit précédemment pour la dosimétrie des protons, sauf que dans ce cas le rayon de la cellule (R_C), le rayon nucléaire (R_N) et l'épaisseur de la membrane ont été fixés à $7\,\mu$m, $5\,\mu$m et 10 nm, respectivement. Puisque le noyau cellulaire est considéré comme la structure critique à irradier afin d'induire la mort cellulaire, seules les configurations ayant le noyau comme cible ont été considérées. Les simulations ont été réalisées avec des électrons ayant des énergies initiales obtenues à partir du spectre de chaque radionucléide. Les spectres ont été tirés de la publication 107 de l'ICRP [18]. On a pris en compte les spectres β^- complets. En revanche, pour les électrons Auger et de conversion interne, les spectres abrégés ont été considérés. De plus, seuls les électrons Auger et de conversion interne avec des probabilités supérieures à 0.1‰ ont été inclus dans les simulations. De même, la contribution des photons aux facteurs S a été négligée dans CELLDOSE car elle est beaucoup plus petite que celle des électrons au niveau cellulaire [19]. Un algorithme a été mis en œuvre pour construire la distribution de probabilité cumulée pour le spectre de chaque radionucléide en tenant compte de tous les rayonnements mentionnés ci-dessus. Ensuite, un échantillonnage aléatoire a été effectué sur cette distribution de probabilité pour obtenir la liste des énergies des électrons à simuler dans CELLDOSE.

On a calculé l'énergie déposée dans le noyau cellulaire par tous les électrons (primaires et secondaires). Chaque électron a été suivi jusqu'à ce que son énergie tombe

en dessous de 7.4 eV (le seuil d'excitation de la molécule d'eau). L'énergie restante a été considérée comme absorbée localement. Le volume et la masse volumique de la cible étant connus, le calcul du facteur S a été simple (cf. éq. IV.11). Toutes les régions cellulaires ont été modélisées par de l'eau avec une masse volumique $\rho = 1.0\,\mathrm{g\,cm^{-3}}$, sauf lorsque nous avons effectué un test pour étudier l'effet du changement de la composition du noyau (en considérant soit l'ADN hydraté soit l'eau avec une masse volumique rééchelonnée à $1.29\,\mathrm{g\,cm^{-3}}$). De plus, nous avons considéré les suivantes distributions du radionucléide: uniquement à la surface cellulaire (CS); seulement dans le cytoplasme (Cy); seulement dans le noyau (N); une distribution uniforme dans toute la cellule (C). Dans chaque cas on a simulé 10^6 désintégrations du radionucléide sélectionné. Ce nombre de désintégrations était suffisamment important pour réduire les fluctuations statistiques à $\sim$1%, tout en conservant un temps de calcul raisonnable. Les facteurs S fournies par CELLDOSE ont été multipliées par un facteur de renormalisation égal au rapport entre l'énergie moyenne libérée par désintégration et l'énergie moyenne des radiations tirées au sort sur le spectre du radionucléide. Cette rénormalisation était nécessaire pour compenser le fait que le code prend une seule valeur d'énergie par désintégration, lorsqu'en réalité plusieurs électrons avec des énergies différentes peuvent être émis par désintégration.

Puisque les radionucléides n'ont pas la même énergie par désintégration (cf. tableaux IV.1 et IV.2), les doses absorbées au noyau d'une cellule tumorale isolée ont été normalisées en supposant que 1 MeV est libéré par $\mu\mathrm{m}^3$ [16, 17]. Cette hypothèse signifie que pour notre cellule avec un volume de $1436\,\mu\mathrm{m}^3$, 1436 MeV ont été libérés dans l'une des régions d'intérêt définies ci-dessus.

Pour aller au-delà du cas de la cellule isolée, nous avons également étudié l'irradiation de micrométastases en considérant un petit amas de cellules tumorales. L'amas était composé d'un total de 19 cellules: i) une cellule centrale; ii) 6 cellules formant le premier voisinage, en contact direct avec la cellule centrale; iii) 12 cellules formant le deuxième voisinage. Chaque cellule dans l'amas avait les mêmes dimensions que la cellule tumorale isolée décrite ci-dessus. De plus, on a supposé que toutes les cellules étaient marquées de la même manière, c'est-à-dire qu'elles contenaient une distribution uniforme du radionucléide dans l'une des régions spécifiques d'intérêt définies ci-dessus (surface cellulaire; ou cytoplasme; ou noyau; ou la cellule entière). Les cellules ont été disposées selon un modèle de structure cubique simple (cf. fig. IV.6b). Comme pour la cellule tumorale isolée, les doses absorbées normalisées ont été obtenues en supposant que 1 MeV était libéré par $\mu\mathrm{m}^3$, c'est-à-dire 1436 MeV libérés par cellule. En outre, l'espace intercellulaire a été supposé ne contenir aucune activité et a été modélisé comme de l'eau. Nous avons évalué la dose au noyau de la cellule centrale, ainsi qu'aux noyaux des cellules appartenant aux premier et deuxième voisinages.

Radionucléides émetteurs α

Nous avons utilisé la dernière version de CELLDOSE pour calculer les facteurs S cellulaires de plusieurs émetteurs α prometteurs (^{211}At, ^{212}Pb, ^{213}Bi, ^{223}Ra, ^{225}Ac et ^{227}Th) dans le but d'évaluer leur efficacité relative et de les comparer avec l'émetteur β^- de référence, le ^{177}Lu. Dans cette étude, nous avons utilisé le même modèle de cellule décrit pour les émetteurs d'électrons et les mêmes distributions du radionucléide dans la cellule. Comme d'habitude, seules les radiations avec des probabilités supérieures à 0.1‰ répertoriées dans la publication 107 de l'ICRP [18] ont été incluses dans nos simulations. La contribution des photons et des noyaux de recul aux facteurs S a été négligée. CELLDOSE a été mis à jour pour effectuer le tirage au sort des radiations émises lors d'une désintégration α. Le principe reste le même que pour les émetteurs d'électrons, mais maintenant la distribution de probabilité cumulée inclut la contribution de toutes les radiations d'intérêt (des particules α, des particules β^-, des électrons Auger et de conversion interne) pour chaque radionucléide dans une chaîne de désintégration. En outre, lorsque plusieurs modes de désintégration existent pour un radionucléide père donné, les émissions des noyaux fils sont ajustées en multipliant leurs intensités d'émission par le rapport d'embranchement correspondant associé au mode de désintégration spécifique. Le nombre de désintégrations simulées avec CELLDOSE a varié entre 10^5 et 10^6 selon le radionucléide et la distribution étudiés afin de réduire l'incertitude statistique à environ 1–2%, tout en conservant un temps de calcul raisonnable. Nous avons calculé les facteurs S pour les radionucléides individuels et aussi pour toute leur chaîne de désintégration. Comme pour les émetteurs d'électrons, une renormalisation finale a été faite en multipliant les facteurs S calculés par le rapport entre l'énergie moyenne libérée par désintégration et l'énergie moyenne des radiations tirées au sort sur le spectre du radionucléide.

Résultats

Paramètres physiques pour le transport de protons, de particules α et d'électrons

Protons

Concernant le transport des protons dans l'eau, pour des énergies incidentes supérieures à 30 keV on a observé un bon accord (écart < 10%) entre le pouvoir d'arrêt électronique calculé avec *TILDA-V* et les données expérimentales disponibles (cf. fig. III.4). Pour des énergies incidentes plus faibles, nos résultats ont sous-estimé les valeurs expérimentales, un comportement qui a été attribué au modèle *prior* CDW-EIS utilisé dans notre code.

Dans le cas de l'ADN, faute de données expérimentales, nous avons comparé nos prédictions avec les quelques calculs trouvés dans la littérature [20, 21]. Des différences importantes ont été observées pour les énergies incidentes inférieures à 200 keV. Les pouvoirs d'arrêt électroniques maximaux pour l'eau (97.5 keV μm^{-1}) et l'ADN hydraté (110 keV μm^{-1}) ont été observés à la même énergie incidente, 70 keV, avec une différence d'environ 13% entre les deux milieux.

Le parcours des protons dans l'eau calculé à partir de nos simulations a été comparé aux données provenant de diverses sources [10, 22–24]. Des différences ont été observées à basse énergie incidente ($E_{\text{inc}} < 100$ keV, cf. fig. III.7). Nous avons également calculé le rapport entre le parcours des protons dans l'eau et l'ADN hydraté en fonction de l'énergie incidente. On a constaté que le parcours des protons dans l'ADN hydraté est toujours plus court que dans l'eau (la différence est d'environ 10% pour $E_{\text{inc}} > 100$ keV et diminue progressivement jusqu'à environ 6% pour des énergies incidentes plus faibles).

Nous avons calculé avec *TILDA-V* la distribution de dose radiale pour des protons de 200 keV, 1 MeV, 3 MeV, 10 MeV et 100 MeV dans l'eau. Nos résultats sont en excellent accord avec les mesures expérimentales rapportées par Wingate et Baum [25] pour des protons de 1 MeV et 3 MeV dans un gaz équivalent tissu. La comparaison de nos résultats avec d'autres calculs MC [26–30], a également révélé un bon accord, en particulier à haute énergie incidente (10 MeV et 100 MeV, cf. fig. III.8). Des écarts importants n'ont été observés qu'avec les résultats de Bäckström *et al.* [31] et ont été attribués aux sections efficaces utilisées dans ce travail pour le transport des électrons secondaires.

Particules α

Le pouvoir d'arrêt électronique pour les particules α dans l'eau a été calculé avec *TILDA-V* en utilisant deux ensembles différents de sections efficaces: le premier incluait les sections efficaces théoriques (*prior* CDW-EIS), tandis que le second était composé uniquement de sections efficaces semi-empiriques. Lors de l'utilisation des sections efficaces théoriques, la courbe du pouvoir d'arrêt montrait des écarts importants avec les données expérimentales disponibles [32, 33] et avec les valeurs fournies dans le rapport 49 de l'ICRU [10], en particulier pour des énergies incidentes $\lesssim 2$ MeV (cf. fig. V.2). Les raisons derrière ces écarts sont en cours d'étude, et il semble probable que l'amélioration du modèle théorique sera nécessaire pour faire face à ce problème. En attendant, nous avons décidé d'utiliser dans *TILDA-V* les sections efficaces semi-empiriques dérivées des travaux d'Uehara et Nikjoo [4]. Cette décision a été prise pour permettre une étude dosimétrique fiable des émetteurs de particules α.

En utilisant les sections efficaces semi-empiriques, nous avons calculé le parcours des particules α dans l'eau. Les différences trouvées entre nos valeurs et celles du rapport 49 de l'ICRU [10] sont inférieures à 3% pour des énergies incidentes ≤ 10 MeV

et augmentent à environ 10% pour des énergies incidentes plus élevées (cf. fig. V.3).

Electrons

En utilisant le code EPOTRAN, nous avons calculé et comparé les pouvoirs d'arrêt massiques des électrons dans l'eau et l'ADN hydraté (cf. fig. III.10). Les résultats ont montré un comportement similaire, avec une différence maximale d'environ 13% entre les deux milieux. De plus, nous avons trouvé un pouvoir d'arrêt maximal de 232 MeV cm^2 g^{-1} à 160 eV et 223 MeV cm^2 g^{-1} à 130 eV pour l'eau et l'ADN, respectivement.

Nos résultats pour l'eau sont en excellent accord (écart $<$ 5%) avec les données provenant de diverses sources [21, 34–37] pour des énergies incidentes supérieures à quelques centaines d'eV. Néanmoins, des écarts importants (jusqu'à 19%) ont été observés à basse énergie incidente dans certains cas, notamment par rapport à la valeur maximale du pouvoir d'arrêt [21, 36]. Cela a été attribué au modèle utilisé dans dans ces calculs (le formalisme diélectrique), qui surestime les sections efficaces inélastiques autour de la région du pic. En général, un comportement similaire a été observé pour l'ADN hydraté lorsque nous avons comparé nos prédictions avec les quelques calculs disponibles [21, 36].

Nous avons calculé la pénétration des électrons dans l'eau, l'eau avec une masse volumique rééchelonnée à 1.29 g cm^{-3} et l'ADN hydraté. Pour des énergies incidentes $E_{\text{inc}} \lesssim 700$ eV, nos résultats pour l'eau étaient entre ceux rapportés par Meesungnoen *et al.* [11] et Bordage *et al.* [38]. Des écarts importants ont été observés à de faibles énergies incidentes pour tous les calculs trouvés dans la littérature (cf. fig. III.11). En revanche, toutes les prédictions sont en accord pour des énergies incidentes supérieures à 1 keV. Dans toute la gamme d'énergie considérée, la pénétration des électrons dans l'ADN hydraté était plus courte que dans l'eau. La pénétration des électrons dans l'eau avec une masse volumique rééchelonnée à 1.29 g cm^{-3} et dans l'ADN hydraté est assez similaire pour des énergies incidentes supérieures à $\sim$500 eV.

Dosimétrie des protons

Nous avons calculé l'énergie et la dose déposées par des protons dans le noyau d'une cellule tumorale isolée en fonction de l'énergie incidente (cf. fig. III.13). Une surestimation de la dose a été observée quand l'eau a été utilisée à la place de l'ADN pour décrire la composition du noyau. En plus, utiliser l'eau avec une masse volumique rééchelonnée à 1.29 g cm^{-3} ne permet pas de reproduire les résultats obtenus pour l'ADN hydraté. Nous avons conclu que ni les valeurs calculées avec l'approche habituelle consistant à utiliser l'eau comme substitut des tissus mous ni les résultats obtenus en appliquant une correction basée uniquement sur un rééchelonnement de la masse volumique de l'eau ne

reflètent la complexité sous-jacente du milieu biologique.

Dosimétrie de radionucléides émetteurs β^- et Auger

Les facteurs S cellulaires obtenues avec CELLDOSE pour les émetteurs d'électrons β^- et Auger ont été comparées avec des calculs réalisés avec le code MIRDcell [39] et les travaux de Falzone *et al*. [40] (cf. tab. IV.3), sauf pour le ^{161}Tb, le ^{71}Ge, le ^{161}Ho et le ^{189m}Os, pour lesquels aucune donnée équivalente n'a été trouvée. Un excellent accord a été observé avec les travaux de Falzone *et al*. [40], avec une différence maximale de -4.2% pour le ^{125}I localisé à la surface cellulaire. Cet accord a été attribué à l'utilisation de spectres et d'une méthodologie similaires. En revanche, des différences beaucoup plus significatives (jusqu'à environ 42%) ont été trouvées entre nos résultats et ceux de MIRDcell, notamment pour les distributions surfacique et intracytoplasmique de ^{103m}Rh, ^{125}I et ^{193m}Pt. Les écarts ont été attribués aux limites bien connues de la méthode du MIRD.

On a calculé les doses absorbées normalisées au noyau d'une cellule tumorale isolée. Les doses les plus faibles ont été observées lorsque le radionucléide était localisé à la surface cellulaire, et les plus élevées lorsqu'il était incorporé dans le noyau lui-même (cf. tab. IV.4 et fig. IV.5). Une comparaison entre les émetteurs β^- ^{177}Lu et ^{161}Tb a montré que ce dernier délivre toujours des doses plus élevées que le ^{177}Lu à des cellules tumorales isolées, quelle que soit la distribution du radionucléide. En revanche, on a observé que les doses absorbées normalisées pour le ^{131}I et le ^{90}Y étaient beaucoup plus faibles que pour le ^{177}Lu ou le ^{161}Tb, confirmant que le ^{131}I et le ^{90}Y sont meilleurs pour irradier les grosses tumeurs que les cellules tumorales isolées ou les micrométastases. En ce qui concerne les émetteurs Auger, les résultats ont montré que le ^{119}Sb et le ^{189m}Os sont d'excellents candidats pour l'irradiation de cellules isolées (et en fait meilleurs que le ^{161}Tb et le ^{177}Lu à cet effet), quel que soit la localisation de la molécule radiomarquée dans la cellule. De plus, on a conclu que le ^{125}I et le ^{161}Ho seraient aussi efficaces que le ^{119}Sb et le ^{189m}Os lorsqu'ils sont situés à l'intérieur du noyau, mais leurs performances seraient inférieures lorsqu'ils sont situés dans le cytoplasme ou à la surface de la cellule. Enfin, la dose absorbée normalisée pour le ^{71}Ge est tout à fait remarquable pour une distribution intranucléaire ou pour une distribution uniforme dans la cellule entière, mais très faible dans le cas d'une localisation intracytoplasmique ou à la surface cellulaire.

Concernant les simulations réalisées avec l'amas de cellules, il est clair que l'ajout des 18 cellules voisines augmente la dose absorbée normalisée au noyau de la cellule centrale (cf. tab. IV.6 et fig. IV.7). De plus, nous avons observé que pour un radionucléide donné, l'augmentation exacte de la dose dépend de la distribution du radionucléide dans les cellules entourant la cible. Pour tous les radionucléides, l'augmentation de

dose était plus prononcée dans le cas d'une distribution dans la surface cellulaire. Pour les émetteurs β^-, le deuxième voisinage ajoutait encore une contribution significative à la dose (augmentant la dose en irradiation croisée d'un facteur $\sim$2 pour toutes les distributions). De manière similaire au cas d'une cellule tumorale isolée, les doses délivrées par le ^{161}Tb étaient systématiquement plus élevées que celles délivrées par le ^{177}Lu, ce qui confirme l'idée que le ^{161}Tb serait plus adapté que le ^{177}Lu pour irradier des cellules tumorales isolées et des micrométastases. En ce qui concerne les émetteurs Auger, la contribution spécifique du deuxième voisinage à la dose absorbée normalisée varie sensiblement en fonction du radionucléide. Dans la plupart des cas, en particulier pour le ^{119}Sb et le ^{189m}Os, cette contribution était bien inférieure à celle du premier voisinage. En revanche, pour le ^{103m}Rh et le ^{193m}Pt, la contribution du deuxième voisinage était presque égale à celle du premier voisinage.

Dosimétrie de radionucléides émetteurs α

Les facteurs S cellulaires obtenues avec CELLDOSE pour les radionucléides émetteurs α et leurs chaînes de désintégration ont été comparés avec des calculs réalisés avec MIRDcell [39] et le travail de Lee *et al.* [41], basé sur des simulations faites avec le code PHITS (cf. tableaux V.2 et V.3). Dans l'ensemble, les facteurs S ont augmenté progressivement lorsqu'on a passé d'une distribution dans la surface cellulaire, vers une distribution intracytoplasmique, vers une distribution uniforme dans la cellule entière, pour finalement atteindre la valeur maximale pour une distribution intranucléaire. Ce comportement est identique à celui observé pour les émetteurs d'électrons.

Dans le cas des radionucléides seuls, des résultats très similaires ont été trouvés pour le ^{223}Ra, le ^{225}Ac et le ^{227}Th pour toutes les distributions des radionucléides. De plus, les plus petites facteurs S ont été obtenus pour le ^{212}Pb, un émetteur β^- pur. Une augmentation significative des facteurs S a été observée lorsque la chaîne de désintégration complète a été prise en compte dans les calculs. Les facteurs S ont augmenté d'un facteur $\sim$2 pour le ^{211}At, 28–29 pour le ^{213}Bi, 3.5 pour le ^{223}Ra et le ^{225}Ac, et 4.5 pour le ^{227}Th. La plus grande variation a été trouvée pour le ^{212}Pb, pour lequel les facteurs S de la chaîne de désintégration étaient de 37 à 80 fois plus grands que pour le radionucléide tout seul, en fonction de la distribution. Dans l'ensemble, les facteurs S maximales ont été obtenues pour le ^{227}Th. Nos facteurs S concordent à 8% près avec ceux fournis par MIRDcell et ceux de Lee *et al.* [41] (à 6% près dans le cas des radionucléides seuls).

Nous avons comparé les facteurs S cellulaires des émetteurs α avec les valeurs trouvées pour l'émetteur β^- ^{177}Lu, en calculant le « facteur d'amélioration ». Celui-ci a été défini comme le rapport des facteurs S, i.e., S(émetteur α)/S(^{177}Lu). Il a été observé

que la désintégration d'un émetteur α pur tel que le ^{223}Ra, le ^{225}Ac ou le ^{227}Th donne des facteurs S environ 87–134 supérieures à ceux du ^{177}Lu (cf. tab. V.5). L'amélioration est moins significative pour les radionucléides ayant plusieurs modes de désintégration, en particulier si la désintégration α a un petit rapport d'embranchement. Les facteurs d'amélioration pour le ^{211}At (41.8% α) et ^{212}Bi (35.9% α) étaient d'environ 36 à 54 et de 30–45, respectivement, alors que pour le ^{213}Bi (2.1% α) étaient seulement entre 2.2 et 3.2. Le cas extrême était celui de ^{212}Pb seul, ses facteurs S étant environ entre 1.27 et 1.89. Quand la chaîne de désintégration complète a été considérée, l'amélioration maximale a été trouvée pour le ^{227}Th, suivi, par ordre décroissant, du ^{223}Ra, le ^{225}Ac, le ^{211}At, le ^{212}Pb et le ^{213}Bi. Le facteur S du ^{227}Th pour une distribution dans la surface cellulaire était 589 fois plus grand que le facteur S correspondant au ^{177}Lu; le facteur d'amélioration a diminué à 534 pour une distribution intracytoplasmique, à 441 pour une distribution uniforme dans la cellule entière, et à 393 pour une distribution intranucléaire.

Contents

Résumé ix

Abstract xi

Résumé substantiel xiii

Contents xxvii

List of Figures xxxi

List of Tables xxxv

List of abbreviations xxxvii

General introduction 1

Introduction générale 5

I The Monte Carlo method and its applications in radiation transport 9

I.1 Introduction . . . 9

I.2 Basic aspects of Monte Carlo simulations for radiation transport . . . 11

I.2.1 Assumptions in Monte Carlo radiation transport simulations . . . 11

I.2.2 Random sampling of probability distributions . . . 13

I.2.2.1 Random number generation . . . 13

I.2.2.2 General approach for the random sampling of a physical quantity . . . 13

I.2.2.3 Distance to next event . . . 14

I.2.2.4 Type of interaction . . . 15

I.3 Monte Carlo codes for radiation transport . . . 15

I.3.1 The condensed-history Monte Carlo approach . . . 15

I.3.1.1 EGSnrc . . . 16

I.3.1.2 MCNP . . . 16

I.3.1.3 GEANT4 . . . 17
I.3.1.4 FLUKA . . . 18
I.3.1.5 PENELOPE . . . 18
I.3.1.6 PHITS . . . 19
I.3.2 The Monte Carlo track structure approach . . . 19
I.3.2.1 KURBUC . . . 22
I.3.2.2 PARTRAC . . . 24
I.3.2.3 GEANT4-DNA . . . 25
I.4 The ***TILDA-V*** MCTS code . . . 27
I.4.1 General features . . . 27
I.4.2 Input data and simulation setup . . . 30
I.4.3 Outlook . . . 35
Conclusions . . . 35

II Ion and electron impact on biological targets **37**
II.1 Introduction . . . 38
II.2 The description of the biological medium . . . 39
II.2.1 Gas-phase or condensed-phase? . . . 39
II.2.2 Water . . . 40
II.2.3 DNA . . . 41
II.3 Physical processes induced by the impact of ions . . . 43
II.3.1 Classification of interactions . . . 43
II.3.2 The electronic excitation process . . . 44
II.3.3 The ionization process . . . 47
II.3.3.1 The CDW-EIS model . . . 48
II.3.3.2 Alternative approaches . . . 54
II.3.4 The electron capture process . . . 59
II.3.4.1 The CDW-EIS model . . . 60
II.3.4.2 Semiempirical models . . . 63
II.3.5 The electron loss process . . . 66
II.3.6 The elastic scattering process . . . 68
II.3.7 Summary of total cross sections for ion impact . . . 71
II.4 Physical processes induced by the impact of electrons . . . 73
II.4.1 The electronic excitation process . . . 73
II.4.2 The ionization process . . . 75
II.4.2.1 The relativistic binary-encounter-Bethe model . . . 75
II.4.2.2 The distorted wave Born approximation . . . 77
II.4.3 The elastic scattering process . . . 81

II.4.4 Summary of total cross sections for electron impact 84
Conclusions 85

III Charged particle transport simulations **87**
III.1 Introduction 87
III.2 Track parameters 88
III.2.1 Inelastic mean free path 88
III.2.2 Stopping power 90
III.2.3 Range 91
III.2.4 Radial dose distribution 92
III.3 Results for proton transport 92
III.4 Results for electron transport 102
III.5 Single cell irradiation by proton beams 107
Conclusions 112

IV Radiation dosimetry of β^- and Auger electron emitters **113**
IV.1 Introduction 113
IV.2 The β and electron capture decay processes 114
IV.3 The isomeric transition, internal conversion and Auger electron emission processes 116
IV.4 Targeted radionuclide therapy 119
IV.5 Electron emitters for TRT 120
IV.5.1 β^- emitters for TRT 120
IV.5.1.1 ^{131}I 120
IV.5.1.2 ^{90}Y 121
IV.5.1.3 ^{177}Lu 121
IV.5.1.4 ^{161}Tb 122
IV.5.2 AE emitters for TRT 124
IV.5.2.1 ^{71}Ge 124
IV.5.2.2 ^{103m}Rh 124
IV.5.2.3 ^{119}Sb 125
IV.5.2.4 ^{125}I 126
IV.5.2.5 ^{161}Ho 126
IV.5.2.6 ^{189m}Os 127
IV.5.2.7 ^{193m}Pt 127
IV.5.2.8 ^{195m}Pt 128
IV.6 S-values and absorbed doses in single tumor cells 131
IV.6.1 Determination of cellular S-values 131

IV.6.2 Normalized absorbed doses to the nucleus of a single tumor cell . 136
IV.6.3 Influence on dose of the nucleus composition 138
IV.7 Cell cluster 141
Conclusions 146

V Radiation dosimetry of α-particle emitters **147**
V.1 Introduction 147
V.2 Track parameters for α-particles transport in water 149
V.2.1 Stopping power 149
V.2.2 Range 153
V.3 The α decay process 154
V.4 α-particle emitting radionuclides for TRT 155
V.4.1 ^{211}At 155
V.4.2 ^{212}Pb/^{212}Bi 158
V.4.3 ^{213}Bi 159
V.4.4 ^{223}Ra 161
V.4.5 ^{225}Ac 162
V.4.6 ^{227}Th 164
V.5 Cellular S-values for α-particle emitters 168
Conclusions 175

Conclusions and outlook **177**

Conclusions et perspectives **181**

References **185**

Appendices **223**
A MO-SCF-LCAO description of water 223
B LCAO representation of DNA components 224

List of Figures

I.1 Slowing-down of a proton in water 30
I.2 The workflow of a *TILDA-V* simulation. 33
I.3 The workflow for electron transport. 34

II.1 The deoxyribonucleic acid (DNA) structure 42
II.2 Excitation cross sections for protons in water 46
II.3 Excitation cross sections for proton impact on DNA components 47
II.4 The coordinate system considered in the continuum distorted wave - eikonal initial state (CDW-EIS) model 49
II.5 Ionization cross sections for hydrogen ions in water 52
II.6 Ionization cross sections for α-particles in water 53
II.7 TICS for hydrogen ions in DNA components 54
II.8 SDCS for protons and α-particles in water vapor 57
II.9 Comparison of theoretical and experimental Total ionization cross section (TICS) for H^+ and He^{2+} impact on water vapor 58
II.10 total cross section (TCS) for electron capture by H^+ in water and DNA components 61
II.11 TCS for single-electron capture by He^{2+} in water 62
II.12 Electron capture cross sections for He^{2+} and He^+ in water 63
II.13 Comparison between theoretical and semiempirical TCS for electron capture by H^+ in water 65
II.14 Electron loss cross sections for neutral hydrogen atoms in water and DNA components 67
II.15 Electron loss cross sections for He^+ and He^0 in water 68
II.16 The collision system in the elastic scattering process 70
II.17 Total inelastic cross sections for hydrogen ions in water and hydrated DNA 72
II.18 Total excitation cross sections for electron impact on water and DNA components 74
II.19 Total ionization cross sections for electron impact on water obtained with the RBEB model 76

II.20 Double differential cross section (DDCS) for ionization of the water molecule by electron impact computed in the distorted wave Born approximation (DWBA) framework . . . 78
II.21 SDCS for ionization of the water molecule by electron impact computed in the DWBA framework . . . 79
II.22 TICS for electron impact on water . . . 80
II.23 TICS for electron impact on DNA components computed within the first Born approximation framework . . . 81
II.24 SDCS for the elastic scattering of electrons in water vapor . . . 83
II.25 TCS for the elastic scattering of electrons in water vapor . . . 84
II.26 TCS for electrons in water and hydrated DNA . . . 85

III.1 Equilibrium charge fractions for hydrogen ions in water vapor as a function of the incident energy . . . 89
III.2 inelastic mean free path (IMFP) for protons in water, water with a density rescaled to 1.29 g cm^{-3} and hydrated DNA . . . 93
III.3 IMFP for protons in water and DNA. Comparison with other works . . . 94
III.4 Electronic stopping power for protons in water and DNA . . . 96
III.5 Comparison of the electronic stopping power for protons in water vapor and liquid water . . . 98
III.6 Mass electronic stopping power for protons in water vapor. Comparison with other calculations . . . 99
III.7 Range for protons in water and DNA . . . 100
III.8 Radial dose distribution for protons in water . . . 101
III.9 IMFP for electrons in water and hydrated DNA . . . 103
III.10 Mass electronic stopping power for electrons in water vs. hydrated DNA . 105
III.11 Penetration range for electrons in water, density-rescaled water and hydrated DNA . . . 106
III.12 Irradiation of a single cell impacted by protons . . . 108
III.13 Energy and dose deposited in the nucleus of a single cell irradiated by protons . . . 109

IV.1 β^- spectrum of ^{90}Y . . . 115
IV.2 Energy spectrum of ^{161}Ho . . . 116
IV.3 Atom relaxation following a vacancy in the K-shell by radiative and non-radiative transitions . . . 117
IV.4 The track in water of an Auger electron of 5.25 keV emitted by ^{161}Tb . . . 118
IV.5 Normalized absorbed doses to the nucleus of a single tumor cell for different distributions of β^- and Auger electron (AE) emitters . . . 137

IV.6 Single tumor cell and cell cluster models 141
IV.7 Normalized absorbed doses to the nucleus of the central cell in a cluster for different distributions of β^- and AE emitters 143

V.1 Equilibrium charge fractions for helium ions in water vapor 151
V.2 Electronic stopping power for α-particles ($^4_2He^{2+}$) in water 152
V.3 Range for α-particles ($^4_2He^{2+}$) in water 153
V.4 Schematic representation of the α decay of ^{225}Ac 155
V.5 Decay series of ^{211}At 156
V.6 Decay series of ^{212}Pb 158
V.7 Decay series of ^{225}Ac, ^{213}Bi, ^{227}Th and ^{223}Ra 160

List of Tables

I.1 Some existing Monte Carlo track structure (MCTS) codes 21
I.2 Physical processes and set of models used in *TILDA-V* 28

II.1 Atomic orbital populations and binding energies of the H_2O molecular orbitals 40
II.2 Fitting parameters for computing the excitation cross sections for protons in water 45
II.3 Fitting parameters for computing the excitation cross sections for H^+ and H^0 in DNA 46
II.4 Semiempirical parameters for computing the ionization cross sections in Rudd's model for water vapor 55
II.5 Parameter set for computing the electron capture cross sections in the model of Dingfelder *et al.* 65
II.6 Mean excitation energies used in *TILDA-V* for the DNA components . . . 75

III.1 Nuclear dose ratios for some values of the incident proton energy. 111

IV.1 Main properties of β^- emitters for targeted radionuclide therapy (TRT) . 123
IV.2 Main properties of AE emitters for TRT 129
IV.3 Cellular S-values for β^- and AE emitters 134

V.2 Cellular S-values for individual α-particle emitters 170
V.3 Cellular S-values for the decay series of α-particle emitters 171
V.4 $S(\mathrm{N} \leftarrow \mathrm{N})$ values for ^{211}At and ^{225}Ac uniformly distributed in the nucleus of spherical cells of different sizes 173
V.5 Enhancement factor of α-particle emitters over ^{177}Lu 174
A.1 Ground state of H_2O in the molecular orbital self-consistent field linear combination of atomic orbitals (MO-SCF-LCAO) description 223
B.1 Population, ionization potentials and average kinetic energies of the molecular orbitals (MOs) of adenine 224

B.2 Population, ionization potentials and average kinetic energies of the MOs of thymine 225
B.3 Population, ionization potentials and average kinetic energies of the MOs of cytosine 226
B.4 Population, ionization potentials and average kinetic energies of the MOs of guanine 227
B.5 Population, ionization potentials and average kinetic energies of the MOs of the sugar-phosphate backbone 228

List of abbreviations

a.u.	Atomic units
AE	Auger electron
BEA	Binary encounter approximation
BEB	Binary-encounter-Bethe
BED	Binary-encounter-dipole
CDW	Continuum distorted wave
CDW-EIS	Continuum distorted wave - eikonal initial state
CE	Internal conversion electron
CM	Center-of-mass
CNDO	Complete neglect of differential overlap
CSDA	Continuous slowing down approximation
CT	Computed tomography
DDCS	Double differential cross section
DNA	Deoxyribonucleic acid
DSB	Double-strand break
DWBA	Distorted wave Born approximation
EC	Electron capture
ELF	Energy loss function
FBA-CW	First Born approximation - Coulomb wave
HOMO	Highest occupied molecular orbital
IAEA	International Atomic Energy Agency
IC	Internal conversion
ICRP	International Commission on Radiological Protection
ICRU	International Commission on Radiation Units and Measurements
IMFP	Inelastic mean free path
IT	Isomeric transition
LCAO	Linear combination of atomic orbitals
LET	Linear energy transfer
LINAC	Linear particle accelerator

MC	Monte Carlo
MCCH	Monte Carlo condensed-history
MCTS	Monte Carlo track structure
MFP	Mean free path
MIRD	Committee on Medical Internal Radiation Dose
MO	Molecular orbital
MO-SCF-LCAO	Molecular orbital self-consistent field linear combination of atomic orbitals
NHL	Non-Hodgkin's lymphoma
NIST	National Institute of Science and Technology
PET	Positron emission tomography
PRRT	Peptide receptor radionuclide therapy
PSMA	Prostate-specific membrane antigen
PWBA	Plane-wave first Born approximation
RBEB	Relativistic binary-encounter-Bethe
RHF	Roothaan-Hartree-Fock
RN	Recoil daughter nucleus
SCF	Self-consistent field
SDCS	Single differential cross section
SPECT	Single-photon emission computed tomography
SSB	Single-strand break
TAT	Targeted alpha therapy
TCS	Total cross section
TDCS	Triple differential cross section
TICS	Total ionization cross section
TRT	Targeted radionuclide therapy
XML	Extensible Markup Language

GENERAL INTRODUCTION

Cancer remains nowadays a leading cause of mortality worldwide. In some cases, such as metastatic tumors, the best therapies currently available have only limited success at improving patient survival. Besides, after a period of remission (which may extend from some months up to several years after the treatment of the original tumor), cancer may come back because of occult isolated tumor cells or micrometastases. For these reasons, alternative therapeutic strategies able to reduce the risk of cancer recurrence, as well as to prolong patients' survival and their quality of life must be explored. In this context, targeted radionuclide therapy (TRT) is a cancer treatment approach that has regained interest in recent years. The basic principle of TRT is attaching a radioactive isotope to tumor-specific carrier molecules that target the tumor cells or the tumor microenvironment for delivering a cytotoxic radiation dose to the tumor. The radioactive source may emit β^--particles, Auger electrons, α-particles or a combination of all these radiations. However, thus far the clinical applications of TRT have almost exclusively made use of high-energy β^- emitters. The latter have shown to be effective in the treatment of advanced disease, but they are less adapted to the treatment of micrometastases or minimal residual disease, and have the drawback of increasing the toxicity to the surrounding healthy tissue. On the other hand, several studies have suggested that Auger electron and α-particle emitting radionuclides may be more appropriate against small lesions, particularly for irradiating isolated tumor cells and micrometastases.

The introduction of new radionuclides for clinical use is a long and complex process that must begin with a detailed investigation of the radionuclide's physical and chemical properties. It is only after gathering enough preclinical evidence and exploring all the risks and benefits of a new radiopharmaceutical that clinical translation can be contemplated. It is in the context of preclinical studies that numerical simulations can provide valuable information about the performance of a given radionuclide. In particular, Monte Carlo codes are extremely useful tools to determine the pattern of energy deposition in tumors following the decay of a radionuclide.

The main purpose of this thesis is to extend the Monte Carlo track structure code

TILDA-V to model the full transport of α-particles in a biological medium, for using it as an assessment tool in TRT.

The specific objectives of this thesis are:

- To investigate the track parameters of protons and electrons in biological media through the improvement and validation of *TILDA-V* and EPOTRAN, two homemade Monte Carlo track structure codes.
- To evaluate the effect of the biological medium description (water versus DNA) on key physical quantities characterizing charged particle transport and, more specifically, on the radiation absorbed dose.
- To extend the *TILDA-V* Monte Carlo track structure code to simulate the transport of α-particles in a biological medium, considering the various charge states and interactions of helium ions.
- To investigate, by means of Monte Carlo simulations, the relative performance of some promising β^-, Auger electron and α-particle emitting radionuclides at irradiating tumor cells (isolated or within a cell cluster), in order to determine their potential for TRT.

This manuscript is structured as follows:

- Chapter I introduces the basic concepts behind the Monte Carlo method, as applied in the field of radiation transport. The purpose of this chapter is to present the underlying assumptions common to most Monte Carlo simulations, highlighting the advantages and limitations of this methodology, used throughout the thesis. The two types of Monte Carlo codes for radiation transport (condensed-history and track structure) are described and a brief review of the main existing codes is provided as well. Finally, we discuss the *TILDA-V* Monte Carlo code, its unique features compared to other codes, its state at the beginning of this thesis and its current capabilities.
- Chapter II is devoted to the description of the biological medium as modeled in this work, as well as to the description of all relevant physical processes that must be taken into account to simulate the full slowing-down of protons, α-particles and electrons in matter. Particular emphasis is given to the theoretical and semiempirical models chosen to calculate the cross sections of the different charged particle interactions.
- In Chapter III, we explain the benchmark process carried out to validate our proton and electron transport simulations in water and DNA. We present our calculations of

track parameters (mean free paths, stopping power, range, radial dose distribution) and perform a comprehensive comparison of our results with available data in the literature. We also report a first *in silico* dosimetry study regarding the proton irradiation of a single tumor cell.

- In Chapter IV, we discuss some of the most interesting β^- and Auger electron emitters for TRT. We describe in detail the simulations carried out with CELLDOSE (an extension of the EPOTRAN code for dosimetry applications) to evaluate the performance of these radionuclides at irradiating single tumor cells and a cell cluster representing a micrometastasis. We report our results in terms of cellular S-values and normalized absorbed doses to the nuclei of the tumor cells. We analyze the impact of changing the nucleus composition and varying the radionuclide distribution within the cell on the absorbed dose to the cell nucleus.

- In Chapter V, we use the new version of *TILDA-V* to compute the stopping power and range of α-particles in water. Then, we review the fundamental aspects of α-decay and discuss the characteristics of some promising α-particle emitting radionuclides for TRT. We explain the approach implemented in our code to model the decay series of these radionuclides and the subsequent transport of the emitted radiations. Finally, we report the cellular S-values computed with CELLDOSE for the α-particle emitters and compare them with the results previously obtained for ^{177}Lu, a β^- emitter currently seen as the reference in TRT.

INTRODUCTION GÉNÉRALE

Le cancer reste aujourd'hui une des principales causes de mortalité dans le monde. Dans certains cas, comme les tumeurs métastatiques, les meilleures thérapies actuellement disponibles n'ont qu'un succès limité pour augmenter les taux de survie. En outre, après une période de rémission (qui peut s'étendre de quelques mois à plusieurs années après le traitement de la tumeur primitive), le cancer peut réapparaître à cause de cellules tumorales occultes isolées ou de micrométastases. Pour ces raisons, des stratégies thérapeutiques alternatives capables de réduire le risque de récidive du cancer, ainsi que de prolonger la survie des patients et leur qualité de vie doivent être explorées. Dans ce contexte, la radiothérapie interne vectorisée (RIV) est une approche thérapeutique qui a regagné de l'intérêt ces dernières années. Le principe de base de la RIV est d'attacher un isotope radioactif à des molécules vectrices spécifiques de la tumeur pour cibler les cellules tumorales ou le microenvironnement tumoral afin de délivrer une dose de rayonnement cytotoxique à la tumeur. La source radioactive peut émettre des particules β^-, des électrons Auger, des particules α ou une combinaison de toutes ces radiations. Cependant, jusqu'à présent, les applications cliniques de la RIV ont utilisé presque exclusivement des émetteurs β^- de haute énergie. Ces derniers se sont révélés efficaces dans le traitement de la maladie avancée, mais ils sont moins adaptés au traitement des micrométastases ou de la maladie résiduelle minime, et présentent l'inconvénient d'augmenter les effets toxiques sur les tissus sains avoisinants. D'autre part, plusieurs études ont suggéré que les radionucléides émetteurs d'électrons Auger et de particules α pourraient être plus appropriés contre les petites tumeurs, en particulier pour l'irradiation de cellules tumorales isolées et de micrométastases.

L'introduction de nouveaux radionucléides à usage clinique est un processus long et complexe qui doit commencer par une étude détaillée des propriétés physiques et chimiques du radionucléide. Ce n'est qu'après avoir rassemblé suffisamment de preuves précliniques et étudié tous les risques et avantages d'un nouveau radiopharmaceutique que la translation clinique peut être envisagée. C'est dans le cadre des études précliniques que les simulations numériques peuvent fournir des informations précieuses sur la performance d'un radionucléide donné. En particulier, les codes Monte Carlo sont des

outils extrêmement utiles qui peuvent fournir une « cartographie » des dépôts d'énergie dans les tumeurs suite à la désintégration d'un radionucléide.

Le but principal de cette thèse est d'étendre le code Monte Carlo de structure de trace *TILDA-V* pour modéliser le transport complet des particules α dans un milieu biologique, afin de l'utiliser comme outil d'évaluation en RIV.

Les objectifs spécifiques de cette thèse sont:

- Étudier les paramètres physiques pertinents dans le transport de protons et des électrons dans des milieux biologiques grâce à l'amélioration et à la validation des simulations avec *TILDA-V* et EPOTRAN, deux codes Monte Carlo de structure de trace maison.

- Évaluer l'effet de la description du milieu biologique (de l'eau par opposition à l'ADN) sur les grandeurs physiques clés caractérisant le transport des particules chargées et, plus spécifiquement, sur la dose absorbée.

- Étendre le code Monte Carlo de structure de trace *TILDA-V* pour simuler le transport de particules α dans un milieu biologique, en considérant les différents états de charge et les interactions des ions d'hélium.

- Étudier, au moyen de simulations Monte Carlo, l'efficacité relative de certains radionucléides émetteurs de particules β^-, d'électrons Auger et de particules α prometteurs pour irradier des cellules tumorales (isolées ou dans un amas de cellules), afin de déterminer leur potentiel pour la RIV.

Ce manuscrit est structuré comme suit:

- Le Chapitre I présente les concepts de base de la méthode Monte Carlo, telle qu'elle est appliquée dans le domaine du transport des rayonnements. Le but de ce chapitre est de présenter les hypothèses sous-jacentes communes à la plupart des simulations Monte Carlo, en soulignant les avantages et les limites de cette méthodologie, utilisée tout au long de la thèse. Les deux types de codes Monte Carlo pour le transport des rayonnements (histoire condensée et structure de trace) sont décrits et une brève analyse des principaux codes existants est également fournie. Enfin, nous abordons le code Monte Carlo *TILDA-V* , ses caractéristiques uniques par rapport aux autres codes, son état au début de cette thèse et ses capacités actuelles.

- Le Chapitre II est consacré à la description du milieu biologique tel qu'il est modélisé dans ce travail, ainsi qu'à la description de tous les processus physiques qui doivent être pris en compte pour simuler le ralentissement complet des protons,

des particules α et des électrons dans la matière. Un accent particulier est mis sur les modèles théoriques et semi-empiriques choisis pour calculer les sections efficaces pour les différentes interactions des particules chargées.

- Dans le Chapitre III, nous expliquons le processus de benchmark réalisé pour valider nos simulations de transport de protons et d'électrons dans l'eau et l'ADN. Nous présentons nos calculs des paramètres physiques pertinents (libre parcours moyen, pouvoir d'arrêt, parcours [range], distribution de dose radiale) pour simuler le transport de ces particules et effectuons une comparaison complète de nos résultats avec les données trouvées dans la littérature. Nous rapportons également une première étude de dosimétrie *in silico* concernant l'irradiation par protons d'une cellule tumorale isolée.

- Dans le Chapitre IV, nous abordons les émetteurs β^- et d'électrons Auger les plus intéressants pour la RIV. Nous décrivons en détail les simulations réalisées avec CELLDOSE (une extension du code EPOTRAN pour les applications en dosimétrie) pour évaluer l'efficacité de ces radionucléides à irradier des cellules tumorales isolées et un amas de cellules représentant une micrométastase. Nous rapportons nos résultats en termes de facteurs S (dose moyenne absorbée par unité d'activité cumulée) cellulaires et de doses absorbées normalisées aux noyaux des cellules tumorales. Nous analysons l'impact sur la dose absorbée au noyau cellulaire de modifier la composition du noyau et la distribution des radionucléides dans la cellule.

- Dans le Chapitre V, nous utilisons la nouvelle version de *TILDA-V* pour calculer le pouvoir d'arrêt et le parcours des particules α dans l'eau. Ensuite, nous passons en revue les aspects fondamentaux de la désintégration α et discutons les caractéristiques de certains radionucléides émetteurs de particules α prometteurs pour la RIV. Nous expliquons l'approche mise en œuvre dans notre code pour modéliser les chaînes de désintégration de ces radionucléides et le transport ultérieur des radiations émises. Enfin, nous rapportons les facteurs S cellulaires calculées avec CELLDOSE pour les émetteurs α et nous les comparons aux résultats précédemment obtenus pour le ^{177}Lu, un émetteur β^- actuellement vu comme référence en RIV.

CHAPTER I

THE MONTE CARLO METHOD AND ITS APPLICATIONS IN RADIATION TRANSPORT

Contents

I.1 Introduction **9**

I.2 Basic aspects of Monte Carlo simulations for radiation transport . . . **11**

I.2.1 Assumptions in Monte Carlo radiation transport simulations . 11

I.2.2 Random sampling of probability distributions 13

I.3 Monte Carlo codes for radiation transport **15**

I.3.1 The condensed-history Monte Carlo approach 15

I.3.2 The Monte Carlo track structure approach 19

I.4 The ***TILDA-V*** MCTS code **27**

I.4.1 General features 27

I.4.2 Input data and simulation setup 30

I.4.3 Outlook 35

Conclusions **35**

I.1 Introduction

The interactions of radiation with matter are intrinsically stochastic phenomena. When charged particles traverse a material, many variables come into play that in the end may determine macroscopic outcomes, such as the energy deposition pattern in the medium of interest, the mean range of the particles and the energy loss per length unit. However, the history or fate of a single incident particle is mainly governed by randomness. It

seems then reasonable to make use of probabilistic or non-deterministic approaches to deal with the random behavior of radiations.

The Monte Carlo (MC) method is the best known example of a non-deterministic approach applied to radiation transport. The MC method is basically a numerical technique that helps solving real-world problems by means of statistical samplings. In the case of radiation transport, random samplings are applied to determine the microscopic details of the radio-induced interactions in order to describe, step by step, the slowing-down of the incident particle. The full history of the radiation transport is then accessible, interaction after interaction, leading to macroscopic information on the energy transfers in the medium of interest.

While the roots of the MC method can be traced back to the eighteenth century with the needle problem formulated by Comte de Buffon, the term "Monte Carlo method" and its modern interpretation were officially "born" in 1949 with the paper of Metropolis and Ulam [42]. Since then the MC method has been exploited in very different domains with various purposes, going from the design of nuclear weapons to the forecast of stock prices in finance, to medical applications related to radiation dosimetry for cancer treatment. It is well beyond the scope of this dissertation to provide a comprehensive review on the history and evolution of the MC method and its applications in medical physics, even more so when excellent works have already been published on the subject (see for example [43, 44] and references therein). Let us, however, mention as a point of departure for the following discussion some of the milestones in this field. The seminal work of Berger [45] summarized the physical aspects behind a MC simulation and introduced the condensed-history technique for electron and photon transport, which is still used nowadays in many general-purpose MC codes [43] (see Section I.3.1). The first MC track structure codes appeared some years later, as the need of having a complete detailed description of all the interactions along a charged particle track became evident to understand the chemical and biological responses to ionizing radiation [46]. The revolution in the computer industry also played a major role in the development of such track structure codes.

The purpose of this chapter is to present the general aspects of the MC method, its basic assumptions for applications in radiation transport and the specificities of the technique as implemented in our MC code. The chapter is structured as follows:

- The basic ideas behind MC simulations for radiation transport are discussed in Section I.2.

- In Sections I.3.1 and I.3.2, we introduce the two most common techniques implemented in MC simulations, namely, the condensed-history and the track structure approaches. The features of some well-known MC codes are also presented.

- Finally, we provide in Section I.4 the details of the *TILDA-V* code, the main subject of this thesis.

I.2 Basic aspects of Monte Carlo simulations for radiation transport

Contrary to deterministic methods which deal directly with the linear Boltzmann transport equation, the MC method provides a probabilistic solution to radiation transport problems. As mentioned above, such an approach is well-suited for this purpose given the stochastic behavior of ionizing radiation interacting with matter. In a MC simulation, radiation transport is seen from the perspective of an individual particle propagating through a medium and taking part in a series of events (interactions or collisions) according to its nature. These events are described by probability distributions obtained from the interaction cross sections. Each event is defined by a set of parameters necessary to account for the energy transfers and angular changes resulting from a physical process. These parameters include:

- The potential energy, locally deposited in the target when ionization or excitation occurs.
- The kinetic energy of the scattered primary particle.
- The kinetic energy of the secondary particles (e.g., electrons emitted as a result of target ionization, projectile electron loss or target relaxation via Auger effect).
- The scattering and ejection angles of the primary and secondary particle, respectively.

I.2.1 Assumptions in Monte Carlo radiation transport simulations

The application of the MC method in radiation transport is based on the following assumptions [47]:

1. The classical view of a particle's trajectory is retained. According to Heisenberg uncertainty principle, the uncertainty on the position of a particle, Δx, is given by its de Broglie wavelength, λ, which must be smaller than the characteristic length L of the system:

$$\Delta x \approx \lambda \ll L \ . \tag{I.1}$$

   For MC simulations, the particle's trajectory is well-defined if its de Broglie wavelength λ is small compared to the mean free path (MFP), $\overline{\lambda}$. In addition, if $\overline{\lambda}$ is

large compared to the interatomic distance d in the material, then the condition to satisfy becomes:

$$\lambda \ll d \ . \tag{I.2}$$

The uncertainty Δx in the position of a particle can be computed as:

$$\Delta x \ (\text{Å}) \approx \frac{4.5 \times 10^{-2}}{\sqrt{A_{\text{ion}} E_{\text{ion}}}} \ , \tag{I.3}$$

where A_{ion} is the mass of the ion in atomic mass units (amu), and E_{ion} the kinetic energy of the ion in eV. For the ion energy range considered in this work (10 keV u^{-1} – 100 MeV u^{-1}) the maximum uncertainty in the position is of the order of 10^{-4} Å for protons and α-particles, which is smaller than the O-H bond length in the water molecule ($\sim$ 0.96 Å).

2. The history of each particle can be described as a sequence of binary collisions between the incident particle and the atoms or molecules in the traversed medium. This assumption implies that particles are represented by wave packets which have a short extension compared to the interatomic distance. Besides, the range of the interaction potential must be weak compared to the interatomic distance. However, the latter is not true for the Coulomb interaction, which has infinite range. Charged particles can induce collective excitations of the valence electrons (plasmons) by Coulomb interactions at large distances, a process that cannot be taken into account in binary collisions. The energy E_p associated to this type of interaction is given by:

$$E_p = \hbar \omega_p \ , \tag{I.4}$$

where ω_p is the plasma frequency of the medium. For liquid water, usually used as a substitute for biological material, $E_p = 21$ eV. The contribution of this energy to the damage induced by inelastic interactions will be small because it is distributed over many electrons. Moreover, in this work the medium is always considered in vapor state, thus plasmon contributions are neglected.

3. Interactions between secondary electrons are neglected. The average energy of the emitted electrons during ionization is of some tens of eV. Given the low velocity of these electrons, they are expected to interact with each other before propagating in the medium. A MC simulation cannot include these interactions. However, given the low-energy and short range of the emitted electrons, the energy deposits resulting from their interaction will take place close to the primary ion track. Since the density of events along and around the ion track is very large, it is assumed that the effect of the interactions between secondary electrons will have no appreciable effect on the spatial energy distribution.

4. Closely related to the previous assumptions is the fact that each event is indepen-

dent of any other. In other words, the particle has no memory about past events: the distance to the next interaction and the type of interaction depend only on the type of the particle and its current energy. Interactions occur instantaneously and the particle moves with constant speed and direction between two events.

I.2.2 Random sampling of probability distributions

The definition of an event in a MC simulation requires to determine several quantities, such as the distance traveled by the particle before a collision takes place and the type of interaction. These quantities are obtained by means of random sampling on probability distributions. To perform random sampling, pseudo-random number generators must be used.

I.2.2.1 Random number generation

Random number generation is a fundamental aspect of MC simulations. By definition, in a sequence of random numbers it is not possible to predict the number N_{i+1} based on the knowledge of the N_i previous numbers. The common approaches to generate random numbers are based either on experiments or on computer algorithms. The former approach provides true randomness and random number sequences can be obtained, for instance, from counting the number of decays in a radioactive sample over a specified time interval [48]. This approach has, however, two major disadvantages, namely: 1) the procedure is too slow and unpractical to be used in a MC code. It would require either some sort of interface between the system producing the random numbers and the computer performing the simulations, or the storage of large amounts of data; 2) the lack of repeatability, needed for debugging MC codes. Indeed, to find and correct errors in a MC code, it is usually necessary to perform tests with exactly the same number sequence [49]. For these reasons, pseudo-random number generators based on computer algorithms are preferred.

The MC simulations performed in this work were based on the Mersenne Twister pseudo-random number generating algorithm [50], as implemented in C++. The Mersenne Twister is a very fast random number generator of period $2^{19937} - 1$. It is used in many computer applications and is considered reliable for MC simulations.

I.2.2.2 General approach for the random sampling of a physical quantity

The underlying physics in a MC simulation is contained in the interaction cross sections. To be used for random sampling, the cross sections are converted to probability densities. Then, cumulative probability distributions are obtained by integration. For instance, for a continuous random variable x representing a physical quantity having a non-uniform

probability density $p(x)$ in the interval [a,b], the cumulative probability is given by:

$$P(x) = \int_a^x p(x')dx' \,. \tag{I.5}$$

By using an appropriate pseudo-random number generator, a random variable η with uniform distribution $q(\eta)$ over [0,1] is obtained. The relation between x and η can be written as [48]:

$$p(x)dx = q(\eta)d\eta \,. \tag{I.6}$$

By integrating

$$\int_a^x p(x')dx' = \int_0^\eta d\eta' \,, \tag{I.7}$$

or

$$P(x) = \eta \tag{I.8}$$

The variable x can then be obtained in terms of the random number η by inversion:

$$x = P^{-1}(\eta) \,. \tag{I.9}$$

I.2.2.3 Distance to next event

The distance λ traveled by the particle to the next interaction is described by a Poisson process with a probability density function given by:

$$p(\lambda) = \frac{1}{\overline{\lambda}} \exp\left(\frac{-\lambda}{\overline{\lambda}}\right) \,, \tag{I.10}$$

where $\overline{\lambda}$ is the average distance between two events, i.e., the mean free path (MFP), which can be written as:

$$\overline{\lambda} = \frac{1}{N_0\, \sigma_T} \,, \tag{I.11}$$

where σ_T denotes the total cross section, which includes the contributions of all interactions considered for the incident particle. N_0 is the number of atoms or molecules in the medium per unit volume, computed as:

$$N_0 = \frac{\rho N_A}{A_{\text{mol}}} \,, \tag{I.12}$$

with N_A the Avogadro constant, and ρ and A_{mol} the density and the molar mass of the material, respectively. For the media simulated in this thesis, $N_0 = 3.3 \times 10^{22}$ molecules cm^{-3} for water and $N_0 = 8.2 \times 10^{20}$ molecules cm^{-3} for hydrated DNA (see Chapter II). The cumulative probability distribution is given by:

$$P(\lambda) = \int_0^\lambda \frac{1}{\overline{\lambda}} \exp\left(\frac{-\lambda'}{\overline{\lambda}}\right) d\lambda' = 1 - \exp\left(\frac{-\lambda}{\overline{\lambda}}\right) \,. \tag{I.13}$$

By using Eq. I.9 and a random number η uniformly distributed over [0,1], the distance to the next event is obtained:

$$\lambda = P^{-1}(\eta) = -\overline{\lambda}\ln(1-\eta) = -\overline{\lambda}\ln(\eta') \tag{I.14}$$

with $0 \leq \eta' \leq 1$ as well.

I.2.2.4 Type of interaction

After determining the distance at which an event takes place, the next step is the random sampling of the type of interaction occurring at that point. In this case, we deal with a discrete random variable. The probability of occurrence of an interaction of type i is given by:

$$P_i = \frac{\sigma_i}{\sigma_T} = \frac{\overline{\lambda}_i^{-1}}{\sum_k \overline{\lambda}_k^{-1}} \tag{I.15}$$

with σ_i and $\overline{\lambda}_i$ the cross section and the MFP associated to the interaction of type i, respectively. The type of interaction is obtained from a uniform random number η by satisfying the relation:

$$\sum_{j=0}^{i-1} P_j \leq \eta \leq \sum_{j=0}^{i} P_j \ . \tag{I.16}$$

Additional random samplings are carried out to determine the molecular orbital involved in the inelastic processes (ionization or electron capture), or the excited state of the molecule (electronic excitation), by using the partial cross sections. Finally, in case of K-shell ionization or electron capture, the energy of the emitted Auger electron is obtained by a random sampling procedure using the non-radiative transition probabilities (see Ref. [1]).

I.3 Monte Carlo codes for radiation transport

MC radiation transport codes can be divided into two groups, depending on how the particles are tracked: Monte Carlo condensed-history (MCCH) codes and Monte Carlo track structure (MCTS) codes. Both approaches are described in the following sections.

I.3.1 The condensed-history Monte Carlo approach

In Monte Carlo condensed-history (MCCH) codes, also known as general-purpose MC codes, a particle's path is divided into discrete steps, each step encompassing a large number of collision processes. The deflection of the particle resulting from elastic collisions is determined using multiple scattering theories. Energy losses are computed from tabulated stopping power values. Thus, both angular changes in the particle's trajectory and energy losses are approximated at the end of each step [51].

There are basically two classes of condensed-history algorithms. A class I algorithm groups all collisions, uses a predetermined set of path lengths and performs the random sampling of interactions at the end of the step [52]. The class I scheme allows to consider energy loss straggling, but the correlation between large energy losses and

secondary particle creation is lost. Class II algorithms classify the collisions as "soft" or "catastrophic", according to a given threshold. Soft collisions, i.e., those below the threshold, are grouped; catastrophic collisions, however, are simulated in an analog manner (event-by-event) [53].

MCCH codes have the important advantage of drastically reducing computation time and provide results accurate enough for most applications in radiation therapy, where relevant dimensions are always of the order of or greater than 1 mm.

On the other hand, MCCH codes may have significant shortcomings when dealing with very small geometries or low-energy transfers [54]. Even though it is difficult to establish a strict limit in terms of energy to change from a condensed-history technique to an event-by-event approach, MCCH codes are not considered very reliable for simulating electron transport below 1 keV, even when a careful choice of the simulation parameters is made [55, 56]. Moreover, they are not seen as the appropriate tool for microdosimetry or to study the interaction of radiation with the constituents of a cell or with biomolecules.

A great number of MCCH codes have been developed since the introduction of the MC method. Some well-known MCCH codes are EGSnrc, MCNP, GEANT4, FLUKA, PENELOPE and PHITS.

I.3.1.1 EGSnrc

EGSnrc is perhaps the most widely used MC code in medical physics applications. It is the most recent version of the EGS (**E**lectron **G**amma **S**hower) code, originally developed at the Stanford Linear Accelerator Center (SLAC) in the 1970s, and now developed by the National Research Council (NRC) of Canada. EGSnrc is able to simulate the coupled transport of electrons, positrons and photons in arbitrary geometries and materials for energies ranging from a few tens of keV up to a few hundred GeV. In EGSnrc, all particles are transported in steps of random length and the code goes seamlessly from a single scattering model for short steps to an accurate multiple scattering model at large steps [57]. EGSnrc is well-suited for modeling radiation sources for diagnostic and therapy purposes, including the simulation of linear particle accelerators (LINACs). EGSnrc unique features include the tracking of separate electron spins and the treatment of Doppler broadening, which are interesting for research on synchrotron radiation light sources [44].

I.3.1.2 MCNP

The MCNP (**M**onte **C**arlo **N**-**P**article) code was created in 1977 at Los Alamos National Laboratory (LANL). A very versatile code, MCNP can be used in a variety of contexts, including radiation dosimetry, radiation shielding, medical physics, nuclear criticality safety studies and radiation detector design. Although it was originally conceived for

simulating the transport of neutrons and photons, and is indeed particularly powerful for that end, the latest version of the code (MCNP6) is able to transport 37 particle types. The models and data libraries integrated into MCNP cover different energy regimes: from thermal (< 1 eV) up to TeV energies for neutrons; 1 eV – 100 GeV for photons; 10 eV – 1 GeV for electrons and positrons; and energies ≥ 1 MeV for protons and heavy ions [58]. A single-event approach [59] was introduced in MCNP to extend the electron/photon transport to energies below 1 keV, which means that it can emulate the behavior of a track structure code for low-energy electrons and photons.

I.3.1.3 GEANT4

The GEANT4 (**GE**ometry **AN**d **T**racking) code is developed and maintained by an international collaboration of scientists and software engineers. First released in 1998, GEANT4 has experienced many updates and expansions and is presently a robust and complex object-oriented open-source MC simulation toolkit with a variety of application domains. For instance, GEANT4 is widely used for high-energy physics experiments at the Large Hadron Collider (LHC) and for the design of spacecraft at the European Space Agency (ESA) and the National Aeronautics and Space Administration (NASA) [60]. In medical physics, the development of the GATE (GEANT4 Application for Emission Tomography) platform has enabled the modeling of positron emission tomography (PET), single-photon emission computed tomography (SPECT) and X-ray computed tomography (CT) imaging systems, as well as of radiation therapy experiments [61].

In accordance with its object-oriented design implemented in C++, GEANT4 organizes particle types and interaction models into classes ("physics lists") and modules ("physics constructors"). The electromagnetic interactions of leptons, photons, hadrons and ions are implemented in GEANT4 through several constructors. The models included in the standard EM package can simulate particles with energies from 1 keV up to 10 PeV. In addition, the models contained in the low-energy EM package extend the applicability of GEANT4 down to 100 eV [62].

Among other interesting features, GEANT4 has a module to simulate radioactive decays. The module can handle α, β^-, β^+, isomeric transition (IT) and electron capture (EC) decays, and can be applied to generic ions both in flight and at rest. The decay data is taken from the Evaluated Nuclear Structure Data File (ENSDF) [60].

Last but not least, the GEANT4-DNA project (see Section I.3.2.3) has extended the physics models and processes of GEANT4 to allow the event-by-event simulation of particle interactions in liquid water down to a few tens of eV, with the purpose of investigating the biological damage of low-energy ionizing radiation.

I.3.1.4 FLUKA

FLUKA (**FLU**ktuierende **KA**skade) is a MCCH code jointly developed by the European Organization for Nuclear Research (CERN) and the Italian Institute for Nuclear Physics (INFN). The code simulates the interaction and transport of hadrons, heavy ions and electromagnetic particles with energies ranging from 1 keV up to 10 PeV. The simulations can be performed in arbitrary materials and complex geometries, including particle transport in magnetic fields. The transport of charged particles is performed through an original multiple Coulomb scattering algorithm, supplemented by an optional single scattering method [63].

FLUKA has been used to simulate high-energy physics experiments at the LHC, as well as in various medical applications, including hadrontherapy [64]. Its graphical user interface, Flair, is equipped with an intuitive PET scanner geometry generator, and is able to translate DICOM (Digital Imaging and Communications in Medicine) files into voxel geometry or 3D dose distributions. For more details, the reader is referred to the article by Battistoni *et al*. [63] and references therein.

I.3.1.5 PENELOPE

PENELOPE (**PEN**etration and **E**nergy **LO**ss of **P**ositrons and **E**lectrons) is a general-purpose MC code first released in 1996. The code is written in FORTRAN and is able to simulate the coupled transport of electrons, positrons and photons in arbitrary materials and complex geometries limited by quadric surfaces [65].

The following photon interactions are included in PENELOPE: Rayleigh and Compton scattering, photoelectric absorption, and pair production. For electrons and positrons, the code takes into account elastic scattering, inelastic collisions, inner-shell ionization, Bremsstrahlung emission, and positron annihilation.

PENELOPE uses a mixed (class II) scheme for electrons and positrons. Hard interactions, i.e., those for which the scattering angle or the energy loss is larger than certain cutoff values, are simulated by random sampling from the corresponding differential cross sections. The combined effect of all soft interactions in a step is simulated as a single artificial event for which the energy loss and the angular deflection of the particle are obtained from multiple-scattering distributions [65].

In principle, PENELOPE can follow particles within the energy range from 50 eV to 1 GeV. Nevertheless, Salvat [65] has recently explained that simulations results for energies below 1 keV should be regarded as semi-quantitative.

The PENELOPE system has been used for different medical physics applications, such as medical imaging [66], dosimetric characterization of brachytherapy sources [67], characterization of radiation fields produced by LINACs [68], and TRT [40, 69], among others.

I.3.1.6 PHITS

PHITS (**P**article and **H**eavy **I**on **T**ransport code **S**ystem) is a general-purpose MC code developed under collaboration between several institutes, including the Japan Atomic Energy Agency (JAEA), the Research Organization for Information Science and Technology (RIST) and the High Energy Accelerator Research Organization (KEK).

PHITS implements various physics models to allow the transport of many types of particles (including photons, electrons, neutrons, protons, α-particles and heavy ions) over a wide energy range extending from 0.1 meV up to 1 TeV u^{-1} (see Ref. [70] and references therein).

The energy losses of protons, α-particles and all other charged particles (except for electrons and positrons) are computed by default with a modified version of the ATIMA algorithm [71]. On the other hand, the transport of electrons and positrons is based on the EGS5 algorithm [72].

In addition, PHITS can switch from a condensed-history to a track structure mode, although for the latter only the cross sections of liquid water have been implemented in the code [70]. The track structure mode allows the detailed simulation of electrons and positrons down to 1 meV (instead of the conventional low-energy cutoff of 1 keV), which is useful for investigating radiation-induced DNA damages. Very recently (from version 3.20 onward), this mode was extended to enable the track structure for proton and carbon ions based on the algorithms of the KURBUC code [73].

PHITS has been used in various areas of study, including accelerator design, radiation shielding and protection, medical physics, and cosmic-ray research (a comprehensive list of the studies performed with PHITS in these areas is available at `https://phits.jaea.go.jp/Reference.html`).

Some interesting features of PHITS in the context of medical physics include: the simulation of radioactive sources (and their time evolution), for which the nuclear decay data is based on the International Commission on Radiological Protection (ICRP) Publication 107 [18]; modules that allow the conversion of CT image data written in the DICOM format to PHITS-readable format.

I.3.2 The Monte Carlo track structure approach

Contrary to MCCH codes, Monte Carlo track structure (MCTS) codes follow both the primary and the secondary particles in an event-by-event manner, until their energy falls below a fixed cutoff value, usually determined by the validity of the interactions models.

Track structure simulations consist in a series of random samplings, which first determine the distance traveled by the particle, then the type of interaction taking place at the point of arrival and finally the full kinematics of the secondary particles eventually

created. To properly simulate the transport of particles in a given medium, MCTS codes require total and differential cross sections for describing the various particle-induced interactions. Most of the time, these cross sections are obtained using a combination of experimental data and theoretical models. It is worth noting that, in the end, the effectiveness and reliability of the code will depend on how accurate and complete the cross section database is [74].

The preferred medium for the simulations in most of the existing MCTS codes designed for applications in radiobiology and medical physics is water, since it has long been considered a good surrogate for tissue. A few codes have also included models which allow to explore in more detail the radiation-induced damage to biological targets, in particular to the DNA molecule.

MCTS codes are seen as a great tool to compute microdosimetry parameters with a high level of accuracy. Moreover, they are virtually the only technique capable of simulating quantitatively the DNA damages arising from the direct and indirect effects of ionizing radiation [54]. On the other hand, the results of MCTS simulations at very low incident energies and at the nanometer scale should always be interpreted with care. Some researchers have pointed out that a "classical" MC transport approach might be incorrect for electrons with energies below 1 keV, particularly in condensed media [75].

A review about the different MCTS codes used in radiation research has been given by Nikjoo *et al*. [76]. We have summarized in Table I.1 the basic features of some of these codes. In the following sections, we discuss in more detail the capabilities of the three most advanced MCTS codes found in the literature: KURBUC, PARTRAC and GEANT4-DNA.

Code name	Particle	Material / medium	Energy range	References
KURBUC (**K**yushu **U**niversity and **R**adio**B**iology **U**nit **C**ode)	Electrons and light ions	Water vapor and liquid water	Electrons: 10 eV – 10 MeV; protons: 1 keV – 300 MeV; α-particles: 1 keV u^{-1} – 2 MeV u^{-1}; carbon ions: 1 keV u^{-1} – 10 MeV u^{-1}	[4, 22, 77–80]
PARTRAC (**PAR**ticles **TRAC**ks)	Electrons, photons, protons, α-particles and other bare ions	Liquid water	Electrons: 10 eV – 10 MeV; protons and α-particles: 1 keV – 1 GeV	[81–83]
GEANT4-DNA	Electrons, protons, α-particles and other ions	Liquid water	Electrons: 7.4 eV – 1 MeV; protons: 100 eV – 100 MeV; α-particles: 1 keV – 400 MeV	[38, 84, 85]
LIonTrack (**L**ight **Ion** **Track**)	Protons, α-particles and other light ions	Liquid water	1 MeV u^{-1} – 300 MeV u^{-1}	[31]
PITS (**P**ositive **I**on **T**rack **S**imulation)	Positive ions	Various materials	$\geq$ 0.3 MeV u^{-1}	[86]
TRION	Electrons, photons and ions of Z $\leq$ 10	Water vapor	Electrons: 10 eV – 2 MeV; ions: 0.3 MeV u^{-1} – 200 MeV u^{-1}	[87]
MC4	Electrons, protons, α-particles and bare ions of Z $<$ 10	Water vapor and liquid water	Electrons: $>$ 10 eV; ions: $>$ 0.3 MeV u^{-1}	[88, 89]
NOREC (**N**ew **O**ak **R**idge **E**lectron transport **C**ode)	Electrons	Liquid water	10 eV – 1 MeV	[90]
RITRACKS / RETRACKS (**R**elativistic **I**on/**E**lectron **TRACKS**)	Electrons, light and heavy ions	Liquid water	Electrons: 1 eV – 100 MeV; ions: 0.1 MeV u^{-1} – 10 GeV u^{-1}	[91, 92]
PTra (**P**hysikalisch-Technische Bundesanstalt **Tra**ck-structure code)	Electrons, protons and α-particles	Various media, including liquid water and DNA	Electrons: 10 eV – 10 keV; protons: 0.3 – 10 MeV; α-particles: 1 – 10 MeV	[93, 94]

Table I.1 Some existing MCTS codes.

I.3.2.1 KURBUC

The **K**yushu **U**niversity and **R**adio**B**iology **U**nit **C**ode is a suite of MCTS codes for simulating the full slowing-down of electrons [77, 79], protons [22, 78], α-particles [4] and carbon ions in water [80]. KURBUC includes modules for simulating the prechemical and chemical stages of charged particle tracks in liquid water, being thus able to calculate the time-dependent yields of 11 radiolytic species produced by charged-particle impact [95]. We summarize here below the methods implemented to compute the interaction cross sections used in the code for the transport of electrons, protons and α-particles.

Electrons

KURBUC can simulate the slowing-down of electrons in water vapor with incident energies going from 10 eV up to 10 MeV. The code takes into account the processes of ionization, excitation and elastic scattering. Bremsstrahlung is neglected in the code because of its minor influence in the energy range considered in the simulations [77].

For kinetic energies $T > 10$ keV, the single differential cross sections (SDCS) for electron-impact ionization were computed with Seltzer's formula based on the Weizsäcker-Williams method [96], and then integrated to obtain the partial (i.e., per molecular orbital) and total ionization cross sections (TICS). In this energy range, total cross sections (TCS) for excitation were derived from an empirical approach provided by Berger and Wang [97]. For $T \leq 10$ keV, the inelastic cross sections were determined by appropriate fittings to the data of Paretzke [37].

The elastic scattering cross sections were calculated with the Rutherford formula considering the screening factor given by Molière [98]. For $T < 50$ keV a fitting to the experimental data of Nishimura [99] and Katase *et al.* [100] was performed.

The electron code was updated to include liquid water cross sections for simulations with energies in the range 10 eV – 10 keV [79].

Protons

KURBUC is able to simulate protons in the energy range 1 keV – 300 MeV. The code takes into account the change in the charge state of the projectiles. For proton beams that means considering both H^+ and the formation of H^0 (neutral hydrogen atoms). In the following, we will refer to both charge states as hydrogen ions.

TICS for protons of $T < 1$ MeV were obtained by means of a least-squares fit to the experimental data of Rudd *et al.* [101], while for neutral hydrogen atoms they were computed with the formula given by Green and McNeal [102]. For $T \geq 1$ MeV, the TICS for hydrogen ions were assumed to be equal to those for electrons of the same speed. The SDCS for hydrogen ions of $T \leq 1$ MeV were computed from the Rudd model [103]. Above this energy, SDCS were calculated from the binary encounter approximation

(BEA). Double differential cross sections (DDCS) were assumed to be equal for both hydrogen ions. For $T < 1$ MeV, the DDCS were obtained from various experimental data sets [104, 105], while for higher energies a classical kinematical relationship was applied [78].

The TCS for charge-transfer interactions (electron capture and electron loss) and excitation were computed using the formulas provided in the work by Miller and Green [5]. For the latter process, 28 excitation states were considered.

The elastic scattering cross sections for hydrogen ions with incident energies $T < 10$ MeV were determined from classical mechanics trajectory methods. For higher incident energies, the Mott scattering formula was applied (see [22, 78] and references therein).

Alpha particles

KURBUC can simulate the tracks of α-particles (He^{2+}) in the range 1 keV u^{-1} – 2 MeV u^{-1}, including the charge states He^{+} and He^{0}.

As for protons, the SDCS and TCS for elastic scattering were obtained from classical mechanics trajectory calculations, but using different screening parameters [4].

Charge-transfer cross sections were obtained by fitting available experimental data on different energy intervals. TCS for single- and double-electron capture for He^{2+} were fitted to the data of Rudd *et al.* [106]; TCS for electron capture and electron loss for He^{+} were fitted to the data of Rudd *et al.* [107] and Sataka *et al.* [108]; single-electron loss cross sections for He^{0} were fitted to the data of Allison [109] and Sataka *et al.* [108]; finally, TCS for double-electron loss for He^{0} were fitted to the data of Sataka *et al.* [108]. Smooth extrapolation was made for energies for which experimental data were lacking [4].

TICS for He^{2+} and He^{+} were obtained by fitting the experimental data of Rudd *et al.* [106, 107] and Toburen *et al.* [110]. Since for He^{0} no experimental cross sections were available, for energies lower than 100 keV u^{-1} the TICS were adjusted to fit the stopping powers recommended in the Report 49 of the International Commission on Radiation Units and Measurements (ICRU) [10]; for energies above 100 keV u^{-1}, it was assumed that the TICS for He^{0} were equal to those for He^{+}. SDCS for He^{2+} and He^{+} were obtained from a modified version of the Rudd model for protons [4, 103]. SDCS for He^{0} were assumed to be the same as for He^{+}. To determine the angular distribution of secondary electrons, the authors used random sampling from experimental and interpolated data for helium ions as well as for protons. This decision was made on the assumption that the differences in angular distributions between these ions were not very large, and because no model provided satisfactory results in the low-energy range considered in the simulations [4].

Finally, the excitation cross sections for all helium ions (He^{2+}, He^{+}, He^{0}) were assumed to be the same as for protons.

I.3.2.2 PARTRAC

PARTRAC (**PAR**ticles **TRAC**ks) is a state-of-the-art MCTS code designed to investigate the radiation-induced biological effects at the nanometer and micrometer scales. The code consists of several modules written in FORTRAN and interacting with one another to provide the necessary inputs for a given simulation [81, 82]. PARTRAC is able to simulate the transport of electrons, photons, protons, α-particles and other bare ions in liquid water. PARTRAC offers the possibility of simulating the physico-chemical and chemical stages of water radiolysis. In this sense, PARTRAC is, as KURBUC, a 4D MCTS code, i.e., it provides not only the spatial distribution of interactions, but also the time evolution of the chemical species generated by ionizing radiation. Therefore, the code covers both the direct and indirect radiation-induced damages to DNA. PARTRAC implements a multi-scale DNA model on which the physical and chemical track structures computed in liquid water are superposed. The DNA modeling in PARTRAC takes into account its different structural levels (double helix, chromatin fiber, chromosomes) and is based on an atom-by-atom description [82]. The code can calculate the levels of DNA single-strand breaks (SSB), simple and complex double-strand breaks (DSB), and chromosomal aberrations. Moreover, PARTRAC is able to simulate the repair of DSB via the non-homologous end-joining pathway [83].

Electrons and photons

PARTRAC can simulate the tracks of electrons with energies in the range 10 eV – 10 MeV. Inelastic cross sections for electrons were computed within the plane-wave first Born approximation (PWBA) with a model for the dielectric function of liquid water [111]. Five ionization levels and five excited states were considered. For incident energies greater than 10 keV, the relativistic Bethe approximation was used. For electrons below 500 eV, a semiempirical correction factor was applied [111]. Electron exchange was considered by means of a semiempirical model [81]. Electron elastic scattering was based on the atomic cross sections from the National Institute of Science and Technology (NIST) [112] for energies down to 1 keV. Phase-shift calculations were made for lower energies [113].

The cross sections for photon interactions in liquid water used in PARTRAC were obtained by applying the additivity rule and a density scaling to the atomic data contained in the Evaluated Photon Data Library, 1997 version (EPDL97). The database includes the processes of coherent scattering, photoelectric effect, Compton scattering, pair production, and relaxation through the emission of fluorescence photons or Auger

electrons [82].

Protons, alpha particles and heavier ions

PARTRAC simulates the tracks of protons and α-particles of energies between 1 keV and 1 GeV, taking into account all charge states: H^+ and H^0 for proton beams; He^{2+}, He^+ and He^0 for α-particle beams. Similar to electrons, the cross sections for excitation and ionization processes for H^+ and He^{2+} ions with energies above 1 MeV were modeled by the PWBA and Bethe approximations. At lower incident energies, semiempirical models were used: the Rudd model [103] and the Miller and Green model [5] for ionization and excitation cross sections, respectively. For H^0, only ionization was considered and the cross sections were obtained by applying a scaling function (depending only on the incident energy) to the ones for H^+, in order to reflect the screening of the nuclear charge by the electron in the hydrogen atom [114]. Ionization and excitation cross sections for He^+ and He^0 were obtained using an effective-charge scaling [115].

Angular distributions of secondary electrons were modeled as a superposition of the binary encounter peak (hard collisions) and of the dipole interaction (soft collisions) in the framework of the non-relativistic Bethe formula (see Ref. [116] for more details).

Cross sections for all charge-transfer processes were obtained from semiempirical models based on available experimental data on water vapor.

In PARTRAC, the elastic scattering of ions has been neglected.

The cross sections to simulate heavier (i.e., with atomic number $Z > 2$) bare ions in PARTRAC were obtained by scaling those of a proton of the same velocity. This scaling is based on the effective charge given by the Barkas formula. For these ions, charge-transfer processes were not considered [82].

I.3.2.3 GEANT4-DNA

GEANT4-DNA [38, 84, 85] is an extension of the GEANT4 MC toolkit to very low-energy interactions in liquid water oriented to radiation microdosimetry and the simulation of the biological damage induced by ionizing radiation. GEANT4-DNA was initiated by the European Space Agency to investigate the effects of radiation in astronauts, but since its first release in 2007 it has been used in many other applications. The code is now the product of an multidisciplinary international collaboration and is subject to a continuous improvement and validation process. GEANT4-DNA can simulate interaction-by-interaction the tracks of electrons, protons, α-particles and some other heavier ions in liquid water at the nanometer scale. GEANT4-DNA can take into account the direct and indirect effects of ionizing radiation. For the latter, GEANT4-DNA simulates the physico-chemical and chemical stages of water radiolysis up to 1 μs after irradiation. Moreover, the code provides several approaches to simulate DNA damage, namely: the

use of clustering algorithms; explicit geometrical models representing the DNA double helix structure; and a mixed approach combining the clustering algorithms with the geometrical models. The number of research studies making use of GEANT4-DNA has rapidly increased in the years since its appearance. Its application domains include conventional external beam radiation therapy, hadrontherapy, TRT and radiobiology. A review of the most relevant studies performed with GEANT4-DNA and published through 2015 was given by Incerti *et al*. [117].

Electrons

Electron transport in GEANT4-DNA covers the energy range from 7.4 eV up to 1 MeV. GEANT4-DNA offers the possibility of using three different sets of physics models for the simulation of electron interactions in liquid water. These sets of models or "physics constructors" are: the default models ("option 2"), the Ioannina models ("option 4") and the CPA100 models ("option 6"). The ionization and excitation cross sections in "option 2" are computed with the dielectric model of Emfietzoglou [118], while the elastic scattering is treated with the partial wave model [119]. The default physics constructor includes the modeling of attachment and vibrational excitation processes. "Option 4" introduces an upgraded version of the dielectric model of "option 2" which leads to a more accurate set of electron cross sections for ionization and excitation; in addition, it offers an alternative treatment to the elastic scattering process through the Uehara screened Rutherford model [77]. "Option 6" implements cross sections of the CPA100 track structure code. Excitation cross sections are calculated with the model developed by Dingfelder and co-workers [111]. For ionization, the binary-encounter-Bethe (BEB) model of Kim and Rudd [120] is applied. Finally, elastic scattering cross sections are based on partial wave calculations using the independent atom approximation. The low-energy cutoff for electrons varies slightly in the three physics constructors: 7.4 eV for "option 2"; 9 eV for "option 4"; and 11 eV for "option 6". For more details about the electron models in GEANT4-DNA, please see [121, 122] and references therein.

Protons and alpha particles

GEANT4-DNA can simulate protons of 100 eV – 100 MeV and α-particles with energies from 1 keV up to 400 MeV. The inelastic cross sections for protons are largely based on the work of Dingfelder *et al*. [114]. For energies above 500 keV, the dielectric formalism is used to obtain ionization and excitation cross sections. Below 500 keV, the semiempirical models of Rudd [103], for ionization, and of Miller and Green [5], for excitation, were applied.

Ionization and excitation cross sections for helium atoms and their charge states were obtained from the same semiempirical models by means of a speed scaling procedure

applied on the corresponding proton cross sections, which takes into account the effective charge of the incident ion [121].

As KURBUC and PARTRAC, GEANT4-DNA takes into account charge-transfer processes for protons and α-particles by means of semiempirical methods. For more details, the reader is referred to the work of Dingfelder *et al*. [114].

Elastic scattering cross sections for protons and α-particles were calculated within the classical framework [123].

Heavier ions

For ions heavier than helium, only the ionization process is considered in the code. The ionization cross sections were obtained using the Rudd formula with relativistic corrections [91]. This approach enables to simulate the impact of ^{7}Li, ^{9}Be, ^{11}B, ^{12}C, ^{14}N, ^{16}O, ^{28}Si and ^{56}Fe ions with energies from 1 MeV u^{-1} to 1 TeV u^{-1} on water targets [124].

I.4 The *TILDA-V* MCTS code

I.4.1 General features

TILDA-V (a French acronym for **T**ransport d'**I**ons **L**ourds **D**ans l'**A**qua et **V**ivo, i.e., "transport of heavy ions in water and living matter") is a homemade MCTS code created by Champion and co-workers [1] to simulate the interactions of ions in biological media. The code is written in C++ with OpenMP (Open Multi-Processing) parallelization. *TILDA-V* was thus far limited to the transport of protons, including neutral hydrogen atoms. In the context of this thesis, *TILDA-V* was extended to simulate the full slowing-down of α-particles, taking into account all helium charge states (He^{2+}, He^{+} and He^{0}). New routines were implemented as well for radiation dosimetry simulations in single cells and micrometastases (see Chapters IV and V).

Simulations can be performed in biological media (water or DNA) for protons and α-particles with kinetic energies in the range from 10 keV u^{-1} to 100 MeV u^{-1}. The secondary electrons are followed with routines initially developed for the EPOTRAN (**E**lectron and **PO**sitron **TRAN**sport) code [2], which were fully integrated into *TILDA-V*. Atom relaxation is only modeled through non-radiative transitions, that is, by Auger electron emission. The emission and transport of photons is not included in *TILDA-V*.

The physical processes currently included in the code are shown in Table I.2. The description of the theoretical and semiempirical models implemented for each process will be given in Chapter II.

Simulated projectile	Charge state	Process	Model
Hydrogen ions	H^+	Ionization	*Prior* CDW-EIS [125]
		Capture	*Prior* CDW-EIS [126]
		Excitation	Miller and Green [1, 5, 114]
		Elastic scattering	Classical description [127]
	H^0	Ionization	*Prior* CDW-EIS [128]
		Electron loss	Miller and Green [1, 5]
		Excitation	Miller and Green [1, 5, 129]
		Elastic scattering	Classical description [130]
Helium ions	He^{2+}	Ionization	*Prior* CDW-EIS† / Uehara and Nikjoo [4]
		Single-electron capture	*Prior* CDW-EIS† / Uehara and Nikjoo [4]
		Double-electron capture	Uehara and Nikjoo [4]
		Excitation	Miller and Green [5]
		Elastic scattering	Classical description
	He^+	Ionization	*Prior* CDW-EIS† / Uehara and Nikjoo [4]
		Capture	Uehara and Nikjoo [4]
		Electron loss	Uehara and Nikjoo [4]
		Excitation	Miller and Green [5]
		Elastic scattering	Classical description
	He^0	Ionization	*Prior* CDW-EIS† / Uehara and Nikjoo [4]
		Single-electron loss	Uehara and Nikjoo [4]
		Double-electron loss	Uehara and Nikjoo [4]
		Excitation	Miller and Green [5]
		Elastic scattering	Classical description
Electrons	e^-	Ionization	DWBA [6] / RBEB [7]
		Excitation	Olivero *et al.* [8]
		Elastic scattering	Partial wave formalism [9]

† Ongoing development and implementation.

Table I.2 Physical processes and set of models used in *TILDA-V*.

The main difference between the MCTS codes reviewed in the previous section and *TILDA-V* is that the latter largely relies on multiple differential and total cross sections computed *ab initio* within a quantum mechanical treatment of interactions and applying a molecular description of both water and DNA, as explained in Chapter II. In addition, it should be noted that *TILDA-V* is based on a cross section database computed for isolated molecules in vapor state. This description was chosen in order to compare our theoretical calculations with available experimental data on water and DNA components, which are largely limited to the gas-phase.

Presently, *TILDA-V* simulations are limited to the physical stage of energy deposition in biological targets. The physical stage describes only the direct effects of ionizing radiation on matter, taking place during the first $\sim 10^{-15}$ s after irradiation. Therefore, the creation and subsequent interaction of free radical species with the DNA molecule, i.e., the indirect effects of ionizing radiation, are not modeled in the code.

Simulations in *TILDA-V* can be carried out either in "stationary" mode or in "slowing-down" mode. In the former, primary particles are allowed to experience a first and unique interaction in the medium. This mode is useful, for instance, to compute the stopping power of ions. On the other hand, in the slowing-down mode the primary ions (and their secondary electrons if requested) are followed until their energy falls below a specified cutoff. This mode is used in most of the simulations, for example to calculate the ion range as well as dosimetric quantities, like the dose deposited in particular volumes (please refer to Chapters III and V for the details about track parameters). The low-energy cutoff can be changed by the user, but the minimum value is set by default to $10\,\mathrm{keV\,u^{-1}}$ for protons and α-particles, and to 7.4 eV (the excitation threshold for water) for electrons. Sub-threshold primary ions as well as secondary electrons are not followed and their energy is assumed as locally deposited at a single point. An electron of 7.4 eV has a thermalization distance (penetration range) of about 20 nm in water [11, 92]. Similarly, protons and α-particles of $10\,\mathrm{keV\,u^{-1}}$ have a range of ≈ 322 nm and ≈ 698 nm in water vapor, respectively [10]. Thus, we estimate that the uncertainty (ascribable to the cutoffs) in the spatial distribution of the energy deposits in our simulations will be of the same magnitude.

Figure I.1 depicts a simplified view of the slowing-down of a proton (H^+) in water. It can be observed that as the primary projectile travels through the medium, it interacts with the surrounding water molecules via inelastic or elastic collisions. Excitation will only induce a local energy deposition at the point of occurrence, while ionization will also produce secondary electrons which are subsequently followed by the code. Elastic scattering will induce a negligible energy loss and a small angular deviation from the original trajectory. A change in the charge state of the ion by electron capture, a physical process frequent at low incident energies, will transform it into a neutral hydrogen atom

(H^0). As the proton, the H^0 will interact by ionization, excitation or elastic scattering. The H^0 will eventually become a proton once more by a process known as electron loss or stripping.

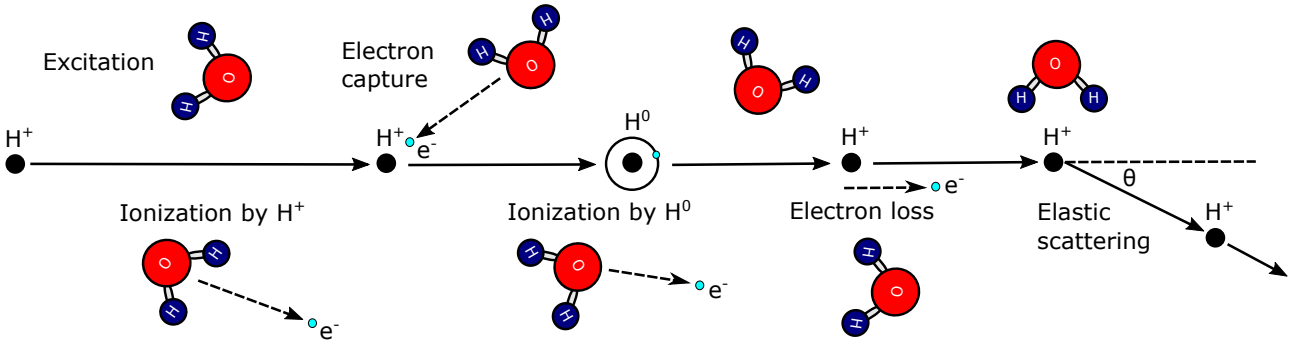

Figure I.1 Illustration of the interactions during the slowing-down of a proton in water.

I.4.2 Input data and simulation setup

The basic input for *TILDA-V* simulations are the interaction cross sections for water and DNA components. These cross sections have been previously calculated and are contained in several text files, which together form a database for *TILDA-V* of several GB. Other relevant data, such as physical constants, ionization potentials, excitation energies, and probabilities and energy transfers for non-radiative transitions (Auger electron emission) are contained in a few header and text files.

A main source file (.cpp) must be created for each simulation. Within this file, the user must call the appropriate routines for the type of simulation he wishes to perform. Several useful routines have already been developed for computing fundamental quantities in simple geometries, including: stopping power and range calculations; radial dose profiles; depth-dose curves; absorbed doses in ellipsoidal, spherical and cylindrical volumes.

The simulation setup is made by means of an Extensible Markup Language (XML) file which contains a list of user-defined parameters, such as:

- The type, mass and charge of the ion.
- The number of primary ions to simulate and their initial energy.
- The type, density and molar mass of the medium. It is possible to devise simulations in which a different material is assigned to each volume, as is the case for the simulations in a cell model (see Chapters III and IV).
- The size and position of the scoring geometry.
- The physical models to use in the simulation for each type of interaction.

- Variables to enable/disable the transport of secondary electrons and Auger electron emission.

Additional parameters can be included in this file as new functionalities or routines are added to the code.

Figure I.2 shows the flowchart of a *TILDA-V* simulation. For the sake of simplicity, the transport of hydrogen ions is illustrated. However, the workflow is essentially the same for simulating helium ions, the sole difference being the number and type of interactions to consider (see Table I.2).

When a simulation starts, the tabulated cross sections for the specified interactions and models are loaded into memory. A first random sampling provides the distance to the next interaction. A second random sampling determines the type of interaction. In the case of ionization or electron capture, the molecular orbital to which the emitted or captured electron belongs is also determined by means of partial cross sections. Each type of interaction is identified by an index.

If ionization takes place, the energy E_{sec} and the polar angle θ_{sec} of emission of the secondary electron are sampled from the cumulative SDCS and DDCS, respectively. The azimuthal angle φ_{sec}, on the other hand, is randomly generated over $[0, 2\pi)$ assuming axial symmetry. The deposited energy E_{dep} is equal to the ionization potential I_i of the corresponding molecular orbital i (i running from 1 to 5 for the water molecule), unless the value of E_{sec} is less than the electron cutoff of 7.4 eV, in which case $E_{\text{dep}} = I_i + E_{\text{sec}}$. In other words, electrons with kinetic energies below the cutoff are not transported and their energy is considered as locally deposited at the point of interaction. In the case of K-shell ionization, an Auger electron is emitted. Its energy E_{Auger} is determined from tabulated non-radiative transition probabilities (see Ref. [1]). The deposited energy is then $E_{\text{dep}} = I_K - E_{\text{Auger}}$, with I_K the ionization potential of the K-shell (for which $i = 5$ in the case of the water molecule). The angles at which the Auger electron is emitted are obtained by random sampling on a uniform distribution.

When excitation occurs, the excitation level is obtained by random sampling. The energy W_j associated to the excitation level j is locally deposited at the point of interaction. For water, five excited states were considered [114].

Electron capture by H^+ converts it into H^0. Similarly to the ionization process, the energy deposited is equal to the binding energy of the molecular orbital to which the captured electron belongs. In this process it is also possible to have Auger electron emission if capture involves the K-shell.

For H^0 the type of interaction is sampled in the same way that for H^+. If electron loss occurs, a secondary electron is emitted with energy E_{sec} equal to [22]:

$$E_{\text{sec}} = E_{\text{inc}} \frac{m_e}{m_p} , \tag{I.17}$$

where E_{inc} is the energy of the incident neutral hydrogen atom, m_e the electron mass and m_p the proton mass. Again, for the electron to be followed its energy must be $\geq 7.4\,\text{eV}$. It is worth mentioning that in *TILDA-V* the electron capture by H^0, which leads to the formation of H^-, is neglected because the cross sections associated to that process are at least one order of magnitude smaller than those corresponding to the electron loss process [131].

Finally, elastic scattering will slightly change the direction of the incident ion. The elastic scattering process is described classically. The calculation of the polar scattering angle θ is based on the Rutherford theory, while the azimuthal scattering angle φ is sampled uniformly in the interval $[0, 2\pi)$ (see Section II.3.6).

The energy and coordinates of all electrons emitted by ionization, electron loss and Auger effect are recorded and used as input for the EPOTRAN routines implemented in *TILDA-V* for electron transport. Figure I.3 shows the workflow for simulating the slowing-down of electrons. It can be seen that the workflow is very similar to the one illustrated for ions in Figure I.2. Three types of interaction are considered for electrons: ionization, excitation and elastic scattering. Secondary electrons produced by ionization are added to the tracking list if the cutoff condition is met. The workflow in Figure I.3 is repeated until all emitted electrons N_{elec} for a given ion are transported.

Ions are stopped when their energy is less than $10\,\text{keV}\,\text{u}^{-1}$. The remaining energy is deposited at the point where the last interaction of the ion took place. The simulation continues until all requested ions (N_{ions}) are transported. At the end, a text file containing some statistics and other relevant data related to the simulation (e.g., stopping power and range values) is generated, along with any other output requested by the user, such as the full history of ion and electron interactions.

It is well known that MCTS simulations are computationally intensive. The duration of a *TILDA-V* simulation in slowing-down mode may largely vary depending on the primary ion energy, the number of primary ions requested and the number of threads specified to take advantage of the parallelization directives. To give an example, simulating 10^6 protons of 100 MeV in water can take several days.

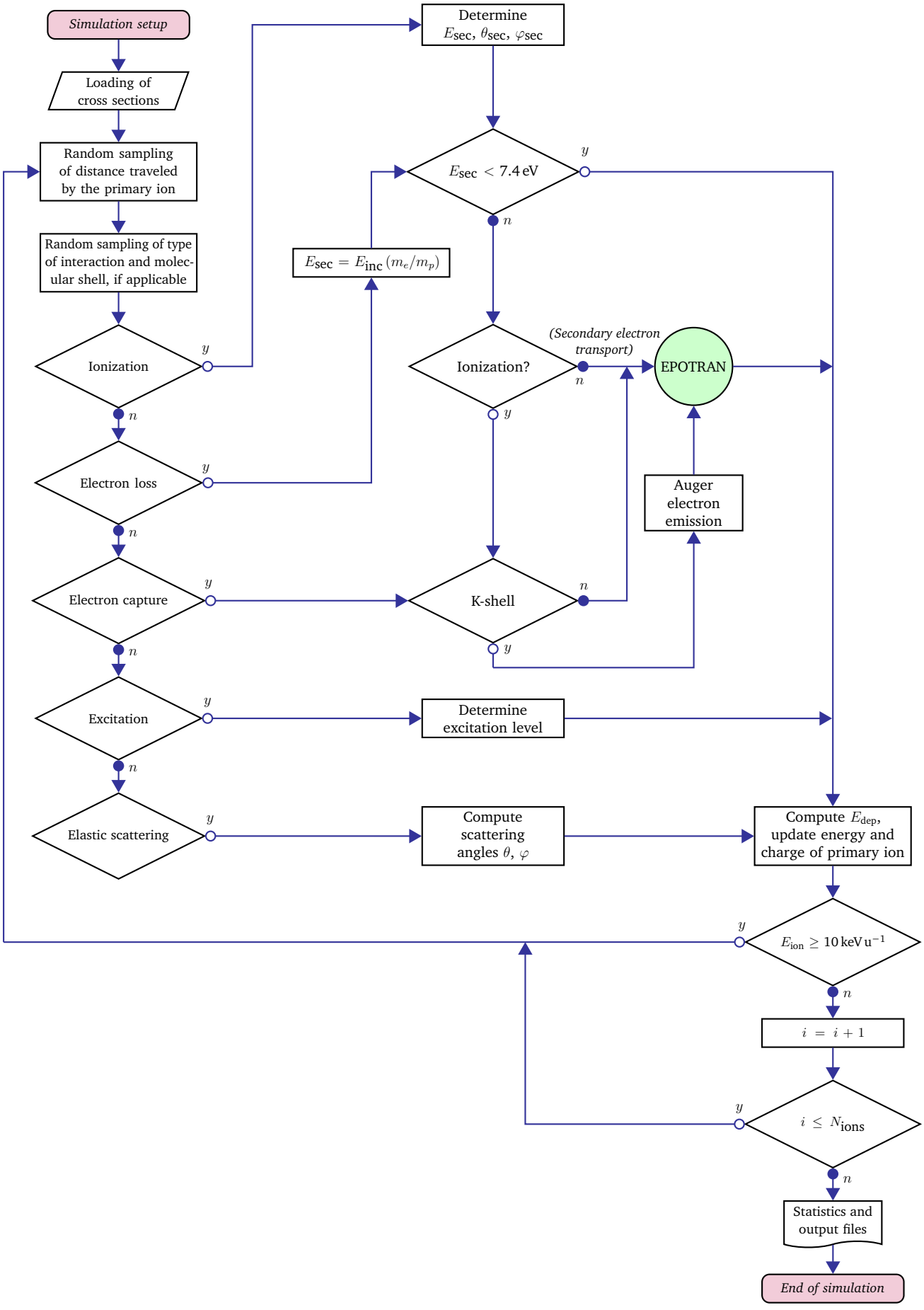

Figure I.2 The workflow of a *TILDA-V* simulation.

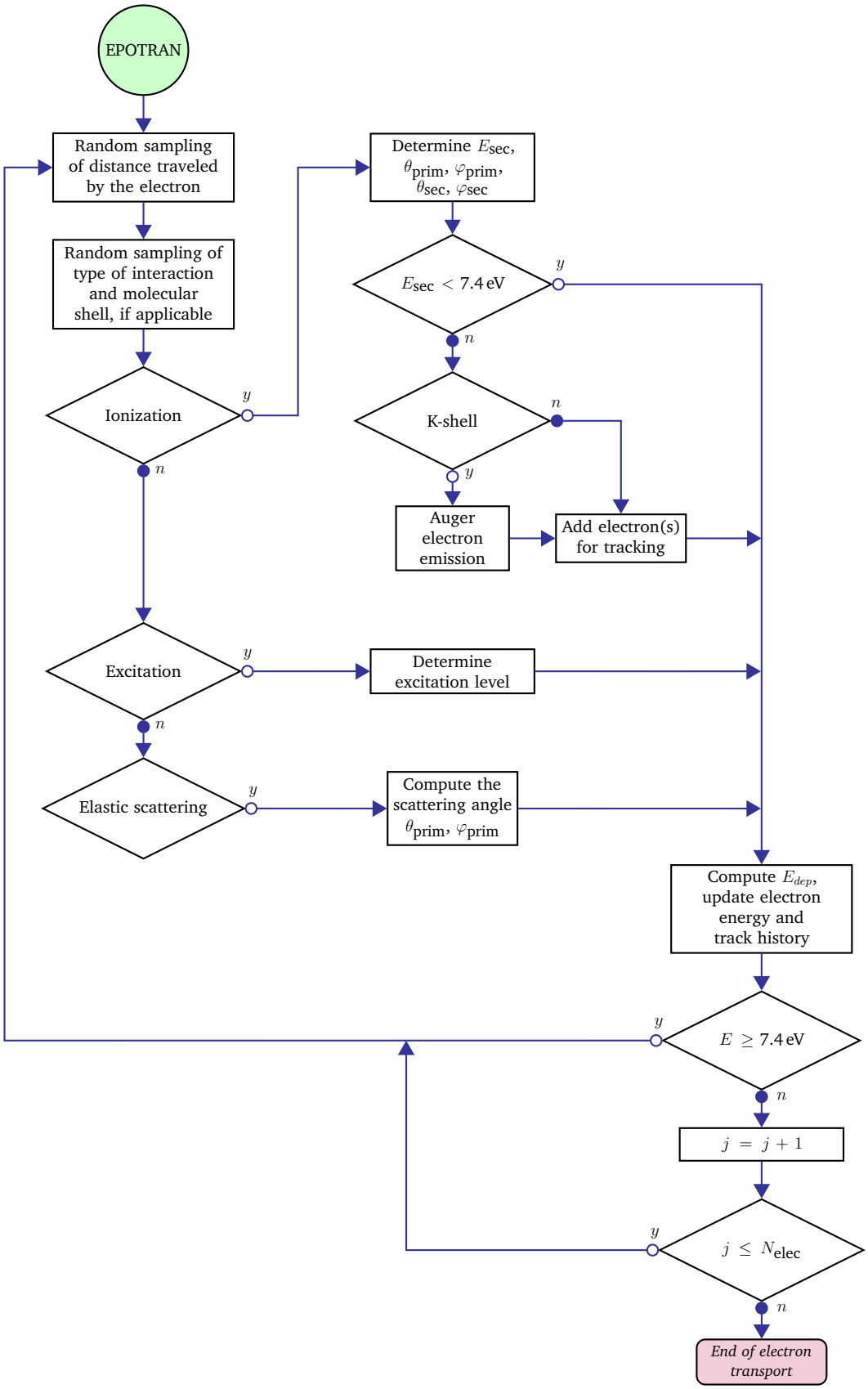

Figure I.3 The workflow for electron transport.

I.4.3 Outlook

As a result of the latest developments aforementioned, *TILDA-V* can be used to simulate the full slowing-down of protons, α-particles and their secondary electrons in water and DNA. Appropriate routines have been validated for computing with ease relevant dosimetric quantities in semi-infinite media (Chapter III) as well as in cells for applications in targeted radionuclide therapy (Chapters IV and V). There are still, however, some important limitations in the code that may be addressed in future improvements:

- The lack of modules taking into account the physico-chemical and chemical stages of radiation action. It is well known that highly chemically reactive species produced in these stages constitute the major contribution to radiation-induced damage. Therefore, the inclusion in *TILDA-V* of these two stages should be envisaged in later versions of the code for a complete description of DNA damage.

- Nuclear non-elastic scattering events are not simulated in *TILDA-V*. These interactions take place when the incident projectile overcomes the Coulomb barrier and enters the nucleus of one of the atoms in the target. In proton beams, this mechanism results in the removal of primary protons from the beam and the subsequent emission of secondary protons, neutrons, photons and heavier ions from the transformed nucleus [132, 133]. Although the TCS of nuclear non-elastic reactions are several orders of magnitude lower than those of the electronic processes in the energy range considered in this work [132], nuclear non-elastic collisions may influence considerably the depth-dose profiles of ion beams [134–136]. Since the precise effects of neglecting this type of interactions in the results of our simulations cannot be quantified, the subject will not be further discussed in this thesis.

- Multiple electronic interactions such as the transfer ionization process, i.e., the simultaneous electron capture and electron emission from the target, or pure multiple ionization, are not considered in the simulations. The only exception is the emission of an Auger electron following inner-shell ionization.

Finally, the implementation in *TILDA-V* of a graphical user interface would make the code more user-friendly.

Conclusions

MC simulations in radiation transport have shown to be extremey useful not only for physicists, but also for physicians, radiochemists and radiobiologists. A myriad of papers have been published in the last fifty years on the medical applications of the MC method,

and new studies on this topic appear each year. This tendency has been favored by the increase in computer power and the corresponding reduction of computing time. Nevertheless, the future of MC simulations is somewhat uncertain. Some authors have predicted a gradual decline of MC applications, while others have emphasized the persistent challenges to be overcome in MCTS simulations [137]. In any case, to quote A. Bielajew, it is sure that the MC method "will remain an essential component of our scientific infrastructure, forever" [44]. When radiation transport or radiation dosimetry studies are performed at the nanometer scale, MCTS codes remain the best tool for the job. The distinctive features of *TILDA-V* compared to other MCTS codes are its inclusion of DNA cross sections to provide a more precise description of the biological medium and the theoretical model from which most of the inelastic interaction cross sections are computed.

Chapter II

Ion and electron impact on biological targets

Contents

II.1 Introduction **38**

II.2 The description of the biological medium **39**

II.2.1 Gas-phase or condensed-phase? 39

II.2.2 Water 40

II.2.3 DNA 41

II.3 Physical processes induced by the impact of ions **43**

II.3.1 Classification of interactions 43

II.3.2 The electronic excitation process 44

II.3.3 The ionization process 47

II.3.4 The electron capture process 59

II.3.5 The electron loss process 66

II.3.6 The elastic scattering process 68

II.3.7 Summary of total cross sections for ion impact 71

II.4 Physical processes induced by the impact of electrons **73**

II.4.1 The electronic excitation process 73

II.4.2 The ionization process 75

II.4.3 The elastic scattering process 81

II.4.4 Summary of total cross sections for electron impact 84

Conclusions **85**

II.1 Introduction

As we have seen in the previous chapter, pseudo-random number generators are one of the key components of a MC code. Another crucial aspect of MC simulations are the interaction cross sections, directly related to the probability of occurrence of a physical process between an incident projectile (ion/electron) and the target (atoms or molecules in the medium). Cross sections depend on the nature of the incident particle, its energy and the characteristics of the target material. For many projectile/target combinations, experimental data are usually unavailable or insufficient to cover the whole energy range required in radiation transport simulations. That is the case for water, which is the medium of reference in radiation research (about 80% of a cell is composed of water). For this reason, various theoretical and semiempirical models have been developed to compute the interaction cross sections for ion and electron collisions with water targets. On the other hand, in recent years efforts have been made to measure as well as to calculate interaction cross sections for ion and electron impact on DNA components (see for instance [138–140] and references therein). The DNA is the critical biological target for radiation-induced cell death. Indeed, a detailed modeling of DNA is of great importance for investigating the effects of ionizing radiation at the smallest scale. Studying the initial radiation damage to DNA may improve the understanding of the factors involved in cancer induction and, conversely, the optimal strategies to eradicate cancer cells. Consequently, some MCTS codes have incorporated geometries for modeling the DNA structure at various levels of complexity (see Chapter I). Nevertheless, the majority of MCTS codes have not yet implemented a database of cross sections specific to DNA, and they base their predictions on a DNA geometry overlapped to radiation tracks simulated in water. In this thesis, simulations were performed in water and DNA with the purpose of highlighting differences arising solely from the composition of the media and their description in quantum mechanical terms, without adopting a particular geometrical model of the targets.

In this chapter, we describe the biological media as they are considered in the simulations with *TILDA-V*. Then, we discuss the different interactions of ions and electrons and the models used to compute the interaction cross sections, their assumptions and the energy range in which they are applicable. Particular attention is given to the models implemented in our MCTS code. Finally, we compare the obtained cross sections with available experimental data found in the literature, in order to validate their use in radiation transport simulations.

II.2 The description of the biological medium

Radiation transport simulations intended for medical and biological applications must be based on targets relevant for that purpose. Modeling the biological medium in its finest details is, however, a complex and challenging task. Furthermore, the nature and scope of a study may not always justify the implementation of a detailed description of the medium. That is why a practical and widely accepted solution in radiation dosimetry is to compute absorbed doses in water, since it is the main constituent of the biological tissue. Let us note, however, that a more faithful representation of the biological medium is warranted to explore and elucidate the radiation-induced effects at the nanometer scale. In summary, a balance must be found between the accuracy of the target description needed for a given application and the computer time and resources associated to that choice. In the following section, we explain how the water and DNA targets are modeled in the *TILDA-V* code.

II.2.1 Gas-phase or condensed-phase?

In living organisms, water is found in the liquid state. Unfortunately, because of experimental difficulties in dealing with liquid water, most of the available experimental data, in terms of interaction cross sections, come from measurements for water vapor. From the theoretical point of view, it is also much simpler to perform first-principles calculations in the gas-phase than in the condensed-phase.

When charged particles interact with condensed matter they polarize the molecules in the medium, which in turn reduces the interaction strength at some distance from the projectile. As a result, the stopping power values in condensed media are smaller than in the gas-phase. For the energy range of interest in this thesis, which extends from $10\,\mathrm{keV\,u^{-1}}$ to $100\,\mathrm{MeV\,u^{-1}}$ for primary ions, the NIST database [141] indicates a maximum difference of about 13% between the mass stopping power values computed for water vapor and those obtained for liquid water. The maximum difference is found at $10\,\mathrm{keV\,u^{-1}}$ and the discrepancy is much less ($\sim$1%) in the range $1\,\mathrm{MeV\,u^{-1}}$ – $100\,\mathrm{MeV\,u^{-1}}$.

For electrons, the influence of the water phase on the elastic scattering and ionization processes is weak at high incident energies, but becomes critical at very low impact energies, i.e., in the sub-keV range [9, 142].

For the reasons above-mentioned, *TILDA-V* simulations are based on cross sections computed considering isolated target molecules in vapor state. Since phase related effects are expected to become important essentially in the lower part of the energy range considered here, we assume that they should not lead to significant errors in the

results reported in this work.

Let us note, however, that nowadays the most common and widely accepted approach for computing the inelastic cross sections of charged particles in condensed matter, and particularly in liquid water, is the dielectric formalism (see Section II.3.3.2). Consequently, many MCTS codes have implemented cross sections for liquid water obtained within this approach (see Section I.3.2).

II.2.2 Water

In *TILDA-V* a molecular description of the biological targets is applied within the quantum mechanical framework. Two different representations were considered for describing the water molecule [1, 143]: the complete neglect of differential overlap (CNDO) approximation and the molecular orbital self-consistent field linear combination of atomic orbitals (MO-SCF-LCAO) approach.

In the CNDO approximation, originally developed by Pople *et al.* [144], MOs for the valence electrons are written as a linear combination of atomic orbitals (LCAO). On the other hand, all inner shells are treated as a part of an unpolarizable core. In this treatment, the overlap distribution of any two atomic orbitals is neglected in all electron repulsion integrals. The calculation of the cross sections is simplified by making use of the method proposed by Senger *et al.* [145]. The cross sections for any MO are obtained as the weighted sum of the atomic cross sections corresponding to the atomic constituents of the molecule [146]. The cross section for a given molecular orbital k is

$$\sigma_k = \sum_{j=1}^{N_k} c_{k,j}\, \sigma_j \ , \tag{II.1}$$

where N_k is the number of atoms that describe each molecular orbital. σ_j is the atomic orbital cross section involved in its LCAO description and $c_{k,j}$ is the corresponding atomic orbital population. Table II.1 shows the atomic orbital populations and molecular binding energies corresponding to the CNDO description of water vapor [147]. The different ground state atomic orbitals are described using Roothaan-Hartree-Fock (RHF) atomic wave functions [148].

Molecular orbital	Atomic orbital populations	Binding energy ϵ_i (eV)
$1a_1$	2.0 O_{1s}	-539.7
$2a_1$	1.48 O_{2s} + 0.52 H_{1s}	-32.2
$1b_2$	1.18 O_{2p} + 0.82 H_{1s}	-18.4
$3a_1$	0.22 O_{2s} + 1.44 O_{2p} + 0.34 H_{1s}	-14.7
$1b_1$	2.0 O_{2p}	-12.6

Table II.1 Atomic orbital populations and binding energies of the H_2O molecular orbitals.

The MO-SCF-LCAO description was proposed by Moccia [149]. The ten bound electrons of the water target are distributed in five molecular orbitals ($j = 5$) which are constructed from a LCAO in a self-consistent field (SCF). Each MO wave function is developed in terms of Slater-type functions centered on the oxygen nucleus. According to this description, the MO wave functions are written as [1, 149]

$$\psi_j(r) = \sum_{k=1}^{N_j} a_{jk} \phi^{\xi_{jk}}_{n_{jk} l_{jk} m_{jk}}(r) \ , \tag{II.2}$$

where N_j is the number of Slater atomic orbitals $\phi^{\xi_{jk}}_{n_{jk} l_{jk} m_{jk}}$ and a_{jk} is the corresponding weight. The atomic components are written as

$$\phi^{\xi_{jk}}_{n_{jk} l_{jk} m_{jk}}(r) = R^{\xi_{jk}}_{n_{jk}}(r) S_{l_{jk} m_{jk}}(\hat{r}) \ , \tag{II.3}$$

with the radial part given by

$$R^{\xi_{jk}}_{n_{jk}}(r) = \frac{(2\xi_{jk})^{2n_{jk}+1/2}}{\sqrt{2n_{jk}!}} r^{n_{jk}-1} \exp(-\xi_{jk} r) \ , \tag{II.4}$$

and the angular part, expressed by means of real spherical harmonics, is given by

$$\begin{cases} \text{if } m_{jk} \neq 0: & S_{l_{jk} m_{jk}}(\hat{r}) = \left(\frac{m_{jk}}{2|m_{jk}|}\right)^{1/2} \\ & \times \left[Y_{l_{jk}-|m_{jk}|}(\hat{r}) + (-1)^{m_{jk}} \left(\frac{m_{jk}}{|m_{jk}|}\right) Y_{l_{jk}|m_{jk}|}(\hat{r}) \right] \ , \\ \text{if } m_{jk} = 0: & S_{l_{jk}0}(\hat{r}) = Y_{l_{jk}0}(\hat{r}) \ . \end{cases} \tag{II.5}$$

The coefficients in Eq. II.2 can be found in Table A.1 of Appendix A. It is worth mentioning that in Moccia's description the wave functions were derived for a particular orientation of the molecule in space. To obtain an arbitrary oriented wave function, the rotation operator must be applied to Eq. II.2 [146].

In general, Moccia's approach is expected to provide better results than the CNDO representation, but the latter requires less computational effort. On the other hand, it has been shown that the initial description of molecular orbitals does not influence significantly the cross sections calculation performed within the continuum distorted wave - eikonal initial state (CDW-EIS) approximation [146]. Therefore, in the context of this thesis, the cross sections used for describing the ion impact on water vapor were based on the CNDO approach, while for electron impact Moccia's description was preferred.

II.2.3 DNA

The DNA molecule plays a fundamental role in all living forms, because it carries the information necessary for the development and reproduction of all organisms. It has been known for a long time that ionizing radiation induces damage on DNA which, if unrepaired or misrepaired, may result in cell death or mutations eventually leading to

cancer [150]. Therefore, radiation transport simulations based on the DNA as the critical target are of great interest.

DNA has a double-helical structure composed of subunits called nucleotides. Each nucleotide consists of a nitrogenous base (or nucleobase), a five-carbon sugar (deoxyribose) and a phosphate group. The nitrogenous base may be either adenine (A), cytosine (C), guanine (G), or thymine (T). The nucleotides are covalently linked together in a chain through alternating sugars and phosphates, which thus form a "backbone". The two resulting chains or strands are antiparallel and are linked together by means of hydrogen bonds between the nitrogenous bases. The sequence of nucleotides in both strands are complementary because a two-ring base (a purine) is always paired with a single-ring base (a pyrimidine): A pairs with T, and G with C [151]. Figure II.1 depicts the DNA structure and its components.

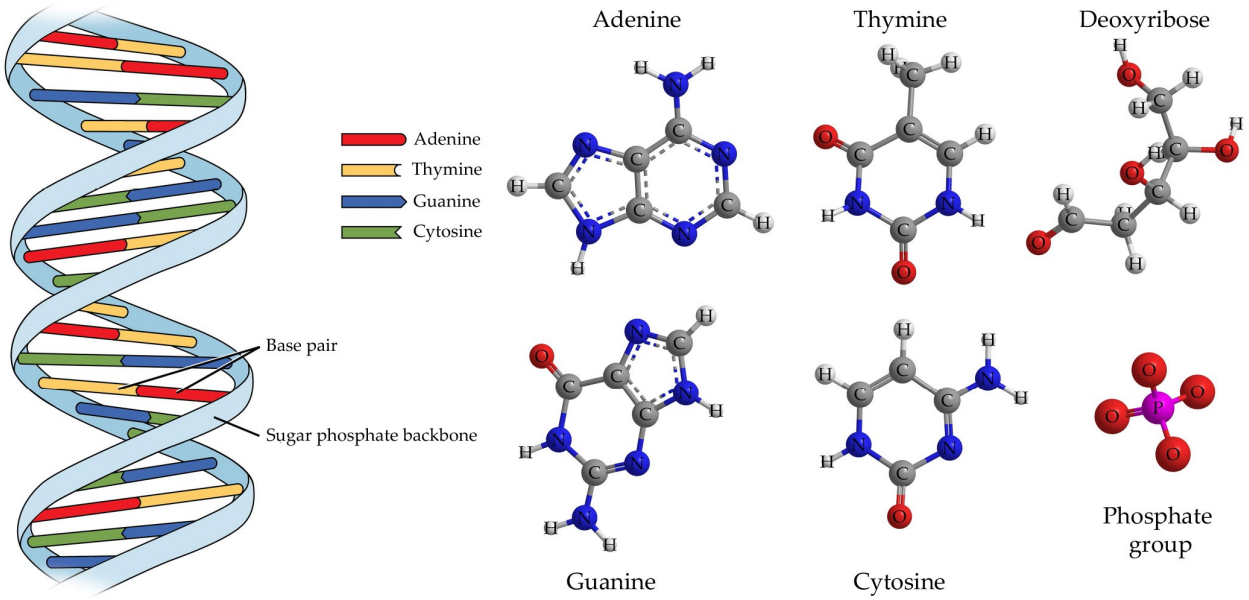

Figure II.1 Left: the DNA double helix (illustration by the OpenStax College, licensed under CC BY 3.0); right: the basic components of DNA.

As for water, a molecular description of the DNA components was implemented to compute the interaction cross sections used in *TILDA-V*. The molecular structure information for DNA components was obtained with the *ab initio* approach proposed by Galassi *et al.* [140]. In this approach, the ground states of DNA components were computed with the Gaussian 09 software [152], by means of a Restricted Hartree-Fock optimization using the 3-21G basis set. The N occupied MOs of each DNA component were taken into account, with $N = 35$, 33, 29, 39, and 48 MOs for adenine, thymine, cytosine, guanine, and sugar-phosphate backbone unit, respectively. Each MO was expressed as a linear combination of atomic wave functions corresponding to the different atomic components, namely, H_{1s}, C_{1s}, C_{2s}, C_{2p}, N_{1s}, N_{2s}, N_{2p}, O_{1s}, O_{2s}, O_{2s}, P_{1s}, P_{2s}, P_{3s},

P_{3p}, and P_{3p}. For each MO, the effective number of electrons associated to the atomic components was derived from a standard Mulliken population analysis and their sum for each occupied MO was very close to 2 [153]. Furthermore, the ionization energies obtained for the occupied MOs were scaled so that their calculated Koopmans ionization energy, i.e., the ionization energy of their highest occupied molecular orbital (HOMO), agrees with the experimental values found in the literature [1, 140, 143]. The ionization energies and the electronic populations for the MOs of the different DNA components are given in Appendix B.

The procedure described above provides only the molecular structure of the isolated DNA constituents. A realistic modeling of the biological target is achieved by considering a DNA unit composed of a nucleobase pair plus two sugar-phosphate groups [154]. Furthermore, to fit the composition of living cells, the relative abundance of nucleobase pairs in the DNA molecule as well as the level of hydration of the medium are taken into account, as reported in the literature. Consequently, we consider a hydrated DNA unit composed of 58% A-T nucleobase pair [21], 42% C-G nucleobase pair [21], 2 groups of sugar-phosphate [154] and 18 molecules of water [155]. The result is a DNA target with a density of $\rho_{\mathrm{DNA}} = 1.29\,\mathrm{g\,cm^{-3}}$ and a molar mass of $947.87\,\mathrm{g\,mol^{-1}}$ [156].

II.3 Physical processes induced by the impact of ions

In this and the next section we discuss separately, as it is customary in the literature, the models employed to compute the interaction cross sections for ions and electrons in the biological media considered here. The general description of the models will center on the water target case, unless otherwise stated, with appropriate remarks regarding the approach followed to compute the cross sections for the DNA components.

II.3.1 Classification of interactions

It is worth mentioning that throughout this thesis the words interaction and collision are used interchangeably. In atomic and molecular physics, collisions are classified as slow or fast depending on the relative velocity of the incident projectile with respect to the orbital velocity of the bound electron of the target participating in the collision. More specifically, the velocity v_0 of the electron in the ground state of the hydrogen atom is taken as reference:

$$v_0 = \frac{\hbar}{m_e a_0} = 2.19 \times 10^6\,\mathrm{m\,s^{-1}}\,, \tag{II.6}$$

where $m_e = 9.11 \times 10^{-31}\,\mathrm{kg}$ is the electron rest mass and $a_0 = 5.29 \times 10^{-11}\,\mathrm{m}$ the Bohr radius. In atomic units (a.u.), $\hbar = m_e = e = a_0 = 1$, so $v_0 = 1$ too. A collision will

be considered fast if the velocity v_{inc} of the incident projectile is greater than v_0, i.e., $v_{\text{inc}} > v_0$, and slow otherwise (if $v_{\text{inc}} < v_0$). By extension, one sometimes speaks of high, intermediate or low incident (kinetic) energies referring to the cases $v_{\text{inc}} > v_0$, $v_{\text{inc}} \approx v_0$ and $v_{\text{inc}} < v_0$, respectively. Thus, for processes involving outer shell target electrons, a fast collision means $v_{\text{inc}} > 1$ a.u., or in terms of the projectile incident energy, $E_{\text{inc}} \gtrsim 25\,\text{keV u}^{-1}$. For inner shell electrons, fast collisions imply that:

$$v_{\text{inc}} \gtrsim \frac{Z}{n} \,, \tag{II.7}$$

in a.u., where Z is the target nuclear charge and n the principal quantum number of the active electron. A useful relationship is:

$$v_{\text{inc}} = 6.35\sqrt{\frac{E_{\text{inc}}}{M_P}} \,, \tag{II.8}$$

where v_{inc} is in a.u., E_{inc} is in MeV, and M_P is in amu [157].

In addition, collisions are either elastic or inelastic in nature. In elastic collisions the total kinetic energy of the collision system is conserved. On the contrary, in inelastic collisions the impact kinetic energy is altered, so that a part of it is spent on changes in the internal structures of the projectile and/or the target [158]. Excitation and ionization are examples of inelastic collisions.

II.3.2 The electronic excitation process

Excitation includes all the processes which modify the internal state of the molecule without emission of electrons [159]. In the electronic excitation process, the energy transferred by the projectile to the target promotes one or more electrons to a higher energy bound state. The process can be written as:

$$P + T \rightarrow P' + T^* \,, \tag{II.9}$$

where T^* represents the excited target. In this process the energy loss is equal to the energy deposited:

$$\Delta E = E_{\text{dep}} = W_j \,, \tag{II.10}$$

where W_j is the energy of the excited state j.

Describing the electronic states of molecular targets remains a challenging task within a quantum mechanical approach. Moreover, to the best of our knowledge, there are no reported experimental excitation cross sections for proton and α-particle impact on water or DNA components. For these reasons, many MCTS codes, including *TILDA-V*, rely on the semiempirical model developed by Miller and Green [5] to describe the electronic excitation of water molecules by ion impact. In this model, a speed scaling procedure based on the electron excitation cross sections is applied, together with extensions towards lower incident proton energies. The excitation cross section associated to the

excited state of energy W_j for protons with kinetic energy E_{inc} is obtained from the following formula:

$$\sigma_{\text{exc}}(E_{\text{inc}}) = \sigma_0 \frac{(Za)^{\Omega}(E_{\text{inc}} - W_j)^{\nu}}{J^{\Omega+\nu} + E_{\text{inc}}^{\Omega+\nu}} , \tag{II.11}$$

where σ_0 =10^{-16} cm^2; Z is the number of electrons in the target molecule (for the water molecule $Z = 10$); ν and Ω are dimensionless parameters, whereas a and J have the dimension of energy. The parameters a and Ω represent the high-energy limit and can be inferred from data on electron impact cross sections using the rule based upon the Born approximation that electrons and protons of equal velocities give identical cross sections. On the other hand, J and ν are parameters related to the low-energy behavior which can be inferred for a variety of substances [5]. In their work, Miller and Green reported the set of parameters for 28 excited states of the water molecule. In *TILDA-V*, however, we use an extension of this model, as described by Dingfelder *et al.* [114], who suggested a slightly modified set of parameters so that the semiempirical approach agrees with the first Born approximation predictions towards the high-energy limit.

The parameters recommended by Dingfelder *et al.* [114] are presented in Table II.2.

Excited State	W_j (eV)	a (eV), H^+	a (eV), H^0	J (eV)	Ω	ν
$\tilde{A}^1B_1$	8.17	876	657	19820	0.85	1
$\tilde{B}^1A_1$	10.13	2084	1563	23490	0.88	1
Ryd A + B	11.31	1373	1030	27770	0.88	1
Ryd C + D	12.91	692	519	30830	0.78	1
Diffuse bands	14.50	900	675	33080	0.78	1

Table II.2 Fitting parameters for computing the excitation cross sections for protons in water [114].

Dingfelder *et al.* [114] neglected the excitation of the water molecule induced by neutral hydrogen atoms. However, in *TILDA-V* the excitation cross sections for H^0 were calculated with the parameters J, Ω and ν listed in Table II.2, and with the parameter a equal to 3/4 of the proton value, as suggested by Miller and Green [5]. The values of a for H^0 are shown as well in Table II.2.

The excitation cross sections for protons in water are plotted in Figure II.2. As Miller and Green themselves noted in their paper, the excitation cross sections obtained with this model are rough estimates proposed in the absence of more detailed theoretical and experimental data. The reliability of the model increases with energy. Nevertheless, it should be noted that the position and height of the maximum in the cross section could easily be in error by a factor of 2, and the nature of the low energy fall-off must be considered as speculative [5].

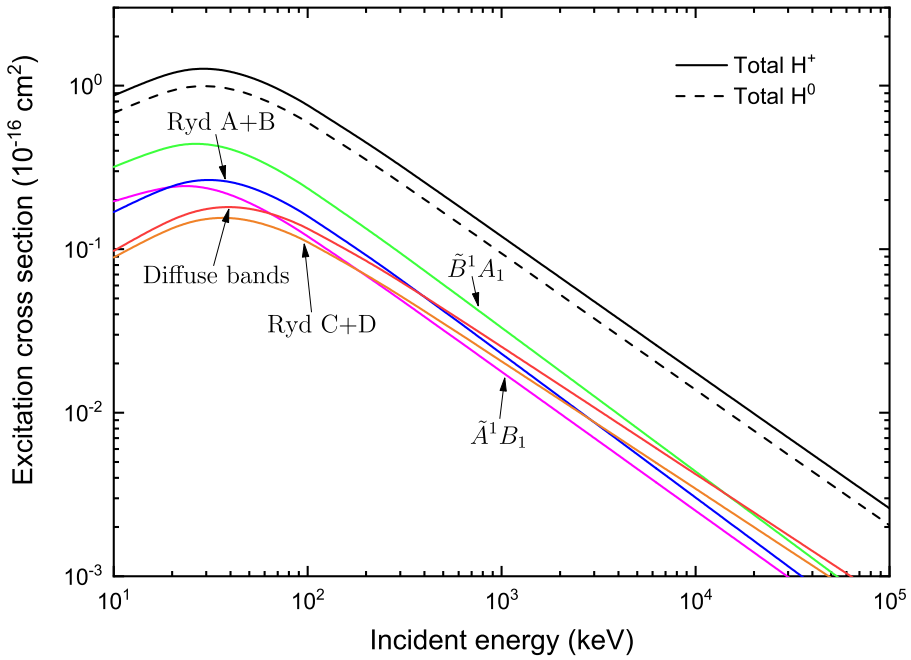

Figure II.2 Excitation cross sections for protons in water computed with the semiempirical model of Miller and Green [5]. The contribution of each excited state to the total excitation cross section is shown for H^+. The total excitation cross section for H^0 is shown for comparison (dashed line).

For α-particles and the other charge states of helium, the assumption made by Uehara and Nikjoo [4] that the total excitation cross sections are the same as those for protons was adopted.

To obtain the excitation cross sections of DNA components for proton impact, a scaling procedure on the electron excitation cross sections, similar to the one proposed by Miller and Green [5], was applied.

DNA component	a (eV), H^+	a (eV), H^0	J (eV)	Z	Ω	ν
Adenine	8024.02	6018.02	5161.65	70	0.7236	1
Thymine	7844.74	5883.55	5161.65	66	0.7236	1
Guanine	8364.37	6273.28	5161.65	78	0.7236	1
Cytosine	7464.75	5598.56	5161.65	58	0.7236	1
Sugar phosphate group	9053.44	6790.08	5161.65	96	0.7236	1

Table II.3 Fitting parameters for computing the excitation cross sections for H^+ and H^0 in DNA [1].

The fitting parameters needed in the semiempirical formula (Eq. II.11) for the DNA components are given in Table II.3. The parameters were extrapolated from poor available experimental data of electron excitation of DNA components, essentially on thymine [1, 143] (see Section II.4.1). To compute the excitation cross sections of DNA

components for neutral hydrogen impact, the same consideration as for water was adopted. The excitation energy W was considered an adjustable parameter, taken as $W = 4\,\mathrm{eV}$ [1].

The excitation cross sections for proton impact on DNA components are shown in Figure II.3.

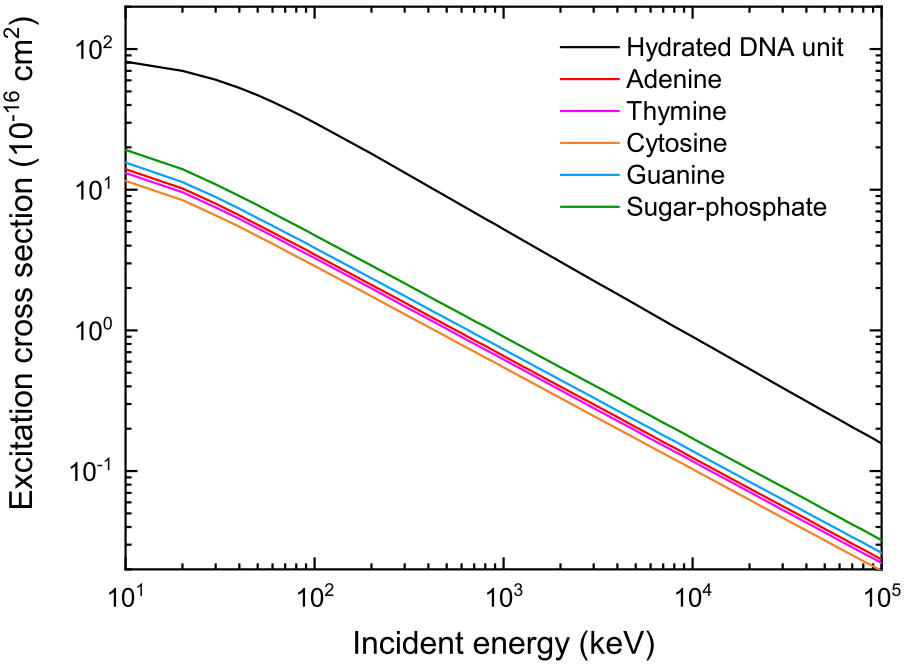

Figure II.3 Excitation cross sections for proton impact on DNA components obtained with the scaling procedure described in the text. The black line represents the total excitation cross section of a hydrated DNA unit as described in Section II.2.3.

II.3.3 The ionization process

Ionization is the most important interaction in terms of energy deposition for ions and electrons. It provides the major contribution to the TCS in most of the incident energy range and particularly at high projectile energies. During ionization, electrons are removed from the target. If only one electron is emitted from the target, the process is called single ionization; conversely, if more than one electron is removed, then multiple ionization occurs. The single ionization interaction can be written as

$$P + T \rightarrow P' + T^+ + e^- \,, \tag{II.12}$$

where P is the incident projectile and T is the target; P' denotes a change in the energy of the projectile. The energy loss in this process is

$$\Delta E = I_i + E_{\mathrm{sec}} \,, \tag{II.13}$$

where I_i is the ionization potential of the molecular orbital i from which the electron is removed, and E_{sec} is the kinetic energy of the ejected electron. As already mentioned in Section I.4, the energy locally deposited in the target is

$$E_{\text{dep}} = I_i \ . \tag{II.14}$$

Presently, the cross sections implemented in *TILDA-V* for treating the ionization process by proton impact are based on the *prior* version of the CDW-EIS approximation. The ionization cross sections for helium ions in water have also been computed with this model. Nevertheless, further work is still needed to validate the theoretical cross sections for helium ions, as explained hereafter.

II.3.3.1 The CDW-EIS model

Among the various existing theoretical approaches for describing the interaction of charged particles with matter, the distorted wave theory has proved very useful. In particular, the continuum distorted wave - eikonal initial state (CDW-EIS) model has been applied with remarkable success for several decades to compute the ionization and electron capture cross sections in ion-atom collisions. The CDW-EIS approximation is a first-order perturbative quantum-mechanical approach introduced by Crothers and McCann [3] to study the single ionization of H by bare ions. The CDW-EIS approximation was proposed to correct the disagreement between the TCS predicted by the continuum distorted wave (CDW) approach and the experiments at intermediate collision velocities, resulting from the non-normalization of the initial distorted wave function in the CDW model. The CDW-EIS approximation was later extended to investigate the ionization of multielectronic atomic targets by bare projectiles [160] and dressed ions [161]. More recently, the model has been employed to study the single ionization of molecular targets of biological interest by bare ions [140]. We explain hereafter the standard formalism to compute the single ionization cross sections within the CDW-EIS approximation for the case of bare ions. Then, we describe the modifications to the CDW-EIS model in order to apply it to dressed projectiles. Atomic units are used in the following sections unless otherwise stated.

Bare ions

Bare ions are atoms in which all electrons have been removed, leaving only the positive-charged nuclei. In the context of this thesis we are interested in two bare ions: protons (H^+) and α-particles (He^{2+}). To make tractable the projectile-target collision problem, the CDW-EIS model employs the independent active electron approximation and the impact parameter approximation. The former means that all target electrons that are not ejected in the ionization process (passive electrons) are assumed to remain frozen in their initial orbitals during the collision. Thus, the problem is reduced to the dynamics of

one active (emitted) electron. This assumption is valid at high enough impact velocities for which the collision time is smaller than the relaxation time of the passive electrons. For molecular targets, it will correspond additionally to collision times smaller than the vibrational and rotational ones [125]. The impact parameter approximation is based on the fact that the nuclei are much more massive than the electrons. This mass relation between the electrons and nuclei masses allows to assume that the heavy particles (projectiles) follow classical trajectories [162]. The classical evolution of the heavy particles generates a time depending potential in which the electrons move, the latter being treated quantically. The impact parameter approximation is valid for intermediate and high collision energies [143].

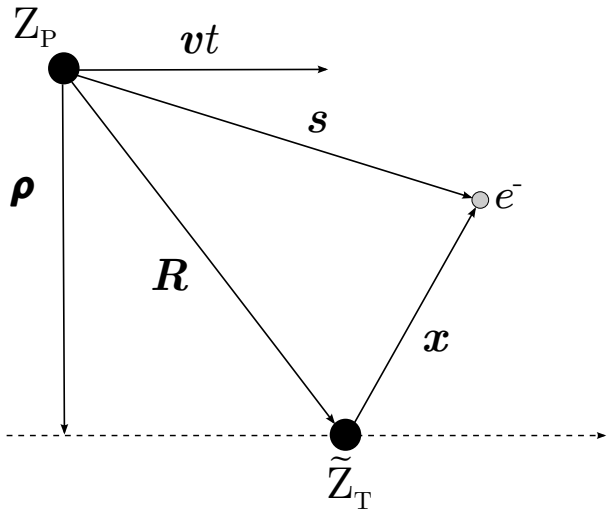

Figure II.4 The coordinate system considered in the CDW-EIS model. Z_P and $\mathbf{v}$ are the charge and velocity of the projectile, respectively; $\tilde{Z}_T$ is an effective charge related to the initial molecular binding energy, $\mathbf{x}$ ($\mathbf{s}$) is the active electron position in the target (projectile) reference frame and $\boldsymbol{\rho}$ is the impact parameter.

In particular, the straight-line version of the impact parameter approximation assumes that at sufficiently high collision energies the projectile describes a rectilinear trajectory defined by:

$$\mathbf{R} = \boldsymbol{\rho} + \mathbf{v}\, t \ , \tag{II.15}$$

where $\mathbf{R}$ is the internuclear vector, $\boldsymbol{\rho}$ the impact parameter, $\mathbf{v}$ the impact velocity ($\boldsymbol{\rho} \cdot \mathbf{v} = 0$), and t the collision time (see Figure II.4). With the previous assumptions, the multielectronic Hamiltonian is reduced to a single-active-electron one given by:

$$H_e = -\frac{1}{2}\nabla^2 + V_T(\mathbf{x}) + V_P(\mathbf{s}) + V_S(\mathbf{R}) \ , \tag{II.16}$$

where $\mathbf{x}$ and $\mathbf{s}$ denote the position vectors of the active electron with respect to the target and the projectile, respectively. The potential $V_T(\mathbf{x})$ contains the interaction of the active electron with the residual target; $V_P(\mathbf{s})$ describes the interaction between the

active electron and the projectile; and $V_S(\mathbf{R})$ represents the interaction of the projectile with the target nucleus and the passive electrons. The potential $V_S(\mathbf{R})$ depends only on the internuclear coordinate $\mathbf{R}$. Within the straight-line version of the impact parameter approximation, it gives rise to a phase factor which only affects the projectile angular scattering and not the electron dynamics [160]. Thus, the term $V_S(\mathbf{R})$ is dropped in the following. In distorted wave theory, the initial and final state wave functions are chosen as the product of the initial (bound) and final (continuum) states of the target active-electron and the corresponding distortions due to its interaction with the projectile. These functions are chosen in order to represent in the best possible way the physics of the problem and to keep the correct asymptotic conditions at large distances [143]. In the CDW-EIS approximation for the ionization process, the initial and final distorted wave functions are defined as:

$$\chi_i^+(\mathbf{x},\mathbf{s},t) = \phi_i(\mathbf{x})\exp\left(-i\varepsilon_i t\right)\mathcal{L}_i^+(\mathbf{s})\ , \tag{II.17}$$

$$\chi_f^-(\mathbf{x},\mathbf{s},t) = \phi_f(\mathbf{x})\exp\left(-i\varepsilon_f t\right)\mathcal{L}_f^-(\mathbf{s}) \tag{II.18}$$

with ϕ_i (ϕ_f) the initial bound (final continuum) active electron wave function; ε_i is the initial bound state binding energy; $\varepsilon_f = k^2/2$ is the final continuum energy with $\mathbf{k}$ the electron momentum on a target-fixed reference frame. The initial and final distortion factors are given by:

$$\mathcal{L}_i^+(\mathbf{s}) = \exp\left[-i\nu\ln\left(v\,s+\mathbf{v}\cdot\mathbf{s}\right)\right]\ , \tag{II.19}$$

$$\mathcal{L}_f^-(\mathbf{s}) = N^*(\zeta)\,{}_1F_1[-i\zeta;1;-i(p\,s+\mathbf{p}\cdot\mathbf{s})]\ , \tag{II.20}$$

respectively, where $\mathbf{v}$ and Z_P are the the velocity and the nuclear charge of the projectile, respectively; $\mathbf{p} = \mathbf{k} - \mathbf{v}$ is the electron momentum from a projectile-fixed reference frame; $\nu = Z_P/v$ and $\zeta = Z_P/p$; ${}_1F_1[b;c;z]$ is the Kummer confluent hypergeometric function and $N(a) = \exp\left(\pi a/2\right)\Gamma(1-ia)$ its normalization factor, with Γ representing Euler's gamma function. The initial-bound wave function, ϕ_i, of each molecular orbital is considered as a LCAO, as described in Sections II.2.2 and II.2.3. The emitted electron final continuum state is approximated by a hydrogenic continuum function with an effective charge $\tilde{Z}_T = \sqrt{-2n^2\varepsilon_i}$, where ε_i is the initial molecular binding energy and n is the principal quantum number of each of the atomic orbitals used to describe the molecular ones. The active electron wave function in the final channel is then:

$$\phi_f(\mathbf{x}) = \frac{\exp\left(i\mathbf{k}\cdot\mathbf{x}\right)}{(2\pi)^{3/2}}N^*(\lambda)\,{}_1F_1\left[-i\lambda;1;-i\left(k\,x+\mathbf{k}\cdot\mathbf{x}\right)\right]\ , \tag{II.21}$$

with $\lambda = \tilde{Z}_T/k$. The transition amplitude in the *prior* version of the CDW-EIS model is written as:

$$a(\boldsymbol{\rho})_{i,f}^- = \int_{-\infty}^{+\infty} dt\,\left\langle\chi_f^-\middle|W_i\middle|\chi_i^+\right\rangle\ , \tag{II.22}$$

where W_i is the perturbative operator acting on the entry channel, expressed as [163]:

$$W_i\,\chi_i^+ = \exp\left(-i\varepsilon_i t\right)\left[\frac{1}{2}\phi_i(\mathbf{x})\nabla_s^2\,\mathcal{L}_i^+(\mathbf{s}) + \nabla_x\,\phi_i(\mathbf{x})\cdot\nabla_s\,\mathcal{L}_i^+(\mathbf{s})\right]\,. \tag{II.23}$$

Thus, the transition amplitude results:

$$\begin{aligned} a(\boldsymbol{\rho})_{i,f}^- = \int_{-\infty}^{+\infty} dt\exp\left(i\Delta\varepsilon t\right)\int d\mathbf{x}\Big\{\phi_f^*(\mathbf{x})\mathcal{L}_f^{-*}(\mathbf{s})\Big[\frac{1}{2}\phi_i(\mathbf{x})\nabla_s^2\,\mathcal{L}_i^+(\mathbf{s}) \\ + \nabla_x\phi_i(\mathbf{x})\cdot\nabla_s\mathcal{L}_i^+(\mathbf{s})\Big]\Big\}\,, \end{aligned} \tag{II.24}$$

with $\Delta\varepsilon = \varepsilon_f - \varepsilon_i$. Moreover, the transition amplitude can be written as a function of the transverse momentum transfer $\boldsymbol{\eta}$, through the relation:

$$\mathcal{R}(\boldsymbol{\eta})_{i,f}^- = \frac{1}{2\pi}\int d\boldsymbol{\rho}\exp\left(i\boldsymbol{\eta}\cdot\boldsymbol{\rho}\right)a(\boldsymbol{\rho})_{i,f}^-\,. \tag{II.25}$$

This allows to find analytical expressions for the transition amplitude $\mathcal{R}$, drastically reducing the calculation times. The DDCS as a function of the emitted electron energy E_k and solid angle Ω_k, are given by:

$$\frac{d^2\sigma}{dE_k\,d\Omega_k} = k\int d\boldsymbol{\rho}\,\left|a(\boldsymbol{\rho})_{i,f}^-\right|^2 = k\int d\boldsymbol{\eta}\,\left|\mathcal{R}(\boldsymbol{\eta})_{i,f}^-\right|^2 \tag{II.26}$$

The numerical integration of Eq. II.26 over the solid angle Ω_k provides the SDCS. Finally, the TCS are obtained by integrating the SDCS over the electron energy E_k.

Dressed ions

The probability of charge-transfer processes increases as the velocity of the projectile decreases. As a result of these interactions, the initially bare projectiles may become dressed ions by capturing electrons from the target. For this reason it is necessary to consider in the simulations the formation and subsequent interactions of H^0, He^+ and He^0. Monti *et al.* [161] extended the CDW-EIS model to describe the ionization process by dressed projectiles.

While for bare projectiles the term $V_P(s)$ in Eq. II.16 is simply given by the Coulomb potential, i.e., $V_P(s) = -Z_P/s$, for dressed projectiles it is necessary to take into account the effect of the projectile electrons. Monti *et al.* [128, 161, 164] proposed to approximate the dressed-projectile potential by means of a Green-Sellin-Zachor (GSZ) potential [165], consisting of a short-range and a long-range term:

$$V_P(s) = V_P^{\mathrm{sr}} + V_P^{\mathrm{a}} = -\frac{1}{s}(Z_P - q)\left\{H[\exp(s/d) - 1] + 1\right\}^{-1} - \frac{q}{s}\,, \tag{II.27}$$

where H and d are adjustable parameters depending on the nuclear charge of the projectile Z_P and its degree of ionization q. The first term in Eq. II.27 provides the short-range correction due to the electrons in the dressed projectile. The second term is the asymptotic Coulomb interaction due to the projectile net charge q. The values of the parameters H and d exist for many ions and can be obtained for many other dressed projectiles by interpolating or extrapolating those available [164]. The short-range term

in Eq. II.27 adds a contribution to the transition amplitude, given by:

$$a(\boldsymbol{\rho})_{i,f}^{-(\mathrm{sr})} = \int_{-\infty}^{+\infty} dt \left\langle \chi_f^- \middle| V_P^{\mathrm{sr}}(s) \middle| \chi_i^+ \right\rangle , \tag{II.28}$$

which must be taken into account when using Eqs. II.25 to II.26 to compute the ionization cross sections.

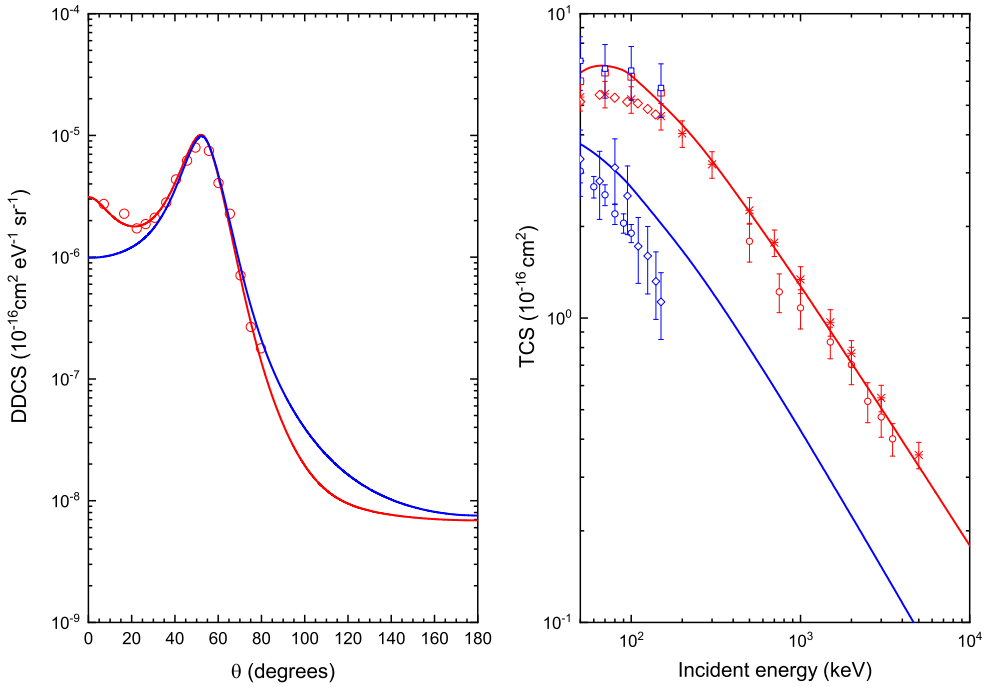

Figure II.5 Ionization cross sections for hydrogen ions in water computed with the *prior* version of the CDW-EIS model. Left panel: DDCS for H^+ (red line) and H^0 (blue line) for an impact energy of 1 MeV and an ejected electron energy of 750 eV. The circles are experimental data taken from Toburen and Wilson [105]. Right panel: TCS for H^+ (red line) and H^0 (blue line). Experimental data for H^+ were taken from Rudd *et al.* [101] (stars), Bolorizadeh and Rudd [104] (squares), Gobet *et al.* [166] (diamonds), and Luna *et al.* [167] (circles). Experimental data for H^0 were taken from Bolorizadeh and Rudd [168] (squares), Gobet *et al.* [169] (diamonds), and Luna *et al.* [167] (circles). Reprinted figures with permission from Ref. [128]. Copyright 2019 by the American Physical Society.

Figure II.5 shows the ionization cross sections for hydrogen ions in water computed with the *prior* version of the CDW-EIS model and used in *TILDA-V*, as reported in Ref. [128].

Figure II.6 shows the ionization cross sections for α-particles and the other charge states of helium in water obtained with the *prior* version of the CDW-EIS model.

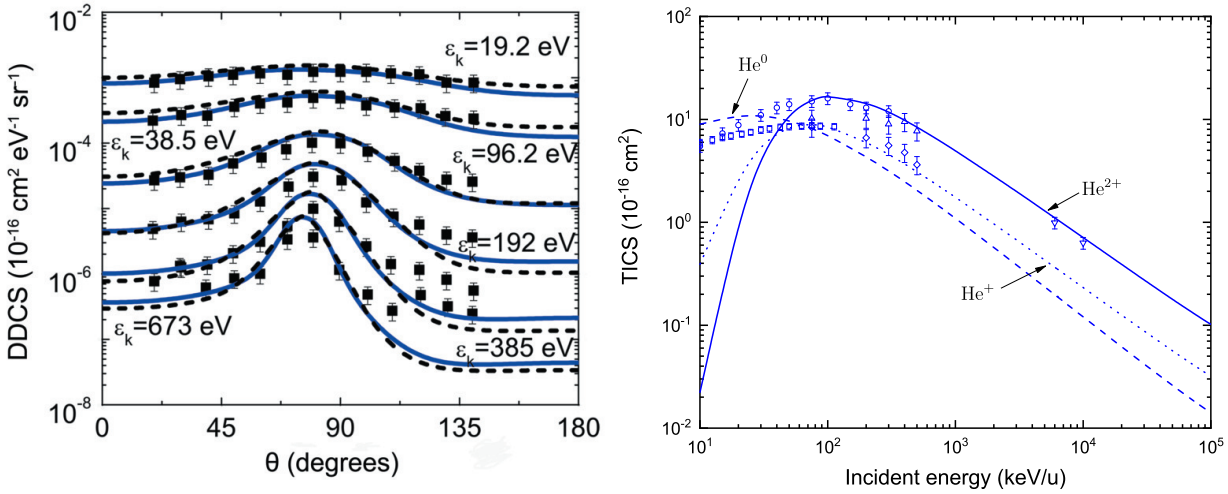

Figure II.6 Ionization cross sections for the impact of α-particles on water molecules obtained with the *prior* version of the CDW-EIS model. Left panel: DDCS for fixed values of the ejected electron energy ε_k, for He^{2+} with an impact energy of 6 MeV u^{-1}. The results using the two descriptions of the water molecule are shown: Moccia's approach (solid lines) and CNDO (dashed lines). The reported experimental results are from Ref. [170] (squares) (adapted and republished with permission of IOP Publishing, Ltd, from Ref. [146]; permission conveyed through Copyright Clearance Center, Inc.). Right panel: TICS for the three charge states of helium. Experimental data for He^{2+} are taken from Rudd *et al.* [106] (circles), Toburen *et al.* [110] (triangles) and Ohsawa *et al.* [171] (down triangles); for He^{+}, the data are taken from Rudd *et al.* [107] (squares) and Toburen *et al.* [110] (diamonds).

Let us note that in spite of the fair agreement observed between the theoretical TICS and the experiments (Figure II.6, right panel), except perhaps at incident energies below ~100 keV u^{-1}, they do not reproduce correctly the expected range and stopping power values for α-particles in the whole energy range of interest for dosimetry studies. Indeed, when these cross sections are used to compute the stopping power and range for α-particles in water, important discrepancies are found with the values of the ICRU Report 49 [10] (see Chapter V). Ongoing work is devoted to improve the ionization cross sections for helium ions within the *prior* CDW-EIS framework. As a temporary alternative, we have implemented in *TILDA-V* a set of semiempirical ionization cross sections based on fittings to available experimental data, as described in the work of Uehara and Nikjoo [4] (see Section I.3.2.1). This allowed us to obtain the expected track parameters and perform the simulations with α-particles reported in Chapter V.

Finally, Figure II.7 presents the TICS for hydrogen ions in DNA components.

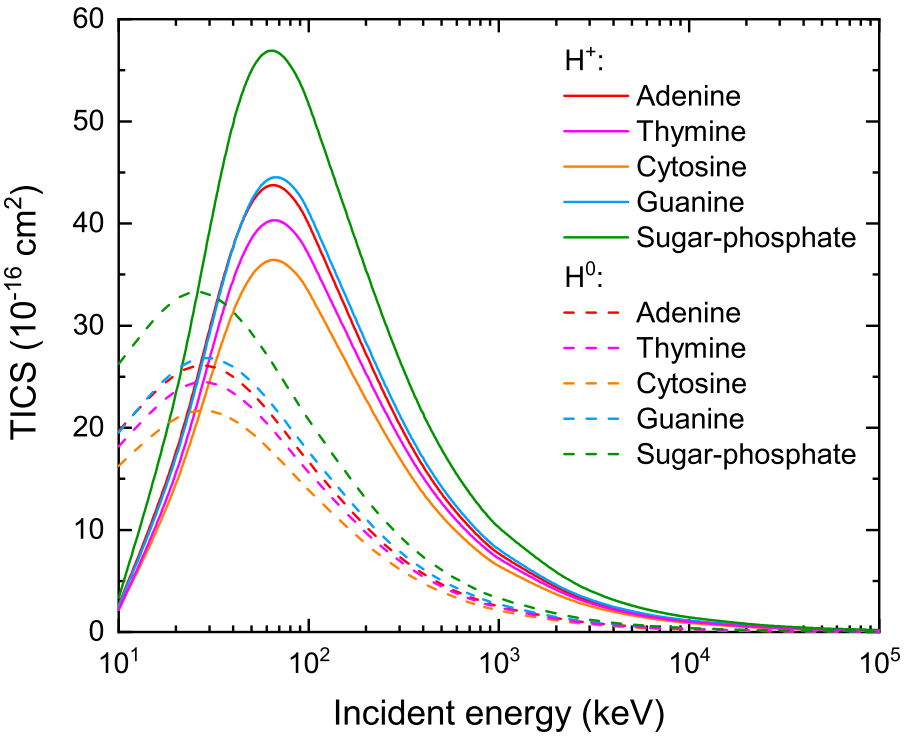

Figure II.7 Total ionization cross sections for hydrogen ions in DNA components obtained with the *prior* version of the CDW-EIS model.

Ongoing work is focused on the calculation of ionization cross sections for helium ions impacting on DNA components.

II.3.3.2 Alternative approaches

Besides the CDW-EIS approximation, there are many other theoretical models (both quantum-mechanical and classical), as well as semiempirical methods proposed to describe the ionization of atoms and molecules by ion impact. In this section we discuss such alternative approaches. Let us note that this is a non-exhaustive survey intended to provide a brief overview of the main models that have been implemented to obtain ionization cross sections for their use in MC simulations.

Rudd's model

Rudd *et al.* [103] proposed a semiempirical formula to compute the SDCS for proton impact. Rudd's model is based on a simple version of the BEA equation modified to agree with the Bethe theory at high energies. The SDCS for the single ionization of an orbital j is written as:

$$\frac{d\sigma_j^{\mathrm{Rudd}}}{dE_e} = \frac{S}{I_j}\frac{F_1 + F_2 w}{(1+w)^3\{1+\exp[\alpha(w-w_c)/v]\}}\,, \tag{II.29}$$

where $S = 4\pi a_0^2 N_j Z_P^2 (\mathrm{Ry}/I_j)^2$; E_e is the energy of the emitted electron; N_j is the number of electrons in the orbital j and I_j the ionization potential for that orbital; Z_P is the

nuclear charge of the projectile; a_0 is the Bohr radius and $\mathrm{Ry} = 13.6\,\mathrm{eV}$; $w = E_e/I_j$, $w_c = 4v^2 - 2v - \mathrm{Ry}/(4I_j)$ and $v = [Tm_e/(m_P I_j)]^{1/2}$ with T the energy of the projectile in $\mathrm{eV\,u^{-1}}$; m_e, m_P are the masses of the electron and the projectile, respectively; F_1, F_2 and α are adjustable fitting parameters determined from experimental data. F_1 and F_2 are given by:

$$F_1(v) = L_1 + H_1\ , \quad L_1 = \frac{C_1 v^{D_1}}{(1 + E_1 v^{D_1+4})}\ , \quad H_1 = \frac{A_1 \ln(1+v^2)}{v^2 + B_1/v^2} \tag{II.30}$$

$$F_2(v) = \frac{L_2 H_2}{L_2 + H_2}\ , \quad L_2 = C_2 v^{D_2}\ , \quad H_2 = \frac{A_2}{v^2} + \frac{B_2}{v^4} \tag{II.31}$$

The fitting parameters in Eqs. II.30 and II.31 are provided in Table II.4.

A_1	A_2	B_1	B_2	C_1	C_2	D_1	D_2	E_1	α
0.97	1.04	82.00	17.30	0.40	0.76	-0.30	0.04	0.38	0.64

Table II.4 Semiempirical parameters for computing the ionization cross sections in Rudd's model for water vapor [103].

TCS are obtained by numerical integration of Eq. II.29. While the model does not have any *a priori* restrictions on primary and secondary energies, it was found that it may underestimate the average energy of the ejected electrons for projectile energies above ∼300 $\mathrm{keV\,u^{-1}}$ (up to ∼30% at 2 $\mathrm{MeV\,u^{-1}}$, see Ref. [4]).

HKS model

The semiempirical model developed by Hansen, Kocbach and Stolterfoht (HKS) [172, 173] allows to estimate single and double ionization cross sections and is based on the impact parameter first Born approximation. The initial and the final electron states are described by means of a hydrogenic function and a plane wave, respectively. In the model, the electron emission by ion impact is written in terms of impact parameter dependent probabilities $P(b, \theta_e, E_e)$, where b is the impact parameter, whereas θ_e and E_e are the ejection angle and the kinetic energy of the ejected electron, respectively. By integrating $P(b, \theta_e, E_e)$ over the impact parameter, the DDCS are obtained. The expressions for the DDCS and the SDCS were provided in the ICRU Report 55 [174]. More recently, however, Bernal and Liendo [175] found inconsistencies in the original version of the HKS model and suggested modified formulas for the double and single ionization cross sections, which are the ones presented hereafter. The DDCS are given by [175]:

$$\frac{d^2\sigma^{\mathrm{HKS}}}{dE_e\, d\Omega_e} = \left(\frac{Z_p}{v}\right)^2 \frac{32}{3\pi\alpha k_c^3} \left[\frac{1}{1 + (\widetilde{K}_m - \tilde{k}_t \cos\theta_e)^2}\right]^3 . \tag{II.32}$$

The SDCS are expressed as:

$$\frac{d\sigma^{\mathrm{HKS}}}{dE_e} = \left(\frac{Z_p}{v}\right)^2 \frac{8}{\alpha k_c^3 \tilde{k}_t} \left\{ \tan^{-1}(\widetilde{K}_m + \tilde{k}_t) - \tan^{-1}(\widetilde{K}_m - \tilde{k}_t) + \frac{5(\widetilde{K}_m + \tilde{k}_t) + 3(\widetilde{K}_m + \tilde{k}_t)^3}{3[1 + (\widetilde{K}_m + \tilde{k}_t)^2]^2} - \frac{5(\widetilde{K}_m - \tilde{k}_t) + 3(\widetilde{K}_m - \tilde{k}_t)^3}{3[1 + (\widetilde{K}_m - \tilde{k}_t)^2]^2} \right\}, \tag{II.33}$$

where Z_P, T and $v = (2T)^{1/2}$ are the projectile charge, the reduced kinetic energy and velocity, respectively; $K_m = (\alpha^2 + k^2)/(2v)$ is the minimum momentum transfer; $\alpha = (2I)^{1/2}$ and $k = (2E_e)^{1/2}$ are the mean initial and final electron momenta, respectively; I and E_e are the ionization potential of the initial state and the final electron energy, respectively; $\widetilde{K}_m = K_m/\alpha_c$ and $\tilde{k}_t = k_t/\alpha_c$ are the normalized momenta. Moreover:

$$\alpha_c = \alpha\left(1 + 0.7\frac{v^2}{v^2 + k^2}\right),$$

$$k_c = \left[k^2 + \frac{2\alpha^2}{\ln(2v^2/\alpha^2)}\right]^{1/2},$$

$$k_t = \left(k^2 + 0.2\alpha^2\sqrt{v/\alpha}\right)^{1/2}.$$

The HKS model provides accurate SDCS for secondary electron energies $\gtrsim$10 eV produced by the impact of protons and α-particles on water at energies above $\sim$0.5 MeV u^{-1} [175]. However, the model yields DDCS that show only a limited agreement with the experimental data. Thus, the HKS model does not faithfully reproduce the angular distribution of the secondary electrons [4, 175].

Figure II.8 shows a comparison of the SDCS computed with various theoretical and semiempirical models for proton and α-particle impact on water for selected projectile energies. It can be seen that, for both projectiles, most of the models reproduce fairly well the experimental data for ejected electrons energies above 10 eV. However, the Rudd model overestimates the SDCS at low incident energies (100 keV and 150 keV in panel a, 300 keV u^{-1} in panel b). In several cases, the energy distribution of the ejected electrons predicted by the CDW-EIS model seems in better agreement with the experiments than the results obtained with the other models, particularly at high incident energies. Moreover, the results for all models tend asymptotically to the same values as the ejected electron energy increases.

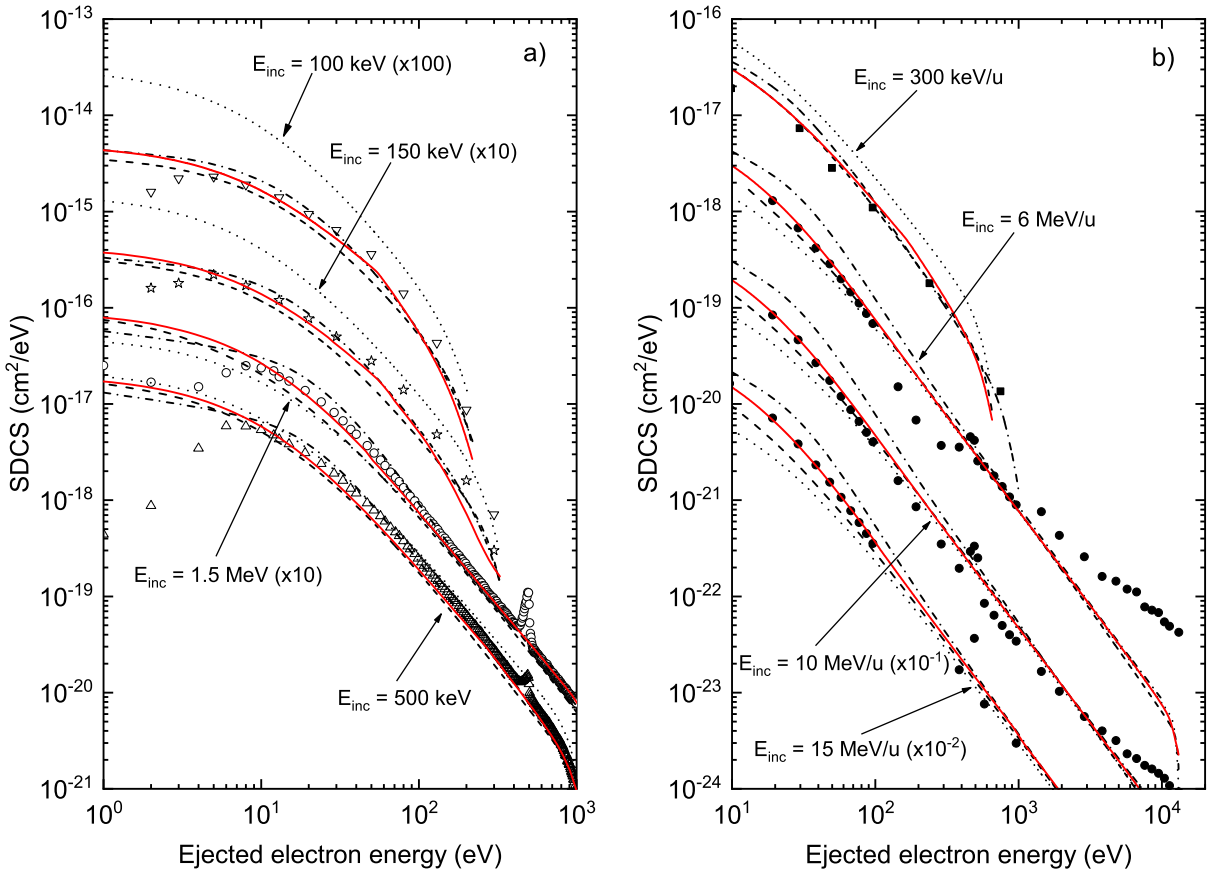

Figure II.8 SDCS for proton (panel a) and α-particle (panel b) impact on water vapor. The SDCS were obtained with the *prior* version of the CDW-EIS model (solid lines), the first Born approximation - Coulomb wave (FBA-CW) model (dash-dotted lines), the HKS model (dashed lines) and Rudd's model (dotted lines). The experimental data for protons were taken from Bolorizadeh and Rudd [104] (down triangles and stars) and Toburen and Wilson [105] (open circles and triangles). For α-particles, the data were taken from Toburen *et al.* [110] (solid squares) and Ohsawa *et al.* [171] (solid circles). Adapted from Champion *et al.* [176].

Similarly, a comparison of the TICS for H^+ and He^{2+} impinging on water molecules is shown in Figure II.9. The CDW-EIS approximation and Rudd's model successfully reproduce the TICS for protons with incident energies down to some tens of keV u^{-1}. For α-particles, however, the CDW-EIS model shows a slightly better agreement with experiments for incident energies between $\sim$80 keV u^{-1} and $\sim$200 keV u^{-1}. It should be reminded that Rudd's model was originally developed for protons. Indeed, the results of Rudd's model for He^{2+} depicted in Figure II.9 were determined by integrating the corresponding SDCS, which in turn were obtained by Z^2 scaling of the proton SDCS. Furthermore, the results using the FBA-CW approach [177] are in excellent agreement with the experimental data for both projectiles at high incident energies. However, the FBA-CW model fails at predicting the TICS for incident energies below some hundreds of

keV u^{-1}. It can be observed that the differences between all the theoretical predictions are greatly reduced at high incident energies.

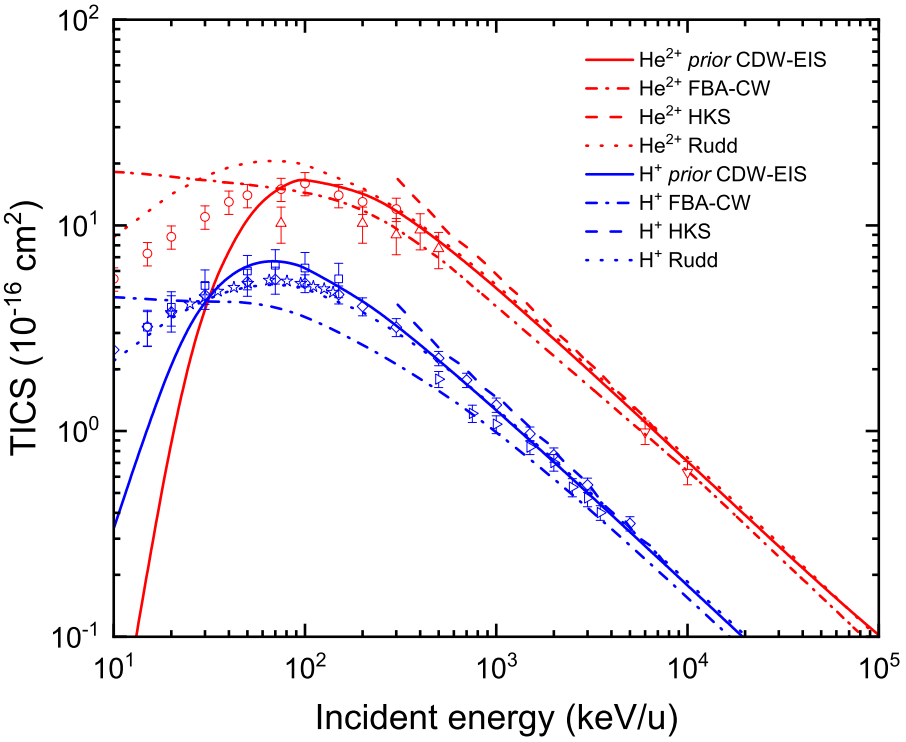

Figure II.9 Comparison of theoretical and experimental TICS for H^+ and He^{2+} impact on water vapor. The TICS computed with the HKS model were taken from Bernal and Liendo [178]. The experimental data were taken from Rudd *et al.* [106] (circles), Toburen *et al.* [110] (triangles), Ohsawa *et al.* [171] (down triangles), Rudd *et al.* [101] (diamonds), Bolorizadeh and Rudd [104] (squares), Gobet *et al.* [166] (stars), and Luna *et al.* [167] (right-pointing triangles).

The dielectric formalism

The dielectric formalism was developed within the framework of the PWBA. It is a widely used method to describe the inelastic scattering and the electronic energy loss of charged particles in liquid water. The main input parameter required in this approach is the energy loss function (ELF), which depends only on the target. The ELF contains all the information regarding the electromagnetic response of the target to the whole spectrum of momentum and energy excitations [179].

Various dielectric models have been proposed in the literature. They mainly differ in the data set chosen for liquid water and the dispersion relations implemented to determine the ELF for arbitrary momentum transfers. Only two sets of experimental data are available for liquid water in the optical limit, i.e., for zero momentum transfer ($k = 0$), the reflectance measurements of Heller *et al.* [180] and the data obtained

from inelastic X-ray scattering spectroscopy by Hayashi *et al.* [181]. Different extension algorithms have been proposed to consider non-zero momentum transfers ($k \neq 0$).

The dielectric formalism has been applied to study the energy loss of ions and electrons on targets of biological interest (see for instance Refs. [20, 21, 182–184]). Recently, de Vera *et al.* [185] presented a method based on the dielectric formalism and semiempirical corrections to obtain the energy and angular distributions for electrons ejected after proton impact on any kind of biological target. In their model, the DDCS for ionizing an electronic shell j as a function of the secondary electron energy W and the solid angle of emission Ω are written as [185]:

$$\left.\frac{d^2\sigma}{dW\,d\Omega}\right|_j = \frac{\alpha e^2}{2\pi^2\hbar^2\mathcal{N}\sin\theta}\frac{M[Z-\rho(k)]^2}{T}\mathrm{Im}\left[\frac{-1}{\epsilon(k,I_j+W)}\right]_j \times \frac{\sqrt{T[T-(I_j+W)]}\sin(\alpha\theta)}{2T-(I_j+W)-2\sqrt{T[T-(I_j+W)]}\cos(\alpha\theta)}\,, \tag{II.34}$$

where T, M and Z are the kinetic energy, mass and atomic number of the projectile, respectively, and $\rho(k)$ is the Fourier transform of its electronic density; θ is the ejected angle of the secondary electron; $\mathcal{N}$ is the molecular density of the target; $\mathrm{Im}[-1/\epsilon(k,E)]$ is the ELF, with $\epsilon(k,E)$ the dielectric function, while the subscript j denotes the contribution of the shell j to the ELF; $E = I_j + W$ is the energy transferred in an ionizing collision, I_j being the ionization potential of the outer shell electrons; α is a constant relating θ to the scattering angle of the projectile at the binary encounter peak. Finally, semiempirical corrections were added to Eq. II.34 to improve the agreement with the experimental DDCS (see Ref. [185] for the details).

II.3.4 The electron capture process

As ions slow down in matter, they may experience charge-transfer (or charge-exchange) interactions, known as electron capture and electron loss (stripping). Similarly to ionization, these processes may involve a single electron or multiple electrons. The electron capture interaction can be expressed as:

$$P^{(Z)} + T \rightarrow P^{(Z-n)'} + T^{n+}\,, \tag{II.35}$$

where Z is the charge of the incident ion and n is the number of electrons captured, assuming that multiple-capture processes are considered. It can be seen from Eq. II.35 that in the electron capture process, the projectile ionizes the target without the emission of secondary electrons. For protons, only single-electron capture, i.e., the transformation of H^+ into H^0, is taken into account in the *TILDA-V* code. The formation of H^- from electron capture by H^0 is neglected owing to its very low probability of occurrence [1]. In the case of α-particles, both single- and double-electron capture must be accounted for, as well as the single-electron capture by He^+. The energy loss in the electron capture

process includes: i) the energy I_i to remove the electron(s) from the target molecule; ii) the energy necessary to provide translational velocity for the electron to move at the speed of the projectile; and iii) the energy released from capture into the bound state of the projectile [30]:

$$\Delta E = I_i + E_{\text{inc}}\frac{m_e}{M_P} - I_P \ , \tag{II.36}$$

where M_P is the mass of the incident projectile and I_P denotes the ionization potential of the state to which the electron is captured. For protons $I_P = I_H = 13.6\,\text{eV}$, while for helium ions $I_P = I_{He} = 24.59\,\text{eV}$. For double-electron capture, the energy loss is two times the value given by Eq. II.36. Only the term I_i in Eq. II.36 represents energy locally deposited in the target.

It is worth mentioning that a charge-exchange interaction can be accompanied by simultaneous target ionization for both electron loss and electron capture. However, this process is normally not included in MCTS codes because of the lack of information regarding the corresponding cross sections [30].

II.3.4.1 The CDW-EIS model

The CDW-EIS approximation has been successfully applied to the single-electron capture process for bare ion impact on different atomic targets [186, 187]. More recently, the model has been used to study the electron capture in ion collisions with molecules of biological interest [126, 188], including the DNA bases [189]. In the CDW-EIS model, the difference between the ionization and electron capture processes is reflected in the final state wave function. As it can be seen from Eqs. II.18, II.20 and II.21, the final state for ionization is a product of continuum states associated with the active electron-residual target and active electron-projectile interactions. On the other hand, for electron capture the final bound state is distorted by a continuum state factor associated with the active electron-residual target interaction [186]. Thus, the distorted wave function in the final channel is given by:

$$\chi_f^- = \phi_{f,nlm}(\mathbf{s})\exp\left[-i\varepsilon_f t + i\mathbf{v}\cdot\mathbf{x} - i\frac{1}{2}v^2 t\right]\mathcal{L}_f^-(\mathbf{x}) \ , \tag{II.37}$$

where $\phi_{f,nlm}$ represents a final projectile bound state, namely a hydrogenic bound state with quantum numbers n, l and m, and binding energy $\varepsilon_f = -Z_P^2/2n^2$. The distortion factor in Eq. II.37 is chosen as:

$$\mathcal{L}_f^-(\mathbf{x}) = N^*(\xi)\,{}_1F_1\left[-i\xi;1;-i\left(v\,x + \mathbf{v}\cdot\mathbf{x}\right)\right] \ , \tag{II.38}$$

with $\xi = \tilde{Z}_T/v$. Similarly to ionization, the transition amplitude can be written in terms of the tranverse momentum transfer (Eq. II.25). The TCS for electron capture is then obtained as:

$$\sigma_{if} = \int d\boldsymbol{\eta}|\mathcal{R}(\boldsymbol{\eta})_{if}^-|^2 \tag{II.39}$$

The TCS for electron capture by H^+ in water and DNA components computed with the *prior* version of the CDW-EIS model and used in *TILDA-V* are shown in Figure II.10.

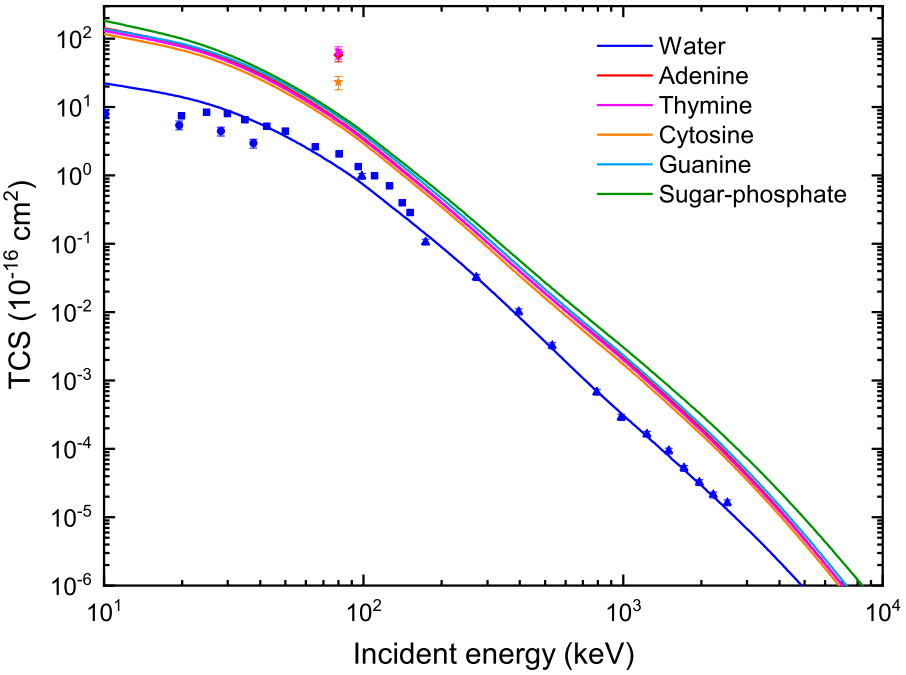

Figure II.10 TCS for electron capture by H^+ in water and DNA components computed with the *prior* CDW-EIS model. Experimental data for water are taken from Toburen *et al.* [190] (triangles), Dagnac *et al.* [191] (circles) and Gobet *et al.* [192] (squares). Experimental data for adenine (diamond), cytosine (star) and thymine (right-pointing triangle) are taken from Tabet *et al.* [193].

Figure II.11 shows the TCS for single-electron capture by He^{2+} in water, as obtained with the *prior* version of the CDW-EIS model.

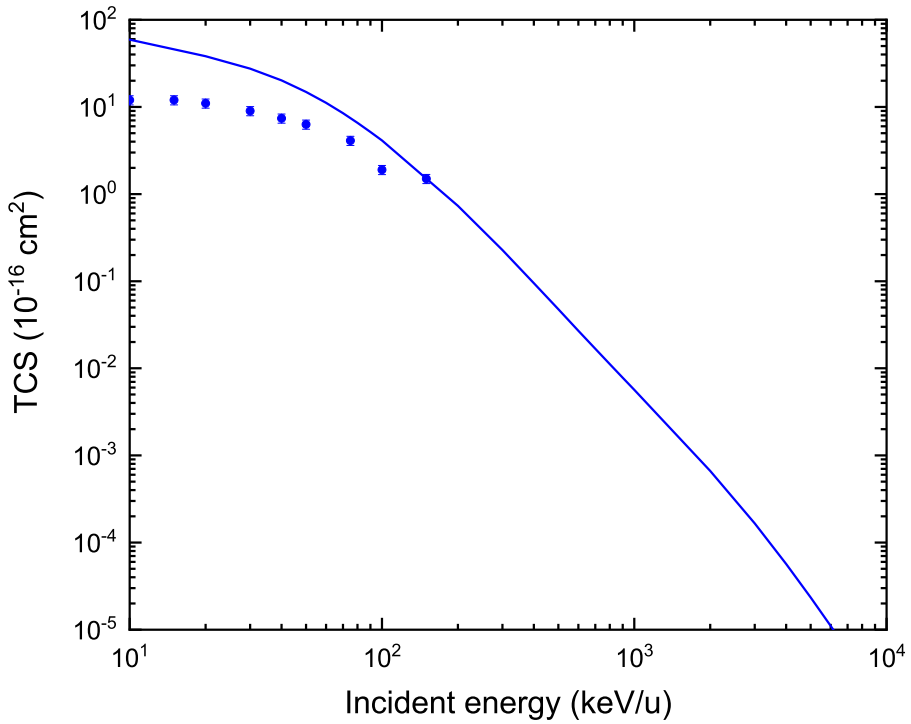

Figure II.11 TCS for single-electron capture by He^{2+} in water: *prior* CDW-EIS (solid line); experimental data taken from Rudd *et al.* [106] (circles).

It can be seen that the current results for the single-electron capture by He^{2+} overestimate the experimental data of Rudd *et al.* [106] for incident energies $< 150\,\mathrm{keV\,u^{-1}}$. Moreover, the cross sections for the other charge-transfer processes required for a full description of the transport of α-particles cannot be computed with the CDW-EIS model. For this reason, we decided to use in *TILDA-V* the electron capture and electron loss cross sections reported by Uehara and Nikjoo [4] for α-particles with incident energies up to $2\,\mathrm{MeV\,u^{-1}}$ in water (see Section I.3.2.1). Extrapolation was made for energies above $2\,\mathrm{MeV\,u^{-1}}$, even though the charge-transfer processes become negligible in the high-energy region. The electron capture TCS for helium ions reported by Uehara and Nikjoo [4] are shown in Figure II.12. For obtaining the single- and double-electron capture cross sections for He^{2+} (denoted as σ_{21} and σ_{20}, respectively), Uehara and Nikjoo [4] performed a least squares fitting to the data of Rudd *et al.* [106]. Since the latter data set only covers the energy range from $5\,\mathrm{keV\,u^{-1}}$ to $150\,\mathrm{keV\,u^{-1}}$, extrapolation was performed for lower and greater energies, assuming a smooth transition at the boundaries [4]. The cross sections for the single-electron capture by He^{+} (σ_{10}) were fitted to the experimental data of Rudd *et al.* [107] between $1\,\mathrm{keV\,u^{-1}}$ and $100\,\mathrm{keV\,u^{-1}}$, and Sataka *et al.* [108] between $75\,\mathrm{keV\,u^{-1}}$ and $500\,\mathrm{keV\,u^{-1}}$. The cross sections for energies above $500\,\mathrm{keV\,u^{-1}}$ were obtained by extrapolation. We have plotted as well in Figure II.12 the cross sections for the single-electron capture by He^{2+} computed with the CDW-EIS model

(solid line). The differences pointed out in Figure II.11 remain noticeable, although slightly reduced, at higher incident energies ($> 300\,\mathrm{keV\,u^{-1}}$), where the values of σ_{21} were extrapolated.

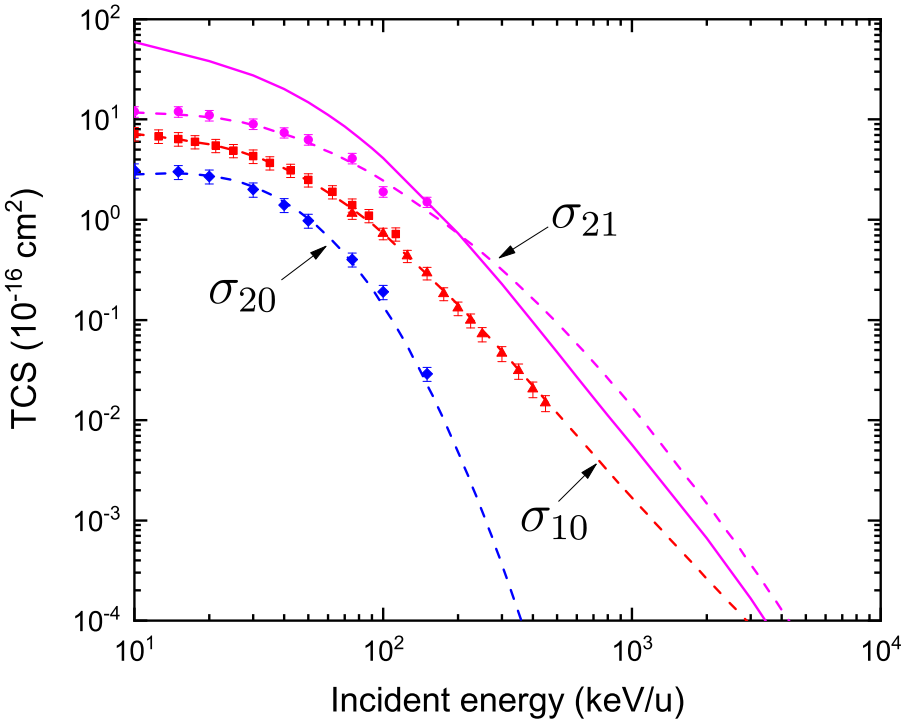

Figure II.12 Electron capture cross sections for He^{2+} and He^{+} in water. The dashed lines represent the cross sections reported by Uehara and Nikjoo [4] and the extrapolation performed in this work for energies above $2\,\mathrm{MeV\,u^{-1}}$ (see text). σ_{10}: single-electron capture by He^{+}, with experimental data from Rudd *et al.* [107] (squares) and Sataka *et al.* [108] (triangles); σ_{21}: single-electron capture by He^{2+}, with data from Rudd *et al.* [106] (circles). The solid line corresponds to the results obtained with the *prior* version of the CDW-EIS model; σ_{20}: double-electron capture by He^{2+}, experimental data were taken from Rudd *et al.* [106] (diamonds).

The calculation of the TCS for single-electron capture by α-particles in DNA components using the CDW-EIS model is underway.

II.3.4.2 Semiempirical models

In addition to the CDW-EIS approximation, semiempirical models can be used as well to obtain the electron capture cross sections. Besides the fitting to experimental data proposed by Uehara and Nikjoo [4] for the charge-transfer cross sections of helium ions (see Section I.3.2.1), some semiempirical formulas have been reported in the literature for the electron capture by protons.

Rudd's approach

In the method proposed by Rudd *et al.* [101], the electron capture cross section σ_c for protons in water is obtained from the relation:

$$\sigma_c = \sigma_+ - \sigma_- \ , \tag{II.40}$$

where σ_+ and σ_- are the measured cross sections for positive and negative charge production, respectively. These terms can be expressed as:

$$\sigma_\pm = \left[\frac{1}{(\sigma_{\text{low}})_\pm} + \frac{1}{\sigma_{\text{high}}}\right]^{-1} , \tag{II.41}$$

where the low- and high-energy components are written (in a.u.) as [194]:

$$(\sigma_{\text{low}})_+ = 4\pi(Ck_i^{2D} + F) \ , \quad (\sigma_{\text{low}})_- = 4\pi Ck_i^{2D} \ , \quad \sigma_{\text{high}} = \frac{4\pi[A\ln(1+k_i^2)+B}{k_i^2}] \ , \tag{II.42}$$

where k_i is the incident momentum. The fitting parameters are: $A = 2.98$, $B = 4.42$, $C = 1.48$, $D = 0.75$ and $F = 4.80$. The cross sections computed in this way are not accurate for energies above 100 keV. Moreover, they tend to a constant value for energies below 1 keV which is also in contradiction with experimental results [114].

Miller and Green approach

For protons in water, Miller and Green [5] fitted the electron capture cross sections measured by Toburen *et al.* [190] and Dagnac *et al.* [191] using the following analytic form:

$$\sigma = \sigma_0\left[\left(\frac{E_{\text{inc}}}{A}\right)^p + \left(\frac{E_{\text{inc}}}{B}\right)^q + \left(\frac{E_{\text{inc}}}{C}\right)^r\right]^{-1} , \tag{II.43}$$

with $\sigma_0 = 2\times10^{-15}\,\text{cm}^2$, $A = 44.1\,\text{keV}$, $B = 6.0\,\text{keV}$, $C = 1.5\,\text{keV}$, $p = 3.52$, $q = 0.667$ and $r = -0.027$. This approach was applied to obtain the electron capture cross sections used in the KURBUC code for protons [22, 78].

Dingfelder model

Based on the available experimental data on water vapor, Dingfelder *et al.* [114] developed an analytic formula to calculate the electron capture cross sections. The formula consists of straight lines for low and high proton energies on a doubly logarithmic scale, both connected by a power law. The cross section (in m^2) is expressed as:

$$\sigma(\tau) = 10^{Y(X)} \ , \tag{II.44}$$

where:

$$X = \log(\tau) \ , \tag{II.45}$$

with τ the kinetic energy in eV and:

$$\begin{aligned} Y(X) = {} & [a_0X + b_0 - c_0(X-x_0)^{d_0}\Theta(X-x_0)]\Theta(x_1-X) \\ & + (a_1X+b_1)\Theta(X-x_1) \ , \end{aligned} \tag{II.46}$$

where $\Theta(x)$ represents the Heaviside step function. The parameters a_0 and b_0 determine the low-energy straight line; a_1 and b_1 the high-energy one; whereas c_0 and d_0 correspond to the power law in between, connected to the low-energy straight line at x_0. The connection point x_1 to the high-energy line and the parameter b_1 are calculated as:

$$\begin{aligned} x_1 &= \left(\frac{a_0 - a_1}{c_0 d_0}\right)^{1/(d_0-1)} + x_0 \ , \\ b_1 &= (a_0 - a_1)x_1 + b_0 - c_0(x_1 - x_0)^{d_0} \ , \end{aligned} \tag{II.47}$$

by using the first derivative. The parameters are given in Table II.5.

a_0	b_0	c_0	d_0	a_1	b_1	x_0	x_1
-0.180	-18.22	0.215	3.550	-3.600	-1.997	3.450	5.251

Table II.5 Parameter set for computing the electron capture cross sections in the model of Dingfelder *et al.* [114].

The parameters were chosen to produce results close to the data of Lindsay *et al.* [195] and Dagnac *et al.* [191] for low and medium energies, and of Toburen *et al.* [190] for higher energies, and by adjusting the contribution of the cross section to the total stopping cross section considering the recommended values for the liquid phase [114].

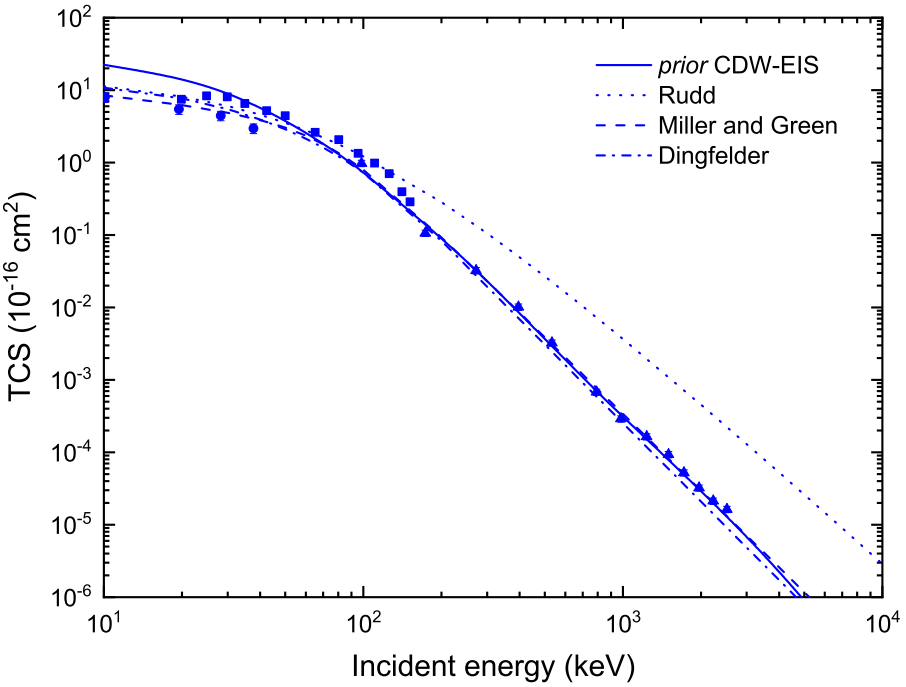

Figure II.13 Comparison between the TCS for electron capture by H^+ in water computed with the *prior* version of the CDW-EIS model and the results obtained with the semiempirical approaches of Rudd *et al.* [101], Miller and Green [5], and Dingfelder *et al.* [114]. The experimental data are the same as in Figure II.10.

Figure II.13 presents a comparison of the TCS for electron capture by H^+ in water obtained with the different models previously discussed. Overall, a good agreement is found between the *prior* CDW-EIS calculations and the semiempirical approaches of Miller and Green [5] and Dingfelder *et al.* [114] for incident energies above ∼100 keV. Conversely, Rudd's approach [101] significantly overestimates the TCS beyond this energy value. Below ∼70 keV, the *prior* CDW-EIS results provide the best agreement with the experimental data of Gobet *et al.* [192] (squares), while the TCS obtained with the Miller and Green approach are closer to the experimental values of Dagnac *et al.* [191] (circles).

II.3.5 The electron loss process

The electron loss or stripping process is equivalent to the ionization of the projectile. A dressed ion may lose one or more electrons by means of single- or multiple-electron loss, respectively. The electron loss interaction can be written as

$$P^{(Z)} + T \rightarrow P^{(Z+n)'} + T + ne^- \ . \tag{II.48}$$

The energy loss in this process is simply the energy required to remove the projectile electron, i.e.,

$$\Delta E = I_P \ . \tag{II.49}$$

The kinetic energy of the stripped electron was provided for in the capture process [30], namely

$$E_{\text{sec}} = E_{\text{inc}} \frac{m_e}{M_P} \ . \tag{II.50}$$

Single-electron loss is included in *TILDA-V* for H^0, He^+ and He^0. For the latter, double-electron loss is also considered, in which case the energy loss is twice the value given by Eq. II.49.

The cross sections used in *TILDA-V* for the electron loss process of H^0 were determined from the semiempirical model of Miller and Green [5], in a similar fashion to the electronic excitation process described in Section II.3.2. Miller and Green made use of the analytical form given in Eq. II.11 to fit the experimental cross sections measured by Toburen *et al.* [190] and Dagnac *et al.* [191]. The best fit was obtained with the parameters $a = 79.3\,\text{keV}$, $J = 27.7\,\text{keV}$, $\Omega = 0.652$, and $\nu = 0.943$ [5].

For the DNA components, neither experimental data nor theoretical predictions are available. Thus, the electron loss cross sections are obtained by applying a simple rescaling procedure to the values obtained for water vapor. This rescaling is based on the number of target electrons, as proposed by Champion *et al.* [156], who showed that the TCS for the ionization and electron capture processes are directly linked to the total number of target electrons. Thus, the total electron loss cross section of a given DNA

component is computed as [143]:

$$\sigma_{\text{eloss}}^{(\text{DNA component})}(E_{\text{inc}}) = \sigma_{\text{eloss}}^{(\text{H}_2\text{O})}(E_{\text{inc}})\,\frac{Z'}{Z}\,, \tag{II.51}$$

where E_{inc} is the kinetic energy of the incident projectile; $\sigma_{\text{eloss}}^{(\text{H}_2\text{O})}(E_{\text{inc}})$ is the total electron loss cross section for water vapor at that energy; $Z = 10$ is the number of electrons of the water molecule; and Z' is the number of electrons of a given DNA component: $Z' = 70, 66, 58, 78, 96$ for adenine, thymine, cytosine, guanine and sugar-phosphate backbone, respectively. The electron loss cross sections for H^0 are presented in Figure II.14.

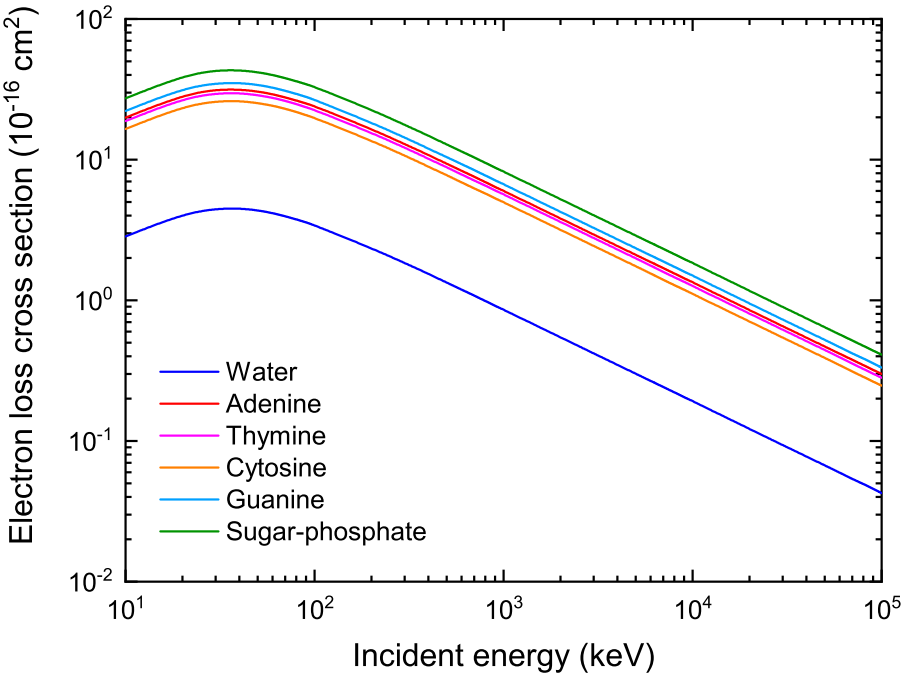

Figure II.14 Electron loss cross sections for neutral hydrogen atoms in water and DNA components computed with the semiempirical model of Miller and Green [5] and Eq. II.51, respectively.

For He^+ and He^0 impact on water, we used the electron loss cross sections implemented in the KURBUC code, as described in the paper by Uehara and Nikjoo [4] (see Section I.3.2.1). Extrapolation was made for energies higher than 2 MeV u^{-1}. The cross sections are reported in Figure II.15.

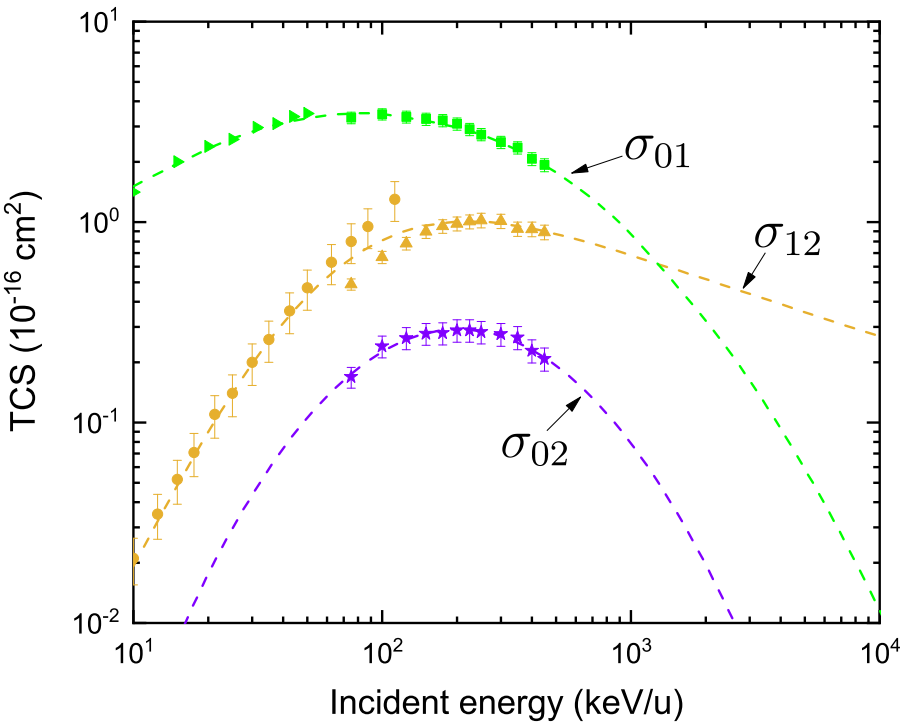

Figure II.15 Electron loss cross sections for He^+ and He^0 in water. The dashed lines represent the cross sections reported by Uehara and Nikjoo [4] and the extrapolation performed in this work for energies above 2 MeV u^{-1} (see text). σ_{01}: single-electron loss by He^0, with experimental data from Allison [109] (right-pointing triangles) and Sataka *et al.* [108] (squares); σ_{12}: single-electron loss by He^+, with data from Rudd *et al.* [107] (circles) and Sataka *et al.* [108] (triangles); σ_{02}: double-electron loss by He^0, with experimental values taken from Sataka *et al.* [108] (stars).

II.3.6 The elastic scattering process

In the elastic scattering process, the incident projectile is deflected from its original trajectory as a result of experiencing the field of the target. The process can be written as:

$$P + T \rightarrow P' + T \,, \tag{II.52}$$

where P' denotes a change in the energy of the projectile. Energetic heavy ions move practically in straight-line trajectories and thus the effect of elastic scattering is sometimes neglected in MC simulations. However, the process becomes important as the ion slows down in matter. Moreover, the nuclear energy loss cannot be neglected at very low energies (i.e., below $< 10\,\mathrm{keV\,u^{-1}}$) [30].

To determine the polar scattering angle θ, we proceeded as follows. We started from the well-known Rutherford differential cross section in the center-of-mass (CM) frame,

namely:

$$\frac{d\sigma}{d\Omega} = \left(\frac{Z_P Z_T e^2}{4E_{\text{inc}}}\right)^2 \sin^{-4}\left(\frac{\theta}{2}\right) , \tag{II.53}$$

where Z_P and Z_T are the nuclear charges of the projectile and the target, respectively ($Z_T = 10$ for water), and e is the elementary charge. $d\Omega$ is the differential solid angle given by:

$$d\Omega = \sin\theta d\theta d\varphi = 2\pi \sin\theta d\theta \, . \tag{II.54}$$

The cumulative probability distribution for the angle θ can then be written as:

$$P(\theta) = \frac{\displaystyle\int_{\theta_{\text{cut}}}^{\theta} \frac{d\sigma}{d\Omega} d\Omega}{\displaystyle\int_{\theta_{\text{cut}}}^{\pi} \frac{d\sigma}{d\Omega} d\Omega} , \tag{II.55}$$

where θ_{cut} is an angle that limits the increase in the scattering probability at low scattering angles [196], given by:

$$\theta_{\text{cut}} \approx \alpha Z_T^{1/3} \left(\frac{m_e c}{p}\right) , \tag{II.56}$$

where $\alpha \approx 1/137$ is the fine-structure constant, c is the speed of light in vacuum, and p is the linear momentum of the particle. Substituting Eqs. II.53 and II.54 in Eq. II.55 gives:

$$P(\theta) = \frac{\displaystyle\int_{\theta_{\text{cut}}}^{\theta} \sin\theta' \sin^{-4}\left(\frac{\theta'}{2}\right) d\theta'}{\displaystyle\int_{\theta_{\text{cut}}}^{\pi} \sin\theta' \sin^{-4}\left(\frac{\theta'}{2}\right) d\theta'} = \frac{\displaystyle\int_{\theta_{\text{cut}}}^{\theta} \cos\left(\frac{\theta'}{2}\right) \sin^{-3}\left(\frac{\theta'}{2}\right) d\theta'}{\displaystyle\int_{\theta_{\text{cut}}}^{\pi} \cos\left(\frac{\theta'}{2}\right) \sin^{-3}\left(\frac{\theta'}{2}\right) d\theta'} ,$$

And solving the integral:

$$P(\theta) = \frac{\sin^{-2}\left(\frac{\theta}{2}\right) - \sin^{-2}\left(\frac{\theta_{\text{cut}}}{2}\right)}{1 - \sin^{-2}\left(\frac{\theta_{\text{cut}}}{2}\right)} , \tag{II.57}$$

By using Eq. II.57 and a random number η uniformly distributed over [0,1], the scattering angle θ is obtained with the following expression:

$$\theta = 2\arcsin\left\{\eta\left[1 - \sin^{-2}\left(\frac{\theta_{\text{cut}}}{2}\right)\right] + \sin^{-2}\left(\frac{\theta_{\text{cut}}}{2}\right)\right\}^{-1/2} . \tag{II.58}$$

The azimuthal scattering angle φ is sampled uniformly in the interval $[0, 2\pi)$, that is:

$$\varphi = 2\pi\eta \, . \tag{II.59}$$

The energy transfer from the projectile to the target in an elastic collision is determined by non-relativistic kinematics (see for instance Ref. [197]). Considering the collision system depicted in Figure II.16 and the relationship between the variables in the laboratory and the CM frames, the energy transfer can be written as:

$$\Delta E = \frac{\mathbf{p}_2'^2}{2M_T} = \frac{(\mathbf{p}' - \mathbf{p})^2}{2M_T} , \tag{II.60}$$

where $\mathbf{p}'_2$ is the momentum transferred to the target after the collision in the laboratory frame; $\mathbf{p}$ and $\mathbf{p}'$ are the momenta before and after the collision in the CM frame. The numerator on the right of Eq. II.60 can be written as:

$$(\mathbf{p}' - \mathbf{p})^2 = 2p^2(1 - \cos\theta) = 4p^2 \sin^2\left(\frac{\theta}{2}\right) , \tag{II.61}$$

with

$$p = \frac{M_T p_1}{M_P + M_T} , \tag{II.62}$$

where M_P and M_T are the masses of the projectile and the target, respectively.

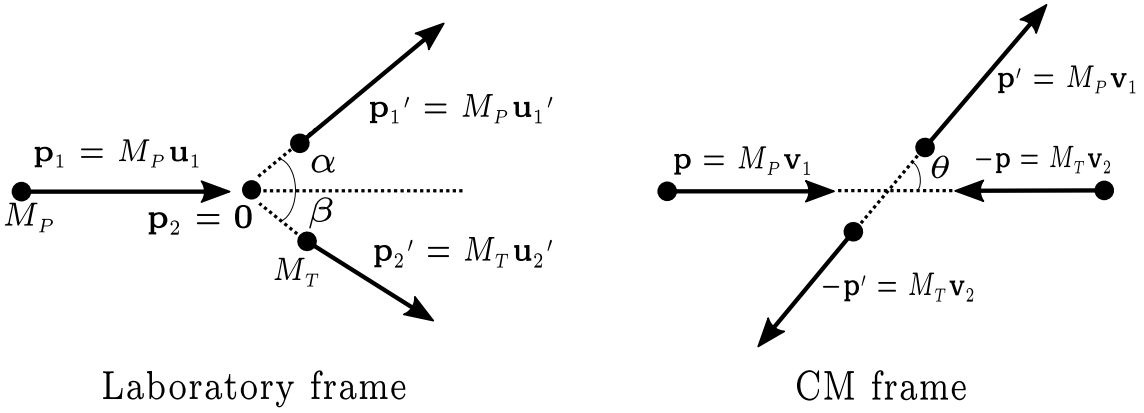

Figure II.16 The collision system in the elastic scattering process and the variables in the laboratory frame and the CM frame. The unprimed (primed) variables correspond to the initial (final) state of the system.

Since the incident energy is given by $E_{\text{inc}} = p_1^2/(2M_P)$, the energy deposited in the elastic scattering process is computed as:

$$E_{\text{dep}} = \Delta E = 4E_{\text{inc}} \frac{M_P M_T}{(M_P + M_T)^2} \sin^2\left(\frac{\theta}{2}\right) , \tag{II.63}$$

The scattering angles α and β in the laboratory frame are related to the scattering angle θ in the CM frame through the following expressions:

$$\tan\alpha = \frac{\sin\theta}{(M_P/M_T) + \cos\theta} , \tag{II.64}$$

$$\beta = \frac{\pi - \theta}{2} . \tag{II.65}$$

Moreover, it can be seen from Eq. II.64 that when $M_P << M_T$, which is the case for protons, $\alpha \approx \theta$ and $\beta \approx (\pi - \alpha)/2$. Therefore, we have assumed in our simulations that the angle θ in the CM frame is equal to the angle α in the laboratory frame.

The elastic scattering cross sections for protons are computed from the classical mechanical theory. The classical SDCS for the elastic scattering of protons is given by:

$$\frac{d\sigma}{d\Omega} = -\frac{\rho}{\sin\theta}\frac{d\rho}{d\theta} , \tag{II.66}$$

where ρ is the impact parameter, i.e., the normal distance between the proton track and

the virtual line crossing the CM of the system, and θ denotes the scattering angle in the CM frame defined by:

$$\theta = \pi - 2\int_{r_{\min}}^{\infty} \frac{\rho}{r^2\sqrt{1 - V(r)/E_{\text{inc}}^{\text{CM}} - \rho^2/r^2}} dr \ , \tag{II.67}$$

where $r_{\min}$ is the distance of closest approach, $V(r)$ is the interaction potential and $E_{\text{inc}}^{\text{CM}}$ is the energy of the incident particle in the CM system. Using the bare Coulomb potential as $V(r)$ in Eq. II.67 yields (through Eq. II.66) the Rutherford differential cross section, Eq. II.53.

The elastic scattering TCS are obtained by numerical integration of the SDCS (Eq. II.66) over the scattering solid angle by using a cutoff angle in order to reduce the divergence due to the high values of the SDCS at low scattering angles [1, 143]. However, the TCS obtained by integrating Eq. II.53 are unrealistic because the screening of the atomic electrons is not considered. For this reason we decided to use in our simulations the elastic scattering TCS for protons and α-particles reported by Uehara and co-workers [4, 22, 78], who performed classical mechanics trajectory calculations using the screening parameters recommended by the ICRU [10]. Moreover, for protons with incident energies higher than 10 MeV the cross sections were computed with the Mott scattering formula for heavy particles [196] to avoid unrealistic tortuous tracks [78].

The elastic scattering TCS for neutral hydrogen atoms in water are derived from a fitting proposed by Endo *et al.* [130] for the hydrogen to proton cross section ratio, namely:

$$\frac{\sigma_{H^0}}{\sigma_{H^+}} = 1 + 0.0224\log(E_{\text{inc}}) + 0.01285\log(E_{\text{inc}})^2 \ , \tag{II.68}$$

This ratio is close to unity within the incident energy range considered here [1, 143]. On the other hand, the elastic scattering TCS for He^+ and He^0 were assumed to be equal to those for He^{2+}.

Work is in progress to compute the elastic scattering cross sections for DNA components. While this work is completed, we apply a scaling factor to the TCS of water to obtain the TCS for each DNA component, namely:

$$\sigma^{(\text{DNA component})}(E_{\text{inc}}) = \sigma^{(\text{H}_2\text{O})}(E_{\text{inc}}) \left[\frac{Z'(M_P + M')M}{Z(M_P + M)M'}\right]^2 \ , \tag{II.69}$$

where M_P is the mass of the projectile; Z' and M' are the charge and the mass of the DNA component, respectively; Z and M are the charge and the mass of the water molecule, respectively.

II.3.7 Summary of total cross sections for ion impact

We provide in Figure II.17 the TCS for all the inelastic interactions considered for the transport of hydrogen ions in water and DNA, as discussed thus far. For the latter

medium, the reported TCS are for a hydrated DNA unit.

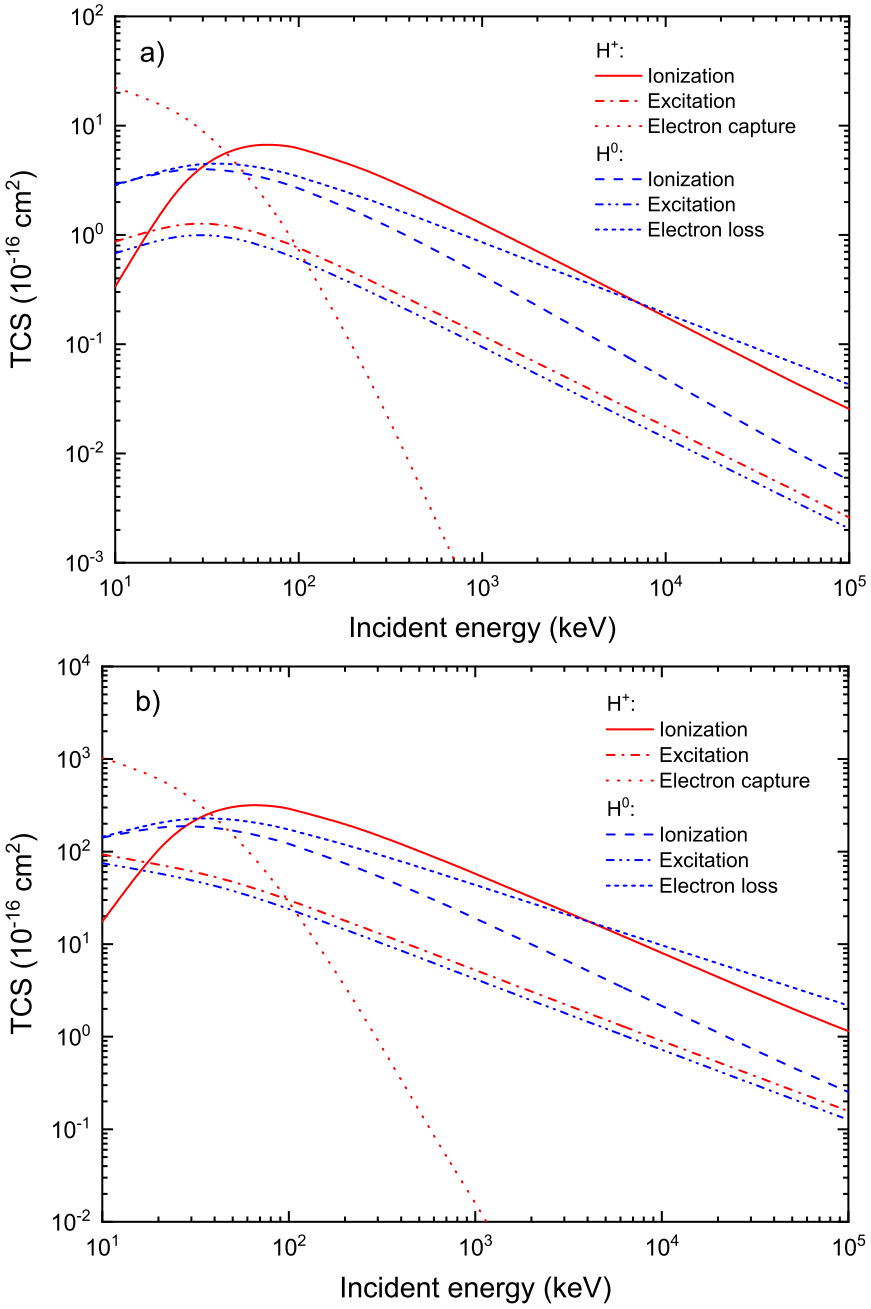

Figure II.17 Total inelastic cross sections for hydrogen ions in water (panel a) and hydrated DNA (panel b).

II.4 Physical processes induced by the impact of electrons

In this section, we provide an overview of the interactions that must be included in a MC code to simulate the transport of electrons. We describe the models allowing to compute the cross sections for each physical process, with particular stress on the models used in the EPOTRAN code. For electron impact on biological media, the processes of ionization, excitation and elastic scattering are considered. In this thesis, the energy range of interest for electrons extends from 7.4 eV to some MeV. More specifically, for the simulations performed with *TILDA-V* the upper energy limit for ions is of 100 MeV u^{-1}, thus the secondary electrons will have a maximum kinetic energy of:

$$E_{\text{sec}}^{(\max)} = 4E_{\text{inc}}\frac{m_e}{m_{\text{ion}}} = (4)(100)\left(\frac{1}{1836}\right) \approx 0.218\,\text{MeV} = 218\,\text{keV}\ , \tag{II.70}$$

which is the maximum energy transfer from an ion to an electron in a classical binary collision. On the other hand, for the simulations involving β^--emitting radionuclides (see Chapter IV), the highest electron energy considered in our work is that of yttrium-90 ($E_{\beta^-}^{(\max)} = 2.28\,\text{MeV}$). Although the models used in EPOTRAN might well remain valid above this energy, the neglect of Bremsstrahlung precludes the application of the code for very high-energy electrons. Indeed, the contribution of Bremsstrahlung to the total electron energy loss in water increases from ∼8% at $E_{\text{inc}} = 10\,\text{MeV}$ to ∼50% at $E_{\text{inc}} = 100\,\text{MeV}$ [198, 199].

II.4.1 The electronic excitation process

As for ions, the cross sections for electron-induced excitation of the water molecule were obtained from a semiempirical model. In this model, the excitation cross section is given by the following analytical expression [8]:

$$\sigma_n(E_{\text{inc}}) = \frac{q_0 K}{W_n^2}\left(\frac{W_n}{E_{\text{inc}}}\right)^{\Omega}\left[1-\left(\frac{W_n}{E_{\text{inc}}}\right)^{\beta}\right]^{\nu}\ , \tag{II.71}$$

where W_n is the excitation energy for the excitation channel labeled n (in some cases it is treated as an adjustable parameter); Ω, β, ν are fitting parameters; $q_0 = 4\pi a_0^2 \text{Ry}^2 = 6.514\times10^{-14}\,\text{cm}^2\,\text{eV}^2$; $K = f_0^{(n)}c_0^{(n)}$, where $f_0^{(n)}$ and $c_0^{(n)}$ are the optical oscillator strength and a constant of normalization, respectively. All the parameters can be found in Table 2 of Ref. [8]. Eq. II.71 was used to obtain the cross sections of the following processes: electronic transitions towards Rydberg states or degenerate states ($\widetilde{A}_1B_1$, $\widetilde{B}_1A_1$, diffuse band); dissociative processes leading to excited radicals (H*, O*, and OH*); and vibrational channels. On the other hand, the cross sections for the dissociative attachment processes leading to the formation of negative ions were

calculated with the following expression [8]:

$$\sigma_n(E_{\text{inc}}) = \frac{A\exp(t)}{U[1+\exp(t)]^2} \tag{II.72}$$

with

$$t = \frac{E_{\text{inc}} - W_n}{U}\,, \tag{II.73}$$

where A and U are fitting parameters reported in Table 3 of Ref. [8].

The electron-induced excitation cross sections for DNA components were also computed with Eq. II.71. For thymine, the necessary parameters were obtained by performing a least-square fit to the experimental data of Levesque *et al.* [200]. The parameters for thymine are [1]: $\nu = 3.8$, $\beta = 2$, $\Omega = 0.7236$, $K = 0.2985$ and $W_n = 4\,\text{eV}$. The excitation cross sections for the other DNA components were obtained by scaling the parameter K proportionally to the number of target electrons, namely: $K = 0.3166$, $K = 0.2623$, $K = 0.3528$, and $K = 0.4342$ for adenine, cytosine, guanine, and the sugar-phosphate group, respectively [1]. Figure II.18 shows the total excitation cross sections for electron impact on water and DNA components.

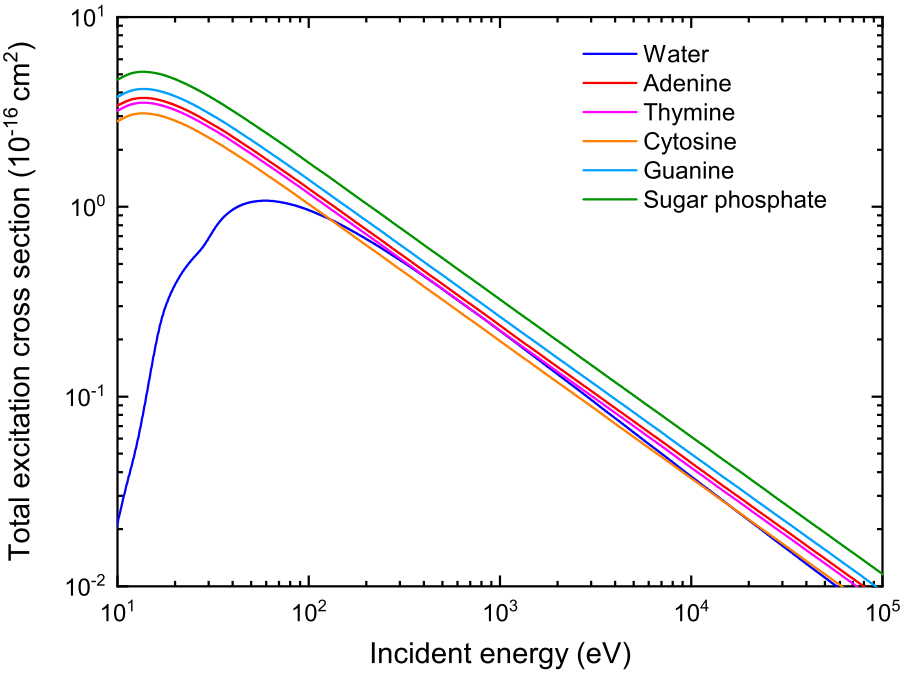

Figure II.18 Total excitation cross sections for electron impact on water and DNA components computed with the semiempirical model of Olivero *et al.* [8].

The energy deposited as a result of the electron-induced excitation of adenine, cytosine and thymine was obtained by averaging the experimental values provided by Michaud *et al.* [201]; for guanine, it was derived from the theoretical values reported by Fleig *et al.* [202] from quantum-mechanical coupled-cluster methods. Finally, due to the absence of data for the sugar-phosphate group, the value of 7.56 eV reported by Bremner

et al. [203] for the tetrahydrofuran molecule was used. It is worth mentioning that this approximation is often made in simple models of the deoxyribose building block [204]. The average excitation energies for DNA components are shown in Table II.6.

DNA component	Energy (eV)
Adenine	5.8
Cytosine	5.39
Guanine	5.38
Thymine	5.5
Sugar-phosphate	7.56

Table II.6 Mean excitation energies used in *TILDA-V* for the DNA components [1]. The value reported for the sugar-phosphate group corresponds to the tetrahydrofuran molecule.

II.4.2 The ionization process

Various theoretical and semiempirical models have been proposed to describe the ionization of atoms and molecules by electron impact. EPOTRAN simulations are currently based on ionization cross sections computed with two different approaches: the relativistic binary-encounter-Bethe (RBEB) model and the distorted wave Born approximation (DWBA).

II.4.2.1 The relativistic binary-encounter-Bethe model

The binary-encounter-Bethe (BEB) model is a simplified version of the binary-encounter-dipole (BED) model introduced by Kim and Rudd [120]. The model results from combining two theories: the Mott theory for the hard collision of two free electrons and the Bethe theory for the dipole interaction (soft collision) between the incident and target electrons at high incident electron energy [120, 205]. The BEB model only requires the knowledge of three quantities in order to compute the ionization cross section for each molecular orbital: the electron occupation number N, the ionization potential I and the average kinetic energy of the target electron U. The model was extended to relativistic incident electron energies by melding the Møller cross section with the relativistic form of the Bethe cross section [7]. The relativistic version (RBEB) is needed for incident electron energies T greater than 20 keV. The ionization cross section for an atomic or molecular orbital is expressed in the RBEB model as [7]:

$$\begin{aligned}\sigma_{\mathrm{RBEB}} = \frac{4\pi a_0^2 \alpha^4 N}{(\beta_t^2+\beta_u^2+\beta_b^2)2b'} \Bigg\{ \frac{1}{2}\left[\ln\left(\frac{\beta_t^2}{1-\beta_t^2}\right) - \beta_t^2 - \ln(2b')\right]\left(1-\frac{1}{t^2}\right) \\ +1 - \frac{1}{t} - \frac{\ln t}{t+1}\frac{1+2t'}{(1+t'/2)^2} + \frac{b'^2}{(1+t'/2)^2}\frac{t-1}{2}\Bigg\} ,\end{aligned} \tag{II.74}$$

where $t = T/I$, a_0 is the Bohr radius, α is the fine-structure constant and the other terms are defined as:

$$\beta_t = v_t/c\ , \quad \beta_t^2 = 1 - \frac{1}{(1+t')^2}\ , \quad t' = T/m_e c^2\ , \tag{II.75}$$

$$\beta_b = v_b/c\ , \quad \beta_b^2 = 1 - \frac{1}{(1+b')^2}\ , \quad b' = I/m_e c^2\ , \tag{II.76}$$

$$\beta_u = v_u/c\ , \quad \beta_u^2 = 1 - \frac{1}{(1+u')^2}\ , \quad u' = U/m_e c^2\ , \tag{II.77}$$

with m_e the electron mass and c the speed of light; v_t is the speed of an electron with kinetic energy T; v_b is the speed of an electron with kinetic energy I; and v_u is the speed of an electron with kinetic energy U. Eq. II.74 provides the cross section for an atomic or molecular orbital, thus the TICS for the target is the sum over all occupied orbitals. For water, the values of I and U for each molecular orbital were taken from the work of Rudd *et al.* [103]. Figure II.19 shows the ionization cross sections provided by this model for the water molecule.

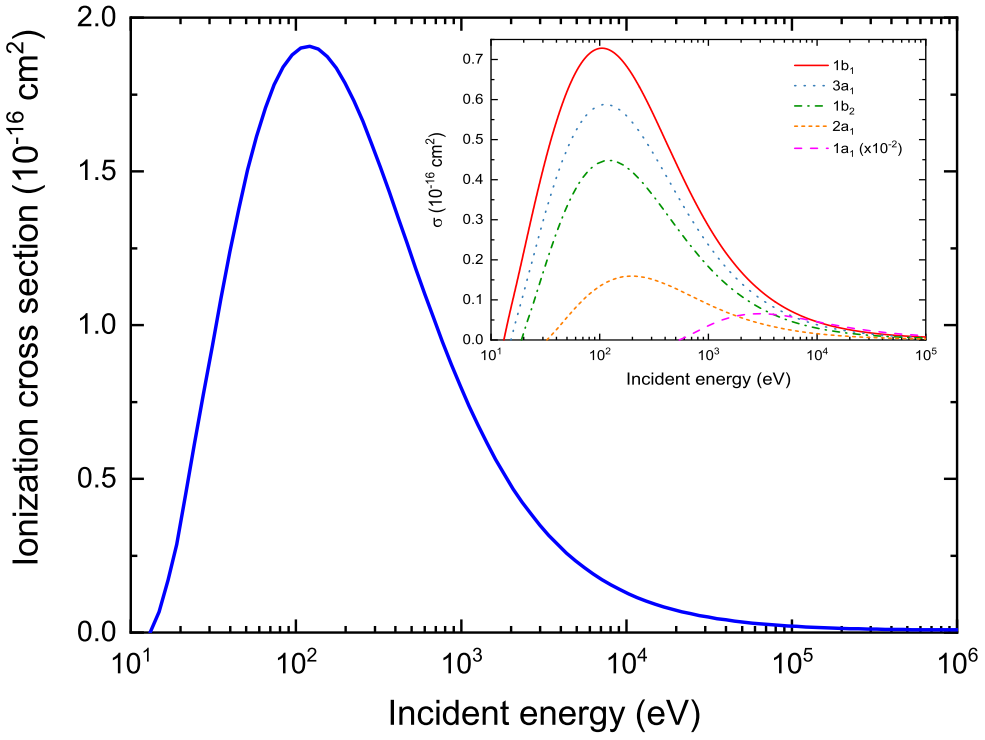

Figure II.19 Total ionization cross sections for electron impact on water obtained with the RBEB model. The inset shows the contribution of each molecular orbital to the total cross section.

The RBEB model was also applied to compute the TICS of the DNA components. In this case, the values of I and U for each DNA component were obtained with the Gaussian 09 software [152] and are provided in Appendix B.

II.4.2.2 The distorted wave Born approximation

In the DWBA framework, the incident and scattered (fast) electrons are described by a plane wave function, whereas the ejected (slow) electron is described by a distorted wave function [206]. The triple differential cross section (TDCS), i.e., differential in the direction of the scattered electron, and in the direction and energy of the ejected electron, are defined as:

$$\sigma^{(3)}(\Omega_{\rm s},\Omega_{\rm e},E_{\rm e}) \equiv \frac{{\rm d}^3\sigma_j}{{\rm d}\Omega_{\rm s}{\rm d}\Omega_{\rm e}{\rm d}E_{\rm e}} = \frac{k_{\rm e}k_{\rm s}}{k_{\rm i}}|M|^2 \ , \tag{II.78}$$

where ${\rm d}\Omega_{\rm s} = \sin\theta_{\rm s}{\rm d}\theta_{\rm s}{\rm d}\phi_{\rm s}$ and ${\rm d}\Omega_{\rm e} = \sin\theta_{\rm e}{\rm d}\theta_{\rm e}{\rm d}\phi_{\rm e}$ denote the scattered and ejected solid angles, respectively. $E_{\rm e}$ is the ejected electron energy. The momenta $\mathbf{k}_{\rm i}$, $\mathbf{k}_{\rm s}$ and $\mathbf{k}_{\rm e}$ are related to the incident, the scattered and the ejected electron, respectively. The transition amplitude M is given by:

$$M = \frac{1}{2\pi}\langle\Psi_{\rm f}|V|\Psi_{\rm i}\rangle \ , \tag{II.79}$$

where V represents the interaction between the incident electron and the target. For the water target it is written as:

$$V = -\frac{8}{r_0} - \frac{1}{|\mathbf{r_0}-\mathbf{R_1}|} - \frac{1}{|\mathbf{r_0}-\mathbf{R_2}|} + \sum_{i=1}^{10}\frac{1}{|\mathbf{r_0}-\mathbf{r_i}|} \ , \tag{II.80}$$

with $R_1 = R_2 = R_{\rm OH} = 1.814$ a.u., while $\mathbf{r_i}$ is the position of the ith bound electron of the target with respect to the oxygen nucleus [6]. The initial state $\Psi_{\rm i}$ is written as the product of two wave functions: a first one $\phi(\mathbf{k}_{\rm i},\mathbf{r_0})$ describing the incident electron by a plane wave and a second one $\varphi_{\rm i}(\mathbf{r_1},\mathbf{r_2},...,\mathbf{r_{10}})$ for the ten bound electrons of the water molecule described by the Slater functions given by Moccia. The final state $\Psi_{\rm f}$ of the collision system is written as the product of a plane wave function (describing the scattered electron) by a continuum wave function defined by a distorted wave function $\mathcal{F}_{\mathbf{k_e}}(\mathbf{r})$ of ejected momentum $\mathbf{k_e}$ with an asymptotic charge $z_e = 1$ (used to describe the ejected electron). The details of the calculations can be found in Ref. [206]. Numerical integration of Eq. II.78 over the scattered solid angle provides the DDCS, which are depicted in Figure II.20.

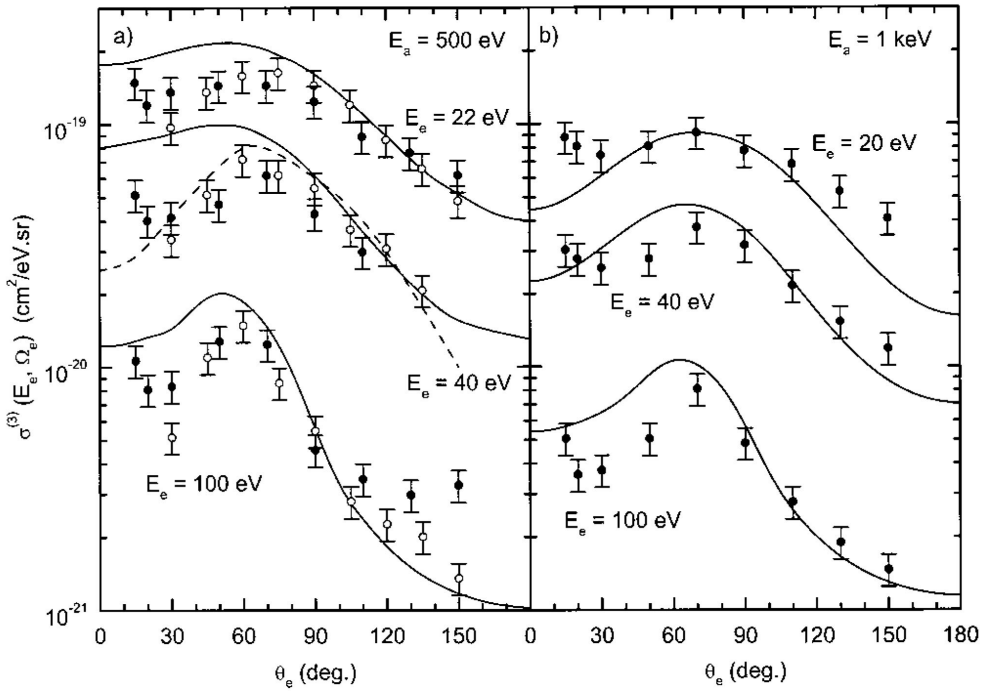

Figure II.20 DDCS for ionization of the water molecule by electron impact computed in the DWBA framework (solid lines). The DDCS are shown for two incident energies, 500 eV (panel a) and 1 keV (panel b), and selected ejected energies E_e. The dashed line represents the theoretical results obtained by Long *et al.* [207] for $E_e = 40\,\mathrm{eV}$. The symbols represent experimental data taken from various sources. Reprinted from Ref. [206], with the permission of AIP Publishing.

The SDCS are determined by numerical integration of the DDCS. Figure II.21 shows the SDCS obtained with the DWBA model.

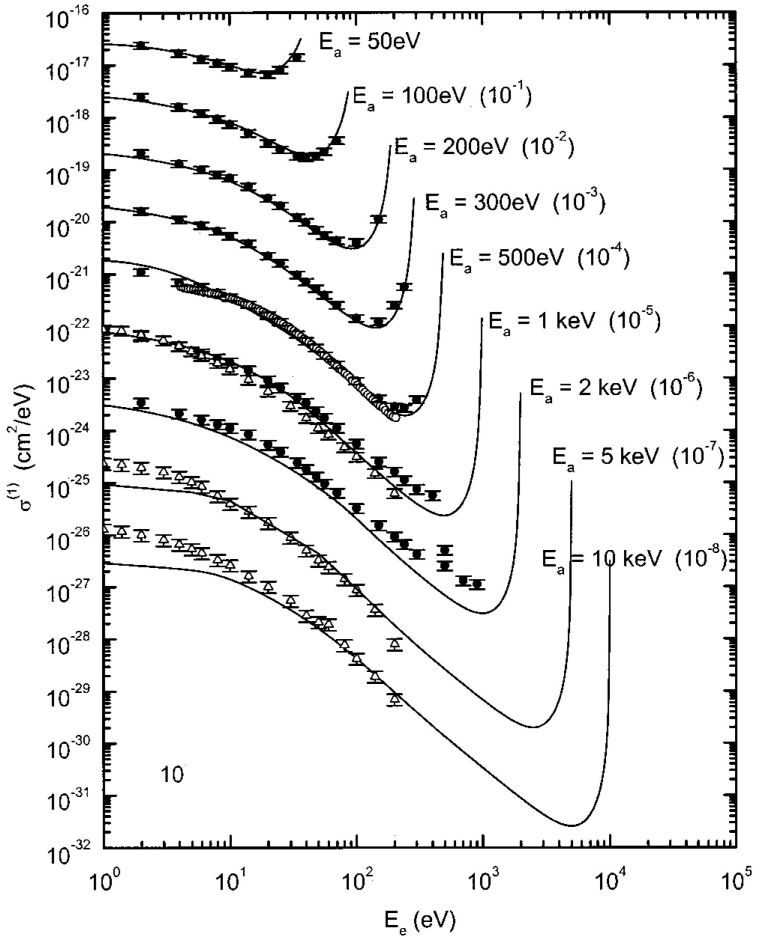

Figure II.21 SDCS for ionization of the water molecule by electron impact computed in the DWBA framework (solid line). The SDCS are shown for several incident electron energies in the range from 50 eV to 10 keV. The symbols represent experimental data taken from various sources. Reprinted from Ref. [206], with the permission of AIP Publishing.

Finally, the TICS are obtained by integration of the SDCS. Figure II.22 presents a comparison of the TICS for water computed with the DWBA and the RBEB models.

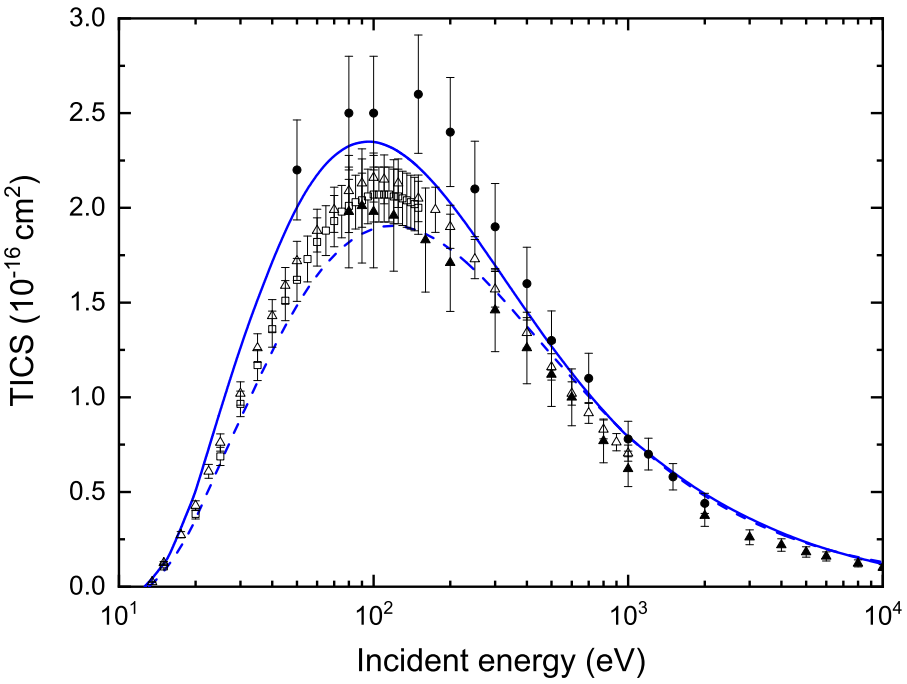

Figure II.22 TICS for electron impact on water. Comparison of the TICS obtained with the DWBA (solid line) and the RBEB (dashed line) models. The experimental data are taken from Bolorizadeh and Rudd [208] (solid circles), Lindsay and Mangan [209] (open triangles), Djurić *et al*. [210] (open squares), and Schutten *et al*. [211] (solid triangles). Adapted from Ref. [206].

It can be seen that for incident energies below ∼200 eV, most of the experimental data displayed in Figure II.22, with the exception of the values reported by Bolorizadeh and Rudd [208], fall between the predictions of the two models, with the RBEB and the DWBA underestimating and overestimating the TICS, respectively. In addition, both models seem to slightly overestimate the TICS for energies > 2 keV. In general, however, the agreement with the experiments is rather satisfactory. It is worth mentioning that, in addition to the DWBA framework, several other models have been proposed in the literature to describe the final state of the collision system. Some of them are more sophisticated than the DWBA (see Ref. [6]). Nevertheless, the DWBA model was chosen for the cross section database in EPOTRAN because it reproduces quite well the experimental multiple-differential and total cross sections without demanding an unreasonable computational time.

Ionization cross sections for the DNA components were computed within the first Born approximation framework by using a similar theoretical support as the one previously described for water. The details can be found in Ref. [212]. Figure II.23 shows the TICS for electron impact on DNA components.

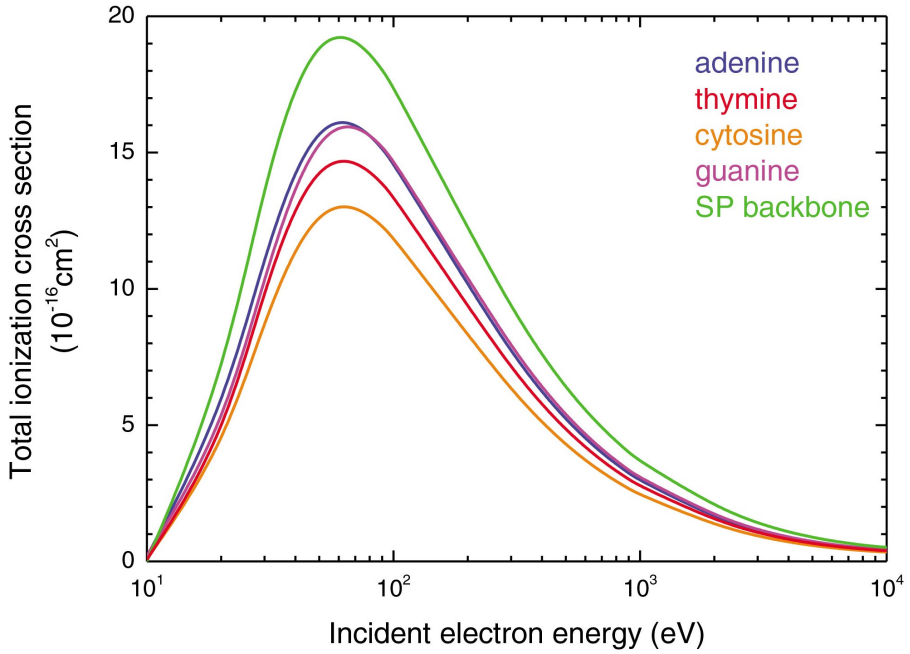

Figure II.23 TICS for electron impact on DNA components computed within the first Born approximation framework. Reprinted from Ref. [212], with the permission of AIP Publishing.

II.4.3 The elastic scattering process

The effect of elastic scattering on the trajectory of light charged particles, e.g., electrons, is much more pronounced than for protons, α-particles or heavier ions. As a result, electrons will follow very tortuous paths in their passage through matter. Furthermore, elastic scattering becomes the most important interaction for electrons with energies below $\sim$100 eV.

The elastic scattering cross sections for electron impact used in EPOTRAN were calculated within the partial wave formalism. Starting from the MO-SCF-LCAO description of the water molecule proposed by Moccia [149] (see Section II.2.2), the associated perturbation potential was approximated considering a spherically symmetric potential $V(r)$ composed of three terms: the static contribution $V_{\rm st}$, the correlation-polarization term $V_{\rm cp}$ and the exchange term $V_{\rm ex}$:

$$V(r) = V_{\rm st}(r) + V_{\rm cp}(r) + V_{\rm ex}(r) \ . \tag{II.81}$$

For water vapor, the static potential $V_{\rm st}(r)$ was numerically calculated from each target molecular wave function by using the spherical average approximation. The static potential is expressed as:

$$V_{\rm st}(r) = \sum_{j=1}^{N_{\rm orb}} [V_{\rm st}^{j}(r)]_{\rm elec} + [V_{\rm st}(r)]_{\rm ion} \ , \tag{II.82}$$

where $[V_{\rm st}^{j}(r)]_{\rm elec}$ and $[V_{\rm st}(r)]_{\rm ion}$ refer to the electronic and ionic target contribution to the

static potential, respectively. Following the notation introduced in Eqs. II.2 to II.5, the electronic contribution of each molecular subshell is given by [9]:

$$[V_{\rm st}^{j}(r)]_{\rm elec} = 2 \sum_{k=1,\ k'=1}^{N_j} a_{jk} a_{jk'} \delta(m_{jk} - m_{jk'}) \delta(l_{jk} - l_{jk'}) \times \int_0^\infty R_{n_{jk} l_{jk}}^{\xi_{jk}}(r') \frac{r'^2}{r_>} R_{n_{jk'} l_{jk'}}^{\xi_{jk'}}(r) dr' \ , \tag{II.83}$$

and the ionic contribution is:

$$[V_{\rm st}(r)]_{\rm ion} = -\frac{8}{r} - \frac{2}{R_>} \ , \tag{II.84}$$

where $r_> = \max(r, r')$, $R_> = \max(r, R_{\rm OH})$, and $R_{\rm OH} = 1.814$ a.u. is the binding length O-H of the water molecule in the gas-phase.

For slow projectiles, it is necessary to take into account the effects of polarization and correlation. The former arises from the polarization of the charge cloud of the target by the electric field of the projectile. The correlation effect appears when the projectile is an electron and it penetrates the target volume, repelling the target electrons and forming a "Coulomb hole" surrounding the projectile position [213]. The correlation-polarization contribution is based on the recommendations of Salvat [213] and is given by:

$$V_{\rm cp}(r) = \begin{cases} \max\{V_{\rm corr}(r), V_{\rm p}(r)\} & \text{for } r < r_{\rm cr} \\ V_{\rm p}(r) & \text{for } r > r_{\rm cr} \ , \end{cases} \tag{II.85}$$

where $r_{\rm cr}$ is defined as the outer radius at which $V_{\rm p}(r)$ and $V_{\rm corr}(r)$ cross. The polarization potential $V_{\rm p}(r)$ is given by:

$$V_{\rm p}(r) = -\frac{\alpha_{\rm d}}{2(r^2 + r_{\rm c}^2)^2} \ , \tag{II.86}$$

where $\alpha_{\rm d} = 9.7949$ a.u. is the static dipole polarizability of the water molecule [214] and $r_{\rm c}$ is the cutoff parameter proposed by Mittleman and Watson [215]:

$$r_{\rm c} = \left[\frac{1}{2} \alpha_{\rm d} z^{-1/3} b_{\rm pol}^2 \right]^{1/4} \ , \tag{II.87}$$

with $z = 10$ and $b_{\rm pol}$ an adjustable parameter given by:

$$b_{\rm pol} = \sqrt{\max\{(E_{\rm inc} - 0.5)/0.01; 1\}} \ . \tag{II.88}$$

The correlation potential is written as [216]:

$$\begin{cases} V_{\rm corr}^{-}(r_{\rm s}) = 0.0311 \ln r_{\rm s} - 0.0584 + 0.006 r_{\rm s} \ln r_{\rm s} \\ \qquad -0.015 r_{\rm s} & \text{for } r_{\rm s} \leq 0.7 \ , \\ V_{\rm corr}^{-}(r_{\rm s}) = -0.07356 + 0.02224 \ln r_{\rm s} & \text{for } 0.7 \leq r_{\rm s} \leq 10 \ , \\ V_{\rm corr}^{-}(r_{\rm s}) = -0.584 r_{\rm s}^{-1} + 1.988 r_{\rm s}^{-3/2} - 2.450 r_{\rm s}^{-2} \\ \qquad -0.733 r_{\rm s}^{-5/2} & \text{for } r_{\rm s} \geq 10 \ , \end{cases} \tag{II.89}$$

where $r_{\rm s} = \left[\frac{3}{4\pi\rho(r)} \right]^{1/3}$ with $\rho(r)$ the molecular charge density.

Finally, the exchange effect takes into account the possibility that the incident and target electrons exchange their place. The exchange potential was treated via the

phenomenological potential $V_{\mathrm{ex}}(r)$ proposed by Riley and Truhlar [217]:

$$V_{\mathrm{ex}}(r) = \frac{1}{2}\left\{ \begin{array}{l} E_{\mathrm{inc}} - (V_{\mathrm{st}}(r) + V_{\mathrm{cp}}(r)) \\ - \left[(E_{\mathrm{inc}} - (V_{\mathrm{st}}(r) + V_{\mathrm{cp}}(r)))^2 + 4\pi\rho(r)\right]^{1/2} \end{array} \right\} . \tag{II.90}$$

The correlation-polarization and exchange effects are perceptible only for small scattering angles and low incident energies [9].

The SDCS and TCS for the elastic scattering of electrons in water are shown in Figures II.24 and II.25, respectively.

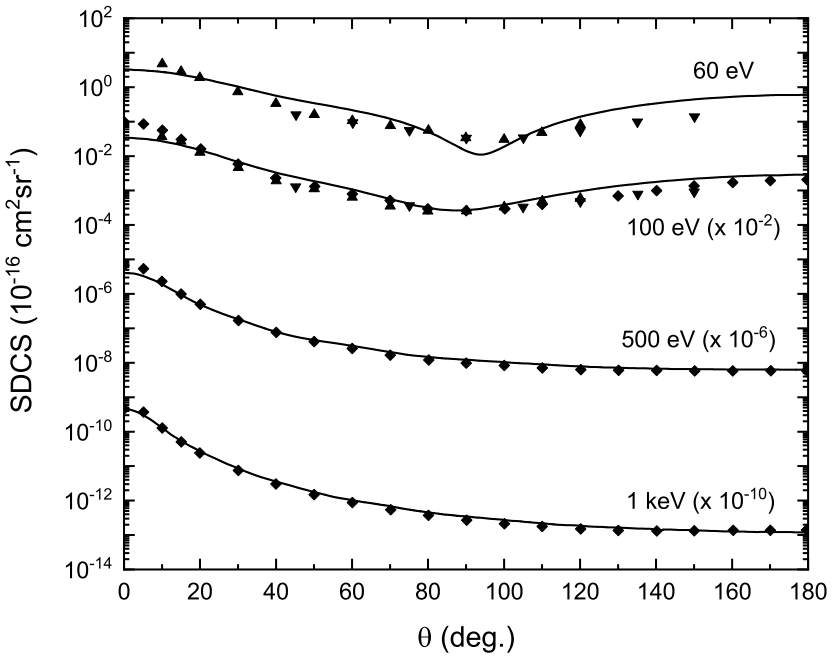

Figure II.24 SDCS for the elastic scattering of electrons in water vapor (adapted from Ref. [9], with permission from Elsevier). Values are shown for selected incident energies (solid lines). The symbols are experimental measurements taken from various sources (see Ref. [9] for the details). Multiplicative factors (shown in parentheses) are introduced for more clarity.

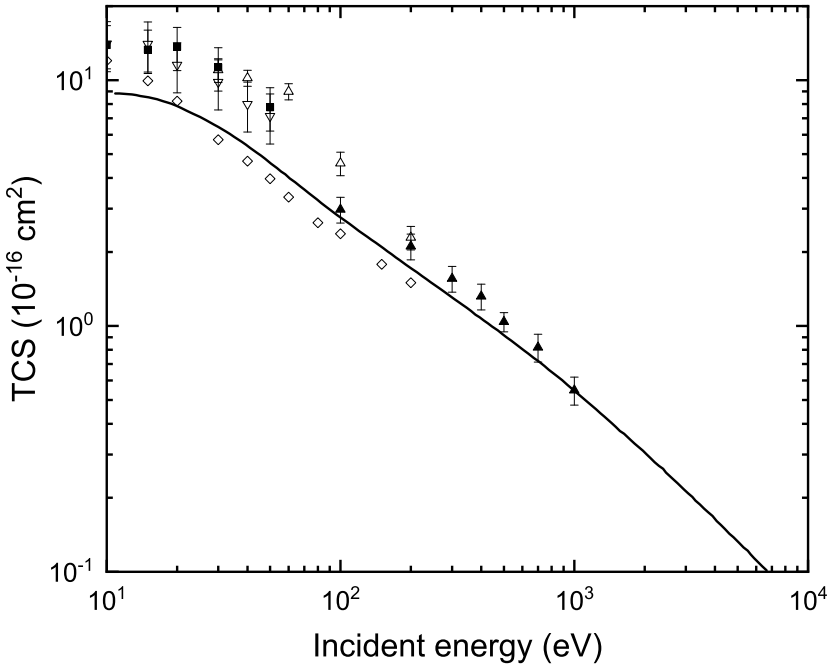

Figure II.25 TCS for the elastic scattering of electrons in water vapor (adapted from Ref. [9], with permission from Elsevier). The solid lines represent the theoretical results. The symbols are experimental measurements taken from various sources (see Ref. [9] for the details).

The elastic scattering cross sections for electron impact on the DNA components were recently calculated by Mokrani *et al.* [218]. They will soon be included in EPOTRAN and *TILDA-V*. Meanwhile, the elastic scattering cross sections for DNA components used in these codes are obtained by simply rescaling the corresponding water cross sections according to the number of electrons of each DNA component, in the same way as is done for the electron loss cross sections (see Eq. II.51).

II.4.4 Summary of total cross sections for electron impact

The TCS for the physical processes aforementioned and currently included in EPOTRAN are depicted in Figure II.26 for incident electron energies ranging from 10 eV to 10 keV. The TCS for both biological media are plotted in the same graph for comparison. The TCS for DNA correspond to a hydrated DNA unit as described in Section II.2.3.

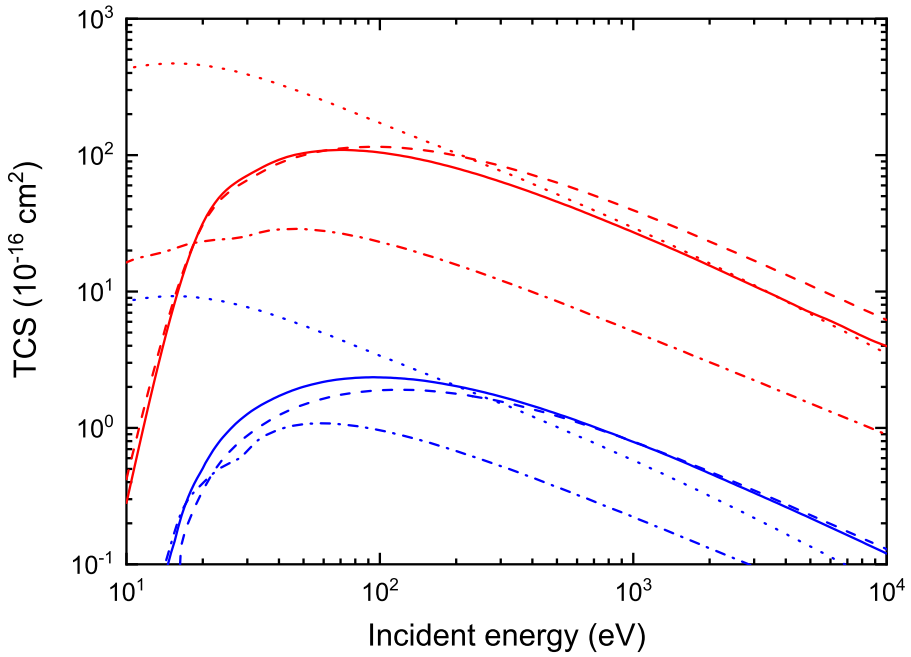

Figure II.26 TCS for electrons in water (blue) and hydrated DNA (red): ionization, as obtained with the DWBA [206, 212] (solid lines) and the RBEB (dashed lines) models; excitation (dash-dotted lines); and elastic scattering (dotted lines).

Conclusions

We have discussed in this chapter the physical processes that must be considered in MCTS codes for modeling the transport of ions and electrons in biological media. The specific models implemented in *TILDA-V* have been described in detail. Moreover, we have shown that the set of cross sections used in our code has been validated by comparison with the available experimental data on water vapor. For DNA components, however, the experimental data is still scarce to draw conclusions about the accuracy of the cross sections computed within the quantum-mechanical framework. Furthermore, we have given an overview of the alternative theoretical and semiempirical approaches that can be applied to calculate the interaction cross sections, some of which have been used in other MCTS codes.

CHAPTER III

CHARGED PARTICLE TRANSPORT SIMULATIONS

Contents

III.1 Introduction **87**

III.2 Track parameters **88**

III.2.1 Inelastic mean free path 88

III.2.2 Stopping power 90

III.2.3 Range 91

III.2.4 Radial dose distribution 92

III.3 Results for proton transport **92**

III.4 Results for electron transport **102**

III.5 Single cell irradiation by proton beams **107**

Conclusions **112**

III.1 Introduction

In the previous chapters we presented the main features of the *TILDA-V* MCTS code and the physical models on which it relies to describe the various possible interactions of ions and electrons with biological targets. The validation of a MC code for radiation transport is usually done by computing, within a simulation, several key macroscopic quantities characterizing the radiation tracks of the incident particles in the medium of interest. Some track parameters useful to verify the reliability of the simulations include, for instance, the stopping power, the range and the radial dose distribution around the ion's path.

In this chapter, we describe the physical quantities used to evaluate the reliability of our MCTS simulations for the transport of protons and electrons in water and DNA. We then report the results of the simulations performed with *TILDA-V* and EPOTRAN in a semi-infinite medium and compare the predictions of both codes with available experimental data and other theoretical results. The differences between the results obtained for water and DNA are analyzed with the purpose of understanding the possible implications of choosing a simpler description of the biological medium over one more realistic. In addition, and in order to make the connection with the radiation dosimetry applications discussed in the following chapters, we present the results for a study in which we simulated the irradiation by protons of a single cell.

We have reported most of the results presented in this chapter in two recent publications [74, 143].

III.2 Track parameters

We define in this section the track parameters that were chosen to test the reliability of our track structure simulations. We explain as well the method to compute these quantities in the simulations, as compared to an analytical calculation.

III.2.1 Inelastic mean free path

The concept of mean free path (MFP) was introduced in Chapter I when we discussed the random sampling of physical quantities in a MC code. The MFP is defined as the average distance traveled by a particle between successive collisions. According to Eqs. I.11 and I.12, the MFP can be expressed as:

$$\overline{\lambda}(E_{\text{inc}}) = \frac{A_{\text{mol}}}{\rho N_A \sigma_T(E_{\text{inc}})} \ , \tag{III.1}$$

where A_{mol} and ρ are the molar mass and the density of the material, respectively; N_A is the Avogadro constant; σ_T is the TCS for the projectile, equal to the sum of the cross sections for all considered physical processes at a given incident energy E_{inc}. On the other hand, if the elastic collisions are neglected in σ_T, one obtains the inelastic mean free path (IMFP), which is a parameter more frequently found in the literature. Moreover, when charge-transfer processes become relevant for the incident ion, σ_T represents the TCS taking into account the relative contribution of each charge state. Therefore, for protons σ_T is computed as:

$$\sigma_T = f_{\text{H}^+}(\sigma_T)_{\text{H}^+} + f_{\text{H}^0}(\sigma_T)_{\text{H}^0} \ , \tag{III.2}$$

where $(\sigma_T)_{H^+}$ and $(\sigma_T)_{H^0}$ are the TCS for protons and neutral hydrogen atoms, respectively, and f_{H^+}, f_{H^0} are the equilibrium charge fractions defined as follows [219]:

$$f_{H^+} = \frac{\sigma_L}{\sigma_L + \sigma_C} , \tag{III.3}$$

and

$$f_{H^0} = \frac{\sigma_C}{\sigma_L + \sigma_C} , \tag{III.4}$$

where σ_L and σ_C denote the TCS for electron loss and electron capture, respectively. Figure III.1 shows the equilibrium charge fractions for hydrogen ions obtained using the cross sections calculated with the *prior* version of the CDW-EIS model.

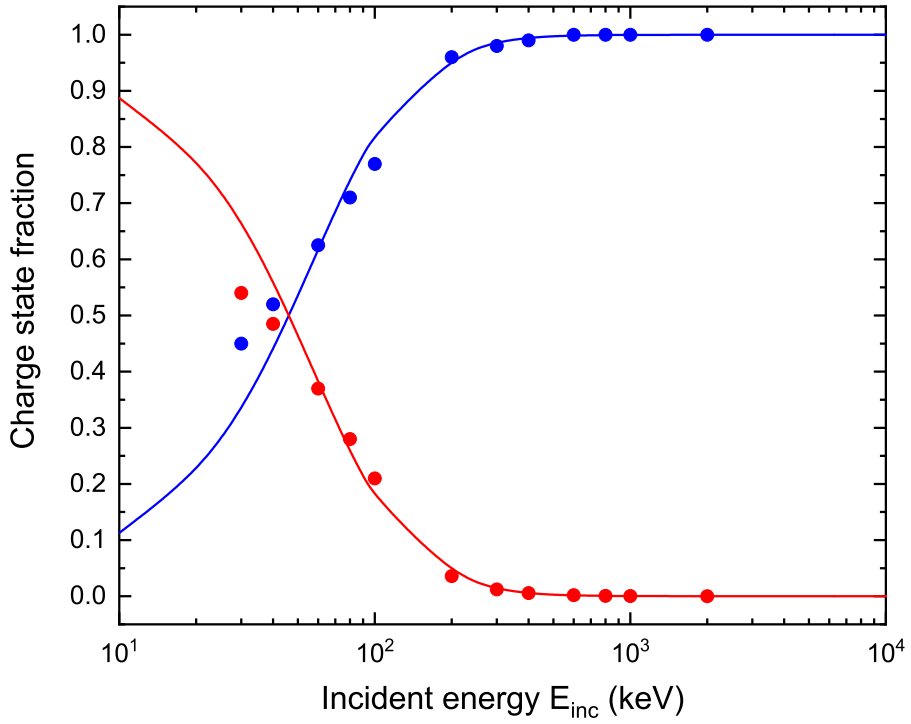

Figure III.1 Equilibrium charge fractions for hydrogen ions in water vapor as a function of the impact energy [143]. Theoretical prediction using the *prior* version of the CDW-EIS model: H^+ (solid blue line); H^0 (solid red line). Experimental data are taken from Barnett *et al.* [220] (circles).

In addition, let us remind that for a hydrated DNA unit (as defined in Chapter II) the TCS for a given charge state at a given incident energy is computed as:

$$\sigma_{DNA} = C_1(\sigma_A + \sigma_T) + C_2(\sigma_C + \sigma_G) + C_3(\sigma_{S-P}) + C_4(\sigma_{H_2O}) , \tag{III.5}$$

where σ_A, σ_T, σ_C, σ_G, σ_{S-P}, σ_{H_2O} are the TCS for adenine, thymine, cytosine, guanine, the sugar-phosphate backbone and water, respectively. The coefficients used in Eq. III.5 correspond to the proportions mentioned in Section II.2.3, i.e., $C_1 = 0.58$, $C_2 = 0.42$, $C_3 = 2$ and $C_4 = 18$.

III.2.2 Stopping power

The stopping power is defined as the average energy loss per unit path length experienced by charged particles when traversing a material [10]. The total stopping power consists of three contributions: the electronic (or collision) stopping power, resulting from the inelastic collisions of the projectile with the electrons of the target; the nuclear stopping power, arising from collisions between the projectile and the target nucleus; and the radiative stopping power, due to Bremsstrahlung. However, for the charged particles and kinetic energies considered in this work only the electronic stopping power is relevant. For protons, the electronic stopping power at a given incident energy E_{inc} can be written as [1]:

$$SP(E_{\mathrm{inc}}) = N_0 \left[f_{\mathrm{H}^+}(E_{\mathrm{inc}}) \sum_{j=1}^{3} \bar{E}_j \sigma_j(E_{\mathrm{inc}}) + f_{\mathrm{H}^0}(E_{\mathrm{inc}}) \sum_{k=1}^{3} \bar{E}_k \sigma_k(E_{\mathrm{inc}}) \right] , \tag{III.6}$$

where N_0 is the number of atoms or molecules in the medium per unit volume defined in Eq. I.12; the indices j and k represent the various inelastic interactions of protons (ionization, excitation, electron capture) and neutral hydrogen atoms (ionization, excitation, electron loss), respectively; σ_j and σ_k denote the cross sections associated to the processes j and k; $\bar{E}_j$ and $\bar{E}_k$ are the mean energy transfers for each interaction type. The quantity defined in Eq. III.6 is sometimes called *linear* electronic stopping power to distinguish it from the *mass* electronic stopping power, which results from dividing the former by density of the absorbing medium. The linear electronic stopping power is commonly expressed in keV μm^{-1}, while the mass electronic stopping power is usually reported in MeV cm^2 g^{-1}. For the sake of brevity, we will omit in the following the adjectives "linear", "mass" and "electronic" when discussing the stopping power, unless the distinction becomes necessary.

From the point of view of the simulations, in many MC codes the stopping power is provided as input data, e.g., through files containing pre-tabulated values for a specific projectile and a set of incident energies. This is not the case in *TILDA-V* and EPOTRAN, in which the stopping power is an outcome computed independently from other track parameters. The stopping power is obtained by simulating a number of projectiles considered large enough to reduce the statistical fluctuations to an acceptable level (usually 10^6 projectiles). The same criterion is applied to the calculation of other track parameters. For projectiles for which the charge state may change during transport, such as protons, a simulation is performed for each charge state. The simulations are run in stationary mode for each projectile energy (we consider by default 37 incident energies on a logarithmic grid covering the whole energy range of interest). Let us remind that in stationary mode, each projectile is followed until it experiences an interaction with the medium. A sum over the energy loss and the distance traveled by each projectile is

carried out and the stopping power is then computed as:

$$SP(E_{\text{inc}}) = \frac{E_{\text{tot}}}{L} \ , \tag{III.7}$$

where E_{tot} is the total energy lost by the projectiles and L is the track length. Taking into account the relative contributions of protons and neutral hydrogen atoms, the total stopping power is written as:

$$SP(E_{\text{inc}}) = f_{\text{H}^+}(SP)_{\text{H}^+} + f_{\text{H}^0}(SP)_{\text{H}^0} \ , \tag{III.8}$$

where $(SP)_{\text{H}^+}$ and $(SP)_{\text{H}^0}$ denote the stopping power for the charge states H^+ and H^0, respectively.

III.2.3 Range

The range is the average path length a charged particle travels before losing all its energy and coming to rest in a material. In general, the range includes the deviations of the projectile from its initial direction of motion, resulting from multiple elastic collisions. Therefore, the range is always greater than the projected range or average penetration depth, which is measured along the original direction of the projectile. Energetic ions can be assumed to follow straight-line trajectories. For protons and α-particles in water, the range and the projected range are almost identical for projectiles with kinetic energies above $\sim$1 MeV u^{-1} [10]. On the other hand, electrons follow very tortuous paths. In this case it is sometimes useful to compute the penetration range, defined as the length of the vector $|\mathbf{R_f} - \mathbf{R_i}|$ from the point of departure ($\mathbf{R_i}$) to the final position ($\mathbf{R_f}$) of the electron after thermalization [11].

If the stopping power is known, the range can be calculated within the continuous slowing down approximation (CSDA). In this approach, energy-loss fluctuations are neglected and charged particles are assumed to lose their energy continuously along their tracks at a rate given by the stopping power. The CSDA range provides a very close approximation to the average path length traveled by a charged particle before coming to rest. The CSDA range is obtained by integrating the reciprocal of the stopping power with respect to energy [10].

To compute the proton range in *TILDA-V*, the simulations are carried out considering a semi-infinite medium and the particles are transported in slowing-down mode, i.e., each primary particle is followed until its energy falls below the fixed cutoff of 10 keV. The range is then obtained by adding the distances traveled by all the primary particles and dividing by the number of simulated projectiles.

The electron range is obtained in EPOTRAN in a similar fashion to the proton range calculation in *TILDA-V*. In addition, to compute the electron penetration range, the coordinates of the final position of each electron are recorded during the simulation.

The distance from the origin to the final position is then determined for each electron. The average penetration range is obtained by adding all these distances and dividing the result by the number of simulated electrons.

III.2.4 Radial dose distribution

The radial dose profile is another track parameter useful to check the validity of a MCTS code. This parameter provides information about the energy deposited by the secondary electrons around the track of the primary ion. To compute the radial dose distribution in *TILDA-V*, we simulate 10^6 protons in stationary mode, but activating the full slowing-down mode for the secondary electrons. The energy deposited by each secondary electron is scored in cylindrical shells having a thickness of 0.1 nm and centered about the path of the primary ion. The height of the cylindrical shells is obtained by averaging the length of the proton tracks. By knowing the volume of these cylindrical shells, the absorbed dose as a function of the radial distance to the primary ion track can be computed.

As in all our simulations, the low-energy cutoff for electron transport is fixed to 7.4 eV, namely, the excitation threshold of the water molecule. Only electrons with energies above this cutoff are considered and therefore transported in the simulations. The energy of the sub-cutoff electrons is assumed to be locally deposited at the point where they were created (along the primary ion track) or at the point in which their last interaction (i.e., the one reducing their energy below 7.4 eV) took place. Finally, let us note that the choice of the electron cutoff may affect the radial dose profile obtained from the simulations, particularly for small radii.

III.3 Results for proton transport

In Section II.3.7 we presented the TCS for the impact of hydrogen ions on water and hydrated DNA. In terms of TCS, substantial differences between both media were observed (see Figure II.17). However, it should be reminded that the hydrated DNA unit considered in our simulations includes the contribution of 18 water molecules. Therefore, it is expected to find TCS values for hydrated DNA much greater than those for water. A more meaningful comparison between both biological media can be achieved by plotting instead the IMFP. Moreover, to demonstrate that the differences between a water and a DNA description of the target cannot simply be explained in terms of the density of the medium, we have calculated the IMFP in water with a density rescaled to 1.29 g cm^{-3} (the density of hydrated DNA), instead of 1.0 g cm^{-3}. The results are depicted in Figure III.2.

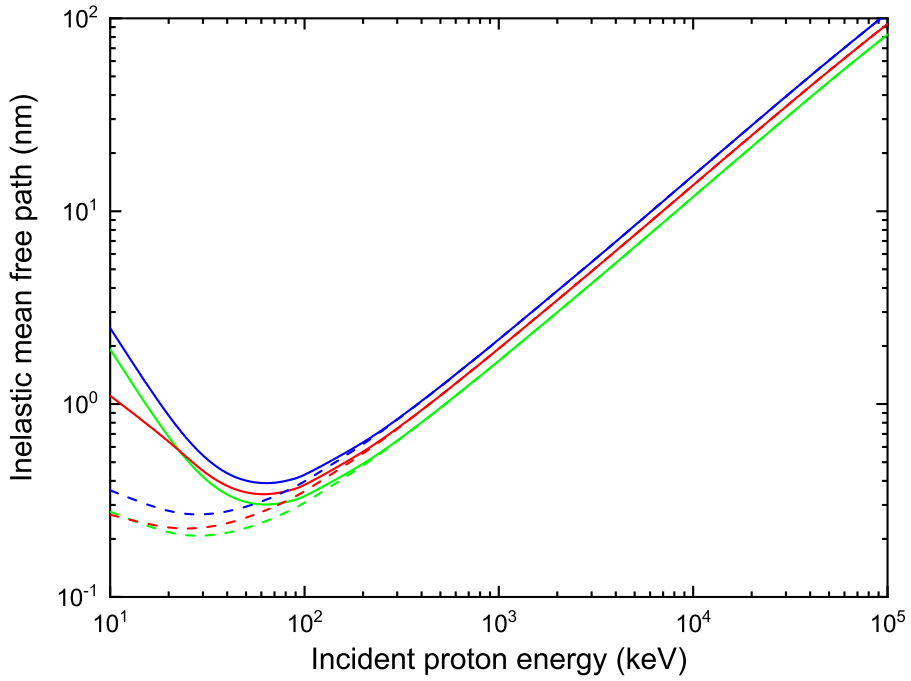

Figure III.2 IMFP for protons in water (blue), water with a density rescaled to 1.29 g cm^{-3} (green) and hydrated DNA (red) as a function of the incident proton energy. Dashed lines: total IMFP; solid lines: IMFP when only the ionization and excitation processes are included.

It can be seen that the IMFP values obtained for water are on average about 13% greater that the ones for DNA in most of the energy range considered here (namely, 10 keV – 100 MeV). About the same relative difference is observed in the results for hydrated DNA and density-rescaled water, the latter having smaller IMFP values than hydrated DNA for energies above some tens of keV. The discrepancies between the media increase slightly as the projectile energy decreases. At incident energies higher than ∼100 keV, the curves of the three media become parallel to one another. Indeed, the curves for hydrated DNA and density-rescaled water do not overlap except in a very limited region at low energies. Clearly, a density scaling procedure is not able to reproduce the results obtained for a description of the biological medium based on hydrated DNA. We have seen in Chapter II that the process of electron capture only becomes relevant for protons with energies below some hundreds of keV. This fact is illustrated once more in Figure III.2, where we have plotted as well the effect of considering only the ionization and excitation cross sections in the calculation of the IMFP (solid lines).

In Figure III.3, we present a comparison of our IMFP results with other calculations found in the literature. For the sake of clarity, we have separated in two panels the results for water and DNA. Furthermore, let us note that all the results reported in Figure III.3 were computed taking into account only the ionization and excitation processes.

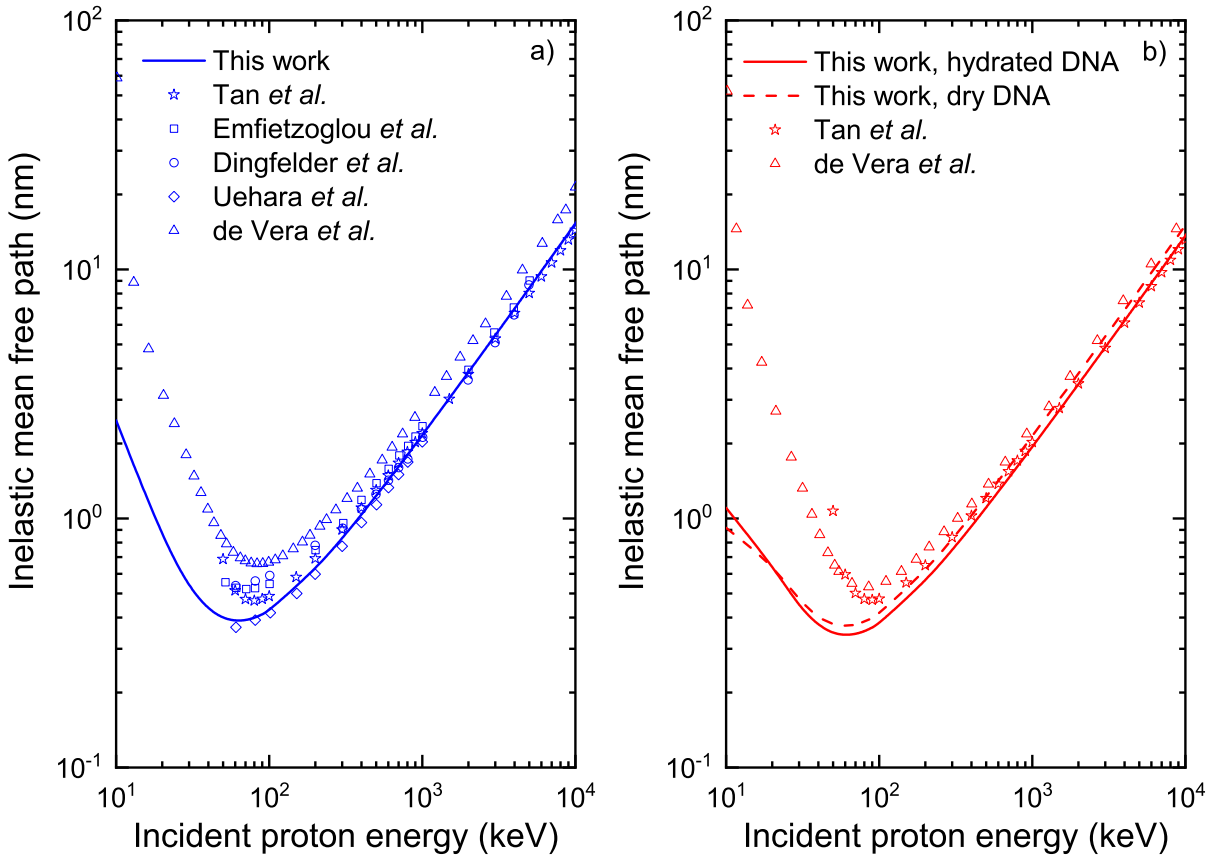

Figure III.3 IMFP for protons in water (panel a) and DNA (panel b), as obtained in this work, when only ionization and excitation by protons are taken into account [143]. Our results are compared with the calculations performed by Dingfelder *et al.* [114], Uehara *et al.* [129], Emfietzoglou *et al.* [221], Tan *et al.* [182] and de Vera *et al.* [183]. The dashed line in panel b shows the predictions of *TILDA-V* when considering dry DNA with the composition described in the work of Tan *et al.* [182].

In the case of water (panel a), all the calculations seem to converge to the same IMFP values at high incident energies ($\gtrsim$ 1 MeV), except for the results reported by de Vera *et al.* [183] (triangles), which remain about 25% greater. Furthermore, in the energy range going from 300 keV to 1 MeV, the difference between our results and those of Refs. [114, 129, 182, 221] is within 10%. The best agreement at low energies is found with the calculations of Uehara and co-workers [129] (diamonds). This is understandable because they considered water vapor targets as well, and it is well-known that phase effects become important as the projectile energy decreases. All the other data sets reported in Figure III.3a are for liquid water. In addition, significant deviations arise between the various calculations for $E_{\mathrm{inc}} \lesssim 300$ keV. This behavior is somewhat expected, since all the models have limitations in the low-energy region. The condensed-phase approaches implemented in Refs. [182, 183, 221] are valid above some hundreds of keV, while the predictions of the CDW-EIS model are considered reliable above ~40 keV.

Figure III.3b depicts the IMFP for protons in DNA. The solid line represents our results for hydrated DNA. Data from Tan *et al.* [182] (stars) and de Vera *et al.* [183] (triangles), who worked with dry DNA, are shown for comparison. Overall, a very similar behavior to the one reported in Figure III.3a is observed for DNA. An excellent agreement is found between our predictions and the calculations of Tan and co-workers [182] for high incident energies, i.e., for $E_{\mathrm{inc}} > 1$ MeV, with differences below 4%; the deviations with respect to the values obtained by de Vera *et al.* [183] in that same energy range are greater ($\sim$19%), but they are smaller than the differences observed in panel a for water ($\sim$25%). These discrepancies grow for decreasing values of the incident energy, reaching about 25% and 40% at 100 keV with respect to the work of Tan *et al.* [182] and de Vera *et al.* [183], respectively. Once more, let us note that the predictions for energies below some hundreds of keV, and for $E_{\mathrm{inc}} \lesssim 40$ keV in the case of the CDW-EIS model, are questionable. Furthermore, to see if a better agreement could be reached by considering dry DNA instead of hydrated DNA, we adopted the same DNA composition as Tan *et al.* [21, 182]. To do so, we subtracted the contribution of the water molecules to the DNA TCS and used in our calculations a density of 1.35 g cm^{-3} and a molar mass of 662 g mol^{-1}, as reported by Tan *et al.* [21]. The results are represented by the dashed line in Figure III.3b. A better agreement is indeed achieved, but only in the interval 200 keV $< E_{\mathrm{inc}} <$ 1 MeV. Thus, the remaining discrepancies between the dashed line and the data of Tan *et al.* [182] should be ascribed to the inherent differences in the models employed to compute the TCS, and not to the DNA description.

The stopping power for protons in water and DNA obtained from *TILDA-V* simulations is shown in Figure III.4. Our results for water are compared with the available experimental data for both phases (water vapor and liquid water).

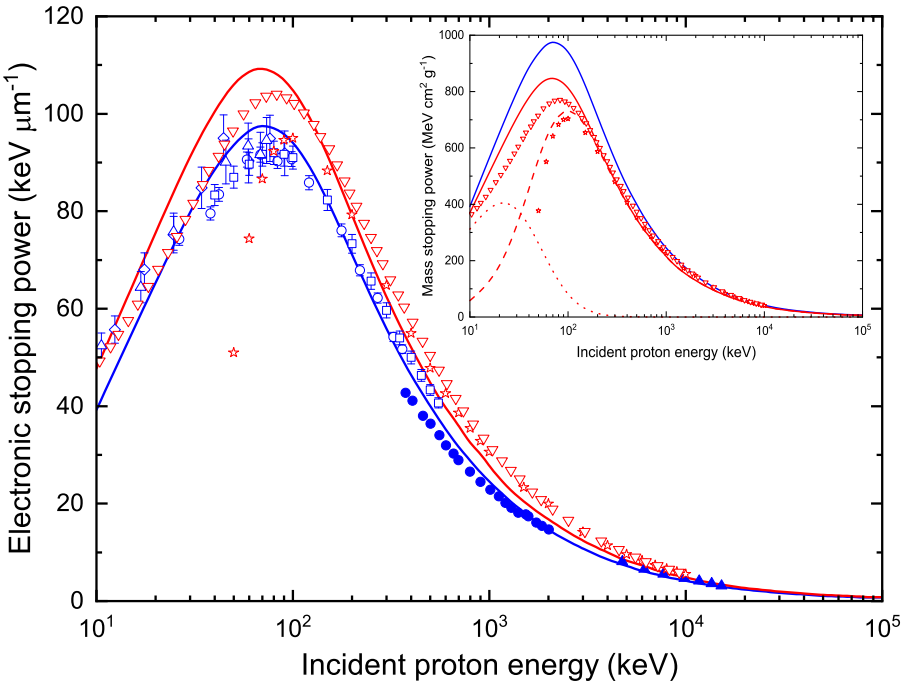

Figure III.4 Electronic stopping power for protons in water (blue line) and hydrated DNA (solid red line) [143]. Experimental data for water vapor are shown in open blue symbols and are taken from: Reynolds *et al.* [222] (squares), Phillips [223] (triangles), Mitterschiffthaler and Bauer [224] (circles) and Baek *et al.* [225] (diamonds). Measurements for liquid water are shown in solid blue symbols and are taken from: Shimizu *et al.* [226] (circles) and Siiskonen *et al.* [227] (triangles). For DNA, the calculations performed by Abril *et al.* [20] (inverted red triangles) and Tan *et al.* [21] (red stars) are shown for comparison. The inset depicts the mass electronic stopping power for protons in water (blue line) and hydrated DNA (solid red line). The dashed and dotted red lines indicate the H^+ and H^0 contributions to the stopping power for protons in hydrated DNA. The symbols correspond once again to the calculations of Abril *et al.* [20] (inverted red triangles) and Tan *et al.* [21] (red stars).

In general, a good agreement can be observed between our predictions for water and the experimental data, especially for energies above 30 keV. More specifically, for $E_{\mathrm{inc}} > 30$ keV our predictions fall most of the time within the estimated errors in the reported measurements for water vapor, with deviations of less than 10%. For lower energies, however, our values underestimate the experimental results, a behavior that can be attributed to the CDW-EIS model used in our code. Furthermore, when comparing our predictions with the available experimental data on liquid water, we found that our results are greater than the ones reported by Shimizu *et al.* [226] (full circles) by about 5–13%. On the other hand, our values are actually smaller than those obtained by Siiskonen *et al.* (full triangles) [227], but it should be noted that the relative differences are only slightly above the total uncertainty reported by the authors (4.6%).

In the case of DNA, because of the lack of experimental data, we have included in Figure III.4 the few theoretical data found in the literature, namely the calculations made by Abril *et al*. [20] and Tan *et al*. [21]. Both research groups considered dry DNA with a density of 1.35 g cm^{-3} and performed their calculations within the dielectric formalism, but using different extension schemes. Clearly, there are important differences between our results and their predictions for incident energies below 200 keV.

The inset in Figure III.4 shows the mass electronic stopping power for protons in water (blue line) and hydrated DNA (solid red line). For the latter, we have plotted the H^+ and H^0 contributions to the stopping power (dashed and dotted red lines, respectively). It can be observed that the neutral hydrogen contribution dominates at low incident energies ($E_{\rm inc} < 30$ keV); on the contrary, for $E_{\rm inc} > 300$ keV, only the contribution of H^+ remains relevant. We have included on that graph as well the calculations by Abril *et al*. [20] and Tan *et al*. [21]. From this graph it is clear that a better agreement is reached between our DNA results and theirs when only the H^+ contribution to the stopping power is taken into account (i.e., frozen-charge approximation). The agreement with both authors is within ∼3% at 100 keV, while once more the deviations become noticeable at lower incident energies as the models go beyond their limit of validity. Nevertheless, it should be stressed that ignoring the charge-exchange processes, i.e. the H^0 contribution, is expected to underestimate the stopping power in the low-energy regime.

Additionally, let us mention that according to our calculations, the maximum stopping power for water (97.5 keV μm^{-1}) and hydrated DNA (110 keV μm^{-1}) is located at the same incident proton energy, namely 70 keV, with a difference of about 13% between both media.

We have mentioned in several occasions that *TILDA-V* simulations are based on cross sections computed in water vapor; correspondingly, the stopping power results presented here were obtained by using the ionization potentials for water vapor. In condensed media, such as liquid water, it is known that the stopping power values are smaller than in the gas-phase as a result of the polarization of the medium by the charged projectile. We have observed that if the ionization potentials for liquid water (as provided by Dingfelder *et al*. [114]) were used instead to calculate the stopping power, while keeping the same cross sections computed for water vapor, the results would be smaller than the ones shown in Figure III.4 (blue line) by about 8% at 10 keV, 4% at 100 keV, and 2–3% for energies up to 100 MeV. This comparison is depicted in Figure III.5 (solid and dashed lines). The latter, although a very simple test, shows that for liquid water smaller stopping power values would be obtained, as expected from the polarization effect. According to the PSTAR database [141], the difference between the stopping power values for protons in water vapor compared to those in liquid water are of 13.8% at 10 keV, 12.6% at 100 keV, 1.4% at 1 MeV, 0.8% at 10 MeV and 0.6% at 100 MeV,

rising again in the GeV region. For comparison, we have plotted as well in Figure III.5 the stopping power values for protons in liquid water taken from the PSTAR database [141] and from GEANT4-DNA simulations [122]. Clearly, the results of the test that we have performed by changing the ionization potentials in the simulations is in qualitative but not quantitative agreement with the predictions for liquid water.

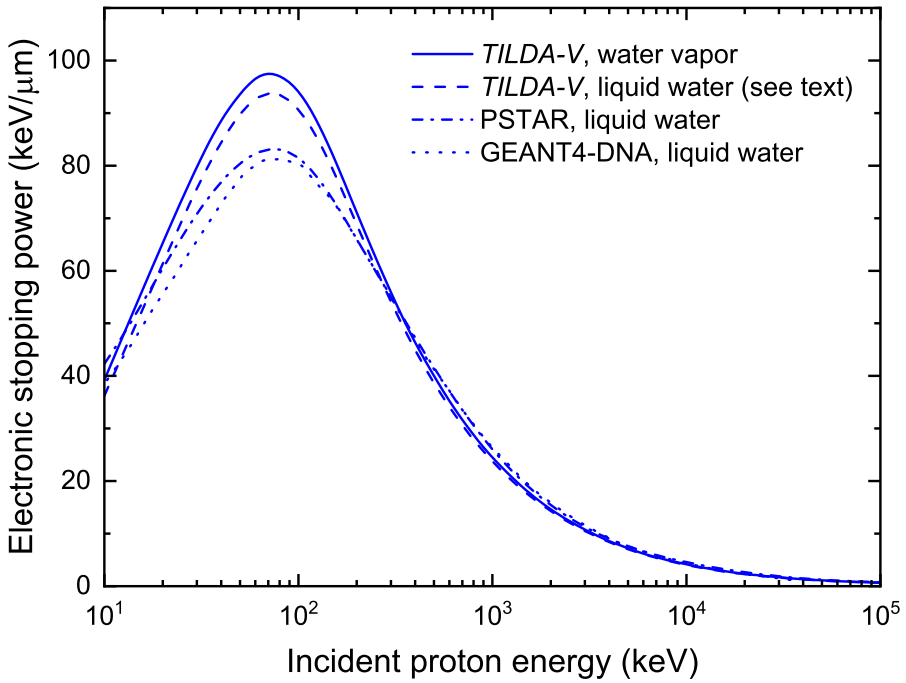

Figure III.5 Comparison of the electronic stopping power for protons in water vapor and liquid water. The dashed line was obtained by using in *TILDA-V* the ionization potentials for liquid water instead of those for water vapor. The dash-dotted and dotted lines represent the values for liquid water taken from the PSTAR database [141] and from GEANT4-DNA simulations [122].

Figure III.6 presents a comparison of the mass electronic stopping powers for protons in water vapor computed with *TILDA-V* and other calculations found in the literature for incident energies from 10 keV to 1 MeV.

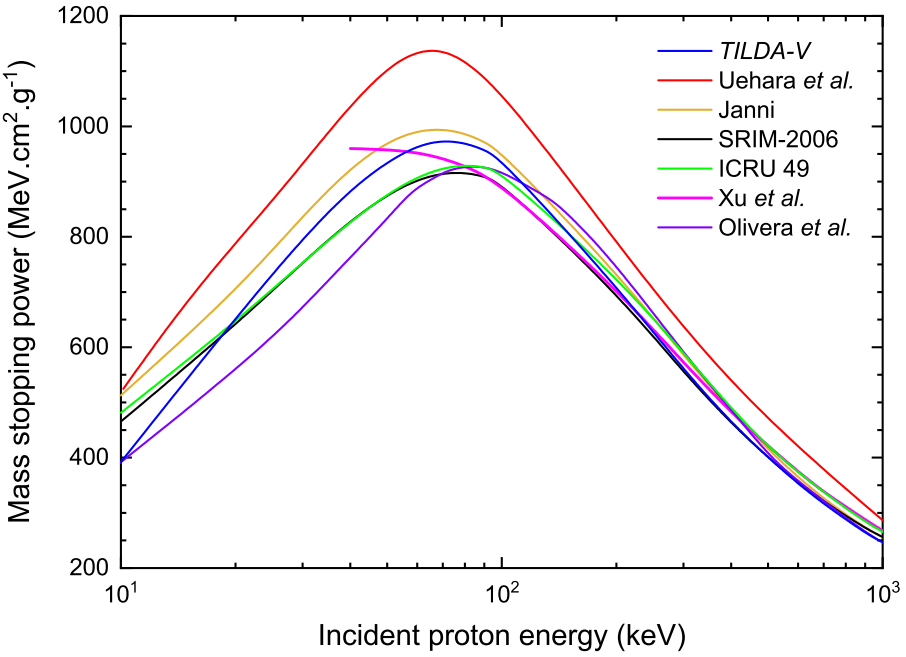

Figure III.6 Mass electronic stopping power for protons in water vapor. The values predicted with *TILDA-V* are compared to calculations from: Uehara *et al.* [22], SRIM-2006 [228], Xu *et al.* [229], Olivera *et al.* [230], the ICRU Report 49 [10] and Janni [23].

The best agreement of our results is found with SRIM-2006 [228], the ICRU Report 49 [10] and Janni's tabulation [23] with differences of less than 7% in the energy range 10 keV $< E_{\text{inc}} <$ 1 MeV. However, the position of the maximum is slightly shifted to the right in the case of SRIM-2006 [228] and the ICRU Report 49 [10] results, which reported a maximum stopping power value of ∼916 MeV cm^2 g^{-1} and ∼930 MeV cm^2 g^{-1}, respectively, at 80 keV. On the other hand, the calculations of Uehara *et al.* [22] show large discrepancies over the whole energy range. This probably stems from the fact that Uehara and co-workers [22] computed the energy transfer during the ionization process based on average binding and emission energies. Furthermore, the calculations of Xu *et al.* [229] performed within a modified local-plasma model are in good agreement with all the results for $E_{\text{inc}} >$ 100 keV, although they predicted the stopping power maximum at lower energies. Finally, we found discrepancies of less than ∼18% between our results and those of Olivera *et al.* [230] for incident energies lower than 100 keV.

Figure III.7 shows the range for protons in water and hydrated DNA computed with *TILDA-V*.

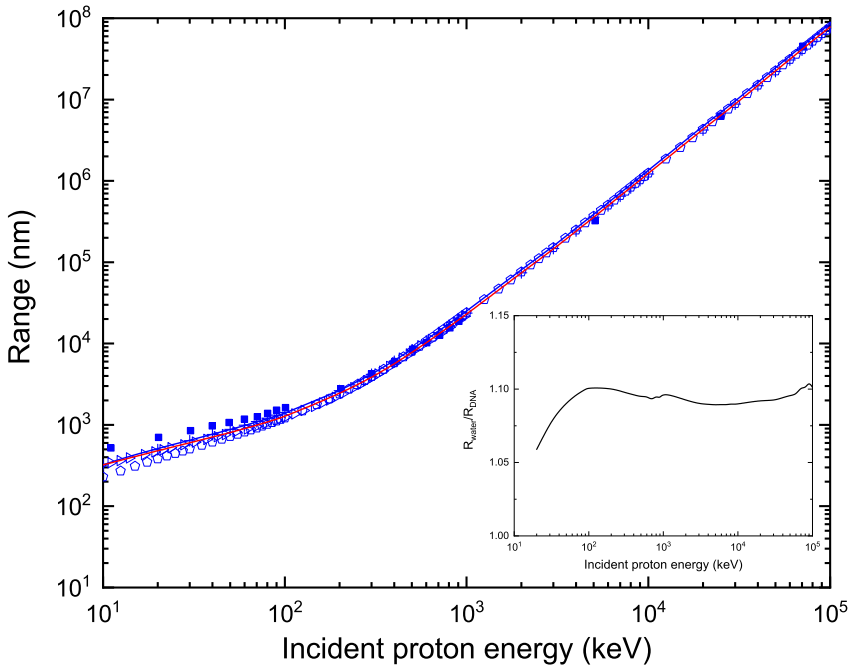

Figure III.7 Range for protons in water (blue line) and hydrated DNA (red line) as provided by *TILDA-V* [143]. Theoretical data for water are taken from: the ICRU Report 49 [10] (crosses), Uehara *et al.* [22] (right-pointing triangles), Janni [23] (pentagons) and Francis *et al.* [24] (solid squares). The inset shows the ratio $\mathrm{R_{water}/R_{DNA}}$, where $\mathrm{R_{water}}$ ($\mathrm{R_{DNA}}$) refers to the proton range in water (hydrated DNA).

It should be noted that because of the low-energy cutoff for protons, the range values computed with *TILDA-V* must be corrected to compensate the path length that a primary particle of 10 keV would traverse until it is fully stopped in the medium. For this reason, the results presented in Figure III.7 (solid lines) have been obtained by adding to the output of *TILDA-V* the CSDA range for protons of 10 keV in water vapor recommended in the ICRU Report 49 [10], which is ≈ 322 nm. This has been done for both water and hydrated DNA, since for the latter there is no equivalent data. The effect of this correction becomes negligible above 1 MeV, because it represents a deviation of less than 1% in the range values. Our results have been compared with calculations and theoretical data for water taken from the ICRU Report 49 [10] (crosses), Uehara *et al.* [22] (right-pointing triangles), Janni [23] (pentagons) and Francis *et al.* [24] (solid squares). The divergences between our predictions and the other models become noticeable in the low-energy regime, i.e., when $E_{\mathrm{inc}} < 100$ keV. The greatest discrepancy is of about 30% for $E_{\mathrm{inc}} = 10$ keV and is found with respect to the values reported by Francis *et al.* [24], who used the GEANT4-DNA Monte Carlo code, which considers liquid water. The inset in Figure III.7 shows the ratio of the proton range in water to the one in hydrated DNA as a function of the incident energy. It can be observed that the range

for protons in hydrated DNA is always shorter than in water. There is a 10% difference between the range values obtained in both media, which remains more or less constant for incident energies above 100 keV. For lower incident energies, the ratio gradually decreases to about 6%.

The radial dose profile for protons in water is depicted in Figure III.8 for incident energies of 200 keV, 1 MeV, 3 MeV, 10 MeV and 100 MeV and radial distances up to 1 μm.

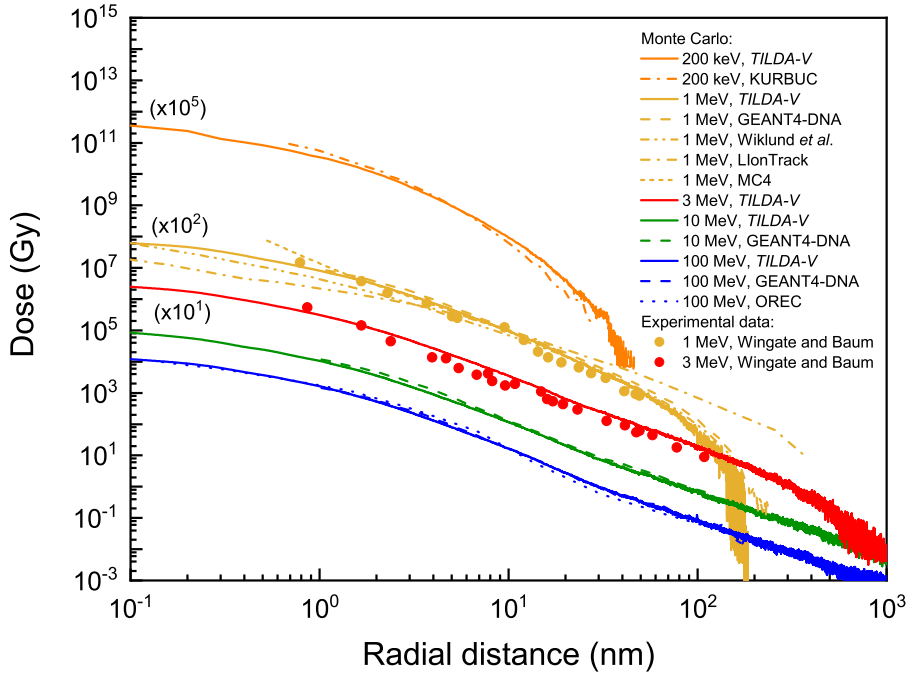

Figure III.8 Radial dose distribution for protons in water. The experimental data for protons of 1 MeV and 3 MeV in tissue-equivalent gas are taken from Wingate and Baum [25]. We report as well the calculations made with other MCTS codes: KURBUC [30], GEANT4-DNA [26], PENELOPE [29], LIonTrack [31], MC4 [28] and OREC [27]. Multiplicative factors are introduced for more clarity.

The agreement between our results and other MC calculations found in the literature is in general quite good, especially at high incident energies (10 MeV and 100 MeV), for which our predictions overlap almost perfectly with those obtained from simulations with GEANT4-DNA [26] and OREC [27]. For protons of 1 MeV the same agreement is seen with the results obtained with GEANT4-DNA [26], with only small deviations arising at radial distances $\gtrsim$ 20 nm. Our results for 1 MeV are also consistent with the ones computed by Emfietzoglou *et al.* [28] using the MC4 code, except for very small radii ($\lesssim$ 1 nm). Similarly, at small radii, our results for 1 MeV slightly overestimate the ones of Wiklund *et al.* [29], who employed the secondary electron production cross sections from the CDW-EIS model, but carried out the electron transport with the PENELOPE code. On the other hand, the disagreement with the radial dose distribution reported

by Bäckström *et al.* [31] and obtained with the LIonTrack code, is more noticeable. The work of Bäckström *et al.* [31] is also based on the CDW-EIS model. Moreover, as in the study of Wiklund *et al.* [29], the electron tracking was performed with the PENELOPE code. However, while Wiklund *et al.* [29] used the default models in PENELOPE, Bäckström *et al.* [31] utilized the cross sections given by Dingfelder *et al.* [111, 113]. As shown by Bäckström *et al.* [31], this choice has profound effects on the frequency distribution of low-energy electrons, which in turn influences the behavior of the radial dose profile. In essence, the default models in PENELOPE may underestimate the frequency of low-energy electrons [31]. The overall effect, observed in Figure III.8, is that the absorbed dose computed by Wiklund *et al.* [29] is higher within the first 2 nm, but decreases faster than the radial dose obtained with LIonTrack [31]. Despite this plausible explanation, it is clear that the results of Wiklund *et al.* [29] seem in better agreement with the measurements of Wingate and Baum [25] and with the rest of MC calculations presented in Figure III.8. This disagreement with the results of LIonTrack was recently pointed out by Quinto *et al.* [231] as well. For lower incident energies, we have compared our radial dose profile for protons of 200 keV with the results of Nikjoo *et al.* [30], who used the KURBUC code. Slight discrepancies are observed, but the agreement is rather satisfactory. Finally, it can be observed that our results are in excellent agreement with the experimental measurements reported by Wingate and Baum [25] for protons of 1 MeV and 3 MeV in tissue-equivalent gas.

III.4 Results for electron transport

Figure III.9 presents our results for the IMFP of electrons in water (panel a) and hydrated DNA (panel b), along with calculations taken from various sources for the sake of comparison. It is worth mentioning that the vast majority of the electron IMFP calculations carried out in recent years have been for liquid water [21, 36, 232–235]. Among the different data sets shown in Figure III.9a, only the calculations of Bigildeev and Michalik [236] and Uehara *et al.* [237] were performed in water vapor, as it is the case in the present study. Besides, except for Blanco *et al.* [233], who worked with an independent atom model with a screening corrected additivity rule procedure (IAM-SCAR), all the calculations for liquid water shown in Figure III.9a were carried out within the dielectric formalism. Several dielectric models have been used to compute the IMFP for low-energy electrons. A review of the "standard" dielectric models used in this context has been recently published by Emfietzoglou *et al.* [234]. We have plotted as well in Figure III.9a the experimental data reported by Michaud *et al.* [238] on amorphous ice and the ones from Thürmer *et al.* [239] on liquid water.

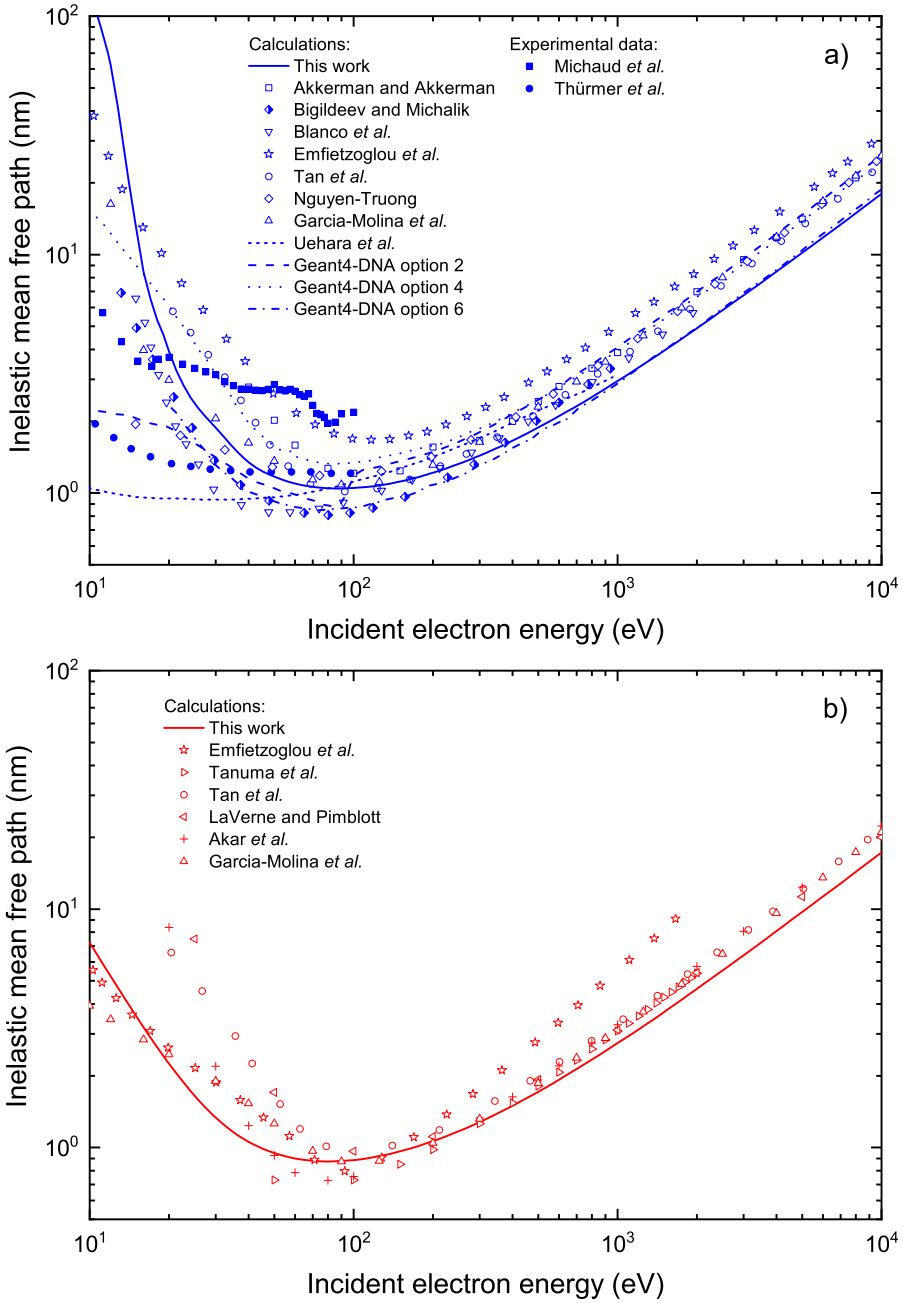

Figure III.9 IMFP for electrons in water (panel a) and hydrated DNA (panel b). Our results are depicted in solid lines. The calculations shown for comparison have been taken from various sources (see the text for the details). For water, we have plotted the experimental data of Michaud *et al.* [238] on amorphous ice and the ones from Thürmer *et al.* [239] on liquid water.

Only the calculations reported by Emfietzoglou *et al.* [234] seem to be in close agreement with the experimental data of Michaud *et al.* [238], and this for incident energies between 50 eV and 100 eV. In contrast, for the same energy range our results are closer to the values found by Thürmer *et al.* [239], with discrepancies $< 12\%$. Moreover, agreement within 15% and 10% is seen with the calculations reported by Tan *et al.* [21] and Blanco *et al.* [233], respectively, but only for $100\,\text{eV} \lesssim E_{\text{inc}} \lesssim 1\,\text{keV}$. A good agreement around the IMFP minimum and even at lower energies is observed too with the work of Garcia-Molina *et al.* [36]. We have also compared our IMFP results for electrons in water with some recent predictions from GEANT4-DNA simulations [122]. It can be observed from Figure III.9a that the best agreement with the results obtained in this work is found with the predictions of GEANT4-DNA "option 6" (see Section I.3.2.3) for incident energies above 100 eV.

It is clear from figure III.9a that the various theoretical predictions cover a large area at low incident electron energies and that no definite behavior of the IMFP for electrons in water can be established for $E_{\text{inc}} < 100\,\text{eV}$. In fact, the mentioned agreement with the results of Garcia-Molina *et al.* [36] for $E_{\text{inc}} < 100\,\text{eV}$ is rather fortuitous, since that region is below the limit of validity of the models. Besides, the paucity of experimental data as well as the evident discrepancies among the available data sets prevents us from drawing definitive conclusions about which theoretical approach is the most accurate in this context. Furthermore, the agreement found between our results and the simulations performed with GEANT4-DNA "option 6" at high incident energies was expected, since ionization is the most important interaction in that energy region and the simulations were performed with the same ionization model (BEB).

Regarding the IMFP for electrons in DNA, there are only theoretical calculations reported in the literature [21, 36, 154, 240–242]. Figure III.9b depicts the IMFP for electrons in DNA. In this case, the best agreement of our IMFP values is found with the calculations of Garcia-Molina *et al.* [36], with deviations of less than 15% for incident energies $E_{\text{inc}} \gtrsim 100\,\text{eV}$. The calculations of Emfietzoglou *et al.* [242] show a discrepancy with the rest of the data sets that increases with the incident energy. According to our results, the IMFP for electrons is on average 12% greater in water than in hydrated DNA.

Figure III.10 presents the mass electronic stopping power for electrons in water versus hydrated DNA.

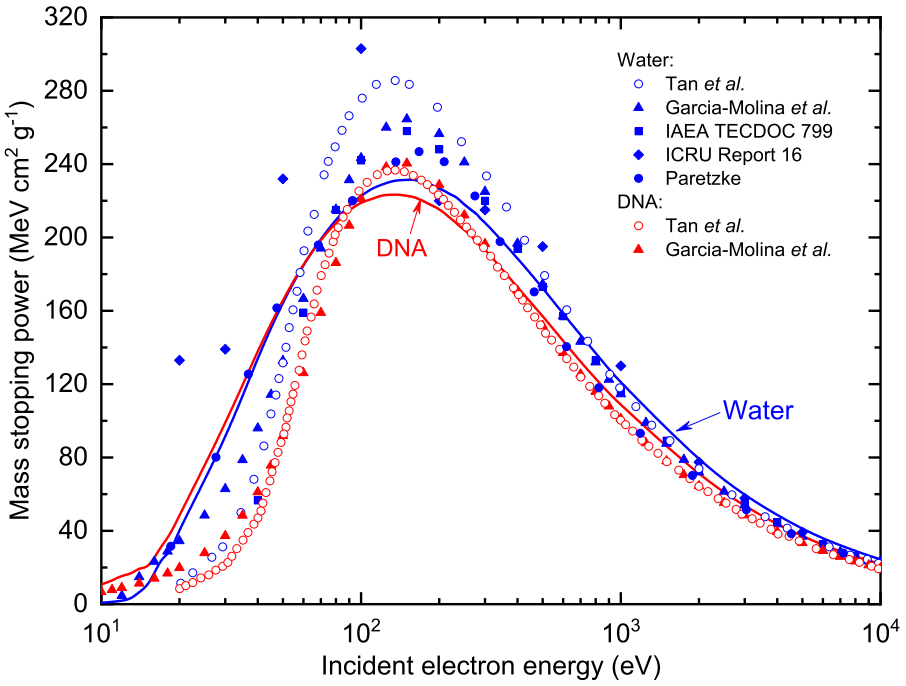

Figure III.10 Mass electronic stopping power for electrons in water (blue) versus hydrated DNA (red), as provided by EPOTRAN (solid lines). The symbols represent stopping power values taken from various sources (see the text for the details).

The results display a similar behavior for both media, with a maximum stopping power of 232 MeV cm^2 g^{-1} at 160 eV and 223 MeV cm^2 g^{-1} at 130 eV for water and hydrated DNA, respectively. The maximum difference found in this work between the mass stopping power values computed for water and hydrated DNA in the energy range shown in Figure III.10 is of about 13%. Furthermore, it can be observed that our mass stopping power values for water are consistent with the data provided in the International Atomic Energy Agency (IAEA) TECDOC 799 [34] for incident energies $E_{\mathrm{inc}} > 300$ eV. Similarly, an agreement within 5% is found with the values of the ICRU Report 16 [35], as well as with the calculations performed by Garcia-Molina *et al.* [36] and Tan *et al.* [21] for $E_{\mathrm{inc}} > 500$ eV. At lower energies, however, important discrepancies are observed, especially with respect to the maximum value of the stopping power, since there is a difference of about 12% and 19% between our values and the predictions of Garcia-Molina *et al.* [36] and Tan *et al.* [21], respectively. This can be explained by the fact that both authors used the dielectric formalism for their calculations, which without all the necessary corrections is known to overestimate the inelastic cross sections at the peak region. In particular, Tan *et al.* [21] estimated that the lack of a perturbation correction in their dielectric model may induce a 10–20% overestimation of the inelastic cross sections around 100 eV.

Finally, our predictions are in agreement with the results obtained by Paretzke [37],

cited in the work by Nikjoo *et al.* [30] (p.186), in most of the energy range here considered, although a slight underestimation of the maximum is still noticeable.

As for water, important differences are observed between our stopping power values in DNA and the ones reported by Tan *et al.* [21] and Garcia-Molina *et al.* [36], particularly for low incident electron energies and near the peak region. Nevertheless, now the maximum stopping power values predicted by Garcia-Molina *et al.* [36] and Tan *et al.* [21] are only 7% and 6% greater than our results, respectively. On the other hand, a good agreement between the three calculations is observed for $E_{\mathrm{inc}} > 300\,\mathrm{eV}$, with deviations of less than 4%.

Figure III.11 presents our results for the penetration range for electrons in water and hydrated DNA.

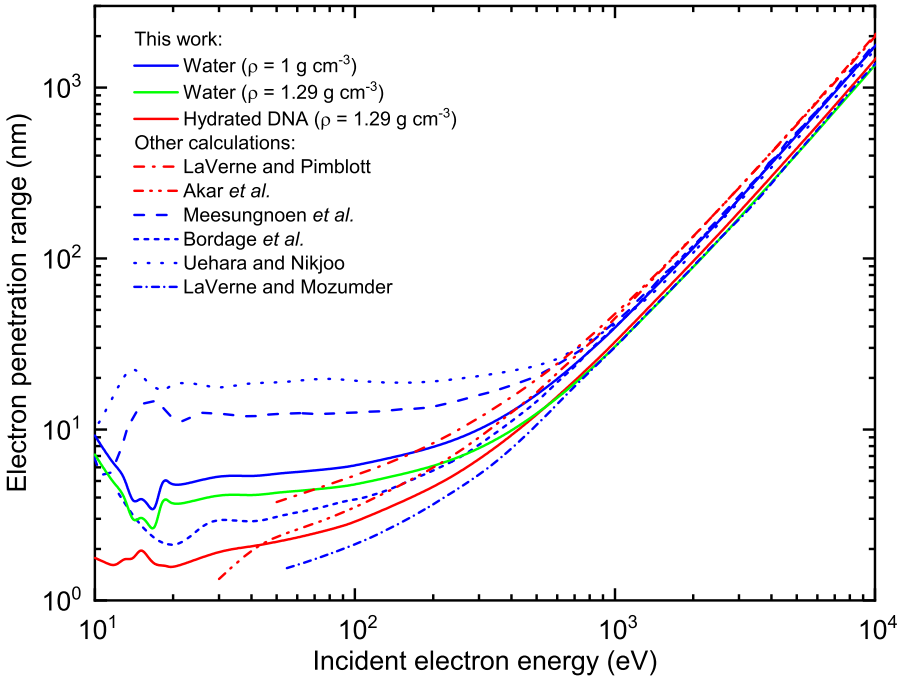

Figure III.11 Penetration range for electrons in water (blue), water with the density rescaled to $\rho = 1.29$ g cm^{-3} (green) and hydrated DNA (red), as compared with other calculations (see the text for the details).

For incident electron energies $E_{\mathrm{inc}} \lesssim 700\,\mathrm{eV}$, our results for water fall between those of Meesungnoen *et al.* [11] and the values computed with GEANT4-DNA, as reported by Bordage *et al.* [38]. The greatest discrepancy, however, is found with the work of Uehara and Nikjoo [95], with a difference of almost 70% at 100 eV. Moreover, it is clear that important discrepancies appear at low incident energies for all calculations reported in Figure III.11. For greater incident energies ($E_{\mathrm{inc}} \gtrsim 1\,\mathrm{keV}$) all predictions overlap perfectly. Besides, we have included in Figure III.11 the root mean square (RMS) penetration range computed by LaVerne and Mozumder [243], which even at high energies remains more than 20% smaller than the penetration range obtained by the other authors.

The penetration range for electrons in hydrated DNA is represented in Figure III.11 by the red solid line. It can be observed that in the whole energy range here considered the penetration range values for hydrated DNA are lower than those for water. More specifically, the difference found between both media is ∼39% at 100 eV, while for energies higher than 1 keV it decreases to about 20%. For DNA, to the best of our knowledge, only CSDA ranges have been published. We have plotted in Figure III.11 the CSDA ranges computed by LaVerne and Pimblott [154] and Akar *et al*. [241]. Since the CSDA range is more closely related to the path length traversed by the particle, which is not a straight line for electrons, we would expect the values taken from Refs. [154, 241] to be greater than our results in the whole energy range. This is indeed the case for the data of LaVerne and Pimblott [154], whereas the values reported by Akar *et al*. [241] are surprisingly smaller than ours for incident energies below ∼200 eV. As already mentioned, however, it is difficult to draw conclusions from comparisons at such low incident energies, particularly because of the lack of experimental data for DNA.

We have also plotted for comparison in Figure III.11 the penetration range in water with the density rescaled to 1.29 g cm^{-3} (green line). The penetration range values for electrons in density-rescaled water and hydrated DNA become quite similar for incident energies above ∼500 eV.

III.5 Single cell irradiation by proton beams

In the previous sections we tested the reliability of our MC simulations by computing several track parameters for protons and electrons. With the purpose of providing a link between a general radiation transport simulation and the various possible applications in radiation dosimetry, we subsequently investigated the irradiation of a single tumor cell by monoenergetic protons beams [143]. The cell was modeled with a simple geometry: three concentric spheres representing the basic regions of a cell, namely, the nucleus, the cytoplasm and the cell membrane. In this study the cell radius, nuclear radius and membrane thickness were fixed to 7 μm, 4 μm [12] and 10 nm [13], respectively. The cell and nucleus dimensions were chosen among a wide variety of possible values considered in cellular dosimetry [19]. It is evident that choosing a different cell model will affect the results of the simulations. However, the key idea to retain about the model is that nuclei in tumor cells are often larger than in normal cells [244]. With respect to the composition of the cell regions, the cytoplasm and the cell membrane were modeled by water with a density of 1.0 g cm^{-3}. To study the variation in the radiation dose deposited inside the cell nucleus depending on its composition, three different simulations were carried out in slowing-down mode for each incident proton energy, assuming the nucleus contained: 1) water (ρ = 1.0 g cm^{-3}); 2) water with the density rescaled to 1.29 g cm^{-3}

and 3) hydrated DNA ($\rho = 1.29\,\mathrm{g\,cm^{-3}}$). The radiation source consisted of protons impinging on the cell from random directions, as shown in Figure III.12.

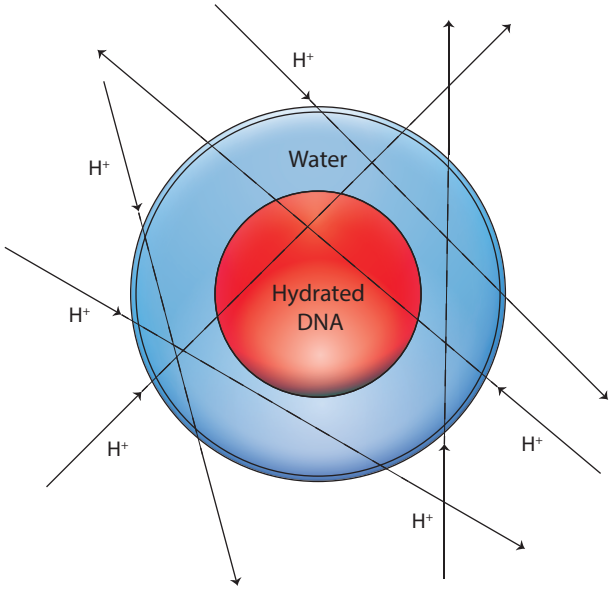

Figure III.12 Irradiation of a single cell impacted by protons arriving at random directions [143]. The innermost sphere colored in red represents the cell nucleus, here assumed to contain only hydrated DNA. The middle and outermost spherical shells colored in blue correspond to the cytoplasm and the cell membrane, respectively, and they are assumed to contain only water.

The energy deposited by all the primary and secondary particles was scored in each sphere. The absorbed dose D to the nucleus was then calculated according to the well-known definition:

$$D = \frac{\Delta E}{\Delta m} = \frac{\Delta E}{\rho \Delta V}\,, \tag{III.9}$$

where ΔE is the energy deposited in the mass Δm, ρ is the density of the medium and ΔV is the volume in which the energy is deposited, i.e., here the volume of the cell nucleus. During the simulations, the energy deposited by protons, neutral hydrogen atoms and secondary electrons was scored separately, so it was possible to distinguish the contribution of each type of projectile to the total absorbed dose.

The energy deposited in the nucleus of a single cell as result of the irradiation by monoenergetic proton beams is reported in Figure III.13a.

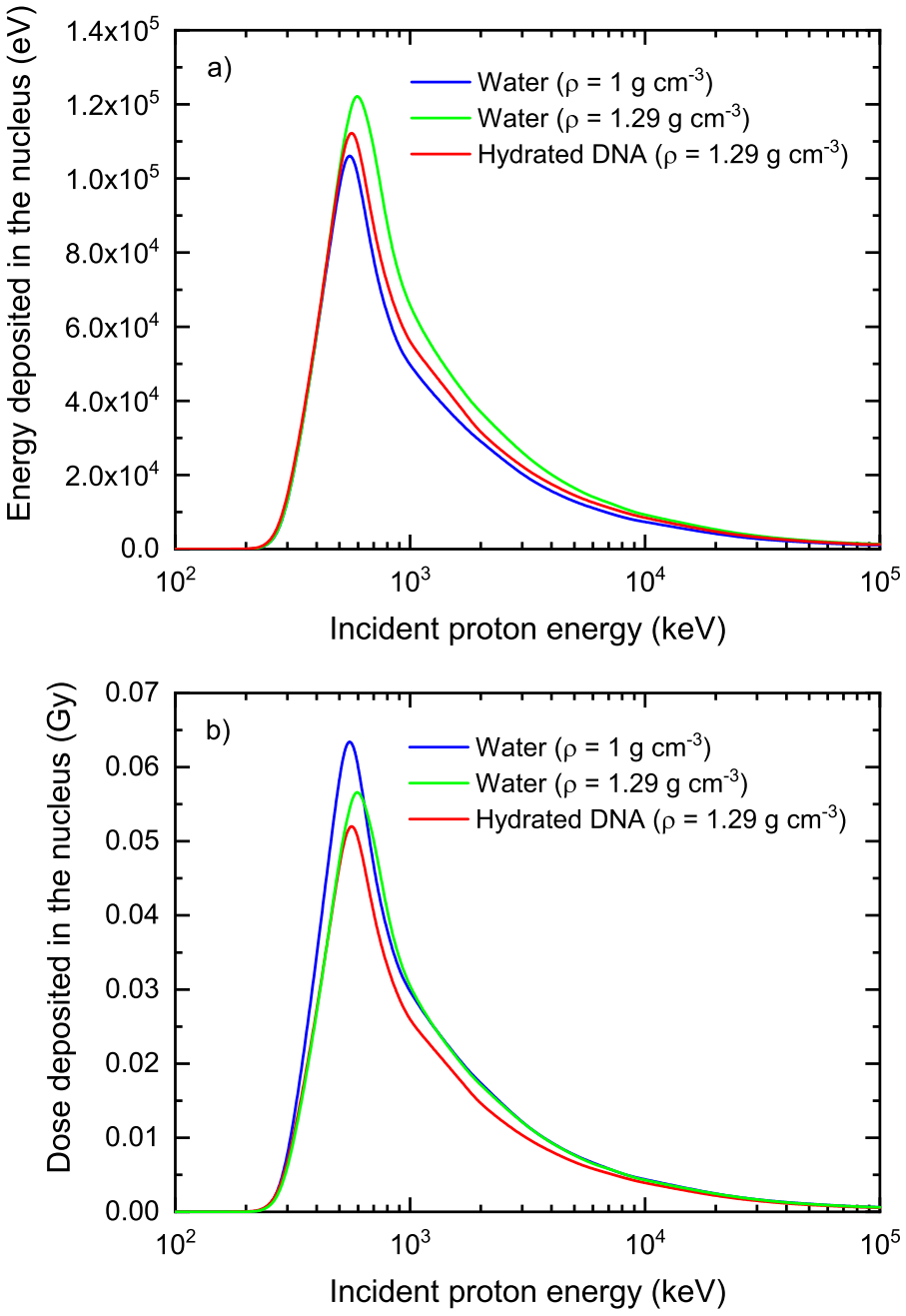

Figure III.13 Energy (panel a) and dose (panel b) deposited in the nucleus of a single cell as a function of the incident proton energy for the configuration illustrated in Figure III.12 and when the nucleus is composed of: water, water with a density rescaled to 1.29 g cm^{-3}, and hydrated DNA [143].

The blue, green and red lines correspond to the energy deposited in the nucleus when it is composed of water ($\rho = 1.0\,\mathrm{g\,cm^{-3}}$), water with the density rescaled to $1.29\,\mathrm{g\,cm^{-3}}$, and hydrated DNA ($\rho = 1.29\,\mathrm{g\,cm^{-3}}$), respectively. Given the dimensions considered in our cell model, a proton must traverse at least $3\,\mu$m of water before reaching the nucleus. The fact that the energy deposited in the nucleus is zero for incident proton energies below $\sim$225 keV it is then consistent with the proton range in water, which is of $2.99\,\mu$m at that energy, according to the ICRU Report 49 [10]. Additionally, the maximum energy deposit occurs for an incident energy of 550 keV in the case of water and hydrated DNA, while for density-rescaled water the peak is located at 600 keV. In the light of our results for the proton range in each medium (see Figure III.7), protons having these initial energies are able to penetrate inside the nucleus, but once there they do not have enough energy left to go out, thus they deposit all the remaining energy in that structure. It is clear from Figure III.13a that, on the one hand, modeling the cell nucleus as water may underestimate the energy deposit up to about 16% if compared to DNA, depending on the incident proton energy. This observation agrees well with the results of a previous work by Champion *et al*. [156], who calculated the mean energy deposited by protons in cylindrical targets of DNA dimensions and found that the energy transfers were about 15% higher when hydrated DNA was used instead of water to model the medium. On the other hand, modeling the nucleus by rescaling the water density to $1.29\,\mathrm{g\,cm^{-3}}$ would have the opposite effect, namely, it may overestimate the energy deposit up to about 28%, if compared to a description of the biological medium based on hydrated DNA. Finally, let us emphasize that neither the values computed with the common approach of using water as a soft-tissue surrogate nor the results obtained by applying a correction based solely on a density rescaling reflect the underlying complexity of the biological medium.

From the point of view of radiation therapy, however, it is more appropriate to express our results in terms of the total dose deposited in the nucleus (see Eq. III.9). The corresponding results are reported in Figure III.13b. It can be seen that reasoning in terms of absorbed dose provides us with a quite different perspective about the irradiated media, since now we clearly observe an overestimation of the dose deposited in the cell nucleus when water is used instead of hydrated DNA for describing the nucleus composition.

In order to better appreciate this fact, the nuclear dose ratios of water to hydrated DNA ($\mathrm{D_{H_2O,1.0}/D_{DNA,1.29}}$) and of density-rescaled water to hydrated DNA ($\mathrm{D_{H_2O,1.29}/D_{DNA,1.29}}$) are given in Table III.1 for selected values of the incident proton energy. Thus, the dose deposited in water is 26% greater than in hydrated DNA at 500 keV, but this percentage drops to less than 15% for incident energies above 1 MeV. With respect to the second ratio, the deposited dose in density-rescaled water is only 1% greater than in hydrated

DNA at 500 keV. This difference increases to about 28% at 700 keV and then decreases again for higher incident energies, without surpassing 18% in the energy range 1 MeV – 100 MeV.

Incident proton energy (keV)	$D_{H_2O,1.0}/D_{DNA,1.29}$	$D_{H_2O,1.29}/D_{DNA,1.29}$
500	1.26	1.01
600	1.19	1.13
700	1.15	1.28
800	1.14	1.22
900	1.13	1.19
1000	1.15	1.18

Table III.1 Nuclear dose ratios for some values of the incident proton energy. $D_{H_2O,1.0}$, $D_{H_2O,1.29}$ and $D_{DNA,1.29}$ denote the dose deposited in the cell nucleus when it is composed of water ($\rho = 1.0\,\mathrm{g\,cm^{-3}}$), water with a density rescaled to $1.29\,\mathrm{g\,cm^{-3}}$, and hydrated DNA ($\rho = 1.29\,\mathrm{g\,cm^{-3}}$), respectively [143].

Finally, we have plotted in Figure III.14 the relative contribution of the primary and the secondary particles to the nuclear dose, when the nucleus is composed of hydrated DNA. At low incident energies, the contribution to the total dose is largely dominated by the neutral hydrogen atoms (H^0, dotted line), while the contribution of protons (H^+, solid line) and electrons (dashed line) is much lower (less than 19% and 3% at an incident energy of 250 keV, respectively). This arises from the fact that the low-energy proton has lost most of its energy while traversing the cell membrane and the cytoplasm as it approaches the nucleus. Thus, its energy falls enough to enter the energy region where the electron capture process becomes more relevant (below 100 keV), the projectile becoming H^0 and interacting in such charge state most of the time until its remaining energy falls below the tracking cutoff of 10 keV. In the case of protons arriving in the nucleus with slightly higher energies, that is for protons with an initial energy of about 300 keV, the three contributions to the dose are almost equal. If the incident energy continues to increase, the secondary electrons provide the most important contribution to the dose. This also stems from the TCS behavior, since ionization by H^+ becomes the most probable interaction. Let us note that for incident energies greater than 700 keV the contribution of H^0 to the dose is essentially zero, and the secondary electron and H^+ contributions remain more or less constant providing around 65–72% and 28–35% of the total nuclear dose, respectively. Let us add that we have only included in Figure III.14 the case of hydrated DNA because we did not find any significant variation in these contributions when the nucleus is modeled with the other media.

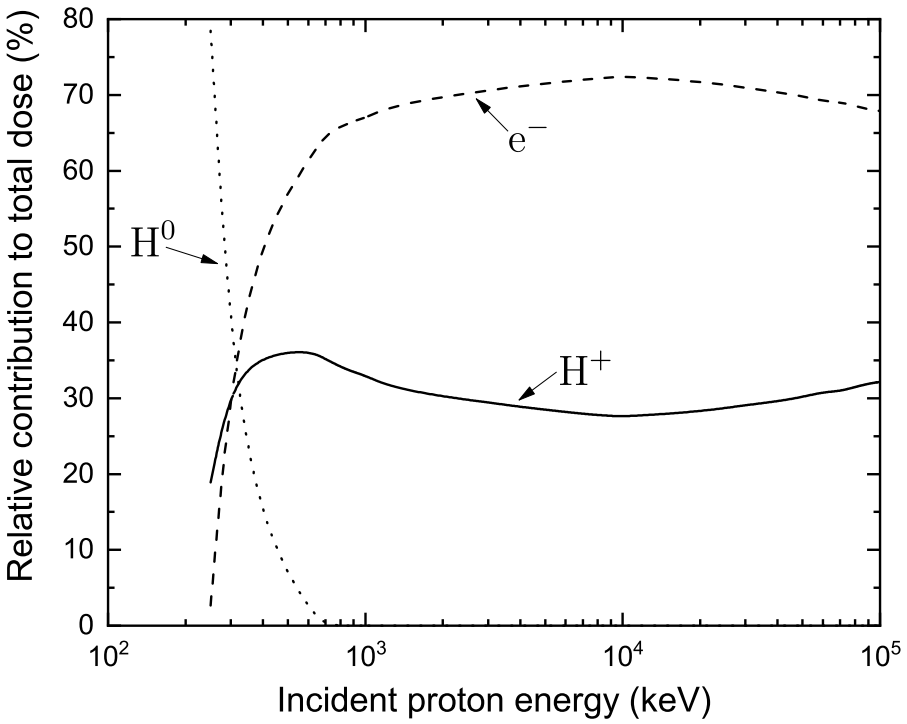

Figure III.14 Relative contributions to the dose deposited in the cell nucleus as a function of the incident proton energy, when the nucleus is modeled by hydrated DNA. The solid, dotted and dashed lines represent the proton, neutral hydrogen and secondary electron contributions, respectively [143].

Conclusions

In this chapter, we have described some of the most important track parameters used to test the reliability of MCTS codes. We have shown that the results provided by the codes *TILDA-V* and EPOTRAN are consistent with the available experimental data for water vapor. Moreover, by including the DNA cross sections in our work, we have gone beyond the common water surrogate to consider a more realistic description of the biological medium. The effects of the latter on the various track parameters have been analyzed, highlighting the differences when hydrated DNA is used instead of water. Since for DNA only a few calculations have been reported in the literature for the track parameters, our work contributes to enrich the theoretical data on this medium. The discrepancies among the various sets of theoretical calculations in both water and DNA clearly show that describing the transport of charged-particles in a biological medium remains a challenge, especially for low incident energies.

In conclusion, the latest versions of *TILDA-V* and EPOTRAN are considered validated to be used in radiation dosimetry applications.

CHAPTER IV

RADIATION DOSIMETRY OF β^- AND AUGER ELECTRON EMITTERS

Contents

IV.1 Introduction **113**

IV.2 The β and electron capture decay processes **114**

IV.3 The isomeric transition, internal conversion and Auger electron emission processes **116**

IV.4 Targeted radionuclide therapy **119**

IV.5 Electron emitters for TRT **120**

IV.5.1 β^- emitters for TRT 120

IV.5.2 AE emitters for TRT 124

IV.6 S-values and absorbed doses in single tumor cells **131**

IV.6.1 Determination of cellular S-values 131

IV.6.2 Normalized absorbed doses to the nucleus of a single tumor cell 136

IV.6.3 Influence on dose of the nucleus composition 138

IV.7 Cell cluster **141**

Conclusions **146**

IV.1 Introduction

Ionizing radiations have deleterious effects on living matter that result from damages induced on DNA. This property of ionizing radiations has been exploited for over a century in medical techniques aiming to kill malignant cells. Even nowadays, radiation

therapy remains one of the most effective treatments against cancer. However, different therapies (e.g., external beam radiation therapy, brachytherapy, targeted radionuclide therapy) or a combination of them may be needed depending on the type, location and size of the tumor. External beam radiation therapy is more effective for treating large tumors, while brachytherapy may provide better results in patients with localized disease. Furthermore, targeted radionuclide therapy has emerged as a promising selective treatment modality for several types of cancer.

In this thesis, we used the *TILDA-V* and EPOTRAN codes to perform radiation dosimetry calculations with the purpose of evaluating and comparing (mainly from a physical point of view) various radionuclides with some interesting properties for targeted radionuclide therapy. In this chapter, we report the results obtained for β^- and Auger electron emitters. The chapter is organized as follows: the physics of the decay processes of interest is briefly reviewed in Sections IV.2 and IV.3; the basic concepts behind targeted radionuclide therapy are given in Section IV.4; the properties of the radionuclides investigated in this context are presented in Section IV.5; the results of our simulations for single tumor cells and cell clusters are presented in Sections IV.6 and IV.7, respectively.

Part of the results reported in this chapter have been recently published in Ref. [245].

IV.2 The β and electron capture decay processes

There are several modes of radioactive decay. The β decay actually encompasses three distinct decay modes in which the atomic number Z of the parent nuclide changes by one unit ($\pm$ 1), while the atomic mass number A remains constant [246]. These processes are[1]:

(i) β^- **decay**. This decay mode occurs in nuclei having an excess of neutrons. A neutron (n) is transformed into a proton (p), with the subsequent emission of an electron (e^-) and an electron antineutrino ($\bar{\nu}_e$), that is:

$$n \rightarrow p + e^- + \bar{\nu}_e \ . \tag{IV.1}$$

If X (Y) is the parent (daughter) nucleus, the transformation can be expressed as:

$${}^{\mathrm{A}}_{\mathrm{Z}}\mathrm{X} \rightarrow {}^{\mathrm{A}}_{\mathrm{Z+1}}\mathrm{Y} + e^- + \bar{\nu}_e \ . \tag{IV.2}$$

(ii) β^+ decay. In this case, a proton-rich radioactive nucleus transforms a proton into neutron and ejects a positron (e^+) and an electron neutrino (ν_e):

$$p \rightarrow n + e^+ + \nu_e \ , \tag{IV.3}$$

[1]N.B. For the sake of simplicity (and because it is enough for the purpose of our study), the description of the decay processes as presented in this Chapter is at the nucleon level. However, the reader should be aware that transformations involve the quark nature of protons and neutrons.

or equivalently:

$$ {}^{\mathrm{A}}_{\mathrm{Z}}\mathrm{X} \rightarrow {}^{\mathrm{A}}_{\mathrm{Z-1}}\mathrm{Y} + e^+ + \nu_e \ . \tag{IV.4} $$

(iii) **Electron capture (EC)**. Similarly to the β^+ decay, this decay mode is common in proton-rich nuclei. A nucleus captures an inner shell orbital electron, transforms a proton into a neutron, and ejects an electron neutrino. Thus, the transformation is written as:

$$ p + e^- \rightarrow n + \nu_e \ , \tag{IV.5} $$

or equivalently:

$$ {}^{\mathrm{A}}_{\mathrm{Z}}\mathrm{X} + e^- \rightarrow {}^{\mathrm{A}}_{\mathrm{Z-1}}\mathrm{Y} + \nu_e \ . \tag{IV.6} $$

Only radionuclides experiencing a β^- decay or EC will be considered in the following.

The decay energy in a β^- decay is shared between three particles: the β^--particle (electron) itself, the electron antineutrino and the recoil nucleus. Moreover, the kinetic energy of the recoil nucleus in a β^- decay $\left({}^{\mathrm{A}}_{\mathrm{Z+1}}\mathrm{Y}\right.$ in Eq. IV.2$\left.\right)$ is very small, of about 10 eV – 100 eV, which is negligible compared to the kinetic energy of the β^--particle [246]. Most of the decay energy therefore is carried by the β^--particle and the antineutrino. A consequence of the latter is that the electrons emitted in a β^- decay are not monoenergetic, but instead have a continuous energy distribution (the β^- spectrum) up to a maximum energy $E_{\beta^-}^{(\mathrm{max})}$. An example of the shape of a β^- spectrum is shown in Figure IV.1 for yttrium-90 (^{90}Y).

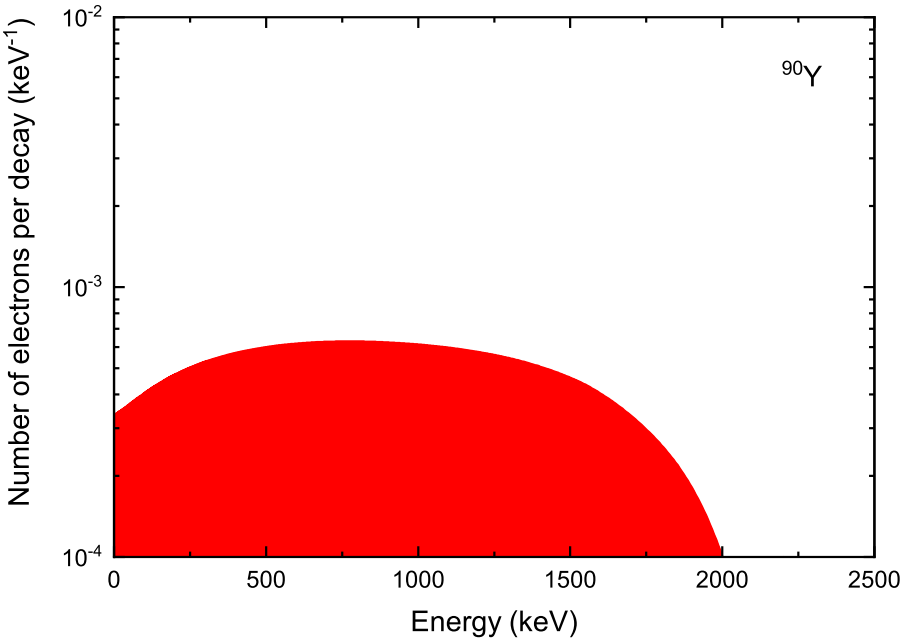

Figure IV.1 β^- spectrum of ^{90}Y.

There are several radionuclides of medical interest undergoing β^- decay. Some

examples include ^{131}I, ^{90}Y, ^{177}Lu and ^{161}Tb, all of which are discussed in Section IV.5.

IV.3 The isomeric transition, internal conversion and Auger electron emission processes

After a β^- or EC decay, the daughter nucleus is often in an excited state. In fact, sometimes the daughter nucleus is produced in a metastable state, that is, in an excited state having a long half-life (greater than about 5 ns [247]). In this case, the state is also called a nuclear isomer, and its decay is known as **isomeric transition (IT)**. Metastable radionuclides are usually designated with an "m" placed after the mass number, e.g., ^{99m}Tc. Moreover, independently of whether metastable states are formed or not after the decay of the parent nucleus, the de-excitation of the daughter nucleus is achieved either by emission of γ-rays or by **internal conversion (IC)**. In the latter process, the de-excitation energy is transferred from the nucleus to an orbital electron of the same atom, usually a K-shell electron. The electron ejected from the atom is thus called **internal conversion electron (CE)**. The decay energy for IC is given by:

$$Q_{\mathrm{IC}} = Q_\gamma - I_i = E_{\mathrm{CE}} + E_{\mathrm{RN}} \ , \tag{IV.7}$$

where Q_γ is the energy difference between two excited nuclear states, equal to the energy of a γ photon in a γ decay; I_i is the ionization potential, i.e., the energy necessary to remove the electron from the atomic shell i; E_{CE} is the kinetic energy of the CE; and E_{RN} is the kinetic energy of the recoil nucleus, which is much smaller than E_{CE} [246].

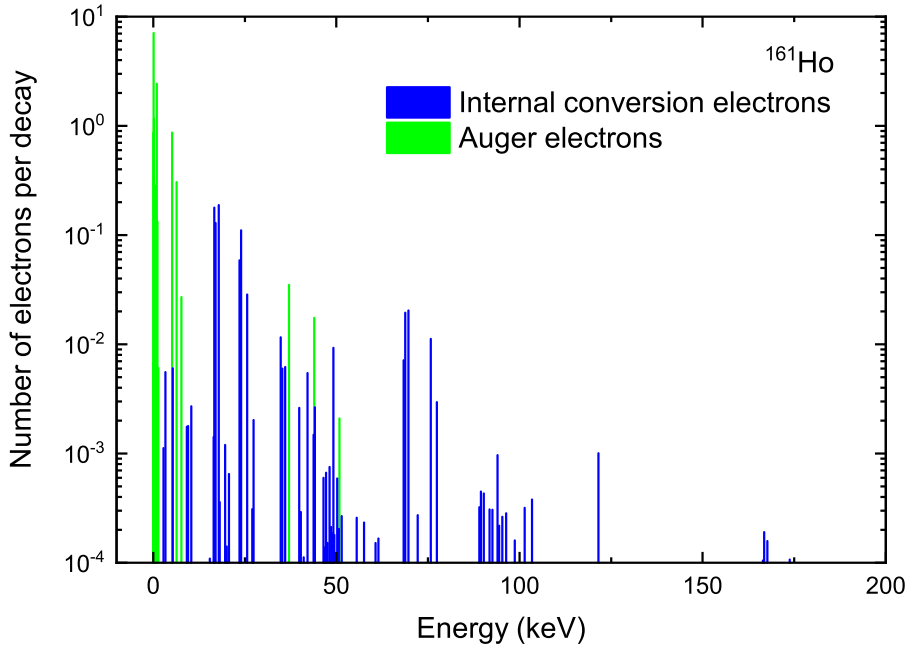

Figure IV.2 Energy spectrum of ^{161}Ho.

Contrary to β-particles, CE are monoenergetic, i.e., they exhibit a discrete energy spectrum. Figure IV.2 presents an example of a radionuclide with a discrete energy spectrum, holmium-161 (^{161}Ho). The blue lines in figure IV.2 represent the CE emitted by ^{161}Ho. Furthermore, the removal of orbital electrons by EC or IC creates vacancies in the atomic shells and leaves the atom in an excited state. The ensuing atomic relaxation can take place through radiative and non-radiative transitions. In the first case, X-rays with characteristic energies are emitted as the outer shell electrons fill the vacancies in the inner shells. The energy of the X-ray is equal to the energy difference between the atomic shells involved in the transition. On the other hand, non-radiative transitions are related to the Auger effect, in which an outer atomic electron, called **Auger electron (AE)**, is emitted instead of a photon as a result of the rearrangement of the atomic electrons to fill the vacancy in an inner shell. Similarly to CE, AE are emitted at discrete energies (e.g., green lines in Figure IV.2). In an AE process denoted XYZ, an electron in an outer shell Y makes a transition to the vacancy in an inner shell X, and an electron is ejected from the outer shell Z. For instance, if X is the K-shell, Y the L_1 sub-shell, and Z the L_2 sub-shell, the electron is called a KL_1L_2 Auger electron [248]. The energy of the AE is then written as:

$$E_{\mathrm{AE}}(XYZ) = I_X - I_Y - I_Z \ , \tag{IV.8}$$

where the terms I_X, I_Y, I_Z denote the ionization potential of each atomic shell involved in the transition. Figure IV.3 illustrates the relaxation of an atom by means of radiative and non-radiative transitions.

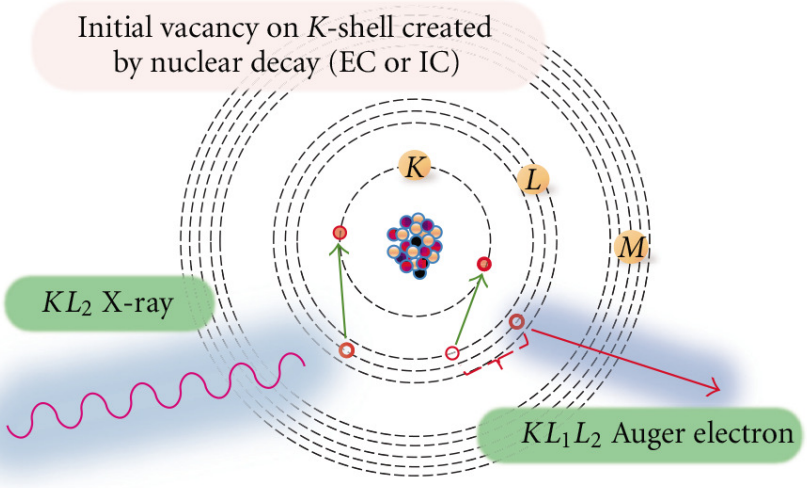

Figure IV.3 Atom relaxation following a vacancy in the K-shell by radiative (X-ray emission) and non-radiative (Auger electron emission) transitions. Image by Lee *et al.* [248], licensed under CC BY 3.0.

In addition, two types of transition receive special names [246]:

(i) The Coster-Kronig effect occurs when the transition energy originates from two sub-shells of a given atomic shell and is transferred to an electron in another shell. The ejected electron is called Coster-Kronig electron.

(ii) When the transition energy originates from two sub-shells of a given atomic shell, and the energy is transferred to an electron in the same shell, one speaks of super Coster-Kronig effect. Thus, the ejected electron is called a super Coster-Kronig electron.

For the sake of simplicity, however, and unless otherwise stated, we will consider hereafter that both Coster-Kronig and super Coster-Kronig electrons are taken into account when we refer to "Auger electrons".

Besides, it is worth noting that AE have low kinetic energies, ranging from a few eV to some tens of keV. Consequently, AE deposit all their energy over very short distances, with ranges in water going from a fraction of a nanometer to several hundreds of micrometers [249]. Figure IV.4 illustrates the track in water of a typical AE taken from the spectrum of ^{161}Tb ($E_{\text{inc}} = 5.25$ keV).

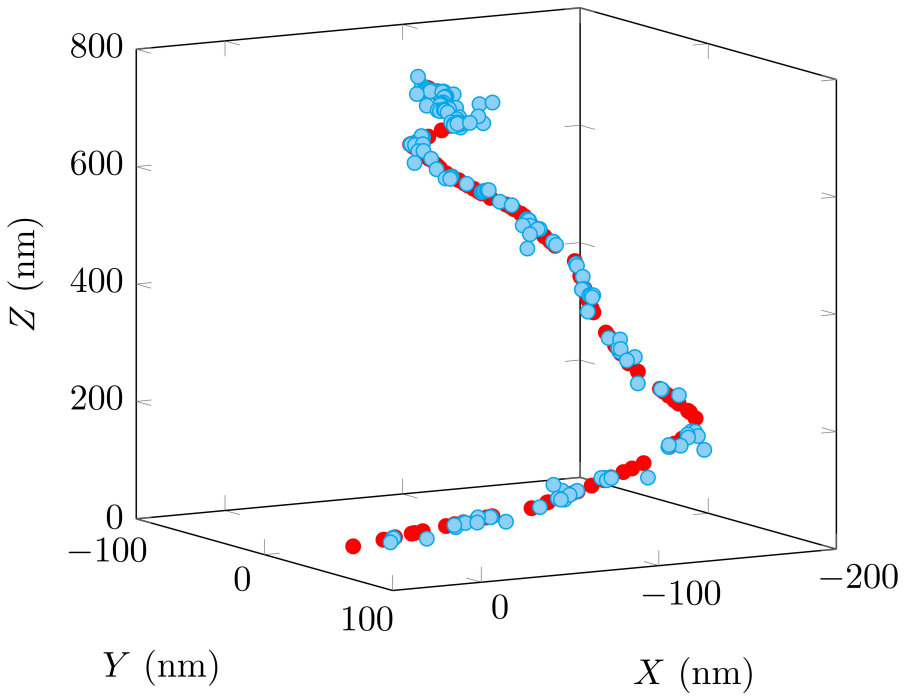

Figure IV.4 The track in water of an Auger electron of 5.25 keV emitted by ^{161}Tb. The energy deposits induced by the primary electron are shown in red, while those induced by the secondary electrons are reported in cyan.

In this context, AE have high linear energy transfer (LET), a property that makes them attractive for cancer therapy. However, the highly localized dose provided by AE implies that they must be emitted in the proximity of critical biological targets, i.e., the nuclear

DNA of tumor cells, to achieve the desired therapeutic effect. It is worth mentioning that, in the literature, it is customary to call "Auger electron emitter" to any radionuclide emitting such electrons after experiencing an EC or IC decay. In this thesis, we have adopted this convention as well. Many radionuclides are known to emit a significant number of AE. Among them, ^{125}I is by far the most well-studied AE emitter in radiation biology. Other examples of AE emitters of interest for targeted radionuclide therapy will be discussed in Section IV.5. It is worth mentioning that some radionuclides experiencing β^- decay emit as well an important number of AE. That is the case for instance of ^{161}Tb, which in addition emits low-energy CE (see Section IV.5.1.4).

IV.4 Targeted radionuclide therapy

Targeted radionuclide therapy (TRT) is a cancer treatment modality that couples a radionuclide to a carrier molecule (e.g., an antibody, a peptide, an oligonucleotide, etc.) able to target the tumor cells or the tumor microenvironment to closely irradiate the tumor, thus minimizing the radiation dose to healthy tissue. The selection of the radionuclide is based on its physical properties (emission characteristics, half-life), as well as in the chemical properties of the element, which determine the feasibility of the binding to the carrier molecule. The location of the radiopharmaceutical is dictated by physiological or biochemical phenomena such as the presence of a receptor, an enzyme or antigen that has an affinity for the carrier molecule [250].

TRT was introduced almost eighty years ago with the application of radioiodine (^{131}I) for the treatment of thyroid disease [251]. Since then, ^{131}I has also been used in TRT of tumors other than thyroid cancer. For example, ^{131}I has been used in the treatment of unresectable or metastatic pheochromocytomas and paragangliomas, and for TRT of non-Hodgkin's lymphoma (NHL) [250]. Furthermore, in the last decades other radionuclides suitable for TRT have been introduced in the clinical practice. For instance, ^{90}Y and ^{177}Lu have been linked to biological vectors and found various therapeutic applications, including targeted treatment of NHL, peptide receptor radionuclide therapy (PRRT) of neuroendocrine tumours and prostate-specific membrane antigen (PSMA) ligands TRT of metastatic prostate cancer [252–254]. In addition, the interest in TRT has grown in recent years with the study of new radionuclides with very promising features, in particular AE emitters and α-particle emitters.

TRT may be performed with β^-, AE or α-particle emitters. Moreover, in certain cases the combined use of radionuclides having different types of radioactive emissions may be advantageous. Such a combined strategy may be interesting for instance for destroying heterogeneous tumors.

The clinical efficiency of TRT is strongly related to the type and energy of the emitted

radiation and the tumor size. The use of medium- or high-energy β^- may be more appropriate to deal with tumor heterogeneity. On the other hand, AE and α-particle emitters seem appropriate to eradicate single tumor cells and micrometastases, because of the short path length and the very localized energy deposition of the emitted radiation [255, 256].

In the following section, we describe the physical properties of some of the β^- and AE emitters that either have been used for TRT or are currently being investigated for applications in TRT. It should be noted that an exhaustive evaluation of all electron emitters considered thus far for TRT is beyond the scope of this thesis. Thus, the selection of the radionuclides analyzed hereafter is rather subjective and is largely based on previous studies suggesting their therapeutic potential.

IV.5 Electron emitters for TRT

The purpose of this section is to provide some basic information about the electron emitters that were considered in our simulations, such as their physical properties, production routes and current or potential medical applications.

IV.5.1 β^- emitters for TRT

IV.5.1.1 ^{131}I

Iodine-131 (^{131}I) is a medium-energy β^- emitter with a half-life $T_{1/2} = 8.02\,\mathrm{d}$. The β^--particles of ^{131}I have a maximum energy $E_{\beta^-}^{(\mathrm{max})} = 807\,\mathrm{keV}$ and an average energy $E_{\beta^-}^{(\mathrm{mean})} = 182\,\mathrm{keV}$. These β^--particles have a maximum range of 3.6 mm in water [257]. ^{131}I decays to excited levels of ^{131}Xe, including the metastable state $^{131\mathrm{m}}$Xe, followed by the emission of high-energy γ-rays. The most probable γ emissions have energies of 364 keV (81.7%), 637 keV (7.2%) and 723 keV (1.8%). The emission of energetic γ-rays allows the visualization of lesions through scintigraphy or SPECT. However, ^{131}I imaging has poor spatial resolution and a better choice for theranostics purposes is the combined use of ^{124}I and ^{131}I [258]. Moreover, the γ radiation emitted by ^{131}I increases the radiation dose to the patient with only low contribution to tumor dose, and has important implications as well for the radiation safety of the medical staff and the patient's relatives.

^{131}I can be produced in nuclear reactors either through the fission of ^{235}U or by neutron irradiation of a tellurium dioxide (TeO_2) target via the ^{130}Te(n,γ)^{131}Te and ^{130}Te(n,γ)$^{131\mathrm{m}}$Te nuclear reactions. ^{131}Te and $^{131\mathrm{m}}$Te experience β^- decay to ^{131}I with half-lives of 25 min and 30 h, respectively [259].

^{131}I has been successfully used for many years in the diagnosis and treatment of thyroid cancer, as well as non-malignant thyroid disorders such as hyperthyroidism. As already mentioned, other therapeutic applications of ^{131}I include the TRT of NHL with ^{131}I-tositumomab (Bexxar), and the treatment of neuroendocrine tumors with ^{131}I-metaiodobenzylguanidine (^{131}I-MIBG) [250].

IV.5.1.2 ^{90}Y

Yttrium-90 (^{90}Y) has a half-life $T_{1/2} = 64.1$ h (2.67 d) and decays to ^{90}Zr by the emission of high-energy β^--particles of $E_{\beta^-}^{(\max)} = 2.28\,\mathrm{MeV}$. These energetic β^--particles have a maximum range of 11.8 mm in water [257]. Furthermore, in contrast to ^{131}I, ^{90}Y has no significant emission of γ photons. Therefore, in clinical practice a theranostic pair is usually formed with ^{111}In to allow SPECT imaging. In addition, post-therapy ^{90}Y Bremsstrahlung or PET imaging is feasible [260]. Indeed, ^{90}Y also emits $\sim 3 \times 10^{-5}$ positrons per β decay [261]. ^{90}Y is generally obtained from a ^{90}Sr/^{90}Y generator. The parent radionuclide, ^{90}Sr, is a long-lived β^- emitter produced in the fission of ^{235}U, and is available in large quantities from spent nuclear fuel.

Radiopharmaceuticals containing ^{90}Y have been successfully used for TRT. For instance, ^{90}Y-ibritumomab tiuxetan (Zevalin) showed clinical benefits for consolidation therapy of NHL [252]. Moreover, it has been demonstrated that PRRT with ^{90}Y-DOTATATE and ^{90}Y-DOTATOC improves the survival of patients with metastatic neuroendocrine tumors [262, 263]. Furthermore, ^{90}Y-labeled PSMA–617 has been shown to be a safe treatment option for patients with metastatic castration-resistant prostate cancer [264]. Finally, ^{90}Y is often used in radioembolization for the treatment of both primary and metastatic liver tumors [265].

IV.5.1.3 ^{177}Lu

Lutetium-177 (^{177}Lu) is a medium-energy β^- emitter with a half-life $T_{1/2} = 6.647$ d. ^{177}Lu emits β^--particles of $E_{\beta^-}^{(\max)} = 497$ keV, having a maximum range in water of 1.9 mm [257]. In addition, ^{177}Lu emits γ photons with energies of 208 keV (11%) and 113 keV (6.4%), suitable for quantitative imaging before and during treatment.

The scope of ^{177}Lu production via the accelerator route is limited. There are two production routes using nuclear reactors [266]:

(i) The direct production route by neutron irradiation of ^{176}Lu targets through the ^{176}Lu(n,γ)^{177}Lu nuclear reaction.

(ii) The indirect production route via the ^{176}Yb(n,γ) ^{177}Yb $\xrightarrow{\beta^-}$ ^{177}Lu nuclear reaction, which requires chemical separation from the ^{176}Yb target atoms.

The main therapeutic applications of ^{177}Lu are similar to those of ^{90}Y. In fact in some cases, such as the treatment of metastatic neuroendocrine tumors, ^{177}Lu has virtually replaced ^{90}Y because it has shown to be equally effective with less toxicity [250]. Indeed, the efficacy and safety of ^{177}Lu-DOTATATE has been demonstrated in patients with advanced, progressive, somatostatin-receptor–positive midgut neuroendocrine tumors [253]. Moreover, ^{177}Lu-PSMA-617 showed high response rates, low toxic effects, and reduction of pain in patients with metastatic castration-resistant prostate cancer [254]. Finally, ^{177}Lu-lilotomab satetraxetan (Betalutin) is currently being investigated as a potential therapy for B-cell NHL [267].

IV.5.1.4 ^{161}Tb

Terbium-161 (^{161}Tb) has gained interest as a potential substitute for ^{177}Lu in TRT. ^{161}Tb has a half-life $T_{1/2} = 6.906\,\mathrm{d}$ and emits β^--particles of $E_{\beta^-}^{(\max)} = 593\,\mathrm{keV}$. Furthermore, ^{161}Tb emits a much higher number of very low-energy AE than ^{177}Lu, as well as low-energy CE (mostly with energies $\leq 40\,\mathrm{keV}$). These low-energy electrons have high LET and then confer to ^{161}Tb an advantage over ^{177}Lu up to about $30\,\mu\mathrm{m}$ from the decay site [16], because they increase the local dose in tumors without exacerbating renal damage [268]. Moreover, ^{161}Tb emits a small percentage of photons (75 keV, 10.2%) that can be useful for post-therapy SPECT imaging, as is the case with ^{177}Lu. On the other hand, ^{161}Tb is compatible with the concept of theranostics, i.e., a diagnostic match may be found among other terbium radioisotopes allowing imaging before therapy, while ^{177}Lu lacks a useful companion diagnostic radionuclide [269, 270]. Besides, ^{161}Tb and ^{177}Lu share chemical properties as radiolanthanides, thus similar radiolabeling techniques can be used for both [271, 272].

No-carrier-added ^{161}Tb can be produced via the ^{160}Gd(n,γ)^{161}Gd$\xrightarrow{\beta^-}$ ^{161}Tb nuclear reaction in the quantity and quality needed for clinical applications [271, 273].

The superiority of ^{161}Tb over ^{177}Lu has been observed in cell survival studies, as well as in studies on mice bearing small tumor xenografts [272, 274, 275]. Moreover, theoretical dose calculations have suggested that ^{161}Tb may outperform ^{177}Lu in very small tumors [16, 17, 276].

Table IV.1 summarizes some relevant properties of the β^- emitters discussed here above.

Radionuclide	^{131}I	^{90}Y	^{177}Lu	^{161}Tb
Half-life (day)	8.02	2.67	6.647	6.906
β^--particles mean energy (keV)	182	932.9	133.3	154.3
Daughter nucleus	^{131}Xe (stable)	^{90}Zr (stable)	^{177}Hf (stable)	^{161}Dy (stable)
CE (intensity per decay)	6.46%	0.01%	15.47%	142%
CE (energy per decay in keV)	9.57	0.2	13.52	39.28
CE energy range in keV†	45.6 – 602.4	1742.7	6.2 – 206.3	3.3 – 98.3
AE (intensity per decay)	69.75%	0.13%	111.65%	1096.4%
AE (energy per decay in keV)	0.41	0.0007	1.13	8.94
AE energy range in keV	0.026 – 32.9	0.022 – 1.8	0.01 – 61.7	0.018 – 50.9
Total electron energy per decay (keV)	191.8	933.1	147.9	202.5
γ or X-ray radiation useful for imaging (energy in keV and % abundance)*	364.5 (81.7%) 330 (1.6%) 284.3 (6.1%) 80.2 (2.6%)	–	208 (11%) 113 (6.4%)	75 (10.2%)
Photons (energy per decay in keV)	382.7	–	35.1	36.35
Total energy per decay in keV (photons + electrons)	574.5	933.1	183	238.9
% of energy emitted as electrons	33.4%	$\sim$100%	80.8%	84.8%
% of energy emitted as photons	66.6%	$\sim$0%	19.2%	15.2%

Table IV.1 Main properties of β^- emitters for TRT [18].

† Only AE and CE with probabilities greater than 0.1‰ are considered in this table and in our simulations (see text). Note that ^{90}Y has only one CE that satisfies this criterion.

* Photon emissions are considered useful for imaging if their energy is between 70–400 keV, i.e., within the approximate energy range in which SPECT detectors operate. Only photon emissions with an abundance $>$ 1% are listed in this table.

IV.5.2 AE emitters for TRT

Various AE emitters have been put forward in the last decades as promising candidates for TRT of small tumors. Some of the most desirable characteristics of the AE emitters considered for this purpose include: having a short half-life (ideally from 1 to 10 days); the energy of the emitted electrons should be low enough, preferably $\lesssim 40$ keV; and the photon-to-electron energy ratio (p/e) should be ≤ 2 to limit the radiation dose to normal tissue [277]. Furthermore, the chemistry of the element in question should be well understood and appropriate chelators should be available to allow the radiolabeling of the targeting molecules. In addition to these criteria, taking into account the logistics of radionuclide production is of vital importance to make viable the use of the radionuclide in the clinical setting. In this section, we describe the basic physical properties and the methods of production of the AE emitters selected in our study. It is worth mentioning that some AE emitters satisfying the criteria aforementioned, such as thulium-167 (^{167}Tm) and tin-117m (^{117m}Sn), were included in preliminary studies in which we assessed the absorbed doses to spheres of different sizes (data not shown). However, they were finally dismissed because of their poor performance compared to the other AE emitters. On the other hand, we decided to keep iodine-125 (^{125}I) in our investigation (in spite of its long half-life and its relatively high p/e ratio) because of its great relevance in radiobiology and the numerous recent studies devoted to its potential applications in TRT. As we stated previously, the choice of the radionuclides is always somewhat subjective.

IV.5.2.1 ^{71}Ge

Germanium-71 (^{71}Ge) has a half-life $T_{1/2} = 11.43$ d and decays to stable gallium-71 (^{71}Ga) by EC. ^{71}Ge emits only low-energy AE ($\lesssim 10$ keV) and X-rays.

^{71}Ge can be produced by proton or deuteron bombardment of ^{71}Ga targets, via the reactions ^{71}Ga(p,n)^{71}Ge and ^{71}Ga(d,2n)^{71}Ge, respectively [278]. The use of natural gallium (^{nat}Ga: 60% ^{69}Ga; 40% ^{71}Ga) also produces the isotope ^{69}Ge ($T_{1/2} = 39$ h), a β^+ emitter attractive for PET due to its low positron energy and low abundance of γ emissions [279]. The combination ^{69}Ge/^{71}Ge is therefore seen as a potential theranostic pair. Moreover, ^{71}Ge was recently listed among the AE emitters for which measurements and comparative modeling calculations are required for improved decay data, according to the consultants of the IAEA Nuclear Data Section [278].

IV.5.2.2 ^{103m}Rh

Rhodium-103m (^{103m}Rh) has a half-life $T_{1/2} = 56.1$ min (0.039 d) and decays to stable ^{103}Rh by IT. CE and AE represent the major components in the decay energy of ^{103m}Rh, with only low-energy photon emissions. Indeed, ^{103m}Rh emits about 30 times as many low-energy (< 40 keV) electrons as photons (2–40 keV) per decay [280].

The use of ^{103m}Rh for TRT of small tumors was suggested long ago [277], but its production in large quantities still presents some challenges. In spite of its short half-life, the *in vivo* use of ^{103m}Rh would be feasible if it is administered locally, e.g., by intratumoral or intracavitary administration [280].

^{103m}Rh can be produced in a generator containing one of its parent radionuclides, namely ruthenium-103 (^{103}Ru, $T_{1/2} = 39.21$ d) or palladium-103 (^{103}Pd, $T_{1/2} = 16.99$ d). There are four ways to produce ^{103m}Rh in therapeutic amounts [281]:

(i) Production of ^{103}Ru by fission via the ^{235}U(n,f)^{103}Ru nuclear reaction.

(ii) Production of ^{103}Ru by neutron irradiation in enriched ^{102}Ru via the ^{102}Ru(n,γ)^{103}Ru nuclear reaction.

(iii) Production of ^{103}Pd by neutron capture in enriched ^{102}Pd.

(iv) Production of ^{103}Pd by irradiation of rhodium targets with protons or deuterons, i.e., via the reactions ^{103}Rh(p,n)^{103}Pd and ^{103}Rh(d,2n)^{103}Pd.

Skarnemark *et al.* [281] described solution-based generator systems to obtain ^{103m}Rh from either ^{103}Ru or ^{103}Pd. They noted, however, that the production route via ^{103}Ru presents some drawbacks, because ^{103}Ru is a β^- and γ emitter. The latter implies that contamination of the eluted ^{103m}Rh with small amounts of ^{103}Ru would eliminate the dosimetric advantages of ^{103m}Rh compared to other AE emitters. Moreover, the ^{103}Ru/^{103m}Rh generator would require adequate radiation shielding during preparation and storage [281]. Nevertheless, the idea of a ^{103}Ru/^{103m}Rh generator has not been abandoned. In fact, a method for the recovery and purification of ^{103}Ru following the proton irradiation of thorium targets, as a preliminary step in the development of a ^{103}Ru/^{103m}Rh generator, was recently reported by Mastren *et al.* [282]. Furthermore, there have been as well recent advances in the development of ^{103}Pd/^{103m}Rh generators. For instance, Jensen *et al.* [280] showed the feasibility of a solid-phase generator of high specific activity ^{103m}Rh from chelated ^{103}Pd, obtained from neutron-activated ^{102}Pd-enriched palladium foils. This generator would be able to produce enough ^{103m}Rh for preclinical studies, but it would be too inefficient for clinical applications [280].

IV.5.2.3 ^{119}Sb

Antimony-119 (^{119}Sb) has a half-life $T_{1/2} = 38.19$ h (1.591 d) and decays to stable tin-119 (^{119}Sn) by EC. The potential of ^{119}Sb for the treatment of small tumors and micrometastases has been highlighted by several authors [277, 283], as well as the possibility of using it in combination with the isotope ^{117}Sb ($T_{1/2} = 2.8$ h) for SPECT-based 3D dosimetry [283, 284]. The following production routes have been proposed to obtain ^{119}Sb in sufficient quantities for clinical applications:

(i) Direct production in a low-energy cyclotron by proton irradiation of an enriched ^{119}Sn target via the reaction ^{119}Sn(p,n)^{119}Sb [284].

(ii) Indirect production by means of a ^{119m}Te/^{119}Sb generator [285]. In this method, high-energy proton sources are used to produce the longer lived parent isotope tellurium-119m (^{119m}Te, $T_{1/2} = 4.7\,\mathrm{d}$), which decays to ^{119}Sb by EC. ^{119m}Te is obtained via the ^{121}Sb(p,3n)^{119m}Te$\xrightarrow{\mathrm{EC}}$ ^{119}Sb and ^{123}Sb(p,5n)^{119m}Te$\xrightarrow{\mathrm{EC}}$ ^{119}Sb nuclear reactions on natural Sb targets.

The indirect production route could produce ^{119}Sb in quantities 10–100 times larger than the direct production route, with the additional advantage of providing access to ^{119}Sb for longer time periods, a key aspect for allowing ^{119}Sb drug development [285].

IV.5.2.4 ^{125}I

Iodine-125 (^{125}I) has a half-life of 59.4 days and decays to stable tellurium-125 (^{125}Te) by EC. The decay of ^{125}I is accompanied by the emission of CE with energies ranging from 3.7 keV to 35.5 keV, and AE with energies going from 23 eV to 30.3 keV. In addition, ^{125}I emits low-energy γ-rays ($\sim$25 keV on average). These γ emissions are exploited in low dose rate brachytherapy with permanent ^{125}I seed implants, but they are rather a drawback for TRT applications and are not useful for imaging purposes.

Large-scale production of ^{125}I is possible in nuclear reactors through the activation of an enriched xenon-124 (^{124}Xe) gaseous target by neutron irradiation via the ^{124}Xe(n,γ)^{125}Xe$\xrightarrow{\beta^-}$ ^{125}I nuclear reaction [259].

^{125}I is by far the most extensively investigated AE emitter. In fact, many assumptions regarding the properties of AE emitters have been tested with this radionuclide, such as the importance of the proximity to nuclear DNA to achieve high levels of cytotoxicity. The potential of ^{125}I for TRT has been investigated for decades. The therapeutic efficacy of ^{125}I was initially demonstrated in experimental studies with several tumor models using ^{125}I-iododeoxyuridine (^{125}IUdR), which is incorporated into DNA as a thymidine analogue [286]. Despite the fact that some agents radiolabeled with ^{125}I have reached phase II clinical trials [287], and that several preclinical studies for other novel agents based on ^{125}I have been performed in recent years [288–290], the use of this radionuclide in TRT remains experimental. Indeed, the long half-life of ^{125}I, among other factors, makes its clinical use logistically challenging [289].

IV.5.2.5 ^{161}Ho

Holmium-161 (^{161}Ho) is an AE-emitting radiolanthanide. It has a half-life $T_{1/2} = 2.48\,\mathrm{h}$ (0.103 d) and decays to stable dysprosium-161 (^{161}Dy) by EC. ^{161}Ho also emits low-energy photons in high abundance. ^{161}Ho is among the low-energy electron-emitting

radionuclides identified by Bernhardt *et al.* [277] as suitable for the treatment of small tumors. ^{161}Ho can be produced with particle accelerators. Different production routes have been investigated in the literature, such as [291]:

(i) Irradiation of terbium-159 (^{159}Tb) with α-particles or helium-3 (^{3}He), via the reactions ^{159}Tb(α,2n)^{161}Ho and ^{159}Tb(^{3}He,n)^{161}Ho.

(ii) Irradiation of dysprosium targets using protons or deuterons, via the reactions ^{161}Dy(p,n)^{161}Ho, ^{162}Dy(p,2n)^{161}Ho, ^{160}Dy(d,n)^{161}Ho and ^{161}Dy(d,2n)^{161}Ho.

After studying these production routes, Tárkányi *et al.* [291] concluded that, on the basis of the production yields, the impurity levels and the requirements for medical applications, the best method to obtain ^{161}Ho is via the ^{161}Dy(p,n)^{161}Ho reaction.

IV.5.2.6 ^{189m}Os

Osmium-189m (^{189m}Os) is another AE emitter listed by Bernhard *et al.* [277] as a candidate for the treatment of small tumors. ^{189m}Os has a half-life $T_{1/2} = 5.8$ h (0.242 d) and decays to the ground state of stable ^{189}Os. Moreover, ^{189m}Os emits about 6 AE per decay and has no relevant photon emissions.

^{189m}Os can be produced in a no-carrier-added way, but with low specific activity, through a generator system by the decay of longer lived iridium-189 (^{189}Ir). The latter has a half-life $T_{1/2} = 13.2$ d and decays by EC to ^{189m}Os with a branching fraction ~7%, while most ^{189}Ir decays to ground state ^{189}Os [18, 292]. To the best of our knowledge, no other production route has been suggested in the literature.

IV.5.2.7 ^{193m}Pt

Platinum-193m (^{193m}Pt) has a half-life $T_{1/2} = 4.33$ d and decays to the ground state of radioactive platinum-193 (^{193}Pt, $T_{1/2} = 50$ years) by IT. ^{193m}Pt emits ~27 AE per decay, with only low photon yields of energies ≤ 135 keV.

The potential of the AE emitters ^{193m}Pt and ^{195m}Pt for applications in TRT is not only due to their suitable decay properties, but also because platinum complexes, e.g., cisplatin, are used in chemotherapy [293].

Basically, three approaches have been proposed thus far to produce ^{193m}Pt:

(i) Production in a nuclear reactor by neutron irradiation of enriched ^{192}Pt targets, via the ^{192}Pt(n,γ)^{193m}Pt nuclear reaction [294]. This method, however, is very expensive and does not provide a final product with a specific activity high enough for therapeutic applications [293].

(ii) Cyclotron production through deuteron bombardment of natural iridium targets, via the ^{193}Ir(d,2n)^{193m}Pt reaction [295]. The drawback in this production route is the low radionuclidic purity [293].

(iii) Cyclotron production through α-particle bombardment of an enriched osmium-192 (^{192}Os) target, via the ^{192}Os(α,3n)^{193m}Pt reaction [293, 296]. This production route seems the most promising, with batch yields of up to 2 GBq, enough for AE therapy. Nevertheless, to reach this amount of ^{193m}Pt improved targetry is still needed in order to use higher beam intensities [296].

IV.5.2.8 ^{195m}Pt

Platinum-195m (^{195m}Pt) has a half-life $T_{1/2} = 4.02$ d and decays by IT to stable ^{195}Pt. ^{195m}Pt is perhaps the most promising candidate among AE emitters for TRT because of the energy and yield of its electronic emissions. Indeed, ^{195m}Pt emits ~36 AE per decay, more than ^{125}I and many other radionuclides. Moreover, it was shown that the energy deposited by ^{195m}Pt in nanometric spheroids was greater than for the AE emitters ^{125}I and ^{111}In [297]. On the other hand, the γ photons emitted by ^{195m}Pt have energies suitable for SPECT imaging.

At least two methods have been reported in the literature for the production of ^{195m}Pt with high specific activity:

(i) An indirect production route by neutron irradiation of iridium-194 (^{194}Ir) via the ^{194}Ir(n,γ)^{195m}Ir$\xrightarrow{\beta^-}$ ^{195m}Pt nuclear reaction [259].

(ii) Production in an electron linear accelerator by irradiation of a gold sample with Bremsstrahlung, via the ^{197}Au(γ,np)^{195m}Pt photonuclear reaction [298].

Cisplatin, cis-diamminedichloroplatinum (II), is a chemotherapeutic drug that has been used for many years to treat various types of cancer. Cisplatin is known to influence the sensitivity of DNA to ionizing radiation. In fact, impressive response rates have been shown in radiochemotherapy with cisplatin and external irradiation, although with significant toxicity [299]. On the other hand, several *in vitro* and *in vivo* studies have shown that cisplatin labeled with ^{195m}Pt (^{195m}Pt-cisplatin) is more effective than non-radioactive cisplatin in terms of antitumor activity and general toxicity [298, 299].

Table IV.2 summarizes some relevant properties of the AE emitters discussed here above. The data was taken from the ICRP Publication 107 [18].

Radionuclide	^{71}Ge	^{103m}Rh	^{119}Sb	^{125}I
Half-life (day)	11.43	0.039	1.591	59.4
Type of decay (%)	EC (100%)	IT (100%)	EC (100%)	EC (100%)
Daughter nucleus	^{71}Ga (stable)	^{103}Rh (stable)	^{119}Sn (stable)	^{125}Te (stable)
CE (intensity per decay)	–	99.06%	83.97%	94.47%
CE (energy per decay in keV)	–	34.97	16.97	7.28
CE energy range in keV†	–	16.56 – 39.76	19.4 – 23.9	3.7 – 35.5
AE (intensity per decay)	520.5%	587.94%	2368%	2300%
AE (energy per decay in keV)	5.01	2.72	8.86	11.96
AE energy range in keV	0.012 – 10.1	0.034 – 22.28	0.011 – 27.9	0.023 – 30.3
Total electron energy per decay (keV)	5.01	37.69	25.83	19.24
γ or X-ray radiation useful for imaging (energy in keV and % abundance)*	–	–	–	–
Photons (energy per decay in keV)	4.07	1.65	23.14	42.5
Total energy per decay in keV (photons + electrons)	9.08	39.34	48.97	61.74
% of energy emitted as electrons	55.2%	95.8%	52.8%	31.2%
% of energy emitted as photons	44.8%	4.2%	47.2%	68.8%
photon-to-electron energy ratio (p/e)	0.81	0.04	0.90	2.21

† Only AE and CE with probabilities greater than 0.1‰ are considered in this table and in our simulations (see text).
* Photon emissions are considered useful for imaging if their energy is between 70–400 keV, i.e., within the approximate energy range in which SPECT detectors operate. Only photon emissions with an abundance $> 1\%$ are listed in this table.

Table IV.2 Main properties of AE emitters for TRT [18].

Radionuclide	^{161}Ho	^{189m}Os	^{193m}Pt	^{195m}Pt
Half-life (day)	0.103	0.242	4.33	4.02
Type of decay (%)	EC (100%)	IT (100%)	IT (100%)	IT (100%)
Daughter nucleus	^{161}Dy (stable)	^{189}Os (stable)	^{193}Pt (radioactive, $T_{1/2} = 50$ y)	^{195}Pt (stable)
CE (intensity per decay)	83.79%	99.99%	299.22%	277.8%
CE (energy per decay in keV)	20.73	22.35	126.8	161.37
CE energy range in keV†	2.8 – 173.8	17.86 – 30.81	1.1 – 135.5	8.2 – 132.7
AE (intensity per decay)	1363%	624.4%	2739.3%	3655%
AE (energy per decay in keV)	12.88	6.26	10.93	23.12
AE energy range in keV	0.018 – 50.9	0.03 – 10.31	0.038 – 73.81	0.037 – 73.8
Total electron energy per decay (keV)	33.61	28.61	137.73	184.5
γ or X-ray radiation useful for imaging (energy in keV and % abundance)*	103.1 (3.9%) 77.4 (1.9%)	–	76 (1.5%)	129.8 (2.8%) 98.9 (11.4%) 78.1 (1.9%) 76 (8.2%) 75.6 (4.3%)
Photons (energy per decay in keV)	57.98	1.93	12.91	76.77
Total energy per decay in keV (photons + electrons)	91.59	30.54	150.64	261.27
% of energy emitted as electrons	36.7%	93.7%	91.4%	70.6%
% of energy emitted as photons	63.3%	6.3%	8.6%	29.4%
photon-to-electron energy ratio (p/e)	1.72	0.07	0.09	0.42

† Only AE and CE with probabilities greater than 0.1‰ are considered in this table and in our simulations (see text).
* Photon emissions are considered useful for imaging if their energy is between 70–400 keV, i.e., within the approximate energy range in which SPECT detectors operate. Only photon emissions with an abundance $> 1\%$ are listed in this table.

Table IV.2 Main properties of AE emitters for TRT (continued).

IV.6 S-values and absorbed doses in single tumor cells

IV.6.1 Determination of cellular S-values

The S-value is a key physical quantity used in nuclear medicine to evaluate the dosimetric potential of radionuclides. It was introduced in the dosimetry schema of the Committee on Medical Internal Radiation Dose (MIRD). The S-value is closely related to the mean absorbed dose D and is defined as the absorbed dose in a target region r_{T} per nuclear transformation in a source region r_{S}. The S-value can be written as [300]:

$$S(r_{\mathrm{T}} \leftarrow r_{\mathrm{S}}) = \frac{1}{M_{\mathrm{T}}} \sum_i \Delta_i \phi(r_{\mathrm{T}} \leftarrow r_{\mathrm{S}}, E_i) \ , \tag{IV.9}$$

where M_{T} is the mass of the target region r_{T}; Δ_i is the mean energy of the i^{th} transition per nuclear transformation, and $\phi(r_{\mathrm{T}} \leftarrow r_{\mathrm{S}}, E_i)$ is the fraction of radiation energy E_i emitted within the source region r_{S} that is absorbed in the target region r_{T}. Then, according to the MIRD system, the mean absorbed dose $D(r_{\mathrm{T}}, T_{\mathrm{D}})$ to a target region r_{T} over a defined dose-integration period T_{D} is given by [300]:

$$D(r_{\mathrm{T}}, T_{\mathrm{D}}) = \sum_{r_{\mathrm{S}}} \tilde{A}(r_{\mathrm{S}}, T_{\mathrm{D}}) S(r_{\mathrm{T}} \leftarrow r_{\mathrm{S}}) \ , \tag{IV.10}$$

where $\tilde{A}(r_{\mathrm{S}}, T_{\mathrm{D}})$ is the time-integrated activity in the source region r_{S} over the time period T_{D}. It should be noted that the S-value is specific to a radionuclide, but it also depends on the geometry and composition of the source and target regions. Many authors have computed S-values for various β^- and AE emitters uniformly distributed in different cell compartments [19, 40, 301–304].

In the context of this thesis, we computed the cellular S-values for the electron emitters described in Section IV.5 by means of CELLDOSE, an extension of the EPOTRAN code to radiation dosimetry applications. CELLDOSE has been used previously to assess the electron dose distribution for several radionuclides in simple geometries [14, 16, 17], as well as in more complex environments [15].

To compute the cellular S-values in CELLDOSE, we used a simple cell model, similar to the one described in Section III.5, i.e., three concentric spheres representing the nucleus, the cytoplasm and the cell membrane. In our simulations, the cell radius ($\mathrm{R_C}$), nuclear radius ($\mathrm{R_N}$) and membrane thickness were fixed to 7 μm, 5 μm and 10 nm, respectively. Since the cell nucleus is regarded as the critical structure to irradiate in order to induce cell death, only configurations having the nucleus as the target region were considered in this work.

The simulations were performed with electrons having initial energies obtained from the spectrum of each radionuclide, as provided in the ICRP Publication 107 [18]. The whole β^- spectra were taken into account. On the other hand, for CE and AE emissions

the abridged spectra were considered. Moreover, only CE and AE with probabilities greater than 0.1‰ were included in the simulations. This cutoff was chosen for practical purposes and, given the small contribution of the omitted radiations to the overall energy spectrum used in the simulations, it should not have any appreciable impact on our results. Similarly, the photon contribution to the S-values was neglected in CELLDOSE as well as in the results obtained within the MIRD formalism reported hereafter. Indeed, the photon contribution to the S-values is much smaller than that of electrons at the cellular level [19, 40]. In the context of this work, we estimated that the photon contribution would be $\leq 1\%$ of the electron contribution to the S-values.

An algorithm was implemented to construct the cumulative probability distribution for the spectrum of each radionuclide taking into account all the radiations aforementioned. Then, a random sampling was performed over this probability distribution (following the basic principles presented in Chapter I) to obtain the list of electron energies to be simulated in CELLDOSE.

The energy deposited in the target region (cell nucleus) by each primary and secondary electron was scored event-by-event until the electron's energy fell below 7.4 eV (the electronic excitation threshold of the water molecule), in which case the remaining energy was considered as locally absorbed. Then, the S-value (in $\mathrm{Gy\,Bq^{-1}\,s^{-1}}$) was calculated as:

$$S(\mathrm{N} \leftarrow r_\mathrm{S}) = \frac{E(\mathrm{N} \leftarrow r_\mathrm{S})}{\frac{4}{3}\pi N_\mathrm{e} R_N^3 \rho} \,, \tag{IV.11}$$

with $r_\mathrm{S} =$ CS (cell surface), Cy (cytoplasm), N (nucleus), or C (whole cell); $E(\mathrm{N} \leftarrow r_\mathrm{S})$ is the total energy deposited in the nucleus from a radioactive source uniformly distributed in the source region r_S; N_e is the number of nuclear transformations (equal to the number of primary electrons specified at the beginning of the simulation); and ρ is the density of the target. In general, all cell compartments were modeled by water with a density $\rho = 1.0\,\mathrm{g\,cm^{-3}}$, except when we carried out a test to study the effect of changing the composition of the nucleus, as explained hereafter (see Section IV.6.3). Furthermore, we considered either of the following specific distributions of the radionuclide: only on the cell surface (CS); only in the cytoplasm (Cy); only within the nucleus (N); a uniform distribution in the whole cell (C). Each simulation consisted of 1×10^6 decays of the selected radionuclide. This number of decays was big enough to reduce the statistical fluctuations to $\sim$1%, while keeping a reasonable computation time.

It is worth mentioning that the S-values provided by CELLDOSE are multiplied by a renormalization factor given as the ratio of the mean energy released by decay divided by the mean energy of the radiations randomly sampled from the radionuclide's spectrum. The need for renormalization is a consequence of the way the random sampling of radiations is performed: only one electron energy is selected by decay, when in reality

more than one electron may be emitted following a radioactive decay.

Table IV.3 presents the cellular S-values obtained for the different electron emitters considered here. With the purpose of validating our results to the extent possible, we have compared our S-values with other calculations reported in the literature, when available. Table IV.3 shows this comparison for most of the radionuclides studied here, with the exception of ^{161}Tb, ^{71}Ge, ^{161}Ho and ^{189m}Os, for which no equivalent data was found. We have included in Table IV.3 the cellular S-values obtained using the software MIRDcell [39], version 2.1 (`http://mirdcell.njms.rutgers.edu/`). In addition, for ^{119}Sb, ^{125}I and ^{195m}Pt, we have reported as well the calculations performed by Falzone *et al*. [40]. In general, an excellent agreement is observed with the work of Falzone *et al*. [40], with a maximum difference of -4.2% found for a cell surface distribution of ^{125}I. The remarkable agreement with the results of Falzone *et al*. [40] is likely due to the use of a similar methodology, that is, S-values obtained from event-by-event MC simulations (the PENELOPE code in their case). Moreover, very similar (if not exactly the same) spectra were employed in both cases [40]. In contrast, much more significant differences (up to about 42%) are found when comparing our results with those provided by MIRDcell [39], notably for cell surface and intracytoplasmic distributions of ^{103m}Rh, ^{125}I and ^{193m}Pt. In this context, it is important to remind that MIRDcell [39] is based on the well-known analytical method of the MIRD (see Eqs. IV.9 and IV.10), as used for instance by Goddu *et al*. [19]. The MIRD approach is known to have some limitations, such as the neglect of energy straggling and δ-ray transport, which become increasingly important at the sub-cellular level [305]. It is generally accepted that MCTS codes are able to overcome such limitations and are therefore expected to provide more accurate cellular S-values. Furthermore, the developers of MIRDcell themselves mention that the S-values computed with this software can vary significantly from those calculated with MC codes for low-energy electron emitters such as ^{125}I [39]. In fact, several authors have pointed out the inconsistencies between the S-values computed with different MC codes and those published by the MIRD [40, 301, 306, 307], particularly when the radiation source is far from the target region, as is the case for cell surface and intracytoplasmic distributions of the radionuclide.

Finally, let us note that in CELLDOSE (and as far as we know in all other S-values calculations for electron emitters found in the literature), the kinetic energy of the recoil nuclei in all the radioactive decay modes considered thus far is neglected. This energy is extremely small for most practical purposes. Some authors suggest, however, that in some cases the energy of the recoil nucleus in a β^- decay might be of interest to determine the local damage to biological materials [246]. While that might be the case for DNA damage studies, i.e., at the nanometer scale, we consider that in the context of the present work the energy of the recoil nuclei can be safely ignored.

Radionuclide	Reference	Cellular S-values [Gy Bq^{-1} s^{-1}] (% difference)†			
		$S(\mathrm{N} \leftarrow \mathrm{CS})$	$S(\mathrm{N} \leftarrow \mathrm{Cy})$	$S(\mathrm{N} \leftarrow \mathrm{N})$	$S(\mathrm{N} \leftarrow \mathrm{C})$
^{131}I	This work	1.52×10^{-4}	2.31×10^{-4}	6.70×10^{-4}	4.07×10^{-4}
	MIRDcell	1.38×10^{-4} (-9.2)	2.08×10^{-4} (-10.0)	6.81×10^{-4} (+1.6)	–
^{90}Y	This work	6.11×10^{-5}	9.10×10^{-5}	2.37×10^{-4}	1.44×10^{-4}
	MIRDcell	6.15×10^{-5} (+0.7)	9.09×10^{-5} (-0.1)	2.54×10^{-4} (+7.2)	–
^{177}Lu	This work	1.98×10^{-4}	3.09×10^{-4}	1.11×10^{-3}	6.02×10^{-4}
	MIRDcell	1.72×10^{-4} (-13.1)	2.78×10^{-4} (-10.0)	1.05×10^{-3} (-5.4)	–
^{161}Tb	This work	7.00×10^{-4}	1.17×10^{-3}	5.41×10^{-3}	2.75×10^{-3}
^{71}Ge	This work	2.78×10^{-7}	8.91×10^{-5}	1.37×10^{-3}	5.56×10^{-4}
^{103m}Rh	This work	3.88×10^{-4}	5.60×10^{-4}	2.07×10^{-3}	1.11×10^{-3}
	MIRDcell	3.04×10^{-4} (-21.7)	4.51×10^{-4} (-19.5)	1.90×10^{-3} (-8.2)	–

† The values in parentheses indicate the percentage difference with respect to this work, computed as: [S-value(other)−S-value(CELLDOSE)]/S-value(CELLDOSE)×100.

Table IV.3 Cellular S-values for β^- and AE emitters. The results of this work are for a cell with $R_C = 7\,\mu$m, $R_N = 5\,\mu$m and considering a membrane thickness of 10 nm. Our cellular S-values are compared with those computed with MIRDcell [39] and the ones reported by Falzone *et al.* [40].

Radionuclide	Reference	Cellular S-values [Gy Bq^{-1} s^{-1}] (% difference)†			
		$S(\mathrm{N} \leftarrow \mathrm{CS})$	$S(\mathrm{N} \leftarrow \mathrm{Cy})$	$S(\mathrm{N} \leftarrow \mathrm{N})$	$S(\mathrm{N} \leftarrow \mathrm{C})$
^{119}Sb	This work	6.22×10^{-4}	9.87×10^{-4}	4.25×10^{-3}	2.17×10^{-3}
	MIRDcell	5.63×10^{-4} (-9.5)	8.06×10^{-4} (-18.3)	3.67×10^{-3} (-13.7)	–
	Falzone *et al.*	6.27×10^{-4} (+0.8)	9.83×10^{-4} (-0.4)	4.23×10^{-3} (-0.5)	–
^{125}I	This work	2.14×10^{-4}	3.31×10^{-4}	3.64×10^{-3}	1.55×10^{-3}
	MIRDcell	1.42×10^{-4} (-33.6)	2.50×10^{-4} (-24.5)	3.50×10^{-3} (-3.9)	–
	Falzone *et al.*	2.05×10^{-4} (-4.2)	3.22×10^{-4} (-2.7)	3.64×10^{-3} (0.0)	–
^{161}Ho	This work	4.37×10^{-4}	8.05×10^{-4}	5.09×10^{-3}	2.37×10^{-3}
^{189m}Os	This work	6.14×10^{-4}	1.00×10^{-3}	4.05×10^{-3}	2.11×10^{-3}
^{193m}Pt	This work	1.69×10^{-4}	6.26×10^{-4}	6.22×10^{-3}	2.66×10^{-3}
	MIRDcell	2.40×10^{-4} (+42.0)	7.46×10^{-4} (+19.2)	6.12×10^{-3} (-1.6)	–
^{195m}Pt	This work	1.06×10^{-3}	1.95×10^{-3}	1.04×10^{-2}	5.05×10^{-3}
	MIRDcell	1.05×10^{-3} (-0.9)	1.85×10^{-3} (-5.1)	9.57×10^{-3} (-8.0)	–
	Falzone *et al.*	1.08×10^{-3} (+1.9)	2.00×10^{-3} (+2.6)	1.05×10^{-2} (+1.0)	–

† The values in parentheses indicate the percentage difference with respect to this work, computed as: [S-value(other)−S-value(CELLDOSE)]/S-value(CELLDOSE)×100.

Table IV.3 Cellular S-values for β^- and AE emitters. The results of this work are for a cell with $R_C = 7\,\mu$m, $R_N = 5\,\mu$m and considering a membrane thickness of 10 nm. Our cellular S-values are compared with those computed with MIRDcell [39] and the ones reported by Falzone *et al.* [40] (continued).

IV.6.2 Normalized absorbed doses to the nucleus of a single tumor cell

Because the radionuclides do not have the same energy per decay (see Tables IV.1 and IV.2), the absorbed doses to the nucleus of a single tumor cell were normalized assuming that 1 MeV was released per μm^3 [16, 17]. This assumption means that for our cell of 1436 μm^3 volume, 1436 MeV were released from one of the regions of interest defined above. The normalized absorbed doses to the nucleus of a single tumor cell for different distributions of the β^- and AE emitters investigated in this work are shown in Table IV.4 and Figure IV.5.

Radionuclide	Normalized absorbed dose [Gy] (enhancement factor over ^{177}Lu)			
	Cell surface	Intracytoplasmic	Intranuclear	Whole cell
^{131}I	1.13 (0.6)	1.73 (0.6)	5.02 (0.5)	3.05 (0.5)
^{90}Y	0.09 (0.05)	0.14 (0.05)	0.36 (0.03)	0.22 (0.04)
^{177}Lu	1.92	3.00	10.7	5.80
^{161}Tb	4.96 (2.6)	8.30 (2.8)	38.6 (3.6)	19.5 (3.4)
^{71}Ge	0.08 (0.04)	25.5 (8.5)	393 (36.7)	159 (27.4)
^{103m}Rh	14.8 (7.7)	21.3 (7.1)	78.9 (7.4)	42.3 (7.3)
^{119}Sb	34.6 (18.0)	54.9 (18.3)	236 (22.1)	121 (20.9)
^{125}I	16.0 (8.3)	24.7 (8.2)	272 (25.4)	116 (20.0)
^{161}Ho	18.7 (9.7)	34.4 (11.5)	218 (20.4)	101 (17.4)
^{189m}Os	30.8 (16.0)	50.2 (16.7)	204 (19.1)	106 (18.3)
^{193m}Pt	1.77 (0.9)	6.53 (2.2)	64.9 (6.1)	27.7 (4.8)
^{195m}Pt	8.25 (4.3)	15.2 (5.1)	81.0 (7.6)	39.3 (6.8)

Table IV.4 Normalized absorbed doses to the nucleus of a single tumor cell for different distributions of β^- and AE emitters. The values in parentheses indicate the enhancement factor with respect to ^{177}Lu, i.e., the ratio Dose(radionulide)/Dose(^{177}Lu). The results are for a cell with $R_C = 7\,\mu m$, $R_N = 5\,\mu m$ and considering a membrane thickness of 10 nm.

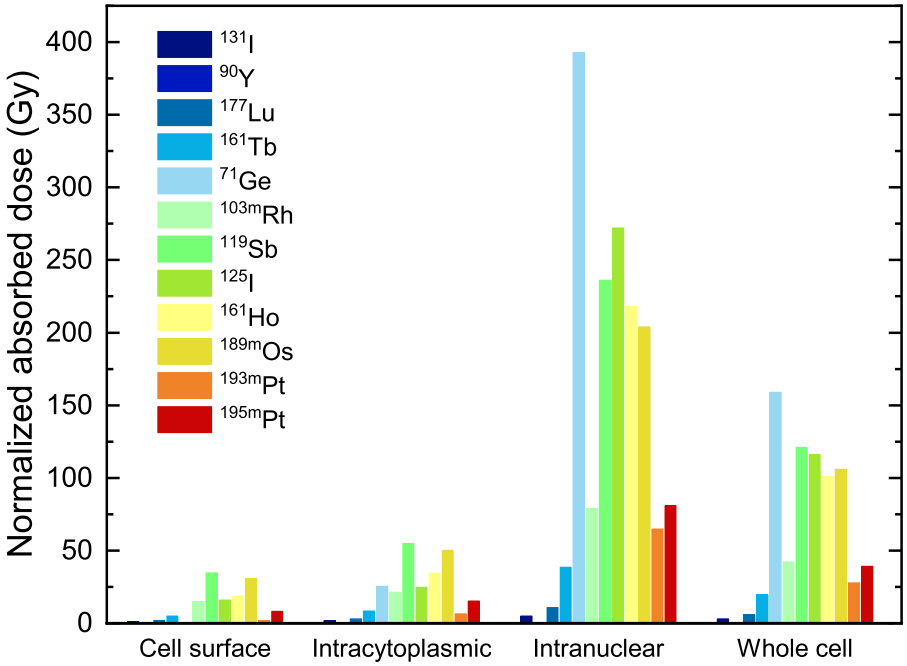

Figure IV.5 Normalized absorbed doses to the nucleus of a single tumor cell for different distributions of β^- and AE emitters.

A common feature for all the radionuclides investigated here is that the normalized absorbed dose to the nucleus of the single cell is lowest when the radionuclide is located on the cell surface, and highest when it is incorporated in the nucleus itself.

In the case of the β^- emitters, the comparison of the normalized absorbed dose for ^{177}Lu and ^{161}Tb is of particular importance, because in recent years it has been suggested that the latter radionuclide may be better than the former for irradiating very small tumors (see Section IV.5.1.4). The results presented in Table IV.4 show that ^{161}Tb delivers higher doses than ^{177}Lu to single tumor cells. Indeed, it can be seen that the dose delivered by ^{161}Tb is always higher than the dose delivered by ^{177}Lu, regardless of the distribution of the radionuclide. Moreover, the comparison between the two radionuclides can be made by computing the enhancement factor, i.e., the normalized absorbed dose ratio ^{161}Tb/^{177}Lu. The enhancement factor is 2.6 in the case of cell surface location and increases up to 3.6 for intranuclear location [245] (see Table IV.4). It is also clear that the normalized absorbed doses for ^{131}I and ^{90}Y are much lower than for either ^{177}Lu or ^{161}Tb, which is in agreement with the prediction that ^{131}I and ^{90}Y are better for irradiating large tumors than single tumor cells or micrometastases.

Regarding the AE emitters, the results show that ^{119}Sb and ^{189m}Os are excellent candidates for single cell irradiation, regardless of the location of the radiolabeled molecule within the cell. In fact, these two radionuclides seem to be much better suited for eradicating single tumor cells than either ^{161}Tb or ^{177}Lu, as it is deduced from the normalized absorbed doses shown in Table IV.4. Indeed, it can be observed that

the maximum enhancement factors for these radionuclides with respect to ^{177}Lu are ^{119}Sb/^{177}Lu = 22.1 and ^{189m}Os/^{177}Lu = 19.1, found for an intranuclear distribution; similarly, when compared to ^{161}Tb, the maximum enhancement factors (not shown in Table IV.4) are ^{119}Sb/^{161}Tb = 7.0 and ^{189m}Os/^{161}Tb = 6.2, obtained for cell surface location. Furthermore, ^{125}I and ^{161}Ho would be as effective as ^{119}Sb and ^{189m}Os when located inside the nucleus, but their performance would be lower when located in the cytoplasm or on the cell surface. Finally, the normalized absorbed dose provided by ^{71}Ge is quite remarkable for an intranuclear or an uniform whole cell distribution of the radionuclide, but a sharp decrease in the normalized absorbed dose is observed in the case of intracytoplasmic or cell surface location (see Figure IV.5).

IV.6.3 Influence on dose of the nucleus composition

In order to test how relevant the description of the biological medium may be for the radiation dosimetry calculations presented here, we assessed the impact on the normalized absorbed dose of changing the composition of the nucleus. We proceeded in a similar fashion as for the case described in Section III.5 for protons, that is, the nucleus was modeled as composed of water ($\rho = 1.0\,\mathrm{g\,cm^{-3}}$), density-rescaled water ($\rho = 1.29\,\mathrm{g\,cm^{-3}}$), or hydrated DNA ($\rho = 1.29\,\mathrm{g\,cm^{-3}}$). The results for the different radionuclides, distributions and nucleus compositions are reported in Table IV.5.

The first thing to note is that for all radionuclide distributions the normalized absorbed doses in water are generally higher than in density-rescaled water and hydrated DNA. This is in agreement with our previous observation (see Section III.5) that modeling the cell nucleus as only water may lead to an overestimation of the absorbed dose. In some cases, however, this trend is somewhat lost (see for instance the values reported in Table IV.5 for ^{131}I and ^{90}Y). The latter is probably due to statistical uncertainties affecting very small doses.

The difference between the media was then studied in terms of the nuclear dose ratio of water to hydrated DNA, $\mathrm{D_{H_2O,1.0}}/\mathrm{D_{DNA,1.29}}$, and that of density-rescaled water to hydrated DNA, $\mathrm{D_{H_2O,1.29}}/\mathrm{D_{DNA,1.29}}$ (data not shown). Based on these ratios, we derive the following conclusions:

- For both ratios, the relative differences between the normalized absorbed doses computed for different nucleus compositions depend on the radionuclide and therefore on the energy of the radiations included in the spectrum.
- For a given radionuclide, larger differences were found for $\mathrm{D_{H_2O,1.0}}/\mathrm{D_{DNA,1.29}}$ than for $\mathrm{D_{H_2O,1.29}}/\mathrm{D_{DNA,1.29}}$.

Radionuclide	Normalized absorbed dose (Gy)					
	Cell surface			Intracytoplasmic		
	H_2O 1.0 g cm^{-3}	H_2O 1.29 g cm^{-3}	DNA 1.29 g cm^{-3}	H_2O 1.0 g cm^{-3}	H_2O 1.29 g cm^{-3}	DNA 1.29 g cm^{-3}
^{131}I	1.13	1.13	1.05	1.73	1.72	1.60
^{90}Y	0.09	0.10	0.09	0.14	0.14	0.14
^{177}Lu	1.92	1.80	1.67	3.00	2.84	2.64
^{161}Tb	4.96	4.25	3.99	8.30	7.19	6.76
^{71}Ge	0.08	0.07	0.07	25.5	20.2	19.8
^{103m}Rh	14.8	14.0	12.8	21.3	20.7	18.8
^{119}Sb	34.6	26.9	26.4	54.9	46.5	44.6
^{125}I	16.0	13.8	12.8	24.7	22.5	21.1
^{161}Ho	18.7	15.2	14.6	34.4	29.2	28.4
^{189m}Os	30.8	25.2	24.3	50.2	43.6	41.9
^{193m}Pt	1.77	1.67	1.55	6.53	5.58	5.43
^{195m}Pt	8.25	6.80	6.52	15.2	13.2	12.9
	Intranuclear			Whole cell		
^{131}I	5.02	5.17	4.92	3.05	2.97	2.81
^{90}Y	0.36	0.37	0.35	0.22	0.22	0.22
^{177}Lu	10.7	10.0	9.58	5.80	5.43	5.15
^{161}Tb	38.6	33.8	32.9	19.5	16.9	16.4
^{71}Ge	393	314	313	159	128	127
^{103m}Rh	78.9	72.0	68.9	42.3	39.4	37.0
^{119}Sb	236	211	205	121	106	103
^{125}I	272	224	222	116	95.8	94.2
^{161}Ho	218	185	181	101	86.1	84.2
^{189m}Os	204	183	176	106	94.5	90.4
^{193m}Pt	64.9	53.0	52.6	27.7	22.9	22.7
^{195m}Pt	81.0	70.3	68.7	39.3	33.8	32.9

Table IV.5 Normalized absorbed doses to the nucleus of a single tumor cell for different distributions of β^- and AE emitters and three different nucleus compositions: water with a density of 1.0 g cm^{-3}; water with the density rescaled to 1.29 g cm^{-3}; and hydrated DNA with a density of 1.29 g cm^{-3}. The results are for a cell with $R_C = 7\,\mu$m, $R_N = 5\,\mu$m and considering a membrane thickness of 10 nm.

- The normalized absorbed dose in water may overestimate the one in hydrated DNA by a few percent up to about $\sim$31%. The maximum relative difference was observed for a cell surface distribution of ^{119}Sb.
- The normalized absorbed doses computed for density-rescaled water are less than 11% higher than the ones obtained for hydrated DNA.

Regarding the last point mentioned above, it is interesting to see that, for this particular study, modeling the biological medium as water with a density rescaled to $1.29\,\mathrm{g\,cm^{-3}}$ instead of hydrated DNA seems to have a minor impact on the absorbed dose than for the proton irradiation simulations described in Chapter III. In the latter case, however, monoenergetic protons were considered, while in the present study we simulated electrons having distinct energies taken from the spectrum of each radionuclide. In addition, let us remind that the precise composition of the biological medium may have a major importance for describing the energy deposited by radiations at the nanometer level. Therefore, the results reported in this section should be taken with caution.

IV.7 Cell cluster

To go beyond the single cell case, we investigated as well the irradiation of micrometastases by considering a small cluster of tumor cells. The cluster consisted of a total of 19 cells: i) one central cell; ii) 6 cells forming the first neighborhood, i.e., in direct contact with the central cell; iii) 12 cells forming the second neighborhood. Each cell of the cluster has the same dimensions as the single tumor cell described in the previous section (see Figure IV.6a).

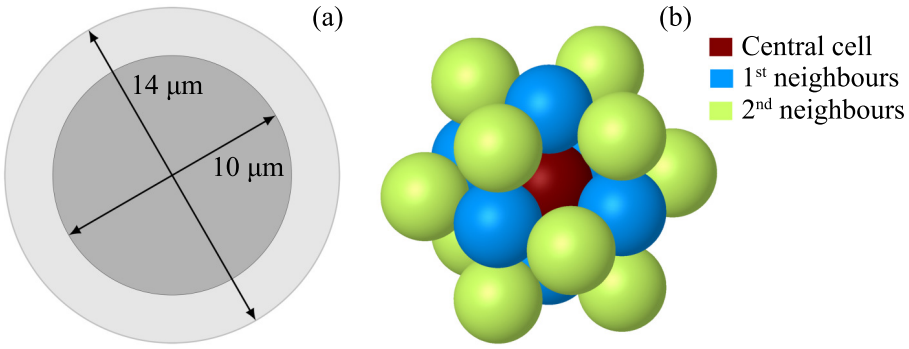

Figure IV.6 (a) Single cell of 14 μm diameter with a nucleus of 10 μm diameter and a total volume of 1436 μm^3; (b) Cell cluster as modeled in this work.

Moreover, all cells were assumed to be labeled in the same way, i.e., to contain a uniform distribution of the radionuclide in one of the specific regions of interest defined above (cell surface; or cytoplasm; or nucleus; or the whole cell). The cells were arranged according to a simple cubic structure model, as depicted in Figure IV.6b. Thus, the distance from the center of the central cell to the center of any cell in the first and second neighborhoods is 14 μm and 19.8 μm, respectively. The maximum diameter of the cluster is 53.6 μm (2 $\times$ 19.8 μm + 14 μm). Similarly to the single tumor cell case, the normalized absorbed doses were obtained assuming that 1 MeV was released per μm^3, i.e., 1436 MeV released per cell. Besides, the intercellular space was assumed to contain no activity and was modeled as water. Given the symmetry of the system, the normalized absorbed dose to a cell in a given neighborhood is representative of the dose received by the other cells of that neighborhood. We assessed the radiation dose to the nucleus of the central cell, as well as to the nuclei of the cells belonging to the first and second neighborhoods. The results for the central cell are presented in detail in Table IV.6, in which we show the self-dose, the cross-dose from the cells in the first and second neighborhoods, and the total dose. Moreover, we have indicated in parentheses the relative contribution of the self-dose to the total dose. The total (normalized) absorbed doses to the nucleus of the central cell are depicted as well in Figure IV.7.

Radionuclide	Normalized absorbed dose [Gy] (% contribution of the self-dose)							
	Cell surface				Intracytoplasmic			
	Self-dose	Neighborhood		Total	Self-dose	Neighborhood		Total
		1st	2nd			1st	2nd	
^{131}I	1.13	1.77	1.53	4.44 (25.5)	1.73	1.70	1.54	4.97 (35.3)
^{90}Y	0.09	0.14	0.13	0.36 (25)	0.14	0.15	0.13	0.42 (33.3)
^{177}Lu	1.92	2.82	2.50	7.20 (26.7)	3.00	2.74	2.52	8.30 (36.3)
^{161}Tb	4.96	5.46	4.63	15.1 (32.8)	8.30	5.04	4.54	17.9 (46.4)
^{103m}Rh	14.8	26.8	22.5	64.1 (23.1)	21.3	26.6	22.1	70.0 (30.4)
^{119}Sb	34.6	15.2	0.33	50.1 (69.1)	54.9	10.7	0.56	66.2 (82.9)
^{125}I	16.0	14.8	4.26	35.1 (45.6)	24.7	14.7	3.55	43.0 (57.5)
^{161}Ho	18.7	11.5	4.32	34.5 (54.2)	34.4	9.61	4.27	48.3 (71.2)
^{189m}Os	30.8	19.1	3.31	53.2 (57.9)	50.2	16.6	2.51	69.3 (72.5)
^{193m}Pt	1.77	2.27	2.27	6.32 (28.0)	6.53	2.19	2.30	11.0 (59.2)
^{195m}Pt	8.25	5.53	2.72	16.5 (50.0)	15.2	4.68	2.57	22.4 (67.7)
	Intranuclear				Whole cell			
	Self-dose	Neighborhood		Total	Self-dose	Neighborhood		Total
		1st	2nd			1st	2nd	
^{131}I	5.02	1.89	1.53	8.44 (59.5)	3.05	1.68	1.48	6.21 (49.1)
^{90}Y	0.36	0.14	0.13	0.63 (57.9)	0.22	0.14	0.13	0.49 (45.3)
^{177}Lu	10.7	2.60	2.41	15.7 (68.1)	5.80	2.66	2.52	11.0 (52.8)
^{161}Tb	38.6	4.55	4.69	47.8 (80.7)	19.5	4.96	4.61	29.1 (67.1)
^{103m}Rh	78.9	26.7	22.5	128 (61.6)	42.3	26.7	22.5	91.5 (46.3)
^{119}Sb	236	5.00	0.00	241 (97.9)	121	9.48	0.00	130 (93.1)
^{125}I	272	10.9	2.97	286 (95.1)	116	11.9	3.10	131 (88.5)
^{161}Ho	218	6.42	4.28	229 (95.2)	101	8.52	3.84	113 (89.4)
^{189m}Os	204	11.6	1.51	217 (94.0)	106	15.1	2.01	123 (86.1)
^{193m}Pt	64.9	2.07	2.15	69.1 (93.9)	27.7	2.25	2.12	32.1 (86.4)
^{195m}Pt	81.0	3.89	2.34	87.2 (92.9)	39.3	4.36	2.57	46.2 (85.1)

Table IV.6 Normalized absorbed doses to the nucleus of the central cell in a cluster for different distributions of β^- and AE emitters. We report the self-dose, the cross-dose induced by each neighborhood and the total dose, i.e., self-dose + cross-dose. The values in parentheses indicate the self-dose contribution to the total dose.

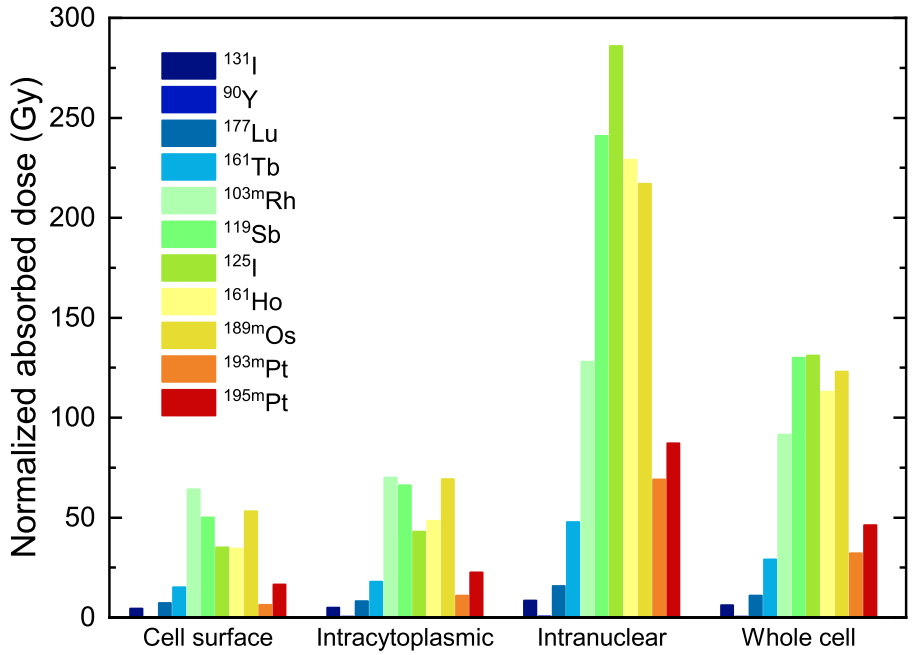

Figure IV.7 Normalized absorbed doses to the nucleus of the central cell in a cluster for different distributions of β^- and AE emitters.

Let us remind that in this study we chose a cell cluster in which the cells are arranged in a simple cubic lattice. However, if only one neighborhood is considered in a compact model, up to 12 cells may be placed in contact with the central cell, and in this case, the cross-doses from this first neighborhood would be twice as high as the values reported in Table IV.6.

Furthermore, let us note that ^{71}Ge was omitted in the cell cluster calculations because the cross-dose contribution to the normalized absorbed dose is negligible for this radionuclide. Indeed, it can be observed from Table IV.4 that the normalized absorbed dose to the nucleus of a single cell is already very low for a cell surface distribution of the radionuclide. Therefore, the effect on the normalized absorbed dose (to the nucleus of the central cell) of adding the neighboring cells will be insignificant. Interestingly, in spite of the dose enhancement observed for the other electron emitters with the addition of labeled neighboring cells, none of them is able to perform better than ^{71}Ge in the case of intranuclear and whole cell distribution of the radionuclide. Thus, ^{71}Ge has an exceptional cytotoxic potential if nuclear incorporation of the radionuclide were feasible, but its net therapeutic effect will depend as well on the homogeneous uptake of the radiopharmaceutical by all tumor cells.

It is evident from Table IV.6 that the addition of the 18 neighboring cells increases the normalized absorbed dose to the nucleus of the central cell. Moreover, for a given radionuclide the exact dose enhancement depends on the radionuclide distribution within the cells surrounding the target. For all radionuclides, the dose enhancement is

more pronounced in the case of cell surface distribution.

As expected, for β^- emitters the second neighborhood still adds a significant contribution to the normalized absorbed dose (it essentially increases the cross-dose by a factor ~2 for all radionuclide distributions). This is due to the relative high energy and long range of the β^- particles emitted by such radionuclides. As previously mentioned, β^- emitters are best suited for irradiating large tumors, therefore their cross-dose will be relevant for many layers of cells. On the other hand, ^{161}Tb differs from the rest of the β^- emitters studied here in that it emits a high number of low-energy CE and AE, which increase the local dose. For this reason, the doses delivered by ^{161}Tb are consistently higher than those delivered by ^{177}Lu. More specifically, the enhancement factor ^{161}Tb/^{177}Lu is 2.1 in case of cell surface distribution and increases up to 3.0 in case of intranuclear location. Furthermore, the self-dose component offered by the low-energy electrons of ^{161}Tb may be interesting even for treating large tumors, known for their heterogeneity, by providing a local boost to labeled tumor cells. These findings support the view that ^{161}Tb may be a better choice than the currently used ^{177}Lu for irradiating single tumor cells and micrometastases, as we recently reported in Ref. [245].

Regarding the AE emitters, the specific contribution of the second neighborhood to the normalized absorbed dose varies substantially depending on the radionuclide. In most cases this contribution is much lower than that of the first neighborhood. That is the case for ^{119}Sb and ^{189m}Os. In fact, for ^{119}Sb the second neighborhood does not contribute at all to the normalized absorbed dose when the radionuclide is located in the nucleus or uniformly distributed in the whole cell. Compared to ^{119}Sb and ^{189m}Os, the cross-dose provided by the second neighborhood is somewhat higher for ^{125}I, ^{161}Ho and ^{195m}Pt. Finally, for ^{103m}Rh and ^{193m}Pt the contribution of the second neighborhood is almost equal to that of the first neighborhood. Nevertheless, in absolute terms ^{193m}Pt provides much lower normalized absorbed doses than ^{103m}Rh: 6.3 Gy vs. 64.1 Gy for cell surface distribution; 11.0 Gy vs. 70.0 Gy for intracytoplasmic distribution; 69.1 Gy vs. 128 Gy for intranuclear location; and 32.1 Gy vs. 91.5 Gy in case of uniform whole cell distribution, as shown in Table IV.6.

Finally, Table IV.7 shows the results for the neighboring cells. It can be seen that the relative contribution of the self-dose (shown in parentheses in Tables IV.6 and IV.7) to the total dose increases as we move from the central cell to the first and second neighborhoods. It also increases as we move from a cell surface distribution to an intranuclear distribution of the radionuclide.

Radionuclide	Normalized absorbed dose [Gy] (% contribution of the self-dose)			
	Cell surface		Intracytoplasmic	
	Neighborhood		Neighborhood	
	1st	2nd	1st	2nd
^{131}I	3.60 (31.4)	2.93 (38.6)	4.23 (40.9)	3.50 (49.4)
^{90}Y	0.30 (29.8)	0.24 (37.0)	0.36 (39.1)	0.30 (47.3)
^{177}Lu	6.04 (31.8)	4.75 (40.4)	7.02 (42.7)	5.82 (51.5)
^{161}Tb	12.40 (40.0)	9.8 (50.6)	15.3 (54.2)	12.9 (64.6)
^{103m}Rh	47.7 (31.0)	34.9 (42.4)	53.6 (39.7)	40.9 (52.1)
^{119}Sb	47.4 (73.1)	39.8 (87.0)	64.2 (85.5)	58.6 (93.7)
^{125}I	30.0 (53.3)	22.8 (70.2)	37.2 (66.4)	31.2 (79.2)
^{161}Ho	31.0 (60.3)	25.4 (73.6)	44.8 (76.8)	40.3 (85.4)
^{189m}Os	47.9 (64.3)	38.2 (80.6)	64.8 (77.5)	56.7 (88.5)
^{193m}Pt	5.35 (33.1)	4.43 (40.0)	10.1 (64.7)	9.18 (71.2)
^{195m}Pt	14.7 (56.1)	12.1 (68.2)	21.1 (72.0)	18.9 (80.4)
	Intranuclear		Whole cell	
	Neighborhood		Neighborhood	
	1st	2nd	1st	2nd
^{131}I	7.72 (65.0)	7.03 (71.4)	5.51 (55.3)	4.78 (63.8)
^{90}Y	0.58 (63.3)	0.52 (69.9)	0.44 (50.7)	0.38 (58.8)
^{177}Lu	14.6 (73.5)	13.5 (79.6)	9.73 (59.6)	8.57 (67.7)
^{161}Tb	45.2 (85.4)	43.1 (89.6)	26.4 (73.8)	24.1 (81.1)
^{103m}Rh	111 (71.1)	98.0 (80.5)	74.6 (56.7)	61.6 (68.7)
^{119}Sb	241 (97.9)	239 (98.7)	129 (93.8)	124 (97.6)
^{125}I	282 (96.5)	277 (98.2)	127 (91.3)	121 (95.9)
^{161}Ho	225 (96.9)	222 (98.2)	110 (91.8)	106 (95.3)
^{189m}Os	214 (95.3)	209 (97.6)	119 (89.1)	112 (94.6)
^{193m}Pt	68.3 (95.0)	67.4 (96.3)	31.2 (88.8)	30.3 (91.4)
^{195m}Pt	85.9 (94.3)	84.6 (95.7)	44.7 (87.9)	42.8 (91.8)

Table IV.7 Total (normalized) absorbed dose to the nucleus of any cell of the 1st and 2nd neighborhoods for different distributions of β^- and AE emitters.

Conclusions

We have reported in this chapter our radiation dosimetry simulations for evaluating some interesting electron emitters for TRT. The evaluation of the therapeutic potential of the radionuclides has been carried out in terms of cellular S-values and normalized absorbed doses to the nucleus of a single tumor cell and to the nuclei of the cells in a small cluster, representing a micrometastasis.

According to our findings, some of the investigated AE emitters would be ideal for the irradiation of single tumor cells, particularly ^{119}Sb and ^{189m}Os. Other AE emitters may also be appropriate for killing single tumor cells, provided that the radionuclide can be incorporated into the cell nucleus. That is the case for instance of ^{71}Ge, ^{125}I and ^{161}Ho. Other electron emitters, such as ^{103m}Rh and ^{161}Tb, would be able to deliver high doses to the targeted cells, but also a significant cross-dose to their immediate neighbors.

The results reported here are strongly influenced by the cell model chosen, and calculations performed with other cell dimensions and geometries will almost certainly yield different values. However, we believe that in a qualitative sense the observations made about the therapeutic potential of the various radionuclides for the treatment of small tumors and micrometastases will remain valid.

On the other hand, it should be reminded that all our results are based on the emission spectra provided by the ICRP Publication 107 [18]. Nevertheless, the urgent need for more accurate and complete data regarding the nuclear decay and AE emission of some radionuclides suitable for medical applications has been stressed by experts in recent international meetings, with clearly defined requirements to be fulfilled in the next years [278, 308, 309]. In particular, for the radionuclides studied in this work, the need for new measurements is being assessed for ^{161}Tb and has already been established for ^{195m}Pt, ^{193m}Pt, ^{119}Sb, ^{103m}Rh and ^{71}Ge [278]. For AE emitters, published spectra differ significantly in the yields and energies of the outer-shell transitions [309, 310]. Therefore, the improvement of the emission spectra resulting from new experimental data will be most welcomed and will probably have an important impact on radiation dosimetry calculations, especially at the nanoscale for AE emitters.

CHAPTER V

RADIATION DOSIMETRY OF α-PARTICLE EMITTERS

Contents

V.1 Introduction **147**

V.2 Track parameters for α-particles transport in water **149**

V.2.1 Stopping power 149

V.2.2 Range 153

V.3 The α decay process **154**

V.4 α-particle emitting radionuclides for TRT **155**

V.4.1 ^{211}At 155

V.4.2 ^{212}Pb/^{212}Bi 158

V.4.3 ^{213}Bi 159

V.4.4 ^{223}Ra 161

V.4.5 ^{225}Ac 162

V.4.6 ^{227}Th 164

V.5 Cellular S-values for α-particle emitters **168**

Conclusions **175**

V.1 Introduction

We discussed in Chapter IV the use of electron emitters in TRT. An alternative (or complementary) line of research has focused on investigating the therapeutic potential of α-particle emitters for TRT, an approach known as targeted alpha therapy (TAT).

α-particles are doubly ionized helium atoms ($^4_2He^{2+}$) that in radioactive decays are emitted with kinetic energies of about 4–10 MeV. These α-particles have much higher LET ($\sim$50–250 keVμm^{-1}, depending on the particle energy) in comparison to other radiations. For example, 2 keVμm^{-1} for 250 kVp X-rays, 4.7 keVμm^{-1} for 10 MeV photons, or $\approx$ 0.2 keVμm^{-1} for β^--particles emitted by ^{90}Y, ^{131}I and ^{177}Lu [311]. Consequently, α-particles travel short distances, depositing all their energy within a few cell diameters ($\sim$30–100 μm). Thus, α-particles are very effective at inducing complex DNA damages difficult to be repaired by irradiated cells [312]. Moreover, the cytotoxic effects associated with α-particles are independent of oxygen concentration in the tumor, a clear advantage that TAT offers over other therapies (chemotherapy, external beam radiation therapy or even TRT with β^- emitters), which often fail to treat poorly oxygenated (hypoxic) tumor regions [313]. In addition, the range of α-particles is short enough to kill tumor cells, while sparing the surrounding healthy tissue. The latter naturally implies that appropriate targeting of the radionuclide is needed to ensure that the radioactive decays will take place near the tumor cells.

It is worth mentioning that both α-particles and AE are high LET radiations. Nevertheless, compared to AE, α-particles have greater path lengths and are able to traverse several cells before stopping. Thus, α-particles may reach the tumor cell nucleus and then induce DNA damages even if they are emitted outside the tumor cell. Consequently, cell internalization and nuclear incorporation of the radionuclide is not necessary for tumor cell killing in TAT [314].

The idea of using α-particles in medical applications, and particularly in TRT, has been investigated for many years. However, only a few α-particle emitting radionuclides have been tested in preclinical and clinical trials. Currently, the major challenges faced by the scientific community to achieve routine clinical use of TAT are:

- Limited supply and high cost of the radionuclides. The techniques and equipment required to produce most of the α-particle emitters of interest are only available in a few facilities around the world. New and better production routes, as well as purification strategies, must be conceived for obtaining the activities required in the clinical setting [315]. Other hurdles in this context include the logistics for transport and distribution of the radionuclides (when on site production is not feasible), and the particular regulatory framework applicable to the handling of α-particle emitters in many countries (e.g., nuclear proliferation concerns of some parent radionuclides).

- The half-life of some α-particle emitters is very short (less than one hour), which imposes severe constraints on logistics and labeling procedures. At the same time, a too short half-life limits the types of tumors that could be treated, because the

radionuclide would only reach the most accessible cancer cells after injection [316]. Some strategies for dealing with the short half-life problem, at least to a certain extent, include the use of *in vivo* generators, the development of automated systems for labeling, and the local injection of the radionuclide.

- Chemistry issues, such as the lack of suitable chelating agents for some radionuclides to form stable complexes *in vivo*. Moreover, for some α-particle emitters the release of the radionuclide's progeny from the chelator also raises toxicity concerns for non-targeted tissues [317, 318].

Furthermore, there is a need for theoretical dosimetry studies to understand the interactions and energy deposits induced in the biological medium by the emitted α-particles. This constitutes the main motivation for the present work.

The purpose of this chapter is to discuss some promising α-particle emitting radionuclides for TAT and to present their cellular S-values computed with CELLDOSE. The chapter is structured as follows: in Section V.2 we discuss the track parameters that were computed to validate the transport of α-particles with *TILDA-V*; then, we describe in Section V.3 the basic aspects of α decay; Section V.4 provides an overview of the main properties of the α-particle emitters investigated in this work; finally, we report in Section V.5 the cellular S-values for the α-particle emitters computed with CELLDOSE.

V.2 Track parameters for α-particles transport in water

Following closely the ideas presented in Section III.2, the new capability of *TILDA-V* to simulate the transport of α-particles was validated by computing two key track parameters: the stopping power and the range, as explained in the following sections.

V.2.1 Stopping power

As for protons, only the electronic stopping power of α-particles is relevant for the energies considered in this work. Indeed, for the lowest energy simulated here, 40 keV (10 keV u^{-1}), the nuclear stopping power represents less than 5% of the total stopping power, and its contribution becomes even smaller at higher incident energies [10]. Analytically, the electronic stopping power of α-particles can be computed as:

$$SP(E_{\text{inc}}) = N_0 \Bigg[f_{\text{He}^{2+}}(E_{\text{inc}}) \sum_{j=1}^{4} \bar{E}_j \sigma_j(E_{\text{inc}}) + f_{\text{He}^{+}}(E_{\text{inc}}) \sum_{k=1}^{4} \bar{E}_k \sigma_k(E_{\text{inc}}) + f_{\text{He}^{0}}(E_{\text{inc}}) \sum_{l=1}^{4} \bar{E}_l \sigma_l(E_{\text{inc}}) \Bigg] , \tag{V.1}$$

where N_0 is the number of molecules in the medium per unit volume defined in Eq. I.12; the indices j, k and l represent the various inelastic interactions of helium ions (ionization, excitation and two charge-exchange processes for each charge state); σ_j, σ_k and σ_l denote the cross sections associated to the interactions j, k and l; similarly, $\bar{E}_j$, $\bar{E}_k$ and $\bar{E}_l$ are the mean energy transfers for each interaction, which can be computed starting from Eqs. II.10, II.13, II.36 and II.49. Furthermore, $f_{\mathrm{He}^{2+}}$, $f_{\mathrm{He}^{+}}$ and $f_{\mathrm{He}^{0}}$ are the equilibrium charge fractions for helium ions, given by [4, 109]:

$$\begin{aligned} f_{\mathrm{He}^{2+}} &= [(a-b)\sigma_{20} + g(a+\sigma_{21}) - f(b+\sigma_{21})]/D \ , \\ f_{\mathrm{He}^{+}} &= (b\sigma_{20} - g\sigma_{21})/D \ , \\ f_{\mathrm{He}^{0}} &= (f\sigma_{21} - a\sigma_{20})/D \ , \end{aligned} \tag{V.2}$$

in which, by definition:

$$\begin{aligned} &a = -(\beta + \sigma_{21}) \ , \quad b = \sigma_{01} - \sigma_{21} \ , \quad f = \sigma_{10} - \sigma_{20} \ , \\ &g = -(\alpha + \sigma_{20}) \ , \quad \alpha = \sigma_{01} + \sigma_{02} \ , \quad \beta = \sigma_{10} + \sigma_{12} \ , \\ &D = ag - bf \ , \end{aligned} \tag{V.3}$$

with the charge-exchange cross sections (σ_{21}, σ_{20}, σ_{10}, σ_{12}, σ_{01}, σ_{02}) as defined in Chapter II. The equilibrium charge fractions for helium ions were computed with Eqs. V.2 and V.3 considering two cases: i) using only the semiempirical charge-exchange cross sections based on the work of Uehara and Nikjoo [4] (see Sections II.3.4 and II.3.5); ii) using the *prior* CDW-EIS cross sections for the single-electron capture process by He^{2+}, and the semiempirical cross sections for all other charge-exchange processes.

The equilibrium charge fractions obtained for both cases are reported in Figure V.1, along with experimental data in H_2 and O_2 taken from Barnett *et al.* [220]. Slight differences are observed in the equilibrium charge fractions computed with the two sets of cross sections. Regardless of these differences, it is clear that for energies above $\sim$1 MeV u^{-1} only the He^{2+} contribution to the electronic stopping power is relevant. Furthermore, it should be noted that Eq. V.1 is simply an extension of Eq. III.6 given previously for protons. In fact, the only difference between Eq. III.6 and Eq. V.1 is in the total number of charge states and inelastic interactions types that is necessary to take into account for an accurate description of the ion's energy loss in its passage through matter. It is worth mentioning that in the context of this work we used Eq. V.1 to verify the stopping power values obtained from *TILDA-V*.

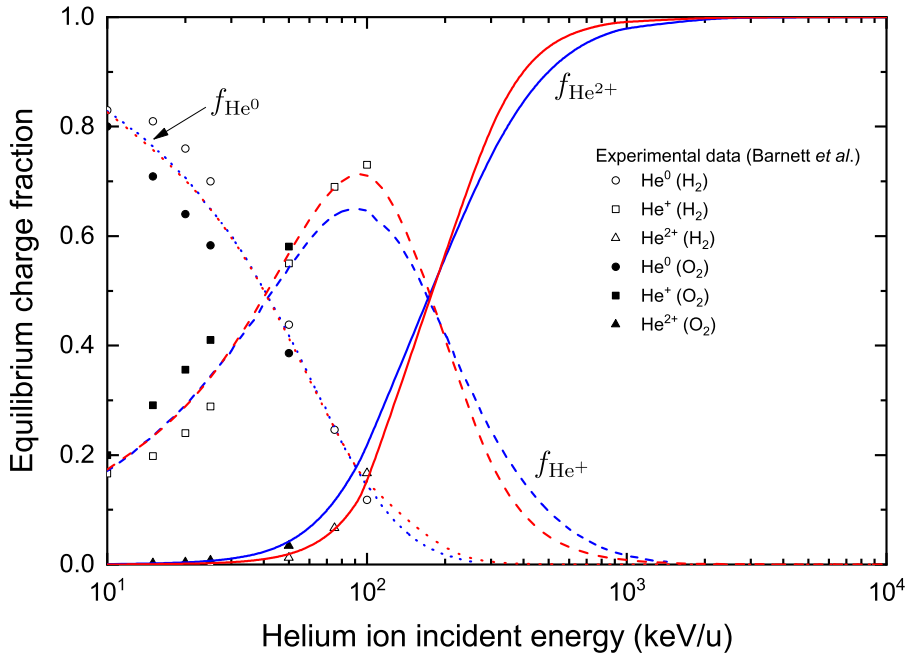

Figure V.1 Equilibrium charge fractions for helium ions in water vapor ($f_{He^{2+}}$, f_{He^+} and f_{He^0}) depicted in solid, dashed and dotted lines, respectively. Blue: calculation from fully semiempirical cross sections. Red: calculation from a combination of theoretical and semiempirical cross sections (see text). The symbols are experimental data in H_2 and O_2 taken from Barnett *et al.* [220]. Adapted with permission from Ref. [4]. Copyright (2002) American Chemical Society.

From the point of view of simulations, the stopping power is calculated following the same approach described in Section III.2.2, i.e., 10^6 projectiles are simulated in stationary mode for each helium charge state (He^{2+}, He^+, He^0) and for each incident energy according to a logarithmic grid. The stopping power for each charge state is then obtained with Eq. III.7. Finally, the total electronic stopping power at an incident energy E_{inc} is obtained by considering the relative contribution of each helium charge state at that energy:

$$SP(E_{inc}) = f_{He^{2+}}(SP)_{He^{2+}} + f_{He^+}(SP)_{He^+} + f_{He^0}(SP)_{He^0} \ , \tag{V.4}$$

Figure V.2 presents the electronic stopping power for α-particles in water computed with *TILDA-V* using two different sets of cross sections. The dashed line shows the results obtained when a full set of semiempirical cross sections, derived from the work of Uehara and Nikjoo [4], is used in the code. On the other hand, the solid line ("theoretical") depicts the stopping power values obtained when using a mixed set of theoretical and semiempirical cross sections, in which: the ionization cross sections for the three charge states of helium as well as the single-electron capture process by He^{2+} (σ_{21}) were computed with the *prior* version of the CDW-EIS model; excitation cross sections were obtained from the semiempirical model of Miller and Green [5], assuming that

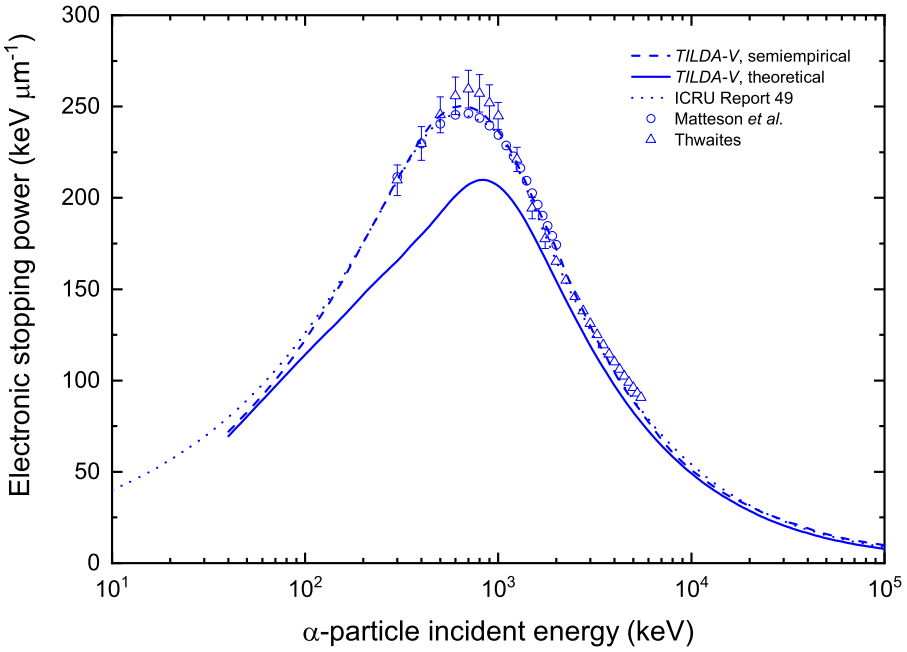

Figure V.2 Electronic stopping power for α-particles ($^4_2He^{2+}$) in water, as provided by *TILDA-V* using two different sets of cross sections (see text). The dotted line shows the values for water vapor taken from the ICRU Report 49 [10]. The symbols represent experimental data for water vapor taken from Matteson *et al.* [32] and Thwaites [33]. For the sake of clarity, error bars are only shown when they are greater than the symbols.

the cross sections for all helium charge states were equal to those for protons; for all other charge-exchange processes (σ_{20}, σ_{10}, σ_{12}, σ_{01}, σ_{02}), the semiempirical cross sections obtained from the work of Uehara and Nikjoo [4] were used.

As it is evident from Figure V.2, when using the "theoretical" set of cross sections, the resulting stopping power curve exhibits large discrepancies with available experimental data [32, 33] and the values provided by the ICRU Report 49 [10], especially for incident energies $\lesssim 2$ MeV. The reasons behind these discrepancies are currently under investigation, and it seems likely that improvements in the theoretical model will be required to cope with this problem. While this work is concluded, we decided to use in *TILDA-V* the full set of semiempirical interaction cross sections derived from the work of Uehara and Nikjoo [4] for all simulations involving α-particles. This decision was made for allowing a reliable dosimetric study of α-particle emitters, as described in Section V.5. Therefore, and unless otherwise stated, all calculations reported hereafter were performed using the semiempirical cross sections.

V.2.2 Range

The range for α-particles in water is obtained by means of full slowing-down simulations with *TILDA-V*. In this context, each α-particle is followed in an event-by-event manner, all interactions and charge state changes taken into account, until its energy falls below the fixed cutoff of 40 keV (10 keV u^{-1}). The range is then obtained by dividing the total distance traveled by the α-particles over the number of simulated projectiles ($\geq 5 \times 10^4$). The range for α-particles in water computed with *TILDA-V* is shown in Figure V.3.

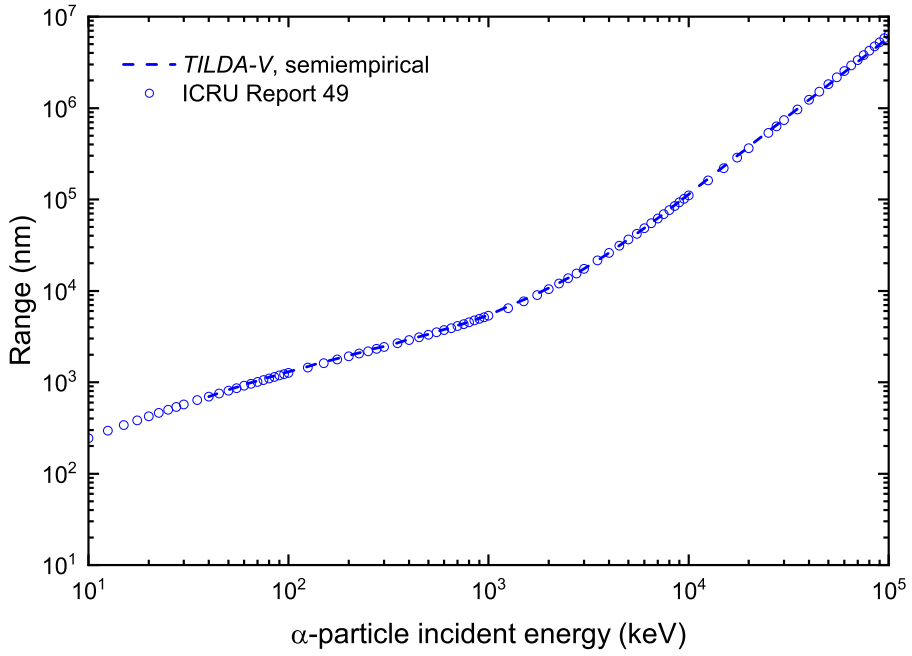

Figure V.3 Range for α-particles ($^4_2He^{2+}$) in water, as provided by *TILDA-V* (dashed line). The open circles are the CSDA range values for α-particles in water vapor taken from the ICRU Report 49 [10].

Let us note that, as for protons, fixing a low-energy cutoff for the tracking of α-particles induces an uncertainty in the range computed with *TILDA-V*. For this reason, the range values reported in Figure V.3 (dashed line) were adjusted to compensate for the average path length that an α-particle of 40 keV would travel before coming to a full stop in water vapor. We assumed that the required correction is equal to the CSDA range for an α-particle of 40 keV in water vapor found in the ICRU Report 49 [10], which is $\approx$ 698 nm. After this correction, we found that the difference between the resulting range values and those of the ICRU Report 49 [10] remains below 3% for incident energies $\leq$ 10 MeV, which corresponds to the maximum kinetic energy of α-particles emitted in a radioactive decay. On the other hand, for incident energies above 10 MeV the differences between the range values computed with *TILDA-V* and those of the ICRU Report 49 [10] may increase to about 10%. Based on the previous observations, we conclude that uncertainties affecting the transport of α-particles in *TILDA-V* are low

enough to allow the use of the code for simulating the decay and energy deposition of α-particle emitting radionuclides.

V.3 The α decay process

α decay is a mode of radioactive decay in which an unstable parent nucleus emits an α-particle to achieve a more stable configuration. α decay is possible because the quantum mechanical effect of tunneling gives the α-particle a certain finite probability for penetrating the potential barrier of the parent nucleus and thus escape. Moreover, α decay is common in heavy nuclei, for which the atomic number $Z \geq 82$ (i.e., starting from lead) [246, 319]. If X (Y) is the parent (daughter) atom, the α decay process can be written as:

$$ {}^{\mathrm{A}}_{\mathrm{Z}}\mathrm{X} \rightarrow {}^{\mathrm{A-4}}_{\mathrm{Z-2}}\mathrm{Y}^{2-} + {}^{4}_{2}\mathrm{He}^{2+} \ , \tag{V.5} $$

where A is the atomic mass number. Thus, in an α decay the atomic mass number of the parent atom is reduced by four and its atomic number by two, resulting in the two protons and two neutrons needed to form the α-particle. If the parent atom is initially neutral, then conservation of the electric charge implies that the daughter atom will have a charge of -2 to compensate the +2 charge of the α-particle, as assumed in Eq.V.5. However, the passage of the α-particle through the parent atom's electron cloud may excite or ionize some of these electrons, leaving the recoiling daughter atom in a state of positive ionization. In fact, some experimental studies suggested that most of the recoiling atoms were neutral or had a +1 charge [320–325]. In addition, α decay may be accompanied by the emission of γ radiation if the daughter nucleus is left at an excited state. The energy released in α decay is given by:

$$ Q_{\alpha} = E_{\alpha} + E_{\mathrm{RN}} + E_{\gamma} \ , \tag{V.6} $$

where E_{α}, E_{RN} and E_{γ} are the kinetic energies of the α-particle, the recoil daughter nucleus (RN) and the γ photon, respectively. While α-particles have discrete kinetic energies, the exact value of E_{α} depends on whether the daughter nucleus is left at an excited state or not. Thus, the maximum value of E_{α} occurs when the daughter nucleus is left at the ground state and therefore no γ photon is emitted ($E_{\gamma} = 0$ in Eq. V.6). The kinetic energy of the RN can be computed with a simple non-relativistic expression:

$$ E_{\mathrm{RN}} = \left(\frac{m_{\alpha}}{m_{\mathrm{RN}}} \right) E_{\alpha} \ , \tag{V.7} $$

with m_{α}, m_{RN} the mass in amu of the α-particle and the RN, respectively. As already mentioned, E_{α} is of the order of a few MeV, while generally E_{RN} ~100 keV. Although the kinetic energy of the RN may seem low compared to that of the α-particle, it is about 1000 times larger than the energy of a chemical bond. This is of great concern for TAT,

because it means that the RN will always break free from the targeting agent, increasing the risk of toxicity to normal tissues [317]. The average path length in water of the RN is ~100 nm [326]. More specifically, the range in water of the RN resulting from the decay of the α-particle emitters investigated in this thesis varies between 89–120 nm, according to estimations performed with the code SRIM [228].

Furthermore, because of conservation of momentum, the decay of the parent nucleus at rest implies that the α-particle and the RN will acquire momenta equal in magnitude but opposite in direction [246], as illustrated in Figure V.4 for the α decay of ^{225}Ac.

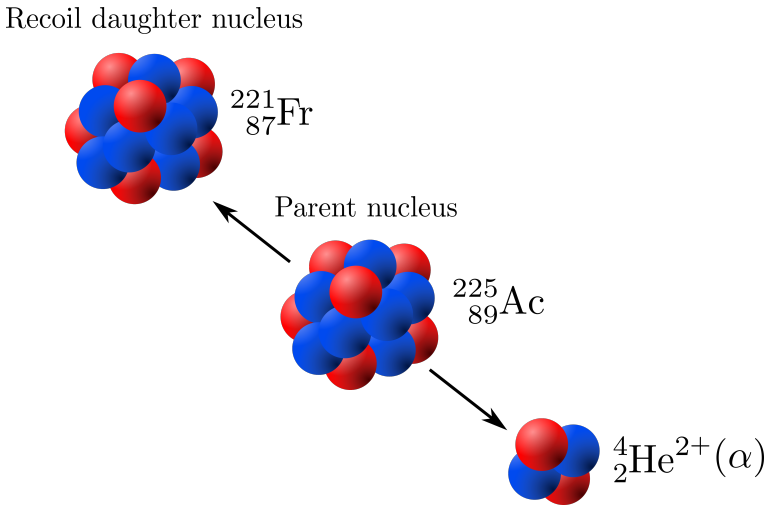

Figure V.4 Schematic representation of the α decay of ^{225}Ac. The protons are depicted in red and the neutrons in blue (illustration adapted from "Nucleus drawing" by Marekich CC BY-SA 3.0).

V.4 α-particle emitting radionuclides for TRT

As we have already mentioned, a radionuclide must satisfy multiple stringent criteria (e.g., appropriate emission characteristics and half-life, availability, *in vivo* stability...) to be considered a good candidate for TRT. Currently, there are only a handful of α-particle emitters that seem to have enough potential to reach wide clinical use. In this section, we present the physical properties and possible production routes of these promising α-particle emitters.

V.4.1 ^{211}At

Astatine-211 (^{211}At) has a half-life $T_{1/2} = 7.21$ h, which is long enough to allow the synthesis of radiopharmaceuticals and *in vivo* distribution after injection [327]. A simplified decay scheme of ^{211}At is shown in Figure V.5.

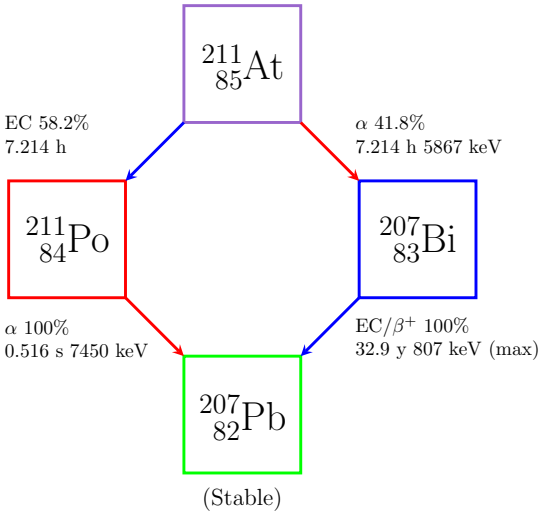

Figure V.5 Decay series of ^{211}At.

It can be seen that ^{211}At emits a single α-particle, either directly through its decay to bismuth-207 (^{207}Bi, with a branching ratio of 41.8%), or through its alternative and more likely (58.2%) decay branch leading to the formation of the short-lived α-particle emitter polonium-211 (^{211}Po). The most energetic α-particles are obtained in the latter case, with a maximum kinetic energy $E_\alpha^{(\max)} = 7.45\,\mathrm{MeV}$. It should be noted that when modeling the decay series of ^{211}At, the disintegration of ^{207}Bi to ^{207}Pb could be omitted. Indeed, because of the long half-life of ^{207}Bi ($T_{1/2} = 32.9\,\mathrm{y}$), its decay will not contribute in any appreciable way to radiation doses. For the sake of completeness, however, we decided to include the decay of ^{207}Bi in our simulations.

^{211}At can be produced in a cyclotron by bombardment of natural bismuth targets with α-particles, through the ^{209}Bi(α,2n)^{211}At nuclear reaction. This production route needs accelerators able to provide beams of α-particles with kinetic energies of about 28–29 MeV at the intensities required to produce useful quantities of ^{211}At. There are currently several institutions around the world with accelerators capable of producing up to a few GBq of ^{211}At using this method, and the associated production costs seem much lower compared to other α-particle emitters. However, scarce availability of ^{211}At is still a problem. On the other hand, an important issue related to the ^{209}Bi(α,2n)^{211}At production route is that the energy of the α-particle beam must be kept below 30 MeV to minimize co-production of the isotope ^{210}At, which decays to the extremely toxic ^{210}Po [316, 327]. Alternative methods proposed in the literature for obtaining ^{211}At are usually based on ^{211}Rn/^{211}At generators. Indeed, radon-211 (^{211}Rn, $T_{1/2} = 14.6\,\mathrm{h}$) decays to either ^{211}At by EC (branching ratio of 73%), or to ^{207}Po (27%) by α decay. The longer half-life of ^{211}Rn would allow more time for shipment. Unfortunately, there are

various issues related to this production route: it requires infrastructures that are even less common than for ^{211}At production, because ^{211}Rn is obtained from either lithium ion bombardment of ^{209}Bi or by high-energy proton spallation of actinide targets. In addition, purification steps are needed to remove the intrinsic ^{207}Po contamination. At best, only activities of ^{211}At suitable for preclinical studies would be achievable unless the production of ^{211}Rn increases by a factor 100 [316, 328, 329].

^{211}At has been coupled to several targeting molecules and used in a number of *in vitro* and *in vivo* experiments to investigate the treatment of different cancer types including, for instance, ovarian, breast and prostate cancers. For a comprehensive list of the preclinical and clinical studies performed with the various promising α-particle emitters, including ^{211}At, see the recent review by Tafreshi *et al.* [330]. Nevertheless, only two small phase I clinical trials have been reported thus far with ^{211}At. In the first one, ^{211}At-ch81C6 was administered to eighteen patients with recurrent malignant brain tumors. The treatment showed an increase in median survival with minimal toxicity [331]. In the second phase I clinical trial, intraperitoneal treatment of nine patients with recurrent ovarian carcinoma using ^{211}At-MX35 F(ab')$_2$ showed no toxicity [332].

Furthermore, as of the writing of this thesis, there are four clinical trials with ^{211}At registered on clinicaltrials.gov to be carried out at the Fred Hutchinson Cancer Research Center (Seattle, Washington, United States):

- A phase I/II clinical trial aims at investigating the side effects and best dose of ^{211}At-BC8-B10 before donor stem cell transplant in treating patients with high-risk acute myeloid leukemia, acute lymphoblastic leukemia, myelodysplastic syndrome, or mixed-phenotype acute leukemia (NCT03128034).

- A phase I/II clinical study to determine the side effects and best dose of ^{211}At-BC8-B10 followed by donor stem cell transplant for the treatment of relapsed or refractory high-risk acute leukemia or myelodysplastic syndrome (NCT03670966).

- A phase I trial to study the side effects and best dose of ^{211}At-OKT10-B10 when given together with chemotherapy before a stem cell transplantation for the treatment of multiple myeloma (NCT04466475).

- A phase I trial to investigate the side effects and best dose of ^{211}At-OKT10-B10 when given together with chemotherapy and low-dose total-body irradiation before donor stem cell transplant for treating newly diagnosed, recurrent or refractory high-risk multiple myeloma (NCT04579523).

As a last remark, let us mention that the decay of ^{211}At yields X-rays with energies of 77–92 keV that allow *in vivo* imaging for biodistribution studies in animal models [333, 334].

V.4.2 ^{212}Pb/^{212}Bi

Lead-212 (^{212}Pb) is a β^- emitter with a half-life $T_{1/2} = 10.64\,\text{h}$. It emits β^--particles with a maximum energy $E_{\beta^-}^{(\max)} = 574\,\text{keV}$. Its interest for TAT actually relies on the α decay of its immediate daughter, bismuth-212 (^{212}Bi), which has a half-life of only 60.55 min. ^{212}Bi has two alternative decay branches: i) β^- decay (64.1%) to polonium-212 (^{212}Po). The latter is an α-particle emitter with an extremely short half-life ($\approx 0.3\,\mu\text{s}$) and emits α-particles with a maximum kinetic energy $E_\alpha^{(\max)} = 8.79\,\text{MeV}$; ii) α decay (35.9%) to the β^- emitter thallium-208 (^{208}Tl). In this case, an α-particle with a kinetic energy between 5.3–6.1 MeV is emitted. Both decay branches of ^{212}Bi end in stable lead-208 (^{208}Pb). In summary, regardless of the specific decay path followed by ^{212}Bi, a single α-particle is emitted by decay. The decay series of ^{212}Pb is depicted in Figure V.6.

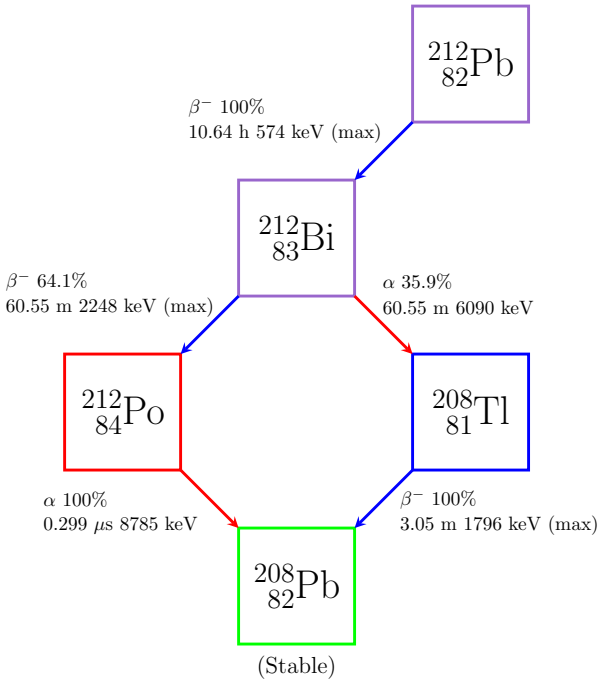

Figure V.6 Decay series of ^{212}Pb.

The short half-life of ^{212}Bi limits its direct application. To overcome this problem, a common strategy is to use ^{212}Pb as an *in vivo* generator of ^{212}Bi. Indeed, the use of a longer-lived radionuclide facilitates the radiolabeling of targeting vectors and the administration of the radiopharmaceutical, among other tasks. Another advantage of ^{212}Pb is that it delivers more than ten times the dose per unit administered activity compared to ^{212}Bi [335]. On the other hand, the release of ^{212}Bi upon ^{212}Pb disintegration may raise concerns [316, 336]. In this context, studies found that when ^{212}Pb is bound to the chelators TCMC or DOTA about 30–40% of ^{212}Bi could be released after the decay of ^{212}Pb [335, 337]. A second disadvantage is that working with ^{212}Pb requires appropriate

radiation shielding because of the highly energetic γ-rays emitted by its granddaughter ^{208}Tl ($E_\gamma = 2.61\,\mathrm{MeV}$) [336]. ^{212}Pb emits as well γ-rays of 238.6 keV with a 43% yield, which can be exploited for biodistribution studies [338]. Besides, a theranostic pair can be formed with the isotope ^{203}Pb, a γ emitter, allowing pre-therapy SPECT imaging for dosimetry studies [339].

The main production route of ^{212}Pb is by means of a ^{224}Ra/^{212}Pb generator. The parent radionuclide radium-224 (^{224}Ra, $T_{1/2} = 3.66$ d) is itself produced from the decay of thorium-228 (^{228}Th, $T_{1/2} = 1.91$ y), which can be obtained from thorium-232 (^{232}Th) or uranium-232 (^{232}U) [336].

Several preclinical studies on mice have been carried out in recent years to determine the efficacy and toxicity of ^{212}Pb for the treatment of a variety of tumors, including for instance: colon, pancreatic and ovarian cancers, as well as melanoma [330]. The preclinical results have shown the potential of ^{212}Pb to improve survival and tumor growth inhibition with limited toxicity. In addition, a first-in-human phase I clinical trial with ^{212}Pb was recently reported. In this trial, the radiopharmaceutical ^{212}Pb-TCMC-trastuzumab was administered intraperitoneally to three patients with ovarian cancer. The results showed little agent-related toxicity, confirming the medical potential and the feasibility of treatments with ^{212}Pb [338, 340]. As of the writing of this thesis, participants are being recruited for a phase I clinical study aiming to determine the safety and dose limiting toxicity of the radiopharmaceutical AlphaMedix™ (^{212}Pb-DOTAMTATE) in patients with unresectable, metastatic somatostatin receptor positive neuroendocrine tumors. The trial should be completed by November 2021 (NCT03466216).

V.4.3 ^{213}Bi

Bismuth-213 (^{213}Bi) has a half-life $T_{1/2} = 45.6$ min. As depicted in Figure V.7a, it is part of the decay series of actinium-225 (^{225}Ac, $T_{1/2} = 10.0$ d) and may undergo β^- or α decay. The β^- decay path has a probability of 97.9% and leads to the very short-lived polonium-213 (^{213}Po, $T_{1/2} = 4.2\,\mu$s) by the emission of β^--particles with a maximum kinetic energy $E_{\beta^-}^{(\max)} = 1422\,\mathrm{keV}$. The daughter ^{213}Po then decays very fast to lead-209 (^{209}Pb, $T_{1/2} = 3.25$ h) by the emission of α-particles with a maximum kinetic energy $E_\alpha^{(\max)} = 8.38\,\mathrm{MeV}$. The alternative decay branch of ^{213}Bi involves α decay (probability of 2.1%, $E_\alpha^{(\max)} = 5.87\,\mathrm{MeV}$) to thallium-209 (^{209}Tl, $T_{1/2} = 2.16$ min), which then experiences β^- decay ($E_{\beta^-}^{(\max)} = 1944\,\mathrm{keV}$) to ^{209}Pb. Finally, the latter also undergoes β^- decay ($E_{\beta^-}^{(\max)} = 644\,\mathrm{keV}$) to the very long-lived bismuth-209 (^{209}Bi, $T_{1/2} = 1.9 \times 10^{19}$ y [341]), which for all practical purposes may be regarded as stable. Irrespective of the initial decay path, each decay of ^{213}Bi will yield one α-particle and two β^--particles. The decay of ^{213}Bi is also accompanied by the emission of a 440 keV photon (emission

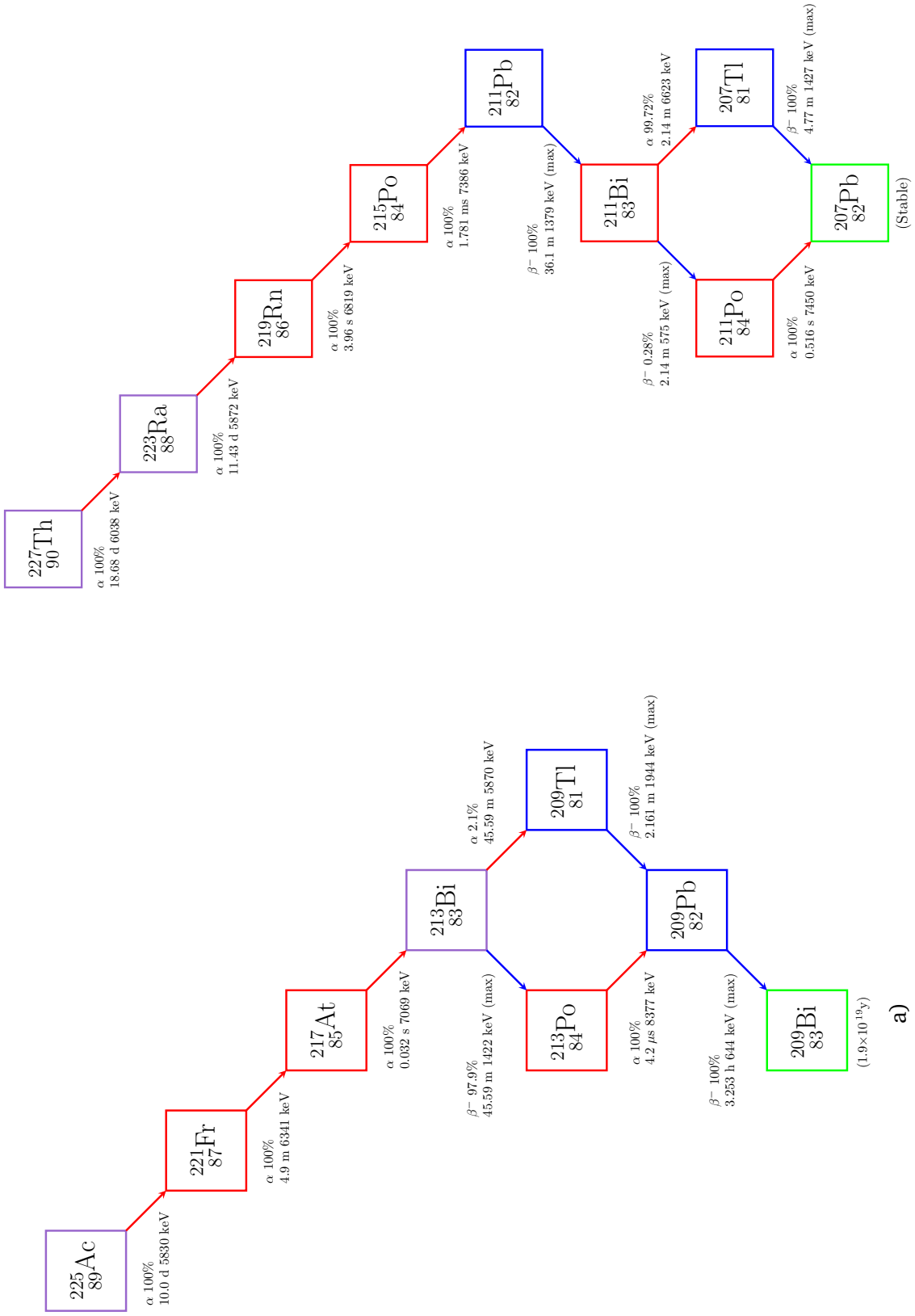

Figure V.7 Decay series of ^{225}Ac and ^{213}Bi (panel a), and of ^{227}Th and ^{223}Ra (panel b).

probability of 26.1%) that can be detected using γ-cameras equipped with commercially available high energy collimators, allowing to perform biodistribution, pharmacokinetic and dosimetric studies [342]. ^{213}Bi is obtained from the decay of its parent radionuclide, ^{225}Ac (see Section V.4.5) by means of ^{225}Ac/^{213}Bi generators. The latter can supply ^{213}Bi of high specific activity for several weeks [342, 343].

To date, there has been an enormous amount of successful work with ^{213}Bi using different targeting molecules (e.g., antibodies, antibody fragments, peptides) [318]. On the preclinical side, encouraging results have been reported for many types of cancer, such as pancreatic adenocarcinoma tumors, advanced bladder carcinoma, multiple myeloma, lymphoma, breast, ovarian and prostate cancers. Several authors have summarized the advances on this topic. For the details, the reader is referred for instance to the recent reviews provided in Refs. [330, 344].

^{213}Bi was the first α-particle emitter to be used in clinical trials for therapy [345], and is also the α-particle emitter used in the largest number of clinical trials to date [330]. Here we only provide some examples of the most recent clinical studies. Kratochwil *et al*. [346] reported a first-in-human experience with ^{213}Bi-DOTATOC in patients with neuroendocrine tumors resistant to treatment with β^- emitters (^{90}Y/^{177}Lu-DOTATOC). TAT with ^{213}Bi was shown to be able to overcome resistance against β^- radiation and resulted in a high number of long-lasting antitumor responses with moderate toxicity. Furthermore, a pilot study to determine the feasibility of ^{213}Bi coupled to an anti-EGFR antibody for the treatment of bladder cancer was reported by Autenrieth *et al*. [347]. The radiopharmaceutical was well tolerated and showed therapeutic efficacy. More recently, treatment of recurrent glioblastoma multiforme with ^{213}Bi-DOTA-SP was found to be safe, well tolerated and to prolong survival [348, 349].

The widespread clinical application of ^{213}Bi is mainly limited by the availability of its parent ^{225}Ac and the challenges imposed by its short half-life. In 2013, a report by the IAEA estimated that, based on the activities of ^{213}Bi administered in clinical studies, all available sources of ^{225}Ac/^{213}Bi would allow the treatment of no more than 100–200 patients per year [316]. On the other hand, the short half-life problem can be somewhat overcome with the use of automated systems for labeling and achieving rapid targeting by means of locoregional application, pretargeting or with fast-diffusible peptides as carrier molecules [342].

V.4.4 ^{223}Ra

Radium-223 (^{223}Ra) is a pure α-particle emitter with a half-life $T_{1/2} = 11.43\,\mathrm{d}$. As depicted in Figure V.7b, it is part of the decay series of thorium-227 (^{227}Th). ^{223}Ra decays to radon-219 (^{219}Rn) by emitting α-particles with kinetic energies between 5.0–

5.9 MeV. The whole decay series of ^{223}Ra yields a total of four α-particles, the most energetic having a kinetic energy $E_\alpha^{(\max)} = 7.45\,\mathrm{MeV}$ (from ^{211}Po).

The production of ^{223}Ra is generally based on a long-term operating generator containing a source of actinium-227 (^{227}Ac, $T_{1/2} = 21.7\,\mathrm{y}$), the parent of ^{227}Th, from which ^{223}Ra is eluted. ^{227}Ac is itself isolated from a preparation of protactinium-231 (^{231}Pa, $T_{1/2} = 3.28 \times 10^4\,\mathrm{y}$) [350]. ^{223}Ra can also be obtained from legacy actinium-beryllium neutron sources and by bombarding natural thorium using high-energy protons. Alternatively, large scale production of ^{223}Ra can be achieved by generating ^{227}Ac through neutron irradiation of radium-226 (^{226}Ra) in nuclear reactors, via the reaction ^{226}Ra(n,γ)^{227}Ra $\xrightarrow{\beta^-}$ ^{227}Ac (for more details, please refer to the paper by Jain *et al.* [351] and references therein).

^{223}Ra is considered a milestone in the medical applications of α-particle emitters. Indeed, in the form of radium-223 dichloride ($^{223}RaCl_2$), it remains to this date the only α-particle emitter approved by several health authorities, including the European Medicines Agency (EMA), the US Food and Drug Administration (FDA), and the Ministry of Health, Labour and Welfare (MHLW) of Japan for the treatment of metastatic castration-resistant prostate cancer [352]. Moreover, the efficacy and safety of $^{223}RaCl_2$ has been investigated as well, with encouraging results, in other tumor types involving bone metastases, such as advanced breast cancer and renal cell carcinoma [353].

It is worth mentioning that ^{223}Ra differs from the other α-particle emitters discussed here in that no targeting molecule is used to carry the radionuclide to the tumor. Radium, as other alkaline earth metals, mimics calcium and therefore has a natural tendency to accumulate in bones [330]. While this makes ^{223}Ra ideal against bone metastases, it is not a useful property for treating other tumors. Unfortunately, no chelator is currently available to form stable complexes with ^{223}Ra, which hampers the broader utilization of this radionuclide in TAT [315].

V.4.5 ^{225}Ac

Actinium-225 (^{225}Ac) is a pure α-particle emitter with a half-life $T_{1/2} = 10.0\,\mathrm{d}$. It decays to francium-221 (^{221}Fr, $T_{1/2} = 4.9\,\mathrm{min}$) by the emission of α-particles with a maximum kinetic energy $E_\alpha^{(\max)} = 5.83\,\mathrm{MeV}$. ^{221}Fr is itself a pure α-particle emitter ($E_\alpha^{(\max)} = 6.34\,\mathrm{MeV}$) that decays to yet another pure α-particle emitter, astatine-217 (^{217}At, $T_{1/2} = 0.032\,\mathrm{s}$, $E_\alpha^{(\max)} = 7.07\,\mathrm{MeV}$). The latter leads to ^{213}Bi, whose decay has been described in Section V.4.3. Thus, taking into account the decay of ^{213}Bi, a total of four α-particles and two β-particles will be emitted per decay of ^{225}Ac (see Figure V.7a). γ-photon emissions useful for *in vivo* imaging are generated in the ^{225}Ac decay series from the disintegration of ^{221}Fr (218 keV, 11.6% emission probability) and ^{213}Bi

(440 keV, 26.1% emission probability) [316].

All the ^{225}Ac used to date in preclinical and clinical studies has been obtained via radiochemical extraction following the decay of the long-lived thorium-229 (^{229}Th, $T_{1/2} =$ 7340 y) through one intermediate radionuclide, radium-225 (^{225}Ra, $T_{1/2} = 14.9$ d). ^{229}Th is the daughter of uranium-233 (^{233}U, $T_{1/2} = 1.592 \times 10^5$ y), and both radionuclides are members of the extinct neptunium series. ^{233}U was produced as part of the United States molten salt breeder reactor research program and is currently stored at Oak Ridge National Laboratory (ORNL) [354]. Besides ORNL, there are presently only two other sites able to produce clinically relevant activities of ^{225}Ac: the Directorate for Nuclear Safety and Security of the Joint Research Centre (JRC) of the European Commission in Karlsruhe, Germany and the Institute of Physics and Power Engineering (IPPE) in Obninsk, Russia. The combined annual production of ^{225}Ac in these three sites is of about 68 GBq [355]. Unfortunately, this production route cannot provide the quantities of ^{225}Ac that would be required for its widespread clinical use. For example, it was estimated that the treatment of 100,000 patients would require $\approx$ 2.8 TBq [356], i.e., more than forty times the maximum activity annually produced worldwide with the current method. For this reason, there is now a great interest and a worldwide effort to find alternative methods for large scale production of ^{225}Ac [356]. The following are some of the alternative production routes currently under investigation:

- Production in a cyclotron by low-energy (8.8–24.8 MeV) proton irradiation of radium-226 (^{226}Ra) via the nuclear reaction ^{226}Ra(p,2n)^{225}Ac [357].

- Accelerator production by means of high-energy (78–192 MeV) proton spallation reactions on natural thorium metal targets. The reaction pathways leading to ^{225}Ac include ^{232}Th(p,α4n)^{225}Ac, ^{232}Th(p,αp3n)^{225}Ra$\xrightarrow{\beta^-}$ ^{225}Ac and ^{232}Th(p,p7n)^{225}Th$\xrightarrow{\text{EC}}$ ^{225}Ac [358]. High ^{225}Ac yields are predicted for proton beam energies of 200 MeV and above [359].

- Production in an electron accelerator (e.g., a LINAC) using Bremsstrahlung photons through the ^{226}Ra(γ,n)^{225}Ra $\xrightarrow{\beta^-}$ ^{225}Ac photonuclear reaction [360].

- ^{225}Ac could also be obtained through the production of ^{229}Th in nuclear reactors via neutron irradiation of ^{226}Ra, ^{227}Ac and ^{228}Ra targets, as it has been performed in the ORNL High Flux Isotope Reactor (HFIR) [361].

A large body of preclinical studies with ^{225}Ac has been published in the last two decades. Let us note, for instance, that the efficacy of ^{225}Ac has been investigated in animal models of lymphoma, neuroendocrine tumors, glioblastoma, metastatic uveal melanoma, as well as in pancreatic, colon, breast, ovarian and prostate cancers. In

most cases, antitumor effect was obtained with low toxicity. In some studies, however, renal toxicity due to the relocation of daughter nuclei was observed. A summary of the preclinical and clinical studies with ^{225}Ac can be found in Ref. [330]. On the clinical side, to the best of our knowledge, the following studies with ^{225}Ac have been reported to date:

- Two phase I and one phase II trials have been performed with ^{225}Ac-lintuzumab in patients with acute myeloid leukemia, demonstrating significant antitumor effects [362].
- TAT based on ^{225}Ac-PSMA-617 in patients with metastatic castration resistant prostate cancer has shown remarkable antitumor response and promising duration of tumor control, with the main side effect being xerostomia (dry mouth) [363–365]. Indeed, the interest in treating this type of cancer with radiopharmaceuticals containing ^{225}Ac has grown. As of the writing of this thesis, there are six phase I clinical trials registered on clinicaltrials.gov involving the use of ^{225}Ac against prostate cancer.
- TAT with ^{225}Ac-DOTATOC in patients with neuroendocrine tumors was well tolerated and demonstrated promising treatment efficacy [366].
- An ongoing study on the safety and therapeutic efficacy of ^{225}Ac-DOTA-SP for the treatment of gliomas [367].

It is worth mentioning that ^{225}Ac is expected to be better or comparable to ^{213}Bi in terms of radiobiology, preclinical and clinical effects and cost [368]. However, the release of the daughter nuclei from the targeting agent upon disintegration of ^{225}Ac (or of any other radionuclide with a decay series involving multiple α decays) is still a matter of concern in TAT.

V.4.6 ^{227}Th

Thorium-227 (^{227}Th) is a pure α-particle emitter with a half-life $T_{1/2} = 18.68\,\mathrm{d}$ and decays to ^{223}Ra by the emission of α-particles of 5.0–6.0 MeV. Moreover, taking into account the whole progeny of ^{227}Th, a total of five α-particles are emitted per decay (see Figure V.7b). ^{227}Th can be obtained from ^{227}Ac using the same methods mentioned in Section V.4.4. Unlike its daughter ^{223}Ra, ^{227}Th can form highly stable chelator complexes and is therefore more attractive for TAT [369, 370]. Furthermore, the half-life of ^{227}Th enables radiolabeling and administration before a significant amount of ^{223}Ra is generated. Besides, the ensuing accumulation of ^{223}Ra in bones may not cause bone marrow toxicity due to the short range of the α-particles [370].

Several *in vitro* and *in vivo* studies have been performed to investigate the therapeutic efficacy of ^{227}Th in different tumor models, e.g., breast, colorectal, lung, ovarian and pancreatic cancers, as well as lymphoma and acute myeloid leukemia. A review of these preclinical studies with ^{227}Th has been recently given by Frantellizzi *et al*. [370]. In general, encouraging results have been reported for TAT with ^{227}Th. Furthermore, as of the writing of this thesis, one phase I clinical trial with ^{227}Th has been completed by Bayer. The trial aimed to evaluate the safety and tolerability of the thorium conjugate BAY1862864 in patients with relapsed or refractory CD22-positive NHL (NCT02581878). To the best of our knowledge, no results have been reported yet. In addition, according to clinicaltrials.gov, there are currently three other phase I clinical trials (also sponsored by Bayer) recruiting participants:

- A first-in-human study to learn about the safety and efficacy of the drug BAY2701439 in patients with HER2 expressing cancers (NCT04147819).
- A first-in-human study to determine the safety, tolerability, pharmacokinetics, antitumor activity and recommended dose for further clinical development of the drug BAY2287411 (a ^{227}Th labeled antibody-chelator conjugate) in patients with tumors known to express the protein mesothelin (NCT03507452).
- A study to evaluate the safety, tolerability, pharmacokinetics, and antitumor activity of the ^{227}Th labeled immunoconjugate BAY2315497 in patients with metastatic castration resistant prostate cancer (NCT03724747).

We have summarized in Table V.1 the main properties of the decay series of the α-particle emitters discussed thus far. In addition to the half-lives and branching ratios associated to the possible decay paths, we have indicated as well the contribution of each radiation type (excluding photons) to the average energy released by each radionuclide. All the information was taken from the ICRP Publication 107 [18]. By adding the contributions listed in the last column of Table V.1 for each decay series, it can be seen that the total energy released per decay is of about 6.97 MeV for ^{211}At, 8.86 MeV for ^{212}Pb, 9.14 MeV for ^{213}Bi, 27.92 MeV for ^{223}Ra, 28.68 MeV for ^{225}Ac, and 33.97 MeV for ^{227}Th. Moreover, α-particles represent in each case about 97%, 88%, 91%, 94%, 96% and 95% of the total energy released per decay, respectively.

Decay series	Radionuclide	Half-life (day)	Type of decay	Daughter	Energy per decay (keV)†					
					α	RN	β	AE	CE	Total
^{211}At	^{211}At	0.301	EC (58.2%) α (41.8%)	^{211}Po ^{207}Bi	2452	47.4	–	5.85	0.072	2505
	^{211}Po	5.972×10^{-6}	α (100%)	^{207}Pb (stable)	4331	83.8	–	4.93×10^{-4}	0.054	4415
	^{207}Bi	1.202×10^{4}	EC/β^+ (100%)	^{207}Pb (stable)	–	–	0.064	4.56	45.2	49.8
^{212}Pb	^{212}Pb	0.443	β^- (100%)	^{212}Bi	–	–	102	4.66	70.2	177
	^{212}Bi	0.042	β^- (64.1%) α (35.9%)	^{212}Po ^{208}Tl	2174	41.8	493	2.33	8.57	2720
	^{212}Po	3.461×10^{-12}	α (100%)	^{208}Pb (stable)	5631	108	–	–	–	5739
	^{208}Tl	2.118×10^{-3}	β^- (100%)	^{208}Pb (stable)	–	–	200	0.359	18.9	219
^{213}Bi	^{213}Bi	0.032	β^- (97.9%) α (2.1%)	^{213}Po ^{209}Tl	122	2.34	425	0.532	18.4	568
	^{213}Po	4.861×10^{-11}	α (100%)	^{209}Pb	8200	157	–	–	–	8357
	^{209}Tl	1.501×10^{-3}	β^- (100%)	^{209}Pb	–	–	13.7	0.060	0.609	14.4
	^{209}Pb	0.136	β^- (100%)	^{209}Bi (1.9×10^{19} y)	–	–	197	–	–	197

† Only α-particles, CE and AE with probabilities greater than 0.1‰ are considered in this table and in our simulations. The values of energy per decay already consider the branching ratios of the radionuclides.

Table V.1 Decay series and main properties of some α-particle emitting radionuclides for TRT [18].

Decay series	Radionuclide	Half-life (day)	Type of decay	Daughter	Energy per decay (keV)†					
					α	RN	β	AE	CE	Total
^{223}Ra	^{223}Ra	11.4	α (100%)	^{219}Rn	5666	104	–	9.21	68.3	5847
	^{219}Rn	4.583×10^{-5}	α (100%)	^{215}Po	6754	126	–	0.307	6.46	6887
	^{215}Po	2.061×10^{-8}	α (100%)	^{211}Pb	7386	140	–	–	–	7526
	^{211}Pb	0.025	β^- (100%)	^{211}Bi	–	–	450	0.163	4.09	454
	^{211}Bi	1.486×10^{-3}	α (99.72%) β^- (0.28%)	^{207}Tl ^{211}Po	6549	127	0.478	0.325	9.20	6686
	^{207}Tl	3.313×10^{-3}	β^- (100%)	^{207}Pb (stable)	–	–	494	5.64×10^{-5}	–	494
	^{211}Po	5.972×10^{-6}	α (100%)	^{207}Pb (stable)	20.5	0.397	–	2.34×10^{-6}	2.56×10^{-4}	20.9
^{225}Ac	^{225}Ac	10.0	α (100%)	^{221}Fr	5784	105	–	4.96	19.5	5913
	^{221}Fr	3.403×10^{-3}	α (100%)	^{217}At	6303	116	–	0.580	8.23	6428
	^{217}At	3.738×10^{-7}	α (100%)	^{213}Bi‡	7067	133	–	2.46×10^{-3}	0.057	7200
^{227}Th	^{227}Th	18.7	α (100%)	^{223}Ra‡	5880	106	–	12.8	61.3	6060

† Only α-particles, CE and AE with probabilities greater than 0.1‰ are considered in this table and in our simulations. The values of energy per decay already consider the branching ratios of the radionuclides.

‡ For the decay series of ^{213}Bi and ^{223}Ra see entries above.

Table V.1 Decay series and main properties of some α-particle emitting radionuclides for TRT (continued).

V.5 Cellular S-values for α-particle emitters

With the purpose of evaluating the relative performance of the various α-particle emitters at irradiating the nucleus of a single tumor cell, we used CELLDOSE to compute the cellular S-values. In this context, we applied the same cell model ($R_C = 7\,\mu$m, $R_N = 5\,\mu$m, and membrane thickness of 10 nm) and methodology previously described in Section IV.6.1 for electron emitters. As in that case, we considered different distributions of the radionuclide within the cell: a cell surface location (CS), intracytoplasmic location (Cy), intranuclear location (N) and a uniform whole cell distribution (C). As usual, only radiations with probabilities greater than 0.1‰ listed in the ICRP Publication 107 [18] were included in our simulations. Besides, all photons were excluded. The number of decays simulated with CELLDOSE varied between 10^5 and 10^6 depending on the radionuclide and distribution under study in order to reduce the statistical uncertainty to about 1–2%, while keeping a reasonable computation time.

It is worth mentioning that modeling the decay of α-particle emitters is somewhat more challenging than modeling the decay of pure β^- or AE emitters, because it often involves working with complex decay series and thus taking into consideration not only the decay of the original radionuclide (i.e., the parent nucleus), but the decays of the daughter nuclei as well. Indeed, if we take a look for instance at the decay schemes depicted in Figures V.5 to V.7, we see that the daughter nucleus is usually radioactive, even more, it can itself be an α-particle emitter. Consequently, in such cases (unless particular equilibrium conditions are present) the whole decay series of the parent radionuclide must be accounted for in dosimetric studies. In addition, for a given radionuclide it is possible to have alternative decay modes/paths with precise branching ratios. That is the case for example of ^{211}At, where α decay competes with electron capture, or of ^{212}Bi, for which β^- decay is much more likely than α decay (see Figures V.5 and V.6). For all these reasons, it was necessary to adapt the algorithm implemented in CELLDOSE for the random sampling of radiations. The principle remains the same as in Section IV.6.1, but now the cumulative probability distribution includes the contribution of all radiations of interest (α-particles, β^- spectra, CE and AE) for every radionuclide in a decay series. Besides, when alternative decay paths are available for a given parent radionuclide, the emissions of the daughter nuclei are adjusted by multiplying their yields by the corresponding branching ratio associated to the specific decay path. However, it should be noted that renormalization of the emission yields is only required for decay series, since the yields of individual radionuclides are already normalized in the data provided by the ICRP Publication 107 [18]. Moreover, it should be reminded that the algorithm in CELLDOSE provides only one particle (and thus one incident energy) by decay. Once the list of particles and energies is generated, another random sampling is

performed to determine the point of departure of each emitted radiation (α-particle or electron) within the cell, depending on the distribution to investigate. Let us note that, as for electron emitters, a final renormalization of the computed S-values is required. This is made by multiplying the computed S-values by the ratio of the mean energy released by decay over the mean energy of the radiations randomly sampled from the radionuclide's spectrum. As for electron emitters, the need for renormalization is a consequence of the way the random sampling of radiations is performed in our code: only one radiation energy is selected by decay, when in reality several particles with distinct energies may be emitted following a single radioactive decay.

On the other hand, we would like to draw attention to the fact that the current version of CELLDOSE cannot simulate the transport of ions or neutral atoms heavier than helium. Therefore, the energy deposits induced directly by the RN were not taken into account in this work. This issue will be discussed hereafter.

As we have mentioned, a correct dosimetric assessment of α-particle emitters must take into account the full decay series of the radionuclide under investigation. Nevertheless, for practical purposes (and to reduce the possible sources of error in our calculations) we computed the S-values with CELLDOSE considering two cases: i) the S-value of individual radionuclides, i.e., the one obtained by considering only the decay of the parent nucleus; ii) the S-value calculated taking into account the full decay series.

The cellular S-values for individual radionuclides obtained in this work are presented in Table V.2, while those for the decay series are shown in Table V.3. In both cases, we have included for comparison the results obtained with the MIRDcell code [39] and those reported in the recent work by Lee *et al*. [41]. Several authors have obtained S-values for α-particle emitters distributed in single tumor cells and micrometastases of different sizes using various methods and codes [19, 41, 371, 372]. However, because of differences in cell geometry and the radionuclides studied in those previous works, a direct benchmark of our results was only possible with the predictions of MIRDcell and Lee *et al*. [41]. Furthermore, for $S(\mathrm{N} \leftarrow \mathrm{C})$ (i.e., the S-value when the radiation source is uniformly distributed in the whole cell) we have reported only our results because this configuration is not included in MIRDcell and was not considered either in Ref. [41]. We have indicated as well in Tables V.2 and V.3 the percentage difference between the S-values obtained from other sources and the ones computed with CELLDOSE (values in parentheses).

Overall, the S-values increase as we move from a cell surface location, to an intracytoplasmic distribution, to a uniform whole cell distribution, to finally reach the maximum value for intranuclear location. This behavior is the same as the one observed for electron emitters in Chapter IV.

Radionuclide	Reference	Cellular S-values [Gy Bq^{-1} s^{-1}] (% difference)†			
		$S(\mathrm{N} \leftarrow \mathrm{CS})$	$S(\mathrm{N} \leftarrow \mathrm{Cy})$	$S(\mathrm{N} \leftarrow \mathrm{N})$	$S(\mathrm{N} \leftarrow \mathrm{C})$
^{211}At	This work	1.07×10^{-2}	1.57×10^{-2}	3.99×10^{-2}	2.43×10^{-2}
	MIRDcell	1.04×10^{-2} (-2.7)	1.51×10^{-2} (-3.7)	4.17×10^{-2} (+4.4)	–
^{212}Pb‡	This work	2.51×10^{-4}	4.42×10^{-4}	2.10×10^{-3}	1.06×10^{-3}
	MIRDcell	2.44×10^{-4} (-2.6)	4.32×10^{-4} (-2.2)	1.97×10^{-3} (-6.1)	–
	Lee *et al.*	2.54×10^{-4} (+1.4)	4.39×10^{-4} (-0.7)	2.05×10^{-3} (-2.2)	–
^{212}Bi	This work	8.96×10^{-3}	1.29×10^{-2}	3.36×10^{-2}	2.05×10^{-2}
	MIRDcell	8.87×10^{-3} (-1.0)	1.29×10^{-2} (-0.3)	3.51×10^{-2} (+4.5)	–
	Lee *et al.*	9.34×10^{-3} (+4.2)	1.35×10^{-2} (+4.3)	3.53×10^{-2} (+5.1)	–
^{213}Bi	This work	6.34×10^{-4}	9.51×10^{-4}	2.49×10^{-3}	1.53×10^{-3}
	MIRDcell	6.26×10^{-4} (-1.2)	9.18×10^{-4} (-3.4)	2.57×10^{-3} (+3.3)	–
	Lee *et al.*	6.40×10^{-4} (+1.0)	9.09×10^{-4} (-4.4)	2.49×10^{-3} (+0.04)	–
^{223}Ra	This work	2.65×10^{-2}	3.76×10^{-2}	9.88×10^{-2}	5.95×10^{-2}
	MIRDcell	2.57×10^{-2} (-2.9)	3.74×10^{-2} (-0.5)	1.03×10^{-1} (+4.2)	–
^{225}Ac	This work	2.55×10^{-2}	3.69×10^{-2}	9.62×10^{-2}	5.78×10^{-2}
	MIRDcell	2.52×10^{-2} (-1.3)	3.66×10^{-2} (-0.9)	9.92×10^{-2} (+3.1)	–
	Lee *et al.*	2.69×10^{-2} (+5.3)	3.88×10^{-2} (+5.0)	1.00×10^{-1} (+3.9)	–
^{227}Th	This work	2.58×10^{-2}	3.83×10^{-2}	9.91×10^{-2}	5.99×10^{-2}
	MIRDcell	2.53×10^{-2} (-1.9)	3.70×10^{-2} (-3.3)	1.03×10^{-1} (+4.0)	–

† The values in parentheses indicate the percentage difference with respect to this work, computed as: [S-value(other)−S-value(CELLDOSE)]/S-value(CELLDOSE)×100.

‡ For ^{212}Pb the S-value is due entirely to electronic emissions.

Table V.2 Cellular S-values for **individual** α-particle emitters. The results reported here are for a cell with $R_C = 7\,\mu$m and $R_N = 5\,\mu$m. Our results are compared with the S-values obtained with MIRDcell [39] and the calculations performed by Lee *et al.* [41]. The percentage difference is shown in parentheses.

Radionuclide	Reference	Cellular S-values [Gy Bq^{-1} s^{-1}] (% difference)†			
		$S(\mathrm{N} \leftarrow \mathrm{CS})$	$S(\mathrm{N} \leftarrow \mathrm{Cy})$	$S(\mathrm{N} \leftarrow \mathrm{N})$	$S(\mathrm{N} \leftarrow \mathrm{C})$
^{211}At	This work	2.19×10^{-2}	3.22×10^{-2}	8.43×10^{-2}	5.09×10^{-2}
	MIRDcell	2.23×10^{-2} (+2.0)	3.25×10^{-2} (+1.1)	8.89×10^{-2} (+5.4)	–
^{212}Pb	This work	2.00×10^{-2}	3.08×10^{-2}	7.78×10^{-2}	4.72×10^{-2}
	MIRDcell	2.06×10^{-2} (+2.8)	3.00×10^{-2} (-2.5)	8.28×10^{-2} (+6.4)	–
	Lee *et al.*	2.15×10^{-2} (+7.3)	3.12×10^{-2} (+1.4)	8.19×10^{-2} (+5.2)	–
^{213}Bi	This work	1.82×10^{-2}	2.69×10^{-2}	6.99×10^{-2}	4.25×10^{-2}
	MIRDcell	1.89×10^{-2} (+4.1)	2.75×10^{-2} (+2.4)	7.50×10^{-2} (+7.3)	–
	Lee *et al.*	1.96×10^{-2} (+7.9)	2.85×10^{-2} (+6.1)	7.49×10^{-2} (+7.2)	–
^{223}Ra	This work	9.10×10^{-2}	1.37×10^{-1}	3.43×10^{-1}	2.07×10^{-1}
	MIRDcell	9.13×10^{-2} (+0.3)	1.33×10^{-1} (-2.7)	3.61×10^{-1} (+5.1)	–
^{225}Ac	This work	8.85×10^{-2}	1.29×10^{-1}	3.32×10^{-1}	2.06×10^{-1}
	MIRDcell	8.90×10^{-2} (+0.6)	1.29×10^{-1} (+0.4)	3.52×10^{-1} (+5.9)	–
	Lee *et al.*	9.36×10^{-2} (+5.8)	1.35×10^{-1} (+5.0)	3.51×10^{-1} (+5.6)	–
^{227}Th	This work	1.17×10^{-1}	1.65×10^{-1}	4.36×10^{-1}	2.65×10^{-1}
	MIRDcell	1.17×10^{-1} (+0.4)	1.70×10^{-1} (+3.0)	4.64×10^{-1} (+6.5)	–

† The values in parentheses indicate the percentage difference with respect to this work, computed as: [S-value(other)−S-value(CELLDOSE)]/S-value(CELLDOSE)×100.

Table V.3 Cellular S-values for the **decay series** of α-particle emitters. The results reported here are for a cell with $R_C = 7\,\mu$m and $R_N = 5\,\mu$m. Our results are compared with the S-values obtained with MIRDcell [39] and the calculations performed by Lee *et al.* [41]. The percentage difference is shown in parentheses.

In the case of individual radionuclides (Table V.2), very similar results were found for ^{223}Ra, ^{225}Ac and ^{227}Th for all radionuclide distributions. The latter can be explained by the fact that the three radionuclides are pure α-particle emitters (no multiple decay paths) and (taken individually) release roughly the same energy per decay (see Table V.1). As expected, the smallest S-values were obtained for ^{212}Pb, a pure β^- emitter. Moreover, when we compared our S-values with the ones provided by MIRDcell and those taken from Lee *et al.* [41], we observed differences below ∼6%. Given that our own results have a statistical uncertainty $\leq$ 2%, the agreement with the other calculations is remarkable. The principles behind the MIRD approach were briefly discussed in Chapter IV. Let us add that MIRDcell, as CELLDOSE, does not consider the contributions of photons and RN to the S-value. On the other hand, the calculations of Lee *et al.* [41] were carried out with the MC code PHITS (version 2.76). In their simulations, Lee *et al.* [41] included the photon contribution, despite the fact that is well known to be negligible in this type of studies. Besides, PHITS (as CELLDOSE) cannot currently take into account the fate of the RN[1], and therefore their energy is not included in dose calculations. In addition, let us note that PHITS, as CELLDOSE, uses the emission spectra taken from the ICRP Publication 107 [18]. To the best of our knowledge, MIRDcell calculations are based on similar data sets, the main difference being the treatment of β spectra [39].

A significant increase in the S-values was observed when the full decay series was considered in the calculations (see Table V.3). The S-values increased by a factor of about 2 for ^{211}At, 28–29 for ^{213}Bi, 3.5 for ^{223}Ra and ^{225}Ac, and 4.5 for ^{227}Th. The largest variation was found for ^{212}Pb, for which the S-values of the decay series were 37–80 greater than for the individual radionuclide, depending on the distribution. Overall, the maximum S-values were obtained for ^{227}Th.

The relative differences between our results and the S-values of MIRDcell and Lee *et al.* [41] were greater for the decay series than for the individual radionuclides, but the agreement is still satisfactory (the discrepancies are < 8%). It is worth mentioning that the percentage differences reported in Tables V.2 and V.3 are actually comparable to those found between MIRDcell and PHITS 2.76 (< 6%) [41]. They are also similar to the differences reported in other benchmark studies. For instance, Rojas-Calderón *et al.* [372] recently used the MCNPX MC code to compute S-values for ^{211}At, ^{225}Ac and monoenergetic α sources placed in the nuclei of spherical cells and of three cancer cell models built from immunofluorescence images. Their $S(\mathrm{N} \leftarrow \mathrm{N})$ values for ^{211}At and ^{225}Ac uniformly distributed in the nucleus of spherical cells of different sizes are presented in Table V.4, along with a comparison of the results obtained with the MIRD formalism [373].

[1]Private communication, PHITS development team.

Cell dimensions (μm)	Radionuclide†	$S(\mathrm{N} \leftarrow \mathrm{N})$ [Gy Bq^{-1} s^{-1}]		Difference‡
		MIRD [373]	MCNPX [372]	
$R_N = 3$, $R_C = 6$	^{225}Ac	2.61×10^{-1}	2.68×10^{-1}	-2.6%
	^{211}At	1.11×10^{-1}	1.15×10^{-1}	-3.5%
$R_N = 5$, $R_C = 10$	^{225}Ac	9.47×10^{-2}	9.68×10^{-2}	-2.2%
	^{211}At	3.99×10^{-2}	4.14×10^{-2}	-3.6%
$R_N = 9$, $R_C = 10$	^{225}Ac	2.99×10^{-2}	3.05×10^{-2}	-2.0%
	^{211}At	1.25×10^{-2}	1.30×10^{-2}	-3.8%

† The emission data were taken from the ICRP Publication 107 [18]. All radiations with yields greater than 1% were included.
‡ Computed as: [S-value(MIRD)−S-value(MCNPX)]/S-value(MCNPX)×100.

Table V.4 $S(\mathrm{N} \leftarrow \mathrm{N})$ values for ^{211}At and ^{225}Ac uniformly distributed in the nucleus of spherical cells of different sizes (R_N = nucleus radius, R_C = cell radius). Adapted from Ref. [372].

It can be seen that the results of Rojas-Calderón *et al.* [372] agree within ∼4% with the calculations based on the MIRD method [373].

Finally, we have estimated the enhancement factor to the S-values provided by the α-particle emitters compared to the conventional β^- emitter ^{177}Lu (taken as the reference). The enhancement factor was simply computed as the S-value ratio, i.e., S(α-particle emitter)/S(^{177}Lu). The results for the two cases discussed here (the radionuclide alone and with its decay series) are reported in Table V.5.

It can be observed that the single decay of a pure α-particle emitter such as ^{223}Ra, ^{225}Ac or ^{227}Th already yields S-values that are about 87–134 greater than those of ^{177}Lu. The enhancement is less significant for radionuclides having multiple decay modes, particularly if the α decay path has a small branching ratio. For instance, the enhancement factors of ^{211}At (41.8% α) and ^{212}Bi (35.9% α) are of about 36–54 and 30–45, respectively, while the S-values of ^{213}Bi (2.1% α) alone are only between 2.2 and 3.2 times greater than those of ^{177}Lu. The extreme case is, once again, that of ^{212}Pb alone, with enhancement factors of only 1.27–1.89 with respect to ^{177}Lu.

When considering the full decay series, the maximum enhancement was found for ^{227}Th, followed by ^{223}Ra, ^{225}Ac, ^{211}At, ^{212}Pb and finally ^{213}Bi. The S-value of ^{227}Th for a cell surface distribution of the radionuclide was 589 times greater than the corresponding S-value of ^{177}Lu; the enhancement factor decreased to 534 for intracytoplasmic location, 441 for a uniform whole cell distribution, and 393 for intranuclear location. This is a clear example of how α-particle emitters outperform β^- emitters, at least in terms of

S-values.

Radionuclide	Case	Enhancement factor over ^{177}Lu			
		$S(\mathrm{N} \leftarrow \mathrm{CS})$	$S(\mathrm{N} \leftarrow \mathrm{Cy})$	$S(\mathrm{N} \leftarrow \mathrm{N})$	$S(\mathrm{N} \leftarrow \mathrm{C})$
^{211}At	alone	54.0	50.7	36.0	40.4
	series	110	104	76.0	84.5
^{212}Pb	alone	1.27	1.43	1.89	1.75
	series	101	100	70.1	78.4
^{212}Bi	alone	45	42	30	34
	series	–	–	–	–
^{213}Bi	alone	3.20	3.08	2.24	2.54
	series	91.7	86.9	63.0	70.6
^{223}Ra	alone	134	122	89.0	98.9
	series	460	442	309	344
^{225}Ac	alone	129	120	86.7	96.0
	series	447	416	299	342
^{227}Th	alone	130	124	89.3	99.5
	series	589	534	393	441

Table V.5 Enhancement factor of α-particle emitters over ^{177}Lu, computed as the S-value ratio, S(α-particle emitter)/S(^{177}Lu).

An issue that remains to be addressed in this context is the effect on dosimetry of the RN. As far as we know, the contribution of RN to the S-values has been neglected in similar works found in the literature. Given the range of the RN and the cell size, this assumption may well be justified for a cell surface distribution of the radionuclide, because the RN would never reach the cell nucleus. Nevertheless, the same cannot be stated with certainty for intracytoplasmic distribution. Moreover, for intranuclear location it is likely that the RN will deposit an important fraction of their energy in the cell nucleus, which may modify the value of $S(\mathrm{N} \leftarrow \mathrm{N})$. Furthermore, it seems that the biological effects of the RN are not clearly established. To the best of our knowledge, there are only a few studies in the literature related to this topic. For instance, in the 1990s Azure *et al.* [374] investigated the role of recoil energy on the radiotoxicity of the α-particle emitter ^{212}Pb localized in the nucleus of mammalian cells. Based on their calculations of the relative biological effectiveness of the α-particles emitted by ^{212}Po and ^{212}Bi (the progeny of ^{212}Pb), as well as on previous experimental observations regarding

cell survival studies, they concluded that recoil energy does not play a significant role in imparting biological damage when α-particle emitters are localized in the cell nucleus. However, the reason behind the apparent ineffectiveness of the recoil energy was not fully elucidated.

In summary, further studies are needed to evaluate the exact effect of including the contribution of RN when computing the S-values of α-particle emitters, as well as to clarify its significance when relating absorbed dose to radiation-induced biological damage. This is, however, well beyond the scope of this thesis.

Conclusions

We have shown in this chapter that both *TILDA-V* and CELLDOSE are now validated for simulating the transport of α-particles in water and performing dosimetry studies with α-particle emitting radionuclides, respectively. An excellent agreement was found with available data in the literature in terms of stopping power, ranges and cellular S-values.

We have computed the S-values for α-particle emitters considering a single cell model and different distributions of the radionuclides. Our results show that α-particle emitters outperform conventional β^- such as ^{177}Lu in terms of energy deposited in the nucleus of a single cell.

Future work on this subject may include: a reevaluation of the cellular S-values reported here using improved theoretical cross sections for helium ions in water; the implementation of interaction cross sections for describing the impact of helium ions on DNA components; a detailed analysis of the energy deposits induced by the recoil daughter nuclei, if possible through refinements to the MC simulations or by means of other numerical tools; simulating the irradiation by α-particles of multicellular systems; and the implementation in CELLDOSE of more complex and realistic cell models, based for instance on microscopy images of tumor cell lines.

CONCLUSIONS AND OUTLOOK

Conclusions

The fight against cancer is one of the most challenging, complex and significant scientific endeavors in human history. Interdisciplinarity is nowadays considered a key factor to advance cancer research. In the case of therapeutic approaches making use of ionizing radiation, physics plays an important role for understanding the interactions of radiation with biological matter. These interactions are described through cross sections, which can be used in Monte Carlo codes to simulate with great accuracy the deposition of radiation energy in tumors.

The purpose of this work was to improve an existing MCTS code (*TILDA-V*) by adding new types of radiation sources in the simulations and to validate the code as a whole for applications in radiation dosimetry, especially for making useful predictions in the field of TRT.

During the first phase of the thesis, a series of studies were carried out to validate the transport of protons and their secondary electrons in water and DNA. While the transport of these particles was already implemented in *TILDA-V* , some aspects of the code had to be updated and/or modified to improve the accuracy and performance of the simulations, as well as to include routines necessary for cellular dosimetry. Therefore, validation of the latest changes was required. A thorough comparison of the inputs and outputs of the code with available theoretical and experimental data in the literature was made at all levels: starting with the multiple-differential and total interaction cross sections, followed by comparisons in terms of track parameters including the stopping power, range and radial dose profiles. In general, the agreement of our results with experimental data and calculations reported by other authors was excellent, except for very low incident energies (below some tens of keV u^{-1} for ions and about 100 eV in the case of electrons). After validation, the code was applied for the first time to investigate the absorbed dose to the nucleus of a single tumor cell irradiated by protons. Furthermore, CELLDOSE, the dosimetric extension to the MCTS code EPOTRAN (in which electrons can be simulated as the primary particles), was modified as well to

model the decay of β^- and AE emitters in single tumor cells and in a small cell cluster.

The main original contribution of this thesis was, however, the development of routines in *TILDA-V* for allowing the transport and dosimetry of α-particles with kinetic energies ranging from 10 keV u^{-1} to 100 MeV u^{-1} in water. As part of this work, a new set of theoretical and semiempirical interaction cross sections was computed and implemented in *TILDA-V* for helium ions (He^{2+}, He^{+}, He^{0}). The new version of *TILDA-V* was tested by computing the stopping power and range of α-particles in water. The results of these transport simulations showed to be reliable and accurate enough (when compared with available experimental data and recommended values taken from the ICRU) for dosimetry purposes. Moreover, we added features to the code that allow the simulation of the full decay series of α-particle emitting radionuclides. In addition to all the code development work previously described, we believe that the calculations of cellular S-values for electron and α-particle emitters reported in this thesis will be relevant for the community of nuclear medicine, and more generally to everyone interested in internal radiation dosimetry at the cellular level. Indeed, the results obtained in terms of S-values and normalized absorbed doses are a good example of the way radiation physics and MC codes can help researchers to choose the most appropriate radionuclide for a given tumor situation, in the context of multidisciplinary efforts to find new and better therapies against cancer.

Outlook

Regarding *TILDA-V*, future developments should focus on improving both the physics behind simulations as well as the code performance. With respect to the first point, the influence on results of physical processes currently not taken into account, namely, multiple ionization and nuclear non-elastic scattering should be investigated in more detail and, if possible, included in the code. Of particular importance is the improvement of the theoretical framework for computing the cross sections for α-particles, especially if the same approach is used for describing the α-particle impact on DNA components. Concerning the code's performance, simulations are already very time-consuming and it may worth the effort to investigate the advantage (and feasibility) of changing from a full OpenMP parallelization to a hybrid approach (OpenMP + MPI).

Further work is also required to allow the user of *TILDA-V* to define more complex geometries in a relatively simple way. This is crucial to perform simulations with more realistic cell and/or DNA models, which is an obvious step to refine the studies carried out in this thesis with electron and α-particle emitters distributed inside single cells and cell clusters.

Other important points that should be addressed in future code developments are

modeling the physico-chemical and chemical stages of radiation damage (either within the code itself or by means of other tools or external modules), and the transport of recoil nuclei produced in radioactive decays. The former is necessary for quantifying the indirect effects of radiation, while the fate of recoil nuclei may be of great interest to fully elucidate the mechanisms of DNA damage induced directly by all the radiations emitted in α decays.

On the other hand, ongoing work with the current version of *TILDA-V* is devoted to analyze the energy deposited by proton, α-particle and electron beams in DNA components. This investigation aims to correlate the energy deposits in DNA components with experimental yields of DNA lesions (base damages, SSB, DSB).

As a last remark, we would like to point out that experimental data in terms of cross sections for ion impact on biological targets, and particularly DNA components, is still scarce. Therefore, future experimental work in this direction will be extremely valuable to confirm the predictions of the current theoretical models implemented in *TILDA-V*, especially in the low- and intermediate-energy ranges.

CONCLUSIONS ET PERSPECTIVES

Conclusions

La lutte contre le cancer est l'une des entreprises scientifiques les plus complexes et importantes de l'histoire de l'humanité. L'interdisciplinarité est aujourd'hui considérée comme un facteur clé pour faire avancer la recherche sur le cancer. Dans le cas des approches thérapeutiques utilisant les rayonnements ionisants, la physique joue un rôle fondamental pour comprendre les interactions des rayonnements avec la matière biologique. Ces interactions sont décrites par des sections efficaces, qui peuvent être utilisées dans des codes Monte Carlo pour simuler avec une grande précision l'énergie déposée par les rayonnements dans les tumeurs.

Le but de ce travail était d'améliorer un code Monte Carlo de structure de trace existant (*TILDA-V*) en ajoutant de nouveaux types de sources de rayonnements dans les simulations, ainsi que valider le code dans son ensemble pour des applications en dosimétrie des rayonnements ionisants, notamment pour faire des prédictions utiles dans le domaine de la RIV.

Pendant la première étape de la thèse, une série d'études ont été menées pour valider le transport des protons et leurs électrons secondaires dans l'eau et l'ADN. Alors que le transport de ces particules était déjà implémenté dans *TILDA-V*, certains aspects du code ont dû être mis à jour et/ou modifiés pour améliorer la précision et la performance des simulations, ainsi que pour inclure les routines nécessaires à la dosimétrie cellulaire. Par conséquent, la validation des dernières modifications était requise. Une comparaison approfondie des entrées et sorties du code avec les données théoriques et expérimentales disponibles dans la littérature a été faite à tous les niveaux: en commençant par les sections efficaces multiplement différentielles et totales d'interaction, suivie de comparaisons en termes de paramètres physiques pertinents au transport des particules chargées, y compris le pouvoir d'arrêt, le parcours (range) et la distribution de dose radiale. En général, la concordance de nos résultats avec les données expérimentales et les calculs rapportés par d'autres auteurs est excellente, sauf à très basse énergie (en dessous de quelques dizaines de $\mathrm{keV\,u^{-1}}$ pour les ions et environ 100 eV dans le cas des

électrons). Après validation, le code a été appliqué pour la première fois pour étudier la dose absorbée au noyau d'une cellule tumorale irradiée par des protons. De plus, CELLDOSE, l'extension dosimétrique du code Monte Carlo de structure de trace EPOTRAN (dans lequel les électrons peuvent être simulés en tant que particules primaires), a également été modifiée pour modéliser la désintégration de radionucléides émetteurs β^- et d'électrons Auger dans des cellules tumorales isolées et dans un petit amas de cellules.

La principale contribution originale de cette thèse a pourtant été le développement de routines en *TILDA-V* pour permettre le transport et la dosimétrie des particules α avec des énergies cinétiques allant de $10\,\mathrm{keV\,u^{-1}}$ à $100\,\mathrm{MeV\,u^{-1}}$ dans l'eau. Dans le cadre de ce travail, un nouvel ensemble de sections efficaces d'interaction théoriques et semi-empiriques a été calculé et implémenté dans *TILDA-V* pour les ions d'hélium (He^{2+}, He^{+}, He^{0}). Cette nouvelle version de *TILDA-V* a été testée en calculant le pouvoir d'arrêt et le parcours (range) des particules α dans l'eau. Les résultats de ces simulations de transport se sont révélés suffisamment fiables et précis (par rapport aux données expérimentales disponibles et aux valeurs recommandées tirées de l'ICRU) pour conclure que le code peut être utilisé à des fins de dosimétrie. De plus, nous avons ajouté des fonctionnalités au code qui permettent la simulation des chaînes de désintégration complètes des radionucléides émetteurs de particules α. En plus de tous les travaux de développement de code précédemment décrits, nous pensons que les calculs des facteurs S cellulaires pour les émetteurs d'électrons et de particules α rapportés dans cette thèse seront pertinents pour la communauté de médecine nucléaire, et plus généralement pour tous les gens intéressés par la dosimétrie interne des rayonnements à l'échelle cellulaire. En effet, les résultats obtenus en termes de facteurs S et de doses absorbées normalisées sont un bon exemple de la manière dont la physique des rayonnements et les codes Monte Carlo peuvent aider les chercheurs à choisir le radionucléide le plus approprié pour une situation tumorale donnée, dans le cadre des efforts multidisciplinaires pour trouver de nouvelles thérapies contre le cancer.

Perspectives

Concernant le code *TILDA-V*, les développements futurs devraient se concentrer sur l'amélioration à la fois de la physique derrière les simulations et la performance du code. En ce qui concerne le premier point, l'influence sur les calculs des processus physiques actuellement non pris en compte, à savoir l'ionisation multiple et les collisions nucléaires inélastiques, devrait être étudiée plus en détail et, si possible, ces processus devraient être rajoutés au code. L'amélioration du modèle théorique pour calculer les sections efficaces des particules α est particulièrement importante, surtout si le même modèle est utilisée pour décrire l'impact des particules α sur les composants de l'ADN. Concernant

la performance du code, les simulations prennent déjà beaucoup de temps. Dans ce contexte, il faudrait étudier si le passage d'une parallélisation OpenMP complète à une approche hybride (OpenMP + MPI) pourrait s'avérer utile pour résoudre ce problème.

Des travaux supplémentaires sont également nécessaires pour permettre à l'utilisateur de *TILDA-V* de définir des géométries plus complexes d'une manière relativement simple. Ceci est crucial pour effectuer des simulations avec des modèles cellulaires et/ou de l'ADN plus réalistes, ce qui serait la suite logique pour affiner les études menées dans cette thèse avec des émetteurs d'électrons et de particules α distribués à l'intérieur de cellules isolées et d'un amas de cellules.

D'autres points importants qui devraient être abordés dans les développements futurs du code sont la modélisation des étapes physico-chimique et chimique des dommages radio-induits dans la matière biologique (soit dans le code lui-même, soit au moyen d'autres outils ou modules externes) et le transport des noyaux de recul produits dans les désintégrations radioactives. Le premier point est nécessaire pour quantifier les effets indirects des rayonnements ionisants, tandis que le sort des noyaux de recul peut être d'un grand intérêt pour élucider pleinement les mécanismes des dommages induits directement sur l'ADN par toutes les particules émises lors d'une désintégration α.

D'autre part, les travaux en cours avec la version actuelle de *TILDA-V* sont consacrés à l'analyse de l'énergie déposée par des faisceaux de protons, de particules α et d'électrons dans les composants de l'ADN. Cette recherche vise à corréler les dépôts d'énergie dans les composants de l'ADN avec les rendements expérimentaux de formation des lésions dans l'ADN (dommages de bases, cassures simple brin, cassures double brin).

Finalement, nous tenons à souligner que les données expérimentales en termes de sections efficaces pour l'impact des ions sur des cibles biologiques, et plus particulièrement sur les composants de l'ADN, sont encore insuffisantes. Par conséquent, de futurs travaux expérimentaux dans ce sens seraient extrêmement précieux pour confirmer les prédictions des modèles théoriques actuels implémentés dans *TILDA-V*, notamment pour des collisions à basse et moyenne énergie.

References

[1] Quinto MA, Monti JM, Weck PF, Fojón OA, Hanssen J, Rivarola RD, *et al.* Monte Carlo simulation of proton track structure in biological matter. *Eur Phys J D*, **71**: 1–14, 2017. DOI: 10.1140/epjd/e2017-70709-6 (see pp. xiv, 15, 27, 28, 31, 40, 41, 43, 46, 47, 59, 71, 74, 75, 90)

[2] Champion C, Le Loirec C, and Stosic B. EPOTRAN: a full-differential Monte Carlo code for electron and positron transport in liquid and gaseous water. *Int J Radiat Biol*, **88**: 54–61, 2012. DOI: 10.3109/09553002.2011.641451 (see pp. xv, 27)

[3] Crothers DSF and McCann JF. Ionisation of atoms by ion impact. *J Phys B At Mol Phys*, **16**: 3229–3242, 1983. DOI: 10.1088/0022-3700/16/17/015 (see pp. xv, 48)

[4] Uehara S and Nikjoo H. Monte Carlo track structure code for low-energy alpha-particles in water. *J Phys Chem B*, **106**: 11051–11063, 2002. DOI: 10.1021/jp014004h (see pp. xv, xxi, 21–23, 28, 46, 53, 55, 56, 62, 63, 67, 68, 71, 150–152)

[5] Miller JH and Green AES. Proton energy degradation in water vapor. *Radiat Res*, **54**: 343–363, 1973. DOI: 10.2307/3573730 (see pp. xv, 23, 25, 26, 28, 44–46, 64–67, 151)

[6] Champion C, Cappello CD, Houamer S, and Mansouri A. Single ionization of the water molecule by electron impact: angular distributions at low incident energy. *Phys Rev A*, **73**: 012717, 2006. DOI: 10.1103/PhysRevA.73.012717 (see pp. xv, 28, 77, 80)

[7] Kim YK, Santos JP, and Parente F. Extension of the binary-encounter-dipole model to relativistic incident electrons. *Phys Rev A*, **62**: 052710, 2000. DOI: 10.1103/PhysRevA.62.052710 (see pp. xv, 28, 75)

[8] Olivero JJ, Stagat RW, and Green AES. Electron deposition in water vapor, with atmospheric applications. *J Geophys Res*, **77**: 4797–4811, 1972. DOI: 10.1029/JA077i025p04797 (see pp. xv, 28, 73, 74)

[9] Aouchiche H, Champion C, and Oubaziz D. Electron and positron elastic scattering in gaseous and liquid water: a comparative study. *Radiat Phys Chem*, **77**: 107–114, 2008. DOI: 10.1016/j.radphyschem.2007.09.004 (see pp. xv, 28, 39, 82–84)

[10] International Commission on Radiation Units and Measurements. *ICRU Report 49. Stopping power and ranges for protons and alpha particles*. ICRU, Bethesda, MD, 1993. DOI: 10.1093/jicru/os25.2.Report49 (see pp. xvi, xxi, 23, 29, 53, 71, 90, 91, 99, 100, 110, 149, 152, 153)

[11] Meesungnoen J, Jay-Gerin JP, Filali-Mouhim A, and Mankhetkorn S. Low-energy electron penetration range in liquid water. *Radiat Res*, **158**: 657–660, 2002. DOI: 10.1667/0033-7587(2002)158[0657:LEEPRI]2.0.CO;2 (see pp. xvii, xxii, 29, 91, 106)

[12] Rosenbluth MJ, Lam WA, and Fletcher DA. Force microscopy of nonadherent cells: a comparison of leukemia cell deformability. *Biophys J*, **90**: 2994–3003, 2006. (see pp. xviii, 107)

[13] Tan Q, Ferrier GA, Chen BK, Wang C, and Sun Y. Quantification of the specific membrane capacitance of single cells using a microfluidic device and impedance spectroscopy measurement. *Biomicrofluidics*, **6**: 034112, 2012. DOI: 10.1063/1.4746249 (see pp. xviii, 107)

[14] Champion C, Zanotti-Fregonara P, and Hindié E. CELLDOSE: A Monte Carlo code to assess electron dose distribution–S values for ^{131}I in spheres of various sizes. *J Nucl Med*, **49**: 151–157, 2008. DOI: 10.2967/jnumed.107.045179 (see pp. xviii, 131)

[15] Hindié E, Champion C, Zanotti-Fregonara P, Rubello D, Colas-Linhart N, Ravasi L, *et al.* Calculation of electron dose to target cells in a complex environment by Monte Carlo code 'CELLDOSE'. *Eur J Nucl Med Mol Imaging*, **36**: 130–136, 2009. DOI: 10.1007/s00259-008-0893-z (see pp. xviii, 131)

[16] Champion C, Quinto MA, Morgat C, Zanotti-Fregonara P, and Hindié E. Comparison between three promising β-emitting radionuclides, ^{67}Cu, ^{47}Sc and ^{161}Tb, with emphasis on doses delivered to minimal residual disease. *Theranostics*, **6**: 1611–1618, 2016. DOI: 10.7150/thno.15132 (see pp. xviii, xix, 122, 131, 136)

[17] Hindié E, Zanotti-Fregonara P, Quinto MA, Morgat C, and Champion C. Dose deposits from ^{90}Y, ^{177}Lu, ^{111}In, and ^{161}Tb in micrometastases of various sizes: implications for radiopharmaceutical therapy. *J Nucl Med*, **57**: 759–764, 2016. DOI: 10.2967/jnumed.115.170423 (see pp. xviii, xix, 122, 131, 136)

[18] International Commission on Radiological Protection. Nuclear decay data for dosimetric calculations. ICRP Publication 107. *Ann ICRP*, **38**: 7–96, 2008. DOI: 10.1016/j.icrp.2008.10.004 (see pp. xviii, xx, 19, 123, 127–129, 131, 146, 165, 166, 168, 172, 173)

[19] Goddu SM, Howell RW, and Rao DV. Cellular dosimetry: absorbed fractions for monoenergetic electron and alpha particle sources and S-values for radionuclides uniformly distributed in different cell compartments. *J Nucl Med*, **35**: 303–316, 1994. (see pp. xviii, 107, 131–133, 169)

[20] Abril I, Garcia-Molina R, Denton CD, Kyriakou I, and Emfietzoglou D. Energy loss of hydrogen- and helium-ion beams in DNA: calculations based on a realistic energy-loss function of the target. *Radiat Res*, **175**: 247–255, 2011. DOI: 10.1667/RR2142.1 (see pp. xxi, 59, 96, 97)

[21] Tan Z, Xia Y, Zhao M, and Liu X. Proton stopping power in a group of bioorganic compounds over the energy range of 0.05–10 MeV. *Nucl Instrum Methods Phys Res B*, **248**: 1–6, 2006. DOI: 10.1016/j.nimb.2006.04.073 (see pp. xxi, xxii, 43, 59, 95–97, 102, 104–106)

[22] Uehara S, Toburen LH, and Nikjoo H. Development of a Monte Carlo track structure code for low-energy protons in water. *Int J Radiat Biol*, **77**: 139–154, 2001. DOI: 10.1080/09553000010012536 (see pp. xxi, 21–23, 31, 64, 71, 99, 100)

[23] Janni JF. Proton range-energy tables, 1 keV–10 GeV, energy loss, range, path length, time-of-flight, straggling, multiple scattering, and nuclear interaction probability. Part I. For 63 compounds. *Atom Data Nucl Data*, **27**: 147–339, 1982. DOI: 10.1016/0092-640X(82)90004-3 (see pp. xxi, 99, 100)

[24] Francis Z, Incerti S, Karamitros M, Tran H, and Villagrasa C. Stopping power and ranges of electrons, protons and alpha particles in liquid water using the GEANT4-DNA package. *Nucl Instrum Methods Phys Res B*, **269**: 2307–2311, 2011. DOI: 10.1016/j.nimb.2011.02.031 (see pp. xxi, 100)

[25] Wingate CL and Baum JW. Measured radial distributions of dose and LET for alpha and proton beams in hydrogen and tissue-equivalent gas. *Radiat Res*, **65**: 1–19, 1976. DOI: 10.2307/3574282 (see pp. xxi, 101, 102)

[26] Incerti S, Psaltaki M, Gillet P, Barberet P, Bardiès M, Bernal MA, *et al.* Simulating radial dose of ion tracks in liquid water simulated with GEANT4-DNA: A comparative study. *Nucl Instrum Methods Phys Res B*, **333**: 92–98, 2014. DOI: 10.1016/j.nimb.2014.04.025 (see pp. xxi, 101)

[27] Waligórski M, Hamm RN, and Katz R. The radial distribution of dose around the path of a heavy ion in liquid water. *Int J Radiat Appl Instrum Part D. Nucl Tracks Radiat Meas*, **11**: 309–319, 1986. DOI: 10.1016/1359-0189(86)90057-9 (see pp. xxi, 101)

[28] Emfietzoglou D, Nikjoo H, Papamichael G, and Pathak A. Proton beam profiling in soft biological matter by detailed Monte Carlo simulation. *Nucl Instrum Methods Phys Res B*, **249**: 670–672, 2006. DOI: 10.1016/j.nimb.2006.03.055 (see pp. xxi, 101)

[29] Wiklund K, Olivera GH, Brahme A, and Lind BK. Radial secondary electron dose profiles and biological effects in light-ion beams based on analytical and Monte Carlo calculations using distorted wave cross sections. *Radiat Res*, **170**: 83–92, 2008. DOI: 10.1667/RR0961.1 (see pp. xxi, 101, 102)

[30] Nikjoo H, Uehara S, and Emfietzoglou D. *Interaction of radiation with matter*. Boca Raton, FL: Taylor & Francis, 2012. (see pp. xxi, 60, 66, 68, 101, 102, 106)

[31] Bäckström G, Galassi ME, Tilly N, Ahnesjö A, and Fernández-Varea JM. Track structure of protons and other light ions in liquid water: applications of the LIonTrack code at the nanometer scale. *Med Phys*, **40**: 064101, 2013. DOI: 10.1118/1.4803464 (see pp. xxi, 21, 101, 102)

[32] Matteson S, Powers D, and Chau EKL. Physical-state effect in the stopping cross section of H_2O ice and vapor for 0.3–2.0-MeV α particles. *Phys Rev A*, **15**: 856–864, 1977. DOI: 10.1103/PhysRevA.15.856 (see pp. xxi, 152)

[33] Thwaites DI. Stopping cross-sections of liquid water and water vapour for alpha particles within the energy region 0.3 to 5.5 MeV. *Phys Med Biol*, **26**: 71–80, 1981. DOI: 10.1088/0031-9155/26/1/008 (see pp. xxi, 152)

[34] International Atomic Energy Agency. *Atomic and Molecular Data for Radiotherapy and Radiation Research IAEA-TECDOC-799*. TECDOC Series IAEA, Vienna, 1995. (see pp. xxii, 105)

[35] International Commission on Radiation Units and Measurements. *ICRU Report 16. Linear energy transfer*. ICRU, Bethesda, MD, 1970. DOI: 10.1093/jicru/os9.1.Report16 (see pp. xxii, 105)

[36] Garcia-Molina R, Abril I, Kyriakou I, and Emfietzoglou D. Inelastic scattering and energy loss of swift electron beams in biologically relevant materials: Energy loss of electron beams in biomaterials. *Surf Interface Anal*, **49**: 11–17, 2017. DOI: 10.1002/sia.5947 (see pp. xxii, 102, 104–106)

[37] Paretzke H. *Simulation von Elektronenspuren im Energiebereich 0.01–10 keV in Wasserdampf GSF-Bericht 24/88*. Gesellschaft für Strahlen- und Umweltforschung mbH, München, 1988. (see pp. xxii, 22, 105)

[38] Bordage MC, Bordes J, Edel S, Terrissol M, Franceries X, Bardiès M, *et al.* Implementation of new physics models for low energy electrons in liquid water in GEANT4-DNA. *Phys Med*, **32**: 1833–1840, 2016. DOI: 10.1016/j.ejmp.2016.10.006 (see pp. xxii, 21, 25, 106)

[39] Vaziri B, Wu H, Dhawan AP, Du P, and Howell RW. MIRD pamphlet No. 25: MIRDcell V2.0 software tool for dosimetric analysis of biologic response of multicellular populations. *J Nucl Med*, **55**: 1557–1564, 2014. DOI: 10.2967/jnumed.113.131037 (see pp. xxiii, xxiv, 133–135, 169–172)

[40] Falzone N, Fernández-Varea JM, Flux G, and Vallis KA. Monte Carlo evaluation of Auger electron-emitting theranostic radionuclides. *J Nucl Med*, **56**: 1441–1446, 2015. DOI: 10.2967/jnumed.114.153502 (see pp. xxiii, 18, 131–135)

[41] Lee D, Li M, Bednarz B, and Schultz MK. Modeling cell and tumor-metastasis dosimetry with the Particle and Heavy Ion Transport code System (PHITS) software for targeted alpha-particle radionuclide therapy. *Radiat Res*, **190**: 236–247, 2018. DOI: 10.1667/RR15081.1 (see pp. xxiv, 169–172)

[42] Metropolis N and Ulam S. The Monte Carlo method. *J Am Stat Assoc*, **44**: 335–341, 1949. DOI: 10.2307/2280232 (see p. 10)

[43] Rogers DWO. Fifty years of Monte Carlo simulations for medical physics. *Phys Med Biol*, **51**: R287–301, 2006. DOI: 10.1088/0031-9155/51/13/R17 (see p. 10)

[44] Bielajew AF. "History of Monte Carlo" in: *Monte Carlo Techniques in Radiation Therapy* ed. by J Seco and F Verhaegen. Boca Raton: CRC/Taylor & Francis, 2013. Chap. 1, pp. 3–16. (see pp. 10, 16, 36)

[45] Berger MJ. Monte Carlo calculation of the penetration and diffusion of fast charged particles. *Methods Comput Phys*, **1**: 135–215, 1963. (see p. 10)

[46] Toburen LH. *Development of Monte Carlo track structure codes* (2014). URL: https://three.jsc.nasa.gov/articles/Monte-Carlo-Track-Structure-Toburen.pdf (visited on Jan. 30, 2020) (see p. 10)

[47] Champion C. *Structure des depots d'energie des ions rapides dans l'eau. Application à l'etude par Monte Carlo de l'inactivation cellulaire*. PhD thesis. 1999. (see p. 11)

[48] Haghighat A. *Monte Carlo methods for particle transport*. Boca Raton: CRC Press, 2014. (see pp. 13, 14)

[49] Bielajew AF. *Fundamentals of the Monte Carlo method for neutral and charged particle transport* (2001). URL: http://umich.edu/~nersa590/basics.pdf (visited on Jan. 30, 2020) (see p. 13)

[50] Matsumoto M and Nishimura T. Mersenne twister: a 623-dimensionally equidistributed uniform pseudo-random number generator. *ACM Trans Model Comput Simul*, **8**: 3–30, 1998. DOI: 10.1145/272991.272995 (see p. 13)

[51] Nahum AE. Condensed-history Monte-Carlo simulation for charged particles: what can it do for us? *Radiat Environ Bioph*, **38**: 163–173, 1999. DOI: 10.1007/s004110050152 (see p. 15)

[52] Andreo P. Monte Carlo techniques in medical radiation physics. *Phys Med Biol*, **36**: 861–920, 1991. DOI: 10.1088/0031-9155/36/7/001 (see p. 15)

[53] Chetty IJ, Curran B, Cygler JE, DeMarco JJ, Ezzell G, Faddegon BA, *et al.* Report of the AAPM Task Group No. 105: Issues associated with clinical implementation of Monte Carlo-based photon and electron external beam treatment planning. *Med Phys*, **34**: 4818–4853, 2007. DOI: 10.1118/1.2795842 (see p. 16)

[54] Nikjoo H, Emfietzoglou D, Liamsuwan T, Taleei R, Liljequist D, and Uehara S. Radiation track, DNA damage and response—a review. *Rep Prog Phys*, **79**: 116601, 2016. DOI: 10.1088/0034-4885/79/11/116601 (see pp. 16, 20)

[55] Kyriakou I, Emfietzoglou D, Ivanchenko V, Bordage MC, Guatelli S, Lazarakis P, *et al.* Microdosimetry of electrons in liquid water using the low-energy models of GEANT4. *J Appl Phys*, **122**: 024303, 2017. DOI: 10.1063/1.4992076 (see p. 16)

[56] Kyriakou I, Ivanchenko V, Sakata D, Bordage MC, Guatelli S, Incerti S, *et al.* Influence of track structure and condensed history physics models of GEANT4 to nanoscale electron transport in liquid water. *Phys Med*, **58**: 149–154, 2019. DOI: 10.1016/j.ejmp.2019.01.001 (see p. 16)

[57] Kawrakow I, Mainegra-Hing E, Rogers D, Tessier F, and Walters B. *The EGSnrc code system: Monte Carlo simulation of electron and photon transport* (2011). URL: https://nrc-cnrc.github.io/EGSnrc/doc/pirs701-egsnrc.pdf (visited on Feb. 5, 2020) (see p. 16)

[58] Goorley JT, James MR, Booth TE, Brown FB, Bull JS, Cox LJ, *et al.*. Initial MCNP6 release overview - MCNP6 version 1.0 Report LA-UR-13-22934. Los Alamos National Laboratory, United States, 2013. DOI: 10.2172/1086758 (see p. 17)

[59] Hughes H. Recent developments in low-energy electron/photon transport for MCNP6. Report LA-UR-12-24213 rev 4. Los Alamos National Laboratory, United States, 2013 (see p. 17)

[60] Allison J, Amako K, Apostolakis J, Arce P, Asai M, Aso T, *et al.* Recent developments in GEANT4. *Nucl Instrum Methods Phys Res A*, **835**: 186–225, 2016. DOI: 10.1016/j.nima.2016.06.125 (see p. 17)

[61] Jan S, Benoit D, Becheva E, Carlier T, Cassol F, Descourt P, *et al.* GATE V6: a major enhancement of the GATE simulation platform enabling modelling of CT and radiotherapy. *Phys Med Biol*, **56**: 881–901, 2011. DOI: 10.1088/0031-9155/56/4/001 (see p. 17)

[62] Ivanchenko V, Apostolakis J, Bagulya A, Abdelouahed HB, Black R, Bogdanov A, *et al.* Recent improvements in GEANT4 electromagnetic physics models and interfaces. *Prog Nucl Sci Technol*, **2**: 898–903, 2011. DOI: 10.15669/pnst.2.898 (see p. 17)

[63] Battistoni G, Boehlen T, Cerutti F, Chin PW, Esposito LS, Fassò A, *et al.* Overview of the FLUKA code. *Ann Nucl Energy*, **82**: 10–18, 2015. DOI: 10.1016/j.anucene.2014.11.007 (see p. 18)

[64] Battistoni G, Bauer J, Boehlen TT, Cerutti F, Chin MPW, Dos Santos Augusto R, *et al.* The FLUKA code: an accurate simulation tool for particle therapy. *Front Oncol*, **6**: 2016. DOI: 10.3389/fonc.2016.00116 (see p. 18)

[65] Salvat F. The PENELOPE code system. Specific features and recent improvements. *Ann Nucl Energy*, **82**: 98–109, 2015. DOI: 10.1016/j.anucene.2014.08.007 (see p. 18)

[66] Del Lama LS, Cunha DM, and Poletti ME. Validation of a modified PENELOPE Monte Carlo code for applications in digital and dual-energy mammography. *Radiat Phys Chem*, **137**: 151–156, 2017. DOI: 10.1016/j.radphyschem.2016.03.004 (see p. 18)

[67] Guerrero R, Almansa JF, Torres J, and Lallena AM. Dosimetric characterization of the ^{60}Co BEBIG Co0.A86 high dose rate brachytherapy source using PENELOPE. *Phys Med*, **30**: 960–967, 2014. DOI: 10.1016/j.ejmp.2014.06.039 (see p. 18)

[68] Sempau J, Badal A, and Brualla L. A PENELOPE-based system for the automated Monte Carlo simulation of clinacs and voxelized geometries-application to far-from-axis fields. *Med Phys*, **38**: 5887–5895, 2011. DOI: 10.1118/1.3643029 (see p. 18)

[69] Borbinha J, Vaz P, and Di Maria S. Dosimetric assessment in different tumour phenotypes with auger electron emitting radionuclides: ^{99m}Tc, ^{125}I, ^{161}Tb, and ^{177}Lu. *Radiat Phys Chem*, **172**: 108763, 2020. DOI: 10.1016/j.radphyschem.2020.108763 (see p. 18)

[70] Sato T, Iwamoto Y, Hashimoto S, Ogawa T, Furuta T, Abe Si, *et al.* Features of Particle and Heavy Ion Transport code System (PHITS) version 3.02. *J Nucl Sci Technol*, **55**: 684–690, 2018. DOI: 10.1080/00223131.2017.1419890 (see p. 19)

[71] Geissel H, Scheidenberger C, Malzacher P, Kunzendorf J, and Weick H. *ATIMA*. GSI, Darmstadt, Germany. URL: http://web-docs.gsi.de/~weick/atima/ (visited on Jan. 28, 2021) (see p. 19)

[72] Hirayama H, Namito Y, Bielajew AF, Wilderman SJ, and Nelson WR. *The EGS5 code system*. Menlo Park, USA and Tsukuba, Japan: SLAC National Accelerator Laboratory and High Energy Accelerator Research Organization. SLAC-R-730 and KEK Report 2005-8, 2015. URL: http://rcwww.kek.jp/research/egs/egs5_manual/slac730-150228.pdf (visited on Jan. 28, 2021) (see p. 19)

[73] Matsuya Y, Kai T, Sato T, Liamsuwan T, Sasaki K, and Nikjoo H. Verification of KURBUC-based ion track structure mode for proton and carbon ions in the PHITS code. *Phys Med Biol*, 2021. DOI: 10.1088/1361-6560/abe65e (see p. 19)

[74] Alcocer-Ávila ME, Quinto MA, Monti JM, Rivarola RD, and Champion C. "Electron transport modeling in biological tissues: from water to DNA" in: *Quantum Collisions and Confinement of Atomic and Molecular Species, and Photons* ed. by PC Deshmukh, E Krishnakumar, S Fritzsche, M Krishnamurthy, and S Majumder. Vol. 230, Springer Proceedings in Physics. Singapore: Springer, 2019. pp. 137–154. DOI: 10.1007/978-981-13-9969-5_13 (see pp. 20, 88)

[75] Thomson RM and Kawrakow I. On the Monte Carlo simulation of electron transport in the sub-1 keV energy range. *Med Phys*, **38**: 4531–4534, 2011. DOI: 10.1118/1.3608904 (see p. 20)

[76] Nikjoo H, Uehara S, Emfietzoglou D, and Cucinotta F. Track-structure codes in radiation research. *Radiat Meas*, **41**: 1052–1074, 2006. DOI: 10.1016/j.radmeas.2006.02.001 (see p. 20)

[77] Uehara S, Nikjoo H, and Goodhead DT. Cross-sections for water vapour for the Monte Carlo electron track structure code from 10 eV to the MeV region. *Radiat Res*, **38**: 1841–1858, 1993. DOI: 10.1088/0031-9155/38/12/010 (see pp. 21, 22, 26)

[78] Liamsuwan T, Uehara S, Emfietzoglou D, and Nikjoo H. Physical and biophysical properties of proton tracks of energies 1 keV to 300 MeV in water. *Int J Radiat Biol*, **87**: 141–160, 2011. DOI: 10.3109/09553002.2010.518204 (see pp. 21–23, 64, 71)

[79] Liamsuwan T, Emfietzoglou D, Uehara S, and Nikjoo H. Microdosimetry of low-energy electrons. *Int J Radiat Biol*, **88**: 899–907, 2012. DOI: 10.3109/09553002.2012.699136 (see pp. 21, 22)

[80] Liamsuwan T and Nikjoo H. A Monte Carlo track structure simulation code for the full-slowing-down carbon projectiles of energies 1 keV u^{-1} – 10 MeV u^{-1} in water. *Phys Med Biol*, **58**: 673–701, 2013. DOI: 10.1088/0031-9155/58/3/673 (see pp. 21, 22)

[81] Friedland W, Dingfelder M, Kundrát P, and Jacob P. Track structures, DNA targets and radiation effects in the biophysical Monte Carlo simulation code PARTRAC. *Mutat Res-Fund Mol M*, **711**: 28–40, 2011. DOI: 10.1016/j.mrfmmm.2011.01.003 (see pp. 21, 24)

[82] Alloni D, Campa A, Friedland W, Mariotti L, and Ottolenghi A. Track structure, radiation quality and initial radiobiological events: considerations based on the PARTRAC code experience. *Int J Radiat Biol*, **88**: 77–86, 2012. DOI: 10.3109/09553002.2011.627976 (see pp. 21, 24, 25)

[83] Friedland W and Kundrát P. "Modeling of radiation effects in cells and tissues" in: *Comprehensive Biomedical Physics* ed. by A Brahme. Vol. 9, Amsterdam: Elsevier, 2014. pp. 105–142. DOI: 10.1016/B978-0-444-53632-7.00906-0 (see pp. 21, 24)

[84] Incerti S, Baldacchino G, Bernal M, Capra R, Champion C, Francis Z, *et al.* The GEANT4-DNA project. *Int J Model Simul Sci Comput*, **1**: 157–178, 2010. DOI: 10.1142/S1793962310000122 (see pp. 21, 25)

[85] Bernal MA, Bordage MC, Brown JMC, Davídková M, Delage E, El Bitar Z, *et al.* Track structure modeling in liquid water: A review of the GEANT4-DNA very low energy extension of the GEANT4 Monte Carlo simulation toolkit. *Phys Med*, **31**: 861–874, 2015. DOI: 10.1016/j.ejmp.2015.10.087 (see pp. 21, 25)

[86] Wilson WE and Nikjoo H. A Monte Carlo code for positive ion track simulation. *Radiat Environ Bioph*, **38**: 97–104, 1999. DOI: 10.1007/s004110050144 (see p. 21)

[87] Lappa AV, Bigildeev EA, Burmistrov DS, and Vasilyev ON. Trion code for radiation action calculations and its application in microdosimetry and radiobiology. *Radiat Environ Bioph*, **32**: 1-19 ST –?, 1993. DOI: 10.1007/BF01213126 (see p. 21)

[88] Emfietzoglou D, Papamichael G, Kostarelos K, and Moscovitch M. A Monte Carlo track structure code for electrons (∼10 eV-10 keV) and protons (∼0.3-10 MeV) in water: partitioning of energy and collision events. *Phys Med Biol*, **45**: 3171–3194, 2000. DOI: 10.1088/0031-9155/45/11/305 (see p. 21)

[89] Emfietzoglou D, Karava K, Papamichael G, and Moscovitch M. Monte Carlo simulation of the energy loss of low-energy electrons in liquid water. *Phys Med Biol*, **48**: 2355–2371, 2003. DOI: 10.1088/0031-9155/48/15/308 (see p. 21)

[90] Semenenko VA, Turner JE, and Borak TB. NOREC, a Monte Carlo code for simulating electron tracks in liquid water. *Radiat Environ Bioph*, **42**: 213–217, 2003. DOI: 10.1007/s00411-003-0201-z (see p. 21)

[91] Plante I and Cucinotta FA. Ionization and excitation cross sections for the interaction of HZE particles in liquid water and application to Monte Carlo simulation of radiation tracks. *New J Phys*, **10**: 125020, 2008. DOI: 10.1088/1367-2630/10/12/125020 (see pp. 21, 27)

[92] Plante I and Cucinotta FA. Cross sections for the interactions of 1 eV–100 MeV electrons in liquid water and application to Monte-Carlo simulation of HZE radiation tracks. *Radiat Prot Dosim*, **11**: 063047, 2009. DOI: 10.1088/1367-2630/11/6/063047 (see pp. 21, 29)

[93] Grosswendt B and Pszona S. The track structure of α-particles from the point of view of ionization-cluster formation in "nanometric" volumes of nitrogen. *Radiat Environ Bioph*, **41**: 91–102, 2002. DOI: 10.1007/s00411-002-0144-9 (see p. 21)

[94] Bug MU, Hilgers G, Baek WY, and Rabus H. Nanodosimetric characterization of ion beams. *Eur Phys J D*, **68**: 541, 2014. DOI: 10.1140/epjd/e2014-50015-9 (see p. 21)

[95] Uehara S and Nikjoo H. Monte Carlo simulation of water radiolysis for low-energy charged particles. *J Radiat Res*, **47**: 69–81, 2006. DOI: 10.1269/jrr.47.69 (see pp. 22, 106)

[96] Seltzer SM. "Cross sections for Bremsstrahlung production and electron-impact ionization" in: *Monte Carlo Transport of Electrons and Photons* ed. by TM Jenkins, WR Nelson, and A Rindi. Vol. 35, Boston, MA: Springer, 1988. pp. 81–114. DOI: 10.1007/978-1-4613-1059-4_4 (see p. 22)

[97] Berger MJ and Wang R. "Multiple-scattering angular deflections and energy-loss straggling" in: *Monte Carlo Transport of Electrons and Photons* ed. by TM Jenkins, WR Nelson, and A Rindi. Boston, MA: Springer, 1988. pp. 21–56. DOI: 10.1007/978-1-4613-1059-4_2 (see p. 22)

[98] Moliere G. Theorie der Streuung schneller geladener Teilchen II Mehrfach-und Vielfachstreuung. *Z Naturf*, **3**: 78–97, 1948. DOI: 10.1515/zna-1948-0203 (see p. 22)

[99] Nishimura H. “Elastic scattering cross-sections of H_2O by low energy electrons” in: *Electronic and Atomic Collisions. Proceedings of the XI International Conference* ed. by N Oda and K Takayanagi. Amsterdam, North-Holland, 1979. pp. 314. (see p. 22)

[100] Katase A, Ishibashi K, Matsumoto Y, Sakae T, Maezono S, Murakami E, *et al.* Elastic scattering of electrons by water molecules over the range 100–1000 eV. *J Phys B At Mol Phys*, **19**: 2715–2734, 1986. DOI: 10.1088/0022-3700/19/17/020 (see p. 22)

[101] Rudd ME, Goffe TV, DuBois RD, and Toburen LH. Cross sections for ionization of water vapor by 7–4000-keV protons. *Phys Rev A*, **31**: 492–494, 1985. DOI: 10.1103/PhysRevA.31.492 (see pp. 22, 52, 58, 64–66)

[102] Green AES and McNeal RJ. Analytic cross sections for inelastic collisions of protons and hydrogen atoms with atomic and molecular gases. *J Geophys Res*, **76**: 133–144, 1971. DOI: 10.1029/JA076i001p00133 (see p. 22)

[103] Rudd ME, Kim YK, Madison DH, and Gay TJ. Electron production in proton collisions with atoms and molecules: energy distributions. *Rev Mod Phys*, **64**: 441–490, 1992. DOI: 10.1103/RevModPhys.64.441 (see pp. 22, 23, 25, 26, 54, 55, 76)

[104] Bolorizadeh MA and Rudd ME. Angular and energy dependence of cross sections for ejection of electrons from water vapor. II. 15–150-keV proton impact. *Phys Rev A*, **33**: 888–892, 1986. DOI: 10.1103/PhysRevA.33.888 (see pp. 23, 52, 57, 58)

[105] Toburen LH and Wilson WE. Energy and angular distributions of electrons ejected from water vapor by 0.3–1.5 MeV protons. *J Chem Phys*, **66**: 5202–5213, 1977. DOI: 10.1063/1.433783 (see pp. 23, 52, 57)

[106] Rudd ME, Goffe TV, and Itoh A. Ionization cross sections for 10–300-keV/u and electron-capture cross sections for 5–150-keV/u $^3He^{2+}$ ions in gases. *Phys Rev A*, **32**: 2128–2133, 1985. DOI: 10.1103/PhysRevA.32.2128 (see pp. 23, 53, 58, 62, 63)

[107] Rudd ME, Itoh A, and Goffe TV. Cross sections for ionization, capture, and loss for 5–450-keV He^+ on water vapor. *Phys Rev A*, **32**: 2499–2500, 1985. DOI: 10.1103/PhysRevA.32.2499 (see pp. 23, 53, 62, 63, 68)

[108] Sataka M, Yagishita A, and Nakai Y. Measurement of charge-changing cross sections in collisions of He and He^+ with H_2, O_2, CH_4, CO and CO_2. *J Phys B At Mol Opt Phys*, **23**: 1225–1234, 1990. DOI: 10.1088/0953-4075/23/7/018 (see pp. 23, 62, 63, 68)

[109] Allison SK. Experimental results on charge-changing collisions of hydrogen and helium atoms and ions at kinetic energies above 0.2 keV. *Rev Mod Phys*, **30**: 1137–1168, 1958. DOI: 10.1103/RevModPhys.30.1137 (see pp. 23, 68, 150)

[110] Toburen LH, Wilson WE, and Popowich RJ. Secondary electron emission from ionization of water vapor by 0.3- to 2.0-MeV He^+ and He^{2+} ions. *Radiat Res*, **82**: 27, 1980. DOI: 10.2307/3575234 (see pp. 23, 53, 57, 58)

[111] Dingfelder M, Hantke D, Inokuti M, and Paretzke HG. Electron inelastic-scattering cross sections in liquid water. *Radiat Phys Chem*, **53**: 1–18, 1998. DOI: 10.1016/S0969-806X(97)00317-4 (see pp. 24, 26, 102)

[112] Berger MJ, Seltzer SM, Wang RQ, and Schechter A. Elastic scattering of electrons and positrons by atoms: database ELAST, Report NISTIR 5188 Gaithersburg, MD, 1993 (see p. 24)

[113] Dingfelder M, Ritchie RH, Turner JE, Friedland W, Paretzke HG, and Hamm RN. Comparisons of calculations with PARTRAC and NOREC: transport of electrons in liquid water. *Radiat Res*, **169**: 584–594, 2008. DOI: 10.1667/RR1099.1 (see pp. 24, 102)

[114] Dingfelder M, Inokuti M, and Paretzke HG. Inelastic-collision cross sections of liquid water for interactions of energetic protons. *Radiat Phys Chem*, **59**: 255–275, 2000. (see pp. 25–28, 31, 45, 64–66, 94, 97)

[115] Friedland W, Dingfelder M, Jacob P, and Paretzke HG. Calculated DNA double-strand break and fragmentation yields after irradiation with He ions. *Radiat Phys Chem*, **72**: 279–286, 2005. DOI: 10.1016/j.radphyschem.2004.05.053 (see p. 25)

[116] Dingfelder M. Cross section calculations in condensed media: charged particles in liquid water. *Radiat Prot Dosim*, **99**: 23–27, 2002. DOI: 10.1093/oxfordjournals.rpd.a006770 (see p. 25)

[117] Incerti S, Douglass M, Penfold S, Guatelli S, and Bezak E. Review of GEANT4-DNA applications for micro and nanoscale simulations. *Phys Med*, **32**: 1187–1200, 2016. DOI: 10.1016/j.ejmp.2016.09.007 (see p. 26)

[118] Emfietzoglou D and Nikjoo H. The effect of model approximations on single-collision distributions of low-energy electrons in liquid water. *Radiat Res*, **163**: 98–111, 2005. DOI: 10.1667/rr3281 (see p. 26)

[119] Champion C, Incerti S, Aouchiche H, and Oubaziz D. A free-parameter theoretical model for describing the electron elastic scattering in water in the GEANT4 toolkit. *Radiat Phys Chem*, **78**: 745–750, 2009. DOI: 10.1016/j.radphyschem.2009.03.079 (see p. 26)

[120] Kim YK and Rudd M. Binary-encounter-dipole model for electron-impact ionization. *Phys Rev A*, **50**: 3954–3967, 1994. DOI: 10.1103/PhysRevA.50.3954 (see pp. 26, 75)

[121] Incerti S, Ivanchenko A, Karamitros M, Mantero A, Moretto P, Tran HN, *et al.* Comparison of GEANT4 very low energy cross section models with experimental data in water. *Med Phys*, **37**: 4692–4708, 2010. DOI: 10.1118/1.3476457 (see pp. 26, 27)

[122] Incerti S, Kyriakou I, Bernal MA, Bordage MC, Francis Z, Guatelli S, *et al.* GEANT4-DNA example applications for track structure simulations in liquid water: a report from the GEANT4-DNA Project. *Med Phys*, e722–e739, 2018. DOI: 10.1002/mp.13048 (see pp. 26, 98, 104)

[123] Tran HN, El Bitar Z, Champion C, Karamitros M, Bernal MA, Francis Z, *et al.* Modeling proton and alpha elastic scattering in liquid water in GEANT4-DNA. *Nucl Instrum Methods Phys Res B*, **343**: 132–137, 2015. DOI: 10.1016/j.nimb.2014.10.016 (see p. 27)

[124] Francis Z, Incerti S, Ivanchenko V, Champion C, Karamitros M, Bernal MA, *et al.* Monte Carlo simulation of energy-deposit clustering for ions of the same LET in liquid water. *Phys Med Biol*, **57**: 209–224, 2012. (see p. 27)

[125] Monti JM, Tachino CA, Hanssen J, Fojón OA, Galassi ME, Champion C, *et al.* Distorted wave calculations for electron loss process induced by bare ion impact on biological targets. *Appl Radiat Isotopes*, **83**: 105–108, 2014. DOI: 10.1016/j.apradiso.2012.12.016 (see pp. 28, 49)

[126] Quinto MA, Montenegro PR, Monti JM, Fojón OA, and Rivarola RD. Electron capture by swift ions from molecules of biological interest. *J Phys B At Mol Opt Phys*, **51**: 165201, 2018. DOI: 10.1088/1361-6455/aad152 (see pp. 28, 60)

[127] Champion C, Incerti S, Tran H, and El Bitar Z. Electron and proton elastic scattering in water vapour. *Nucl Instrum Methods Phys Res B*, **273**: 98–101, 2012. DOI: 10.1016/j.nimb.2011.07.049 (see p. 28)

[128] Quinto MA, Monti JM, Champion C, and Rivarola RD. Neutral hydrogen versus proton-induced ionization in water vapor. *Phys Rev A*, **100**: 042704, 2019. DOI: 10.1103/PhysRevA.100.042704 (see pp. 28, 51, 52)

[129] Uehara S, Toburen L, Wilson W, Goodhead D, and Nikjoo H. Calculations of electronic stopping cross sections for low-energy protons in water. *Radiat Phys Chem*, **59**: 1–11, 2000. DOI: 10.1016/S0969-806X(00)00190-0 (see pp. 28, 94)

[130] Endo S, Yoshida E, Nikjoo H, Uehara S, Hoshi M, Ishikawa M, *et al.* A Monte Carlo track structure code for low energy protons. *Nucl Instrum Methods Phys Res B*, **194**: 123–131, 2002. DOI: 10.1016/S0168-583X(02)00497-4 (see pp. 28, 71)

[131] Abicht F, Prasad R, Borghesi M, Priebe G, Braenzel J, Andreev A, *et al.* Energetic beams of negative and neutral hydrogen from intense laser plasma interaction. *Appl Phys Lett*, **103**: 253501, 2013. DOI: 10.1063/1.4850456 (see p. 32)

[132] International Commission on Radiation Units and Measurements. *ICRU Report 63. Nuclear data for neutron and proton radiotherapy and for radiation protection*. ICRU, Bethesda, MD, 2000. NP DOI: 10.1093/jicru/os32.2.Report63 (see p. 35)

[133] Newhauser WD and Zhang R. The physics of proton therapy. *Phys Med Biol*, **60**: R155–R209, 2015. DOI: 10.1088/0031-9155/60/8/R155 (see p. 35)

[134] Medin J and Andreo P. Monte Carlo calculated stopping-power ratios, water/air, for clinical proton dosimetry (50–250 MeV). *Phys Med Biol*, **42**: 89–105, 1997. DOI: 10.1088/0031-9155/42/1/006 (see p. 35)

[135] Paganetti H. Nuclear interactions in proton therapy: dose and relative biological effect distributions originating from primary and secondary particles. *Phys Med Biol*, **47**: 747–764, 2002. DOI: 10.1088/0031-9155/47/5/305 (see p. 35)

[136] Wroe AJ, Cornelius IM, and Rosenfeld AB. The role of nonelastic reactions in absorbed dose distributions from therapeutic proton beams in different medium: nonelastic reactions in absorbed dose distributions for protons. *Med Phys*, **32**: 37–41, 2004. DOI: 10.1118/1.1824194 (see p. 35)

[137] Toburen LH. Challenges in Monte Carlo track structure modelling. *Int J Radiat Biol*, **88**: 2–9, 2012. DOI: 10.3109/09553002.2011.574781 (see p. 36)

[138] Bug MU, Yong Baek W, Rabus H, Villagrasa C, Meylan S, and Rosenfeld AB. An electron-impact cross section data set (10 eV–1 keV) of DNA constituents based on consistent experimental data: A requisite for Monte Carlo simulations. *Radiat Phys Chem*, **130**: 459–479, 2017. DOI: 10.1016/j.radphyschem.2016.09.027 (see p. 38)

[139] Rudek B, Bennett D, Bug MU, Wang M, Baek WY, Buhr T, *et al.* Double differential cross sections for proton induced electron emission from molecular analogues of DNA constituents for energies in the Bragg peak region. *J Chem Phys*, **145**: 104301, 2016. DOI: 10.1063/1.4962171 (see p. 38)

[140] Galassi ME, Champion C, Weck PF, Rivarola RD, Fojón O, and Hanssen J. Quantum-mechanical predictions of DNA and RNA ionization by energetic proton beams. *Phys Med Biol*, **57**: 2081–2099, 2012. DOI: 10.1088/0031-9155/57/7/2081 (see pp. 38, 42, 43, 48, 224–228)

[141] Berger M, Coursey J, Zucker M, and Chang J.. ESTAR, PSTAR, and ASTAR: Computer programs for calculating stopping-power and range tables for electrons, protons, and helium ions (version 1.2.3). National Institute of Standards and Technology, Gaithersburg, MD 2005 (see pp. 39, 97, 98)

[142] Champion C. Electron impact ionization of liquid and gaseous water: a single-center partial-wave approach. *Phys Med Biol*, **55**: 11–32, 2010. DOI: 10.1088/0031-9155/55/1/002 (see p. 39)

[143] Alcocer-Ávila ME, Quinto MA, Monti JM, Rivarola RD, and Champion C. Proton transport modeling in a realistic biological environment by using *TILDA-V*. *Sci Rep*, **9**: 1–18, 2019. DOI: 10.1038/s41598-019-50270-5 (see pp. 40, 43, 46, 49, 50, 67, 71, 88, 89, 94, 96, 100, 107–109, 111, 112)

[144] Pople JA, Santry DP, and Segal GA. Approximate self-consistent molecular orbital theory. I. Invariant procedures. *J Chem Phys*, **43**: S129–S135, 1965. DOI: 10.1063/1.1701475 (see p. 40)

[145] Senger B, Wittendorp-Rechenmann E, and Rechenmann RV. Ionization cross-sections in the case of medium and low energy heavy charged particles crossing complex media. *Nucl Instrum Methods Phys Res B*, **194**: 437–441, 1982. DOI: 10.1016/0029-554X(82)90560-2 (see p. 40)

[146] Tachino CA, Monti JM, Fojón OA, Champion C, and Rivarola RD. Ionization of water molecules by ion beams. On the relevance of dynamic screening and the influence of the description of the initial state. *J Phys B At Mol Opt Phys*, **47**: 035203, 2014. DOI: 10.1088/0953-4075/47/3/035203 (see pp. 40, 41, 53)

[147] Siegbahn K, Nordling C, Johansson G, Hedman J, Hedén P, Hamrin K, *et al. ESCA Applied to Free Molecules*. Amsterdam: North-Holland, 1969. (see p. 40)

[148] Clementi E and Roetti C. Roothaan-Hartree-Fock atomic wavefunctions: basis functions and their coefficients for ground and certain excited states of neutral and ionized atoms, $Z \leq 54$. *Atom Data Nucl Data*, **14**: 177, 1974. DOI: 10.1016/S0092-640X(74)80016-1 (see p. 40)

[149] Moccia R. One-center basis set SCF MO's. III. H_2O, H_2S, and HCl. *J Chem Phys*, **40**: 2186–2192, 1964. DOI: 10.1063/1.1725491 (see pp. 41, 81, 223)

[150] Willers H, Dahm-Daphi J, and Powell SN. Repair of radiation damage to DNA. *Br J Cancer*, **90**: 1297–1301, 2004. DOI: 10.1038/sj.bjc.6601729 (see p. 42)

[151] Alberts B, Johnson A, Lewis J, Morgan D, Raff M, Roberts K, *et al. Molecular biology of the cell*. 6th ed. New York, NY: Garland Science, 2015. (see p. 42)

[152] Frisch MJ, Trucks GW, Schlegel HB, Scuseria GE, Robb MA, Cheeseman JR, *et al.*. Gaussian 09, Revision A.02. Gaussian Inc. Wallingford, CT, 2009 (see pp. 42, 76)

[153] Mulliken RS. Electronic population analysis on LCAO-MO molecular wave functions. I. *J Chem Phys*, **23**: 1833–1840, 1955. DOI: 10.1063/1.1740588 (see p. 43)

[154] LaVerne JA and Pimblott SM. Electron energy-loss distributions in solid, dry DNA. *Radiat Res*, **141**: 208–215, 1995. DOI: 10.2307/3579049 (see pp. 43, 104, 107)

[155] Birnie G, Rickwood D, and Hell A. Buoyant densities and hydration of nucleic acids, proteins and nucleoprotein complexes in metrizamide. *Biochim Biophys Acta - Nucleic Acids Protein Synth*, **331**: 283–294, 1973. DOI: 10.1016/0005-2787(73)90441-3 (see p. 43)

[156] Champion C, Quinto MA, Monti JM, Galassi ME, Weck PF, Fojón OA, *et al.* Water versus DNA: new insights into proton track-structure modelling in radiobiology and radiotherapy. *Phys Med Biol*, **60**: 7805–7828, 2015. DOI: 10.1088/0031-9155/60/20/7805 (see pp. 43, 66, 110)

[157] Drake GWF, ed. *Springer handbook of atomic, molecular, and optical physics*. 2nd ed. New York, NY: Springer, 2006. (see p. 44)

[158] Belkić D. *Quantum theory of high-energy ion-atom collisions*. Boca Raton, FL: CRC Press, 2009. (see p. 44)

[159] Champion C. Theoretical cross sections for electron collisions in water: structure of electron tracks. *Phys Med Biol*, **48**: 2147, 2003. DOI: 10.1088/0031-9155/48/14/308 (see p. 44)

[160] Fainstein PD, Ponce VH, and Rivarola RD. A theoretical model for ionisation in ion-atom collisions. Application for the impact of multicharged projectiles on helium. *J Phys B At Mol Opt Phys*, **21**: 287–299, 1988. DOI: 10.1088/0953-4075/21/2/013 (see pp. 48, 50)

[161] Monti JM, Rivarola RD, and Fainstein PD. Quantum interferences in swift highly-charged dressed-ion–atom collisions. *J Phys B At Mol Opt Phys*, **41**: 201001, 2008. DOI: 10.1088/0953-4075/41/20/201001 (see pp. 48, 51)

[162] McCarroll R and Salin A. Impact parameter treatment of atomic collisions. *J Phys B At Mol Phys*, **1**: 163–171, 1968. DOI: 10.1088/0022-3700/1/2/305 (see p. 49)

[163] Monti JM, Fojón OA, Hanssen J, and Rivarola RD. Influence of the dynamic screening on single-electron ionization of multi-electron atoms. *J Phys B At Mol Opt Phys*, **43**: 205203, 2010. DOI: 10.1088/0953-4075/43/20/205203 (see p. 51)

[164] Monti JM, Rivarola RD, and Fainstein PD. Distorted wave theories for dressed-ion–atom collisions with GSZ projectile potentials. *J Phys B At Mol Opt Phys*, **44**: 195206, 2011. DOI: 10.1088/0953-4075/44/19/195206 (see p. 51)

[165] Green AES, Sellin DL, and Zachor AS. Analytic independent-particle model for atoms. *Phys Rev*, **184**: 1–9, 1969. DOI: 10.1103/PhysRev.184.1 (see p. 51)

[166] Gobet F, Eden S, Coupier B, Tabet J, Farizon B, Farizon M, *et al.* Ionization of water by (20–150)-keV protons: Separation of direct-ionization and electron-capture processes. *Phys Rev A*, **70**: 1150, 2004. DOI: 10.1103/PhysRevA.70.062716 (see pp. 52, 58)

[167] Luna H, de Barros ALF, Wyer JA, Scully SWJ, Lecointre J, Garcia PMY, *et al.* Water-molecule dissociation by proton and hydrogen impact. *Phys Rev A*, **75**: 2007. DOI: 10.1103/PhysRevA.75.042711 (see pp. 52, 58)

[168] Bolorizadeh MA and Rudd ME. Angular and energy dependence of cross sections for ejection of electrons from water vapor. III. 20–150-keV neutral-hydrogen impact. *Phys Rev A*, **33**: 893–896, 1986. DOI: 10.1103/PhysRevA.33.893 (see p. 52)

[169] Gobet F, Eden S, Coupier B, Tabet J, Farizon B, Farizon M, *et al.* Electron-loss and target ionization cross sections for water vapor by 20–150 keV neutral atomic hydrogen impact. *Chem Phys Lett*, **421**: 68–71, 2006. DOI: 10.1016/j.cplett.2006.01.016 (see p. 52)

[170] Champion C, Boudrioua O, Dal Cappello C, Sato Y, and Ohsawa D. Theoretical and experimental investigations of electron emission in $He^{2+}+H_2O$ collisions. *Phys Rev A*, **75**: 181, 2007. DOI: 10.1103/PhysRevA.75.032724 (see p. 53)

[171] Ohsawa D, Sato Y, Okada Y, Shevelko VP, and Soga F. 6.0–10.0−MeV/u He^{2+} -ion-induced electron emission from water vapor. *Phys Rev A*, **72**: 2005. DOI: 10.1103/PhysRevA.72.062710 (see pp. 53, 57, 58)

[172] Hansen JP and Kocbach L. Ejection angles of fast delta electrons from K-shell ionisation induced by energetic ions. *J Phys B At Mol Opt Phys*, **22**: L71–L77, 1989. DOI: 10.1088/0953-4075/22/3/004 (see p. 55)

[173] Stolterfoht N, DuBois RD, and Rivarola RD. *Electron emission in heavy ion-atom collisions*. Berlin: Springer, 1997. DOI: 10.1007/978-3-662-03480-4 (see p. 55)

[174] International Commission on Radiation Units and Measurements. *ICRU Report 55. Secondary electron spectra from charged particle interactions*. ICRU, Bethesda, MD, 1996. DOI: 10.1093/jicru/os28.2.Report55 (see p. 55)

[175] Bernal MA and Liendo JA. The HKS model for electron production in liquid water by light ions. *Nucl Instrum Methods Phys Res B*, **251**: 171–176, 2006. DOI: 10.1016/j.nimb.2006.07.006 (see pp. 55, 56)

[176] Champion C, Boudrioua O, and Cappello CD. Water molecule ionization by charged particles: a short review. *J Phys Conf Ser*, **101**: 012010, 2008. DOI: 10.1088/1742-6596/101/1/012010 (see p. 57)

[177] Champion C and Dal Cappello C. "Theoretical and experimental investigations of electron emission during water ionization by light ion impact" in: *The Seventh International Symposium on Swift Heavy Ions in Matter*. Lyon, France, 2008. (see p. 57)

[178] Bernal MA and Liendo JA. Inelastic-collision cross sections for the interactions of totally stripped H, He and C ions with liquid water. *Nucl Instrum Methods Phys Res B*, **262**: 1–6, 2007. DOI: 10.1016/j.nimb.2007.05.001 (see p. 58)

[179] Garcia-Molina R, Abril I, Kyriakou I, and Emfietzoglou D. "Energy loss of swift protons in liquid water: Role of optical data input and extension algorithms" in: *Radiation damage in biomolecular systems* ed. by G García Gómez-Tejedor and MC Fuss. Dordrecht: Springer, 2012. pp. 239–261. DOI: 10.1007/978-94-007-2564-5{_}15 (see p. 58)

[180] Heller JM, Hamm RN, Birkhoff RD, and Painter LR. Collective oscillation in liquid water. *J Chem Phys*, **60**: 3483–3486, 1974. DOI: 10.1063/1.1681563 (see p. 58)

[181] Hayashi H, Watanabe N, Udagawa Y, and Kao C. The complete optical spectrum of liquid water measured by inelastic x-ray scattering. *Proc Natl Acad Sci U S A*, **97**: 6264–6266, 2000. DOI: 10.1073/pnas.110572097 (see p. 59)

[182] Tan Z, Xia Y, Zhao M, and Liu X. Proton inelastic mean free path in a group of bioorganic compounds and water in 0.05–10 MeV range – Including higher-order corrections. *Nucl Instrum Methods Phys Res B*, **268**: 2337–2342, 2010. DOI: 10.1016/j.nimb.2010.04.009 (see pp. 59, 94, 95)

[183] de Vera P, Garcia-Molina R, Abril I, and Solov'yov AV. Semiempirical model for the ion impact ionization of complex biological media. *Phys Rev Lett*, **110**: 148104, 2013. DOI: 10.1103/PhysRevLett.110.148104 (see pp. 59, 94, 95)

[184] Garcia-Molina R, Abril I, Kyriakou I, and Emfietzoglou D. Inelastic scattering and energy loss of swift electron beams in biologically relevant materials. *Surf Interface Anal*, **49**: 11–17, 2017. DOI: 10.1002/sia.5947 (see p. 59)

[185] de Vera P, Garcia-Molina R, and Abril I. Angular and energy distributions of electrons produced in arbitrary biomaterials by proton impact. *Phys Rev Lett*, **114**: 018101, 2015. DOI: 10.1103/PhysRevLett.114.018101 (see p. 59)

[186] Martínez AE, Deco GR, Rivarola RD, and Fainstein PD. K-Shell vacancy production in asymmetric collisions. *Nucl Instrum Methods Phys Res B*, **34**: 32–36, 1988. DOI: 10.1016/0168-583X(88)90360-6 (see p. 60)

[187] Abufager PN, Martínez AE, Rivarola RD, and Fainstein PD. CDW-EIS model for single-electron capture in ion–atom collisions involving multielectronic targets. *J Phys B: At Mol Opt Phys*, **37**: 817–827, 2004. DOI: 10.1088/0953-4075/37/4/009 (see p. 60)

[188] Galassi ME, Abufager PN, Fainstein PD, and Rivarola RD. Single-electron capture in collisions of proton beams with molecules of biological interest. *Phys Rev A*, **81**: 062713, 2010. DOI: 10.1103/PhysRevA.81.062713 (see p. 60)

[189] Champion C, Weck PF, Lekadir H, Galassi ME, Fojón OA, Abufager P, *et al.* Proton-induced single electron capture on DNA/RNA bases. *Phys Med Biol*, **57**: 3039–3049, 2012. DOI: 10.1088/0031-9155/57/10/3039 (see p. 60)

[190] Toburen LH, Nakai MY, and Langley RA. Measurement of high-energy charge-transfer cross sections for incident protons and atomic hydrogen in various gases. *Phys Rev*, **171**: 114–122, 1968. DOI: 10.1103/PhysRev.171.114 (see pp. 61, 64–66)

[191] Dagnac R, Blanc D, and Molina D. A study on the collision of hydrogen ions H_1^+, H_2^+ and H_3^+ with a water-vapour target. *J Phys B At Mol Phys*, **3**: 1239–1251, 1970. DOI: 10.1088/0022-3700/3/9/007 (see pp. 61, 64–66)

[192] Gobet F, Farizon B, Farizon M, Gaillard MJ, Carré M, Lezius M, *et al.* Total, partial, and electron-capture cross sections for ionization of water vapor by 20–150 keV protons. *Phys Rev Lett*, **86**: 3751–3754, 2001. DOI: 10.1103/PhysRevLett.86.3751 (see pp. 61, 66)

[193] Tabet J, Eden S, Feil S, Abdoul-Carime H, Farizon B, Farizon M, *et al.* Absolute total and partial cross sections for ionization of nucleobases by proton impact in the Bragg peak velocity range. *Phys Rev A*, **82**: 2010. DOI: 10.1103/PhysRevA.82.022703 (see p. 61)

[194] Champion C, Hanssen J, and Rivarola RD. "The first Born approximation for ionization and charge transfer in energetic collisions of multiply charged ions with water" in: *Advances in quantum chemistry* ed. by D Belkić, JR Sabin, and E Brandas. Vol. 65, Oxford: Academic Press, 2013. pp. 269–313. DOI: 10.1016/B978-0-12-396455-7.00010-8 (see p. 64)

[195] Lindsay BG, Sieglaff DR, Smith KA, and Stebbings RF. Charge transfer of 0.5-, 1.5-, and 5-keV protons with H_2O: Absolute differential and integral cross sections. *Phys Rev A*, **55**: 3945–3946, 1997. DOI: 10.1103/PhysRevA.55.3945 (see p. 65)

[196] International Commission on Radiation Units and Measurements. *ICRU Report 28. Basic aspects of high energy particle interactions and radiation dosimetry*. ICRU, Bethesda, MD, 1978. DOI: 10.1093/jicru/os15.1.Report28 (see pp. 69, 71)

[197] Hestenes D. *New foundations for classical mechanics*. 2nd ed. Dordrecht: Kluwer Academic, 2002. (see p. 69)

[198] Liamsuwan T. *Development of Monte Carlo track structure simulations for protons and carbon ions in water*. PhD thesis. Stockholm University, 2012. (see p. 73)

[199] International Commission on Radiation Units and Measurements. *ICRU Report 37. Stopping powers for electrons and positrons*. ICRU, Bethesda, MD, 1984. DOI: 10.1093/jicru/os19.2.Report37 (see p. 73)

[200] Levesque PL, Michaud M, Cho W, and Sanche L. Absolute electronic excitation cross sections for low-energy electron (5–12 eV) scattering from condensed thymine. *J Chem Phys*, **122**: 224704, 2005. DOI: 10.1063/1.1925610 (see p. 74)

[201] Michaud M, Bazin M, and Sanche L. Measurement of inelastic cross sections for low-energy electron scattering from DNA bases. *Int J Radiat Biol*, **88**: 15–21, 2012. DOI: 10.3109/09553002.2011.577505 (see p. 74)

[202] Fleig T, Knecht S, and Hättig C. Quantum-chemical investigation of the structures and electronic spectra of the nucleic acid bases at the coupled cluster CC2 level. *J Phys Chem A*, **111**: 5482–5491, 2007. DOI: 10.1021/jp0669409 (see p. 74)

[203] Bremner LJ, Curtis MG, and Walker IC. Electronic states of some simple ethers studied by vacuum ultraviolet absorption and near-threshold electron energy-loss spectroscopy. *J Chem Soc Faraday T*, **87**: 1049–1055, 1991. DOI: 10.1039/ft9918701049 (see p. 75)

[204] Bouchiha D, Gorfinkiel JD, Caron LG, and Sanche L. Low-energy electron collisions with tetrahydrofuran. *J Phys B At Mol Opt Phys*, **39**: 975–986, 2006. (see p. 75)

[205] Stone P and Kim YK. An overview of the BEB method for electron-impact ionization of atoms and molecules. *Surf Interface Anal*, **37**: 966–968, 2005. DOI: 10.1002/sia.2089 (see p. 75)

[206] Champion C, Hanssen J, and Hervieux PA. Electron impact ionization of water molecule. *J Chem Phys*, **117**: 197–204, 2002. DOI: 10.1063/1.1472513 (see pp. 77–80, 85)

[207] Long KA, Paretzke HG, Müller–Plathe F, and Diercksen GHF. Calculation of double differential cross sections for the interaction of electrons with a water molecule, clusters of water molecules, and liquid water. *J Chem Phys*, **91**: 1569–1578, 1989. DOI: 10.1063/1.457115 (see p. 78)

[208] Bolorizadeh M and Rudd ME. Angular and energy dependence of cross sections for ejection of electrons from water vapor. I. 50–2000-eV electron impact. *Phys Rev A*, **33**: 882–887, 1986. DOI: 10.1103/physreva.33.882 (see p. 80)

[209] Lindsay BG and Mangan MA. "5.1 Ionization" in: *Interactions of Photons and Electrons with Molecules* ed. by YE Itikawa. Vol. 17C, Springer-Verlag, 2003. Chap. 5, pp. 5001–5077. DOI: 10.1007/10874891_2 (see p. 80)

[210] Djurić N, Čadež IM, and Kurepa MV. H_2O and D_2O total ionization cross-sections by electron impact. *Int J Mass Spectrom Ion Process*, **83**: R7–R10, 1988. DOI: 10.1016/0168-1176(88)80038-7 (see p. 80)

[211] Schutten J, Heer FJ de, Moustafa HR, Boerboom AJH, and Kistemaker J. Gross– and partial–ionization cross sections for electrons on water vapor in the energy range 0.1–20 keV. *J Chem Phys*, **44**: 3924–3928, 1966. DOI: 10.1063/1.1726553 (see p. 80)

[212] Champion C. Quantum-mechanical predictions of electron-induced ionization cross sections of DNA components. *J Chem Phys*, **138**: 184306, 2013. DOI: 10.1063/1.4802962 (see pp. 80, 81, 85)

[213] Salvat F. Optical-model potential for electron and positron elastic scattering by atoms. *Phys Rev A*, **68**: 012708, 2003. DOI: 10.1103/PhysRevA.68.012708 (see p. 82)

[214] Jain A and Thompson DG. Elastic scattering of slow electrons by CH_4 and H_2O using a local exchange potential and new polarisation potential. *J Phys B At Mol Phys*, **15**: L631–L637, 1982. DOI: 10.1088/0022-3700/15/17/012 (see p. 82)

[215] Mittleman MH and Watson KM. Effects of the Pauli principle on the scattering of high-energy electrons by atoms. *Ann Phys (N Y)*, **10**: 268–279, 1960. DOI: 10.1016/0003-4916(60)90024-5 (see p. 82)

[216] Padial NT and Norcross DW. Parameter-free model of the correlation-polarization potential for electron-molecule collisions. *Phys Rev A*, **29**: 1742, 1984. DOI: 10.1103/PhysRevA.29.1742 (see p. 82)

[217] Riley ME and Truhlar DG. Approximations for the exchange potential in electron scattering. *J Chem Phys*, **63**: 2182–2191, 1975. DOI: 10.1063/1.431598 (see p. 83)

[218] Mokrani S, Aouchiche H, and Champion C. Elastic scattering of electrons by DNA bases. *Radiat Phys Chem*, **172**: 108735, 2020. DOI: 10.1016/j.radphyschem.2020.108735 (see p. 84)

[219] Rivarola RD, Galassi ME, Fainstein PD, and Champion C. "Computation of distorted wave cross sections for high-energy inelastic collisions of heavy ions with water molecules" in: *Advances in Quantum Chemistry*. Vol. 65, Elsevier, 2013. pp. 231–267. DOI: 10.1016/B978-0-12-396455-7.00009-1 (see p. 89)

[220] Barnett CF, Ray JA, Ricci E, Wilker MI, McDaniel EW, Thomas EW, *et al. Atomic data for controlled fusion research* tech. rep. ORNL–5206 (Vol. 1) United States: Oak Ridge National Laboratory, 1977 (see pp. 89, 150, 151)

[221] Emfietzoglou D, Nikjoo H, and Pathak A. Electronic cross sections for proton transport in liquid water based on optical-data models. *Nucl Instrum Methods Phys Res B*, **249**: 26–28, 2006. DOI: 10.1016/j.nimb.2006.03.015 (see p. 94)

[222] Reynolds HK, Dunbar DNF, Wenzel WA, and Whaling W. The stopping cross section of gases for protons, 30–600 keV. *Phys Rev*, **92**: 742–748, 1953. DOI: 10.1103/PhysRev.92.742 (see p. 96)

[223] Phillips JA. The energy loss of low energy protons in some gases. *Phys Rev*, **90**: 532–537, 1953. DOI: 10.1103/PhysRev.90.532 (see p. 96)

[224] Mitterschiffthaler C and Bauer P. Stopping cross section of water vapor for hydrogen ions. *Nucl Instrum Methods Phys Res B*, **48**: 58–60, 1990. DOI: 10.1016/0168-583X(90)90073-4 (see p. 96)

[225] Baek WY, Grosswendt B, and Willems G. Ionization ranges of protons in water vapour in the energy range 1–100 keV. *Radiat Prot Dosim*, **122**: 32–35, 2006. DOI: 10.1093/rpd/ncl514 (see p. 96)

[226] Shimizu M, Hayakawa T, Kaneda M, Tsuchida H, and Itoh A. Stopping cross-sections of liquid water for 0.3–2.0 MeV protons. *Vacuum*, **84**: 1002–1004, 2010. DOI: 10.1016/j.vacuum.2009.11.019 (see p. 96)

[227] Siiskonen T, Kettunen H, Peräjärvi K, Javanainen A, Rossi M, Trzaska WH, *et al.* Energy loss measurement of protons in liquid water. *Phys Med Biol*, **56**: 2367–2374, 2011. DOI: 10.1088/0031-9155/56/8/003 (see p. 96)

[228] Ziegler JF, Biersack JP, and Littmark U. *The Stopping and Range of Ions in Solids*. New York: Pergamon Press, 2003. (see pp. 99, 155)

[229] Xu YJ, Khandelwal GS, and Wilson JW. Proton stopping cross sections of liquid water. *Phys Rev A*, **32**: 629–632, 1985. DOI: 10.1103/PhysRevA.32.629 (see p. 99)

[230] Olivera GH, Martínez AE, Rivarola RD, and Fainstein PD. Theoretical calculation of electronic stopping power of water vapor by proton impact. *Radiat Res*, **144**: 241–247, 1995. DOI: 10.2307/3579265 (see p. 99)

[231] Quinto MA, Monti JM, Tachino CA, Weck PF, Fojón OA, Champion C, *et al.* The physics of irradiation of biological matter by ion beams. *Radiat Phys Chem*, **167**: 108337, 2020. DOI: 10.1016/j.radphyschem.2019.05.027 (see p. 102)

[232] Akkerman A and Akkerman E. Characteristics of electron inelastic interactions in organic compounds and water over the energy range 20–10000 eV. *J Appl Phys*, **86**: 5809–5816, 1999. DOI: 10.1063/1.371597 (see p. 102)

[233] Blanco F, Muñoz A, Almeida D, Ferreira da Silva F, Limão-Vieira P, and García G. Clustering and condensation effects in the electron scattering cross sections from water molecules. *Int J Mass Spectrom*, **365–366**: 287–294, 2014. DOI: 10.1016/j.ijms.2014.02.001 (see pp. 102, 104)

[234] Emfietzoglou D, Kyriakou I, Garcia-Molina R, and Abril I. Inelastic mean free path of low-energy electrons in condensed media: beyond the standard models: Low-energy electron inelastic mean free paths. *Surf Interface Anal*, **49**: 4–10, 2017. DOI: 10.1002/sia.5878 (see pp. 102, 104)

[235] Nguyen-Truong HT. Low-energy electron inelastic mean free paths for liquid water. *J Phys Condens Matter*, **30**: 155101, 2018. DOI: 10.1088/1361-648X/aab40a (see p. 102)

[236] Bigildeev E and Michalik V. Charged particle tracks in water of different phases. Monte Carlo simulation of electron tracks. *Radiat Phys Chem*, **47**: 197–207, 1996. DOI: 10.1016/0969-806X(95)00002-F (see p. 102)

[237] Uehara S, Nikjoo H, and Goodhead DT. Comparison and assessment of electron cross sections for Monte Carlo track structure codes. *Radiat Res*, **152**: 202–213, 1999. DOI: 10.2307/3580095 (see p. 102)

[238] Michaud M, Wen A, and Sanche L. Cross sections for low-energy (1–100 eV) electron elastic and inelastic scattering in amorphous ice. *Radiat Res*, **159**: 3–22, 2003. DOI: 10.1667/0033-7587(2003)159[0003:csflee]2.0.co;2 (see pp. 102–104)

[239] Thürmer S, Seidel R, Faubel M, Eberhardt W, Hemminger JC, Bradforth SE, *et al.* Photoelectron angular distributions from liquid water: Effects of electron scattering. *Phys Rev Lett*, **111**: 173005, 2013. DOI: 10.1103/PhysRevLett.111.173005 (see pp. 102–104)

[240] Tanuma S, Powell CJ, and Penn DR. Calculations of electron inelastic mean free paths. V. Data for 14 organic compounds over the 50–2000 eV range. *Surf Interface Anal*, **21**: 165–176, 1993. DOI: 10.1002/sia.740210302 (see p. 104)

[241] Akar A, Gümüş H, and Okumuşoğlu NT. Electron inelastic mean free path formula and CSDA-range calculation in biological compounds for low and intermediate energies. *Appl Radiat Isot*, **64**: 543–550, 2006. DOI: 10.1016/j.apradiso.2005.11.014 (see pp. 104, 107)

[242] Emfietzoglou D, Kyriakou I, Abril I, Garcia-Molina R, Petsalakis I, Nikjoo H, *et al.* Electron inelastic mean free paths in biological matter based on dielectric theory and local-field corrections. *Nucl Instrum Methods Phys Res B*, **267**: 45–52, 2009. DOI: 10.1016/j.nimb.2008.11.008 (see p. 104)

[243] LaVerne JA and Mozumder A. Penetration of low-energy electrons in water. *Radiat Res*, **96**: 219–234, 1983. DOI: 10.2307/3576206 (see p. 106)

[244] Jevtić P, Edens LJ, Vuković LD, and Levy DL. Sizing and shaping the nucleus: mechanisms and significance. *Curr Opin Cell Biol*, **28**: 16–27, 2014. DOI: 10.1016/j.ceb.2014.01.003 (see p. 107)

[245] Alcocer-Ávila ME, Ferreira A, Quinto MA, Morgat C, Hindié E, and Champion C. Radiation doses from ^{161}Tb and ^{177}Lu in single tumour cells and micrometastases. *EJNMMI Phys*, **7**: 33, 2020. DOI: 10.1186/s40658-020-00301-2 (see pp. 114, 137, 144)

[246] Podgoršak EB. *Radiation physics for medical physicists*. Third edition. Switzerland: Springer, 2016. (see pp. 114–117, 133, 154, 155)

[247] Walker PM and Carroll JJ. Feature article: nuclear isomers: recipes from the past and ingredients for the future. *Nucl Phys News*, **17**: 11–15, 2007. DOI: 10.1080/10506890701404206 (see p. 116)

[248] Lee BQ, Kibédi T, Stuchbery AE, and Robertson KA. Atomic radiations in the decay of medical radioisotopes: a physics perspective. *Comput Math Methods Med*, **2012**: 651475, 2012. DOI: 10.1155/2012/651475 (see p. 117)

[249] Kassis AI. The amazing world of Auger electrons. *Int J Radiat Biol*, **80**: 789–803, 2004. DOI: 10.1080/09553000400017663 (see p. 118)

[250] Goldsmith SJ. Targeted radionuclide therapy: A historical and personal review. *Semin Nucl Med*, **50**: 87–97, 2020. DOI: 10.1053/j.semnuclmed.2019.07.006 (see pp. 119, 121, 122)

[251] Fahey FH, Grant FD, and Thrall JH. Saul Hertz, MD, and the birth of radionuclide therapy. *EJNMMI Phys*, **4**: 15, 2017. DOI: 10.1186/s40658-017-0182-7 (see p. 119)

[252] Morschhauser F, Radford J, Van Hoof A, Botto B, Rohatiner AZ, Salles G, *et al.* ^{90}Yttrium-ibritumomab tiuxetan consolidation of first remission in advanced-stage follicular non-Hodgkin lymphoma: updated results after a median follow-up of 7.3 years from the international, randomized, phase III First-Line Indolent Trial. *J Clin Oncol*, **31**: 1977–83, 2013. DOI: 10.1200/jco.2012.45.6400 (see pp. 119, 121)

[253] Strosberg J, El-Haddad G, Wolin E, Hendifar A, Yao J, Chasen B, *et al.* Phase 3 trial of ^{177}Lu-dotatate for midgut neuroendocrine tumors. *N Engl J Med*, **376**: 125–135, 2017. DOI: 10.1056/NEJMoa1607427 (see pp. 119, 122)

[254] Hofman MS, Violet J, Hicks RJ, Ferdinandus J, Thang SP, Akhurst T, *et al.* [^{177}Lu]-PSMA-617 radionuclide treatment in patients with metastatic castration-resistant prostate cancer (LuPSMA trial): a single-centre, single-arm, phase 2 study. *Lancet Oncol*, **19**: 825–833, 2018. DOI: 10.1016/s1470-2045(18)30198-0 (see pp. 119, 122)

[255] Ersahin D, Doddamane I, and Cheng D. Targeted radionuclide therapy. *Cancers*, **3**: 3838–3855, 2011. DOI: 10.3390/cancers3043838 (see p. 120)

[256] Gudkov SV, Shilyagina NY, Vodeneev VA, and Zvyagin AV. Targeted radionuclide therapy of human tumors. *Int J Mol Sci*, **17**: 2016. DOI: 10.3390/ijms17010033 (see p. 120)

[257] Jødal L. Beta emitters and radiation protection. *Acta Oncol*, **48**: 308–313, 2009. DOI: 10.1080/02841860802245163 (see pp. 120, 121)

[258] Nagarajah J, Janssen M, Hetkamp P, and Jentzen W. Iodine symporter targeting with ^{124}I/^{131}I theranostics. *J Nucl Med*, **58**: 34S–38S, 2017. DOI: 10.2967/jnumed.116.186866 (see p. 120)

[259] Knapp FF and Dash A. *Radiopharmaceuticals for therapy*. New Delhi: Springer, 2016. (see pp. 120, 126, 128)

[260] Zade AA, Rangarajan V, Purandare NC, Shah SA, Agrawal AR, Kulkarni SS, *et al.* ^{90}Y microsphere therapy: does ^{90}Y PET/CT imaging obviate the need for ^{90}Y Bremsstrahlung SPECT/CT imaging? *Nucl Med Commun*, **34**: 1090–1096, 2013. DOI: 10.1097/MNM.0b013e328364aa4b (see p. 121)

[261] Selwyn RG, Nickles RJ, Thomadsen BR, DeWerd LA, and Micka JA. A new internal pair production branching ratio of ^{90}Y: the development of a non-destructive assay for ^{90}Y and ^{90}Sr. *Appl Radiat Isot*, **65**: 318–327, 2007. DOI: 10.1016/j.apradiso.2006.08.009 (see p. 121)

[262] Vinjamuri S, Gilbert TM, Banks M, McKane G, Maltby P, Poston G, *et al.* Peptide receptor radionuclide therapy with ^{90}Y-DOTATATE/^{90}Y-DOTATOC in patients with progressive metastatic neuroendocrine tumours: assessment of response, survival and toxicity. *Br J Cancer*, **108**: 1440–1448, 2013. DOI: 10.1038/bjc.2013.103 (see p. 121)

[263] Rogowski W, Wachuła E, Lewczuk A, Buscombe JR, Seklecka N, Sankowski A, *et al.* Long-term efficacy of ^{90}Y-DOTATATE in patients with nonresectable pancreatic and small bowel neuroendocrine neoplasms. *Future Oncol*, **12**: 1877–1885, 2016. DOI: 10.2217/fon-2016-0031 (see p. 121)

[264] Rathke H, Flechsig P, Mier W, Bronzel M, Mavriopoulou E, Hohenfellner M, *et al.* Dosimetry estimate and initial clinical experience with ^{90}Y-PSMA-617. *J Nucl Med*, **60**: 806–811, 2019. DOI: 10.2967/jnumed.118.218917 (see p. 121)

[265] Salem R, Lewandowski RJ, Sato KT, Atassi B, Ryu RK, Ibrahim S, *et al.* Technical aspects of radioembolization with ^{90}Y microspheres. *Tech Vasc Interv Radiol*, **10**: 12–29, 2007. DOI: 10.1053/j.tvir.2007.08.001 (see p. 121)

[266] Dash A, Pillai MR, and Knapp, F. F., Jr. Production of ^{177}Lu for targeted radionuclide therapy: available options. *Nucl Med Mol Imaging*, **49**: 85–107, 2015. DOI: 10.1007/s13139-014-0315-z (see p. 121)

[267] Kolstad A, Madsbu U, Beasley M, Bayne M, Illidge TM, O'Rourke N, *et al.* LYMRIT 37-01: A phase I/II study of ^{177}Lu-lilotomab satetraxetan (Betalutin®) antibody-radionuclide-conjugate (ARC) for the treatment of relapsed non-Hodgkin's lymphoma (NHL) – Analysis with 6-month follow-up. *Blood*, **132**: 2879, 2018. DOI: 10.1182/blood-2018-99-110555 (see p. 122)

[268] Haller S, Pellegrini G, Vermeulen C, Meulen NP van der, Köster U, Bernhardt P, *et al.* Contribution of Auger/conversion electrons to renal side effects after radionuclide therapy: preclinical comparison of ^{161}Tb-folate and ^{177}Lu-folate. *EJNMMI Res*, **6**: 13, 2016. DOI: 10.1186/s13550-016-0171-1 (see p. 122)

[269] Müller C, Zhernosekov K, Köster U, Johnston K, Dorrer H, Hohn A, *et al.* A unique matched quadruplet of terbium radioisotopes for PET and SPECT and for α- and β^- radionuclide therapy: an in vivo proof-of-concept study with a new receptor-targeted folate derivative. *J Nucl Med*, **53**: 1951–9, 2012. DOI: 10.2967/jnumed.112.107540 (see p. 122)

[270] Zhang J, Singh A, Kulkarni HR, Schuchardt C, Müller D, Wester HJ, *et al.* From bench to bedside—The Bad Berka experience with first-in-human studies. *Semin Nucl Med*, **49**: 422–437, 2019. DOI: 10.1053/j.semnuclmed.2019.06.002 (see p. 122)

[271] Lehenberger S, Barkhausen C, Cohrs S, Fischer E, Grünberg J, Hohn A, *et al.* The low-energy β^- and electron emitter ^{161}Tb as an alternative to ^{177}Lu for targeted radionuclide therapy. *Nucl Med Biol*, **38**: 917–924, 2011. DOI: 10.1016/j.nucmedbio.2011.02.007 (see p. 122)

[272] Müller C, Reber J, Haller S, Dorrer H, Bernhardt P, Zhernosekov K, *et al.* Direct in vitro and in vivo comparison of ^{161}Tb and ^{177}Lu using a tumour-targeting folate conjugate. *Eur J Nucl Med Mol Imaging*, **41**: 476–485, 2014. DOI: 10.1007/s00259-013-2563-z (see p. 122)

[273] Gracheva N, Müller C, Talip Z, Heinitz S, Köster U, Zeevaart JR, *et al.* Production and characterization of no-carrier-added ^{161}Tb as an alternative to the clinically-applied ^{177}Lu for radionuclide therapy. *EJNMMI Radiopharm Chem*, **4**: 12, 2019. DOI: 10.1186/s41181-019-0063-6 (see p. 122)

[274] Grünberg J, Lindenblatt D, Dorrer H, Cohrs S, Zhernosekov K, Köster U, *et al.* Anti-L1CAM radioimmunotherapy is more effective with the radiolanthanide terbium-161 compared to lutetium-177 in an ovarian cancer model. *Eur J Nucl Med Mol Imaging*, **41**: 1907–1915, 2014. DOI: 10.1007/s00259-014-2798-3 (see p. 122)

[275] Müller C, Umbricht CA, Gracheva N, Tschan VJ, Pellegrini G, Bernhardt P, *et al.* Terbium-161 for PSMA-targeted radionuclide therapy of prostate cancer. *Eur J Nucl Med Mol Imaging*, **46**: 1919–1930, 2019. DOI: 10.1007/s00259-019-04345-0 (see p. 122)

[276] Uusijärvi H, Bernhardt P, Rösch F, Maecke HR, and Forssell-Aronsson E. Electron- and positron-emitting radiolanthanides for therapy: aspects of dosimetry and production. *J Nucl Med*, **47**: 807–14, 2006. (see p. 122)

[277] Bernhardt P, Forssell-Aronsson E, Jacobsson L, and Skarnemark G. Low-energy electron emitters for targeted radiotherapy of small tumours. *Acta Oncol*, **40**: 602–608, 2001. DOI: 10.1080/028418601750444141 (see pp. 124, 125, 127)

[278] Engle JW, Nichols AL, and Noy RC, eds.. Technical meeting on nuclear data for medical applications. Summary Report INDC(NDS)-0776. INDC International Nuclear Data Committee. Vienna, Austria, 2019 (see pp. 124, 146)

[279] Valdovinos H, Graves S, Barnhart T, Nickles R, and Cai W. 69/71Ge separation from proton irradiated metallic gallium, gallium oxide and gallium-nickel alloy targets. *J Nucl Med*, **55**: 216, 2014. (see p. 124)

[280] Jensen AI, Zhuravlev F, Severin G, Magnus CB, Fonslet J, Köster U, *et al.* A solid support generator of the Auger electron emitter rhodium-103m from [^{103}Pd]palladium. *Appl Radiat Isot*, **156**: 108985, 2020. DOI: 10.1016/j.apradiso.2019.108985 (see pp. 124, 125)

[281] Skarnemark G, Ödegaard-Jensen A, Nilsson J, Bartos B, Kowalska E, Bilewicz A, *et al.* Production of ^{103m}Rh for cancer therapy. *J Radioanal Nucl Chem*, **280**: 371–373, 2009. DOI: 10.1007/s10967-009-0529-1 (see p. 125)

[282] Mastren T, Radchenko V, Hopkins PD, Engle JW, Weidner JW, Copping R, *et al.* Separation of ^{103}Ru from a proton irradiated thorium matrix: A potential source of Auger therapy radionuclide ^{103m}Rh. *PLoS One*, **12**: e0190308, 2017. DOI: 10.1371/journal.pone.0190308 (see p. 125)

[283] Thisgaard H and Jensen M. ^{119}Sb–a potent Auger emitter for targeted radionuclide therapy. *Med Phys*, **35**: 3839–3846, 2008. DOI: 10.1118/1.2963993 (see p. 125)

[284] Thisgaard H and Jensen M. Production of the Auger emitter ^{119}Sb for targeted radionuclide therapy using a small PET-cyclotron. *Appl Radiat Isot*, **67**: 34–38, 2009. DOI: 10.1016/j.apradiso.2008.09.003 (see pp. 125, 126)

[285] Bennett KT, Bone SE, Akin AC, Birnbaum ER, Blake AV, Brugh M, *et al.* Large-scale production of ^{119m}Te and ^{119}Sb for radiopharmaceutical applications. *ACS Cent Sci*, **5**: 494–505, 2019. DOI: 10.1021/acscentsci.8b00869 (see p. 126)

[286] Bodei L, Kassis AI, Adelstein SJ, and Mariani G. Radionuclide therapy with iodine-125 and other Auger-electron-emitting radionuclides: experimental models and clinical applications. *Cancer Biother Radiopharm*, **18**: 861–877, 2003. DOI: 10.1089/108497803322702833 (see p. 126)

[287] Kim JH, Li L, Quang TS, Emrich JG, Yaeger TE, Jenrette JM, *et al.* Phase II trial of anti-epidermal growth factor receptor radioimmunotherapy in the treatment of anaplastic astrocytoma. *J Radiat Oncol*, **2**: 7–13, 2013. DOI: 10.1007/s13566-012-0071-6 (see p. 126)

[288] Gardette M, Viallard C, Paillas S, Guerquin-Kern JL, Papon J, Moins N, *et al.* Evaluation of two ^{125}I-radiolabeled acridine derivatives for Auger-electron radionuclide therapy of melanoma. *Invest New Drugs*, **32**: 587–597, 2014. DOI: 10.1007/s10637-014-0086-5 (see p. 126)

[289] Grudzinski J, Marsh I, Titz B, Jeffery J, Longino M, Kozak K, *et al.* CLR 125 Auger electrons for the targeted radiotherapy of triple-negative breast cancer. *Cancer Biother Radiopharm*, **33**: 87–95, 2018. DOI: 10.1089/cbr.2017.2376 (see p. 126)

[290] Shen CJ, Minn I, Hobbs RF, Chen Y, Josefsson A, Brummet M, *et al.* Auger radiopharmaceutical therapy targeting prostate-specific membrane antigen in a micrometastatic model of prostate cancer. *Theranostics*, **10**: 2888–2896, 2020. DOI: 10.7150/thno.38882 (see p. 126)

[291] Tárkányi F, Ditrói F, Hermanne A, Takács S, and Ignatyuk AV. Investigation of production routes for the ^{161}Ho Auger-electron emitting radiolanthanide, a candidate for therapy. *J Radioanal Nucl Chem*, **298**: 277–286, 2013. DOI: 10.1007/s10967-012-2403-9 (see p. 127)

[292] Hermanne A, Adam Rebeles R, Tárkányi F, and Takács S. Excitation functions of proton induced reactions on ^{nat}Os up to 65 MeV: Experiments and comparison with results from theoretical codes. *Nucl Instrum Methods Phys Res B*, **345**: 58–68, 2015. DOI: 10.1016/j.nimb.2014.12.051 (see p. 127)

[293] Hilgers K, Coenen HH, and Qaim SM. Production of the therapeutic radionuclides ^{193m}Pt and ^{195m}Pt with high specific activity via α-particle-induced reactions on ^{192}Os. *Appl Radiat Isot*, **66**: 545–551, 2008. DOI: 10.1016/j.apradiso.2007.10.009 (see pp. 127, 128)

[294] Azure MT, Sastry KSR, Archer RD, Howell RW, and Rao DV. "Microscale synthesis of carboplatin labeled with the Auger emitter platinum-193m: Radiotoxicity versus chemotoxicity of the antitumor drug in mammalian cells" in: *Biophysical aspects of Auger processes. American Association of Physicists in Medicine symposium proceedings No. 8*. 1992. pp. 336–351. (see p. 127)

[295] Tinker ND, Zweit J, Sharma HL, Downey S, and McAuliffe CA. Production of no-carrier added ^{191}Pt, a radiolabel for the synthesis and biological investigations of platinum anti-tumour compounds. *Radiochim Acta*, **54**: 1991. DOI: 10.1524/ract.1991.54.1.29 (see p. 128)

[296] Uddin MS, Hermanne A, Scholten B, Spellerberg S, Coenen HH, and Qaim SM. Small scale production of high purity ^{193m}Pt by the ^{192}Os(α,3n)-process. *Radiochim Acta*, **99**: 131–135, 2011. DOI: 10.1524/ract.2011.1807 (see p. 128)

[297] Mariani G, Bodei L, Adelstein SJ, and Kassis AI. Emerging roles for radiometabolic therapy of tumors based on Auger electron emission. *J Nucl Med*, **41**: 1519–1521, 2000. (see p. 128)

[298] Bodnar EN, Dikiy MP, and Medvedeva EP. Photonuclear production and antitumor effect of radioactive cisplatin (^{195m}Pt). *J Radioanal Nucl Chem*, **305**: 133–138, 2015. DOI: 10.1007/s10967-015-4053-1 (see p. 128)

[299] Soares MA, Mattos JL, Pujatti PB, Leal AS, dos Santos WG, and dos Santos RG. Evaluation of the synergetic radio-chemotherapy effects of the radio labelled cisplatin for the treatment of glioma. *J Radioanal Nucl Chem*, **292**: 61–65, 2012. DOI: 10.1007/s10967-011-1414-2 (see p. 128)

[300] Bolch WE, Eckerman KF, Sgouros G, and Thomas SR. MIRD Pamphlet No. 21: A generalized schema for radiopharmaceutical dosimetry–standardization of nomenclature. *J Nucl Med*, **50**: 477–484, 2009. DOI: 10.2967/jnumed.108.056036 (see p. 131)

[301] Bousis C, Emfietzoglou D, Hadjidoukas P, and Nikjoo H. Monte Carlo single-cell dosimetry of Auger-electron emitting radionuclides. *Phys Med Biol*, **55**: 2555–2572, 2010. DOI: 10.1088/0031-9155/55/9/009 (see pp. 131, 133)

[302] Šefl M, Incerti S, Papamichael G, and Emfietzoglou D. Calculation of cellular S-values using GEANT4-DNA: The effect of cell geometry. *Appl Radiat Isot*, **104**: 113–123, 2015. DOI: 10.1016/j.apradiso.2015.06.027 (see p. 131)

[303] Falzone N, Lee BQ, Fernández-Varea JM, Kartsonaki C, Stuchbery AE, Kibédi T, *et al.* Absorbed dose evaluation of Auger electron-emitting radionuclides: impact of input decay spectra on dose point kernels and S-values. *Phys Med Biol*, **62**: 2239–2253, 2017. DOI: 10.1088/1361-6560/aa5aa4 (see p. 131)

[304] Rojas-Calderón EL, Torres-García E, and Ávila O. Dose per unit cumulated activity (S-values) for e^- and beta emitting radionuclides in cancer cell models calculated by Monte Carlo simulation. *Appl Radiat Isot*, **90**: 229–233, 2014. DOI: 10.1016/j.apradiso.2014.04.012 (see p. 131)

[305] Emfietzoglou D, Bousis C, Hindorf C, Fotopoulos A, Pathak A, and Kostarelos K. A Monte Carlo study of energy deposition at the sub-cellular level for application to targeted radionuclide therapy with low-energy electron emitters. *Nucl Instrum Methods Phys Res B*, **256**: 547–553, 2007. DOI: 10.1016/j.nimb.2006.12.055 (see p. 133)

[306] Tajik-Mansoury MA, Rajabi H, and Mozdarani H. Cellular S-value of beta emitter radionuclide's determined using GEANT4 Monte Carlo toolbox, comparison to MIRD S-values. *Iran J Nucl Med*, **24**: 37–45, 2016. (see p. 133)

[307] Uusijärvi H, Chouin N, Bernhardt P, Ferrer L, Bardiès M, and Forssell-Aronsson E. Comparison of electron dose-point kernels in water generated by the Monte Carlo codes, PENELOPE, GEANT4, MCNPX, and ETRAN. *Cancer Biother Radio*, **24**: 461–467, 2009. DOI: 10.1089/cbr.2008.0573 (see p. 133)

[308] Nichols AL, Qaim SM, and Noy RC, eds.. Technical meeting on intermediate–term nuclear data needs for medical applications: cross sections and decay data. Summary Report INDC(NDS)-0596. INDC International Nuclear Data Committee. Vienna, Austria, 2011 (see p. 146)

[309] Noy RC, Chung HK, Bartschat K, Dong C, Jonsson P, Kibédi T, *et al.*. Consultants' meeting on Auger electron emission data needs for medical applications. Summary Report INDC(NDS)-0638. INDC International Nuclear Data Committee. Vienna, Austria, 2013 (see p. 146)

[310] Lee BQ, Nikjoo H, Ekman J, Jönsson P, Stuchbery AE, and Kibédi T. A stochastic cascade model for Auger-electron emitting radionuclides. *Int J Radiat Biol*, **92**: 641–653, 2016. DOI: 10.3109/09553002.2016.1153810 (see p. 146)

[311] Song H, Senthamizhchelvan S, Hobbs RF, and Sgouros G. Alpha particle emitter radiolabeled antibody for metastatic cancer: What can we learn from heavy ion beam radiobiology? *Antibodies (Basel)*, **1**: 124–148, 2012. DOI: 10.3390/antib1020124 (see p. 148)

[312] Dekempeneer Y, Keyaerts M, Krasniqi A, Puttemans J, Muyldermans S, Lahoutte T, *et al.* Targeted alpha therapy using short-lived alpha-particles and the promise of nanobodies as targeting vehicle. *Expert Opin Biol Ther*, **16**: 1035–1047, 2016. DOI: 10.1080/14712598.2016.1185412 (see p. 148)

[313] Staudacher AH, Liapis V, and Brown MP. Therapeutic targeting of tumor hypoxia and necrosis with antibody α-radioconjugates. *Antib Ther*, **1**: 55–63, 2018. DOI: 10.1093/abt/tby010 (see p. 148)

[314] Cornelissen B and Vallis KA. Targeting the nucleus: an overview of Auger-electron radionuclide therapy. *Curr Drug Discov Technol*, **7**: 263–279, 2010. DOI: 10.2174/157016310793360657 (see p. 148)

[315] Roscher M, Bakos G, and Benešová M. Atomic nanogenerators in targeted alpha therapies: Curie's legacy in modern cancer management. *Pharmaceuticals (Basel)*, **13**: 2020. DOI: 10.3390/ph13040076 (see pp. 148, 162)

[316] International Atomic Energy Agency. *Alpha emitting radionuclides and radiopharmaceuticals for therapy.* Meeting Report, IAEA,Vienna, 2013. URL: http://www-naweb.iaea.org/napc/iachem/working_materials/TM-44815-report-Alpha-Therapy.pdf (visited on Nov. 2, 2020) (see pp. 149, 156–158, 161, 163)

[317] Kruijff RM de, Wolterbeek HT, and Denkova AG. A critical review of alpha radionuclide therapy–How to deal with recoiling daughters? *Pharmaceuticals (Basel)*, **8**: 321–336, 2015. DOI: 10.3390/ph8020321 (see pp. 149, 155)

[318] Makvandi M, Dupis E, Engle JW, Nortier FM, Fassbender ME, Simon S, *et al.* Alpha-emitters and targeted alpha therapy in oncology: from basic science to clinical investigations. *Target Oncol*, **13**: 189–203, 2018. DOI: 10.1007/s11523-018-0550-9 (see pp. 149, 161)

[319] L'Annunziata MF. *Radioactivity: Introduction and history, from the quantum to quarks*. Second edition. Amsterdam: Elsevier, 2016. (see p. 154)

[320] Szucs S and Delfosse JM. Charge spectrum of recoiling ^{216}Po in the α decay of ^{220}Rn. *Phys Rev Lett*, **15**: 163–165, 1965. DOI: 10.1103/PhysRevLett.15.163 (see p. 154)

[321] Cano GL and Dressel RW. Energy loss and resultant charge of recoil particles from alpha disintegrations in surface deposits of ^{210}Po and ^{241}Am. *Phys Rev*, **139**: A1883–A1892, 1965. DOI: 10.1103/PhysRev.139.A1883 (see p. 154)

[322] Gunter K, Asaro F, and Helmholz AC. Charge and energy distributions of recoils from ^{226}Th alpha decay. *Phys Rev Lett*, **16**: 362–364, 1966. DOI: 10.1103/PhysRevLett.16.362 (see p. 154)

[323] Wieclawik W de and Perrin N. Charge des atomes de recul après émission α. *J Phys-Paris*, **30**: 877–891, 1969. DOI: 10.1051/jphys:019690030011-12087700 (see p. 154)

[324] Meyer J, Paulus JM, and Abbe JC. Charge des atomes de recul ^{208}Pb et ^{208}Tl formés par désintégration α de ^{212}Po et ^{212}Bi. *Radiochim Acta*, **17**: 1972. DOI: 10.1524/ract.1972.17.2.76 (see p. 154)

[325] Rapaport MS. *Atomic electrons shake-off accompanying alpha decay.* Lawrence Berkeley National Laboratory, United States. Report LBL-2978, 1974. URL: https://escholarship.org/uc/item/2g48t118 (visited on Jan. 4, 2021) (see p. 154)

[326] Thijssen L, Schaart DR, Vries D de, Morgenstern A, Bruchertseifer F, and Denkova AG. Polymersomes as nano-carriers to retain harmful recoil nuclides in alpha radionuclide therapy: a feasibility study. *Radiochim Acta*, **100**: 473–482, 2012. DOI: 10.1524/ract.2012.1935 (see p. 155)

[327] Zalutsky MR and Pruszynski M. Astatine-211: production and availability. *Curr Radiopharm*, **4**: 177–185, 2011. DOI: 10.2174/1874471011104030177 (see pp. 155, 156)

[328] Meyer GJ. Astatine. *J Labelled Comp Radiopharm*, **61**: 154–164, 2018. DOI: 10.1002/jlcr.3573 (see p. 157)

[329] Crawford JR, Yang H, Kunz P, Wilbur DS, Schaffer P, and Ruth TJ. Development of a preclinical ^{211}Rn/^{211}At generator system for targeted alpha therapy research with ^{211}At. *Nucl Med Biol*, **48**: 31–35, 2017. DOI: 10.1016/j.nucmedbio.2017.01.011 (see p. 157)

[330] Tafreshi NK, Doligalski ML, Tichacek CJ, Pandya DN, Budzevich MM, El-Haddad G, *et al.* Development of targeted alpha particle therapy for solid tumors. *Molecules*, **24**: 2019. DOI: 10.3390/molecules24234314 (see pp. 157, 159, 161, 162, 164)

[331] Zalutsky MR, Reardon DA, Akabani G, Coleman RE, Friedman AH, Friedman HS, *et al.* Clinical experience with α-particle emitting ^{211}At: treatment of recurrent brain tumor patients with ^{211}At-labeled chimeric antitenascin monoclonal antibody 81C6. *J Nucl Med*, **49**: 30–38, 2008. DOI: 10.2967/jnumed.107.046938 (see p. 157)

[332] Andersson H, Cederkrantz E, Back T, Divgi C, Elgqvist J, Himmelman J, *et al.* Intraperitoneal α-particle radioimmunotherapy of ovarian cancer patients: pharmacokinetics and dosimetry of ^{211}At-MX35 F(ab')2– A phase I study. *J Nucl Med*, **50**: 1153–1160, 2009. DOI: 10.2967/jnumed.109.062604 (see p. 157)

[333] Johnson EL, Turkington TG, Jaszczak RJ, Gilland DR, Vaidyanathan G, Greer KL, *et al.* Quantitation of ^{211}At in small volumes for evaluation of targeted radiotherapy in animal models. *Nucl Med Biol*, **22**: 45–54, 1995. DOI: 10.1016/0969-8051(94)00077-W (see p. 157)

[334] Nakanishi K, Yamamoto S, Watabe T, Kaneda-Nakashima K, Shirakami Y, Ooe K, *et al.* Development of high-resolution YAP(Ce) X-ray camera for the imaging of astatine-211(At-211) in small animals. *Med Phys*, 2020. DOI: 10.1002/mp.14455 (see p. 157)

[335] Westrøm S, Generalov R, Bønsdorff TB, and Larsen RH. Preparation of ^{212}Pb-labeled monoclonal antibody using a novel ^{224}Ra-based generator solution. *Nucl Med Biol*, **51**: 1–9, 2017. DOI: 10.1016/j.nucmedbio.2017.04.005 (see p. 158)

[336] Baidoo KE, Milenic DE, and Brechbiel MW. Methodology for labeling proteins and peptides with lead-212 (^{212}Pb). *Nucl Med Biol*, **40**: 592–599, 2013. DOI: 10.1016/j.nucmedbio.2013.01.010 (see pp. 158, 159)

[337] Mirzadeh S, Kumar K, and Gansow OA. The chemical fate of ^{212}Bi-DOTA formed by β^- decay of ^{212}Pb(DOTA)$^{2-}$. *Radiochim Acta*, **60**: 1–10, 1993. DOI: 10.1524/ract.1993.60.1.1 (see p. 158)

[338] Meredith RF, Torgue J, Azure MT, Shen S, Saddekni S, Banaga E, *et al.* Pharmacokinetics and imaging of ^{212}Pb-TCMC-trastuzumab after intraperitoneal administration in ovarian cancer patients. *Cancer Biother Radiopharm*, **29**: 12–17, 2014. DOI: 10.1089/cbr.2013.1531 (see p. 159)

[339] Dos Santos JC, Schäfer M, Bauder-Wüst U, Lehnert W, Leotta K, Morgenstern A, *et al.* Development and dosimetry of ^{203}Pb/^{212}Pb-labelled PSMA ligands: bringing "the lead" into PSMA-targeted alpha therapy? *Eur J Nucl Med Mol Imaging*, **46**: 1081–1091, 2019. DOI: 10.1007/s00259-018-4220-z (see p. 159)

[340] Meredith R, Torgue J, Shen S, Fisher DR, Banaga E, Bunch P, *et al.* Dose escalation and dosimetry of first-in-human α radioimmunotherapy with ^{212}Pb-TCMC-trastuzumab. *J Nucl Med*, **55**: 1636–1642, 2014. DOI: 10.2967/jnumed.114.143842 (see p. 159)

[341] Marcillac P de, Coron N, Dambier G, Leblanc J, and Moalic JP. Experimental detection of α-particles from the radioactive decay of natural bismuth. *Nature*, **422**: 876–878, 2003. DOI: 10.1038/nature01541 (see p. 159)

[342] Morgenstern A, Bruchertseifer F, and Apostolidis C. Bismuth-213 and actinium-225–generator performance and evolving therapeutic applications of two generator-derived alpha-emitting radioisotopes. *Curr Radiopharm*, **5**: 221–227, 2012. (see p. 161)

[343] McDevitt MR, Finn RD, Sgouros G, Ma D, and Scheinberg DA. An ^{225}Ac/^{213}Bi generator system for therapeutic clinical applications: construction and operation. *Appl Radiat Isot*, **50**: 895–904, 1999. DOI: 10.1016/S0969-8043(98)00151-1 (see p. 161)

[344] Jadvar H. Targeted α-therapy in cancer management: synopsis of preclinical and clinical studies. *Cancer Biother Radiopharm*, **35**: 475–484, 2020. DOI: 10.1089/cbr.2019.3340 (see p. 161)

[345] McDevitt MR, Finn RD, Ma D, Larson SM, and Scheinberg DA. Preparation of α-emitting ^{213}Bi-labeled antibody constructs for clinical use. *J Nucl Med*, **40**: 1722–1727, 1999. (see p. 161)

[346] Kratochwil C, Giesel FL, Bruchertseifer F, Mier W, Apostolidis C, Boll R, *et al.* ^{213}Bi-DOTATOC receptor-targeted alpha-radionuclide therapy induces remission in neuroendocrine tumours refractory to beta radiation: a first-in-human experience. *Eur J Nucl Med Mol Imaging*, **41**: 2106–2119, 2014. DOI: 10.1007/s00259-014-2857-9 (see p. 161)

[347] Autenrieth ME, Seidl C, Bruchertseifer F, Horn T, Kurtz F, Feuerecker B, *et al.* Treatment of carcinoma in situ of the urinary bladder with an alpha-emitter immunoconjugate targeting the epidermal growth factor receptor: a pilot study. *Eur J Nucl Med Mol Imaging*, **45**: 1364–1371, 2018. DOI: 10.1007/s00259-018-4003-6 (see p. 161)

[348] Krolicki L, Bruchertseifer F, Kunikowska J, Koziara H, Królicki B, Jakuciński M, *et al.* Prolonged survival in secondary glioblastoma following local injection of targeted alpha therapy with ^{213}Bi-substance P analogue. *Eur J Nucl Med Mol Imaging*, **45**: 1636–1644, 2018. DOI: 10.1007/s00259-018-4015-2 (see p. 161)

[349] Królicki L, Bruchertseifer F, Kunikowska J, Koziara H, Królicki B, Jakuciński M, *et al.* Safety and efficacy of targeted alpha therapy with ^{213}Bi-DOTA-substance P in recurrent glioblastoma. *Eur J Nucl Med Mol Imaging*, **46**: 614–622, 2018. DOI: 10.1007/s00259-018-4225-7 (see p. 161)

[350] Henriksen G, Hoff P, Alstad J, and Larsen RH. ^{223}Ra for endoradiotherapeutic applications prepared from an immobilized ^{227}Ac/^{227}Th source. *Radiochim Acta*, **89**: 2001. DOI: 10.1524/ract.2001.89.10.661 (see p. 162)

[351] Jain L, Thakare SV, and Gundra K. Theoretical investigation for optimizing the production of ^{223}Ra in research reactors for treatment of bone metastases. *J Radioanal Nucl Chem*, **325**: 905–911, 2020. DOI: 10.1007/s10967-020-07159-9 (see p. 162)

[352] Parker C, Nilsson S, Heinrich D, Helle SI, O'Sullivan JM, Fosså SD, *et al.* Alpha emitter radium-223 and survival in metastatic prostate cancer. *N Engl J Med*, **369**: 213–223, 2013. DOI: 10.1056/NEJMoa1213755 (see p. 162)

[353] Dizdarevic S, McCready R, and Vinjamuri S. Radium-223 dichloride in prostate cancer: proof of principle for the use of targeted alpha treatment in clinical practice. *Eur J Nucl Med Mol Imaging*, **47**: 192–217, 2020. DOI: 10.1007/s00259-019-04475-5 (see p. 162)

[354] Boll RA, Malkemus D, and Mirzadeh S. Production of actinium-225 for alpha particle mediated radioimmunotherapy. *Appl Radiat Isot*, **62**: 667–679, 2005. DOI: 10.1016/j.apradiso.2004.12.003 (see p. 163)

[355] Morgenstern A, Apostolidis C, and Bruchertseifer F. Supply and clinical application of actinium-225 and bismuth-213. *Semin Nucl Med*, **50**: 119–123, 2020. DOI: 10.1053/j.semnuclmed.2020.02.003 (see p. 163)

[356] International Atomic Energy Agency. *Report on joint IAEA-JRC workshop "Supply of actinium-225"*. IAEA, Vienna, 2018. URL: http://www-naweb.iaea.org/napc/iachem/working_materials/Report_Workshop%20on%20Supply%20of%20Ac-225_IAEA_JRC_October2018.pdf (visited on Dec. 14, 2020) (see p. 163)

[357] Apostolidis C, Molinet R, McGinley J, Abbas K, Möllenbeck J, and Morgenstern A. Cyclotron production of Ac-225 for targeted alpha therapy. *Appl Radiat Isot*, **62**: 383–387, 2005. DOI: 10.1016/j.apradiso.2004.06.013 (see p. 163)

[358] Griswold J, Medvedev D, Engle J, Copping R, Fitzsimmons J, Radchenko V, *et al.* Large scale accelerator production of ^{225}Ac: Effective cross sections for 78–192 MeV protons incident on ^{232}Th targets. *Appl Radiat Isot*, **118**: 366–374, 2016. DOI: 10.1016/j.apradiso.2016.09.026 (see p. 163)

[359] Harvey JT. NorthStar perspectives for actinium-225 production at commercial scale. *Curr Radiopharm*, **11**: 180–191, 2018. DOI: 10.2174/1874471011666180515123848 (see p. 163)

[360] Melville G, Meriarty H, Metcalfe P, Knittel T, and Allen BJ. Production of Ac-225 for cancer therapy by photon-induced transmutation of Ra-226. *Appl Radiat Isot*, **65**: 1014–1022, 2007. DOI: 10.1016/j.apradiso.2007.03.018 (see p. 163)

[361] Hogle S, Boll RA, Murphy K, Denton D, Owens A, Haverlock TJ, *et al.* Reactor production of thorium-229. *Appl Radiat Isot*, **114**: 19–27, 2016. DOI: 10.1016/j.apradiso.2016.05.002 (see p. 163)

[362] Jurcic JG. Targeted alpha-particle therapy for hematologic malignancies. *Semin Nucl Med*, **50**: 152–161, 2020. DOI: 10.1053/j.semnuclmed.2019.09.002 (see p. 164)

[363] Kratochwil C, Bruchertseifer F, Giesel FL, Weis M, Verburg FA, Mottaghy F, *et al.* ^{225}Ac-PSMA-617 for PSMA-Targeted α-radiation therapy of metastatic castration-resistant prostate cancer. *J Nucl Med*, **57**: 1941–1944, 2016. DOI: 10.2967/jnumed.116.178673 (see p. 164)

[364] Kratochwil C, Bruchertseifer F, Rathke H, Bronzel M, Apostolidis C, Weichert W, *et al.* Targeted α-therapy of metastatic castration-resistant prostate cancer with ^{225}Ac-PSMA-617: dosimetry estimate and empiric dose finding. *J Nucl Med*, **58**: 1624–1631, 2017. DOI: 10.2967/jnumed.117.191395 (see p. 164)

[365] Kratochwil C, Bruchertseifer F, Rathke H, Hohenfellner M, Giesel FL, Haberkorn U, *et al.* Targeted α-therapy of metastatic castration-resistant prostate cancer with ^{225}Ac-PSMA-617: Swimmer-plot analysis suggests efficacy regarding duration of tumor control. *J Nucl Med*, **59**: 795–802, 2018. DOI: 10.2967/jnumed.117.203539 (see p. 164)

[366] Kratochwil C, Bruchertseifer F, Giesel F, Apostolidis C, Haberkorn U, and Morgenstern A. Ac-225-DOTATOC - an empiric dose finding for alpha particle emitter based radionuclide therapy of neuroendocrine tumors. *J Nucl Med*, **56**: 1232, 2015. (see p. 164)

[367] Krolicki L, Bruchertseifer F, Morgenstern A, Kunikowska J, Koziara H, Królicki B, *et al.* Safety and therapeutic efficacy of ^{225}Ac-DOTA-substance P for therapy of brain tumors. *J Med Imaging Radiat Sci*, **50**: S22, 2019. DOI: 10.1016/j.jmir.2019.03.070 (see p. 164)

[368] Allen BJ. A comparative evaluation of Ac225 vs Bi213 as therapeutic radioisotopes for targeted alpha therapy for cancer. *Australas Phys Eng Sci Med*, **40**: 369–376, 2017. DOI: 10.1007/s13246-017-0534-6 (see p. 164)

[369] Ramdahl T, Bonge-Hansen HT, Ryan OB, Larsen S, Herstad G, Sandberg M, *et al.* An efficient chelator for complexation of thorium-227. *Bioorg Med Chem Lett*, **26**: 4318–4321, 2016. DOI: 10.1016/j.bmcl.2016.07.034 (see p. 164)

[370] Frantellizzi V, Cosma L, Brunotti G, Pani A, Spanu A, Nuvoli S, *et al.* Targeted alpha therapy with thorium-227. *Cancer Biother Radiopharm*, **35**: 437–445, 2020. DOI: 10.1089/cbr.2019.3105 (see pp. 164, 165)

[371] Goddu SM, Rao DV, and Howell RW. Multicellular dosimetry for micrometastases: dependence of self-dose versus cross-dose to cell nuclei on type and energy of radiation and subcellular distribution of radionuclides. *J Nucl Med*, **35**: 521–530, 1994. (see p. 169)

[372] Rojas-Calderón EL, Ávila O, and Ferro-Flores G. Monte Carlo calculations of the cellular S-values for α-particle-emitting radionuclides incorporated into the nuclei of cancer cells of the MDA-MB231, MCF7 and PC3 lines. *Appl Radiat Isot*, **135**: 1–6, 2018. DOI: 10.1016/j.apradiso.2018.01.007 (see pp. 169, 172, 173)

[373] Goddu SM. *MIRD cellular S values: Self-absorbed dose per unit cumulated activity for selected radionuclides and monoenergetic electron and alpha particle emitters incorporated into different cell compartments*. Reston, Va.: Society of Nuclear Medicine, 1997. (see pp. 172, 173)

[374] Azure MT, Archer RD, Sastry KSR, Rao DV, and Howell RW. Biological effect of lead-212 localized in the nucleus of mammalian cells: Role of recoil energy in the radiotoxicity of internal alpha-particle emitters. *Radiat Res*, **140**: 276, 1994. DOI: 10.2307/3578912 (see p. 174)

APPENDICES

A MO-SCF-LCAO description of water

The parameters obtained by Moccia within the MO-SCF-LCAO treatment of the water molecule (see Section II.2.2) are shown in Table A.1.

n	l	m	ξ	$1a_1$	$2a_1$	$3a_1$	$1b_2$	$1b_1$
1	0	0	12.600	0.05167	0.01889	-0.00848	–	–
1	0	0	7.450	0.94656	-0.25592	0.08241	–	–
2	0	0	2.200	-0.01708	0.77745	-0.30752	–	–
2	0	0	3.240	0.02497	0.09939	-0.04132	–	–
2	0	0	1.280	0.00489	0.16359	0.14954	–	–
2	1	0	1.510	0.00107	0.18636	0.79979	–	–
2	1	0	2.440	-0.00244	-0.00835	0.00483	–	–
2	1	0	3.920	0.00275	0.02484	0.24413	–	–
3	2	0	1.600	0.00000	0.00695	0.05935	–	–
3	2	0	2.400	0.00000	0.00215	0.00396	–	–
3	2	2	1.600	-0.00004	-0.06403	-0.09293	–	–
3	2	2	2.400	0.00003	-0.00988	0.01706	–	–
4	3	0	1.950	-0.00004	-0.02628	-0.01929	–	–
4	3	2	1.950	-0.00008	-0.05640	-0.06593	–	–
2	1	-1	1.510	–	–	–	0.88270	–
2	1	-1	2.440	–	–	–	-0.07083	–
2	1	-1	3.920	–	–	–	0.23189	–
3	2	-1	1.600	–	–	–	0.25445	–
3	2	-1	2.400	–	–	–	-0.01985	–
4	3	-1	1.950	–	–	–	0.04526	–
4	3	-3	1.950	–	–	–	-0.06381	–
2	1	1	1.510	–	–	–	–	0.72081
2	1	1	2.440	–	–	–	–	0.11532
2	1	1	3.920	–	–	–	–	0.24859
3	2	1	1.600	–	–	–	–	0.05473
3	2	1	2.400	–	–	–	–	0.00403
4	3	1	1.950	–	–	–	–	0.00935
4	3	3	1.950	–	–	–	–	-0.02691

Table A.1 Ground state of H_2O in the MO-SCF-LCAO description. Adapted from Ref. [149] with the permission of AIP Publishing.

B LCAO representation of DNA components

We present in the tables here below the ionization potentials, average kinetic energies and the LCAO representation of the MOs associated to the different DNA components (see Section II.2.3).

MO	Ionization potential (eV)	Average kinetic energy (eV)	Population
1	8.44	39.89	0.98 N(2p) + 1.02 C(2p)
2	9.98	39.36	1.18 N(2p) + 0.8 C(2p)
3	10.55	52.34	0.10 N(2s) + 1.54 N(2p) + 0.30 C(2p)
4	11.39	42.34	1.64 N(2p) + 0.36 C(2p)
5	11.71	51.56	0.22 N(2s) + 1.36 N(2p) + 0.24 C(2p) + 0.08 H(1s) + 0.02 C(2s)
6	12.88	52.16	0.38 N(2s) + 1.22 N(2p) + 0.18 C(2p) + 0.08 H(1s) + 0.06 C(2s)
7	13.5	35.54	1.24 N(2p) + 0.78 C(2p)
8	15.23	34.34	1.22 N(2p) + 0.76 C(2p)
9	16.34	42.17	0.66 N(2p) + 0.92 C(2p) + 0.36 H(1s)
10	16.85	44.82	0.62 N(2p) + 0.98 C(2p) + 0.34 H(1s) + 0.02 N(2s)
11	17.29	43.82	0.04 N(2s) + 0.82 N(2p) + 0.84 C(2p) + 0.26 H(1s) + 0.02 C(2s)
12	17.5	29.65	0.88 N(2p) + 1.10 C(2p)
13	18.42	47.17	1.06 N(2p) + 0.74 C(2p) + 0.10 H(1s) + 0.02 C(2s)
14	18.99	39.18	0.12 C(2s) + 0.74 N(2p) + 0.56 C(2p) + 0.48 H(1s) + 0.02 N(2s)
15	20.1	42.12	1.02 N(2p) + 0.52 C(2p) + 0.30 H(1s) + 0.12 C(2s)
16	21.32	40.91	0.02 N(2s) + 1.00 N(2p) + 0.54 C(2p) + 0.24 H(1s) + 0.12 C(2s)
17	22.86	44.61	0.30 N(2s) + 0.66 N(2p) + 0.46 C(2p) + 0.24 H(1s) + 0.24 C(2s)
18	23.89	46.20	0.12 N(2s) + 0.66 N(2p) + 0.36 C(2p) + 0.12 H(1s) + 0.66 C(2s)
19	24.4	45.62	0.14 N(2s) + 0.60 N(2p) + 0.40 C(2p) + 0.20 H(1s) + 0.66 C(2s)
20	28.35	49.58	0.18 N(2s) + 0.26 N(2p) + 0.26 C(2p) + 0.06 H(1s) + 1.18 C(2s)
21	31.41	57.95	1.64 N(2s) + 0.06 N(2p) + 0.16 C(2p) + 0.04 H(1s) + 0.06 C(2s)
22	32.3	57.12	1.66 N(2s) + 0.04 N(2p) + 0.26 C(2p) + 0.08 H(1s) + 0.18 C(2s)
23	33.98	53.14	1.36 N(2s) + 0.12 N(2p) + 0.06 C(2p) + 0.08 H(1s) + 0.38 C(2s)
24	35.68	50.52	1.32 N(2s) + 0.16 N(2p) + 0.12 C(2p) + 0.42 C(2s)
25	37.47	48.50	1.26 N(2s) + 0.22 N(2p) + 0.04 C(2p) + 0.02 H(1s) + 0.50 C(2s)
26	303.09	431.87	1.98 C(1s)
27	304.5	431.82	2.0 C(1s)
28	304.85	431.74	2.0 C(1s)
29	304.85	431.91	1.98 C(1s)
30	305.33	431.93	1.98 C(1s)
31	418.63	596.67	1.98 N(1s)
32	418.84	596.72	1.98 N(1s)
33	419.22	596.76	1.98 N(1s)
34	419.27	596.43	1.98 N(1s)
35	420.79	596.50	1.98 N(1s)

Table B.1 Population, ionization potentials and average kinetic energies of the MOs of **adenine** [140]. © Institute of Physics and Engineering in Medicine. Adapted with permission of IOP Publishing.

MO	Ionization potential (eV)	Average kinetic energy (eV)	Population
1	9.14	41.45	1.12 C(2p) + 0.46 N(2p) + 0.34 O(2p) + 0.08 H(1s)
2	10.93	55.08	0.90 N(2p) + 1.08 O(2p) + 0.02 C(2p)
3	11.35	64.04	1.46 O(2p) + 0.20 N(2p) + 0.26 C(2p) + 0.02 C(2s)
4	12.13	62.07	1.44 O(2p) + 0.20 N(2p) + 0.22 C(2p) + 0.04 N(2s) + 0.04 H(1s)
5	13.29	41.07	0.60 N(2p) + 0.50 O(2p) + 0.12 H(1s) + 0.76 C(2p)
6	14.47	34.01	1.06 C(2p) + 0.70 H(1s) + 0.14 O(2p)
7	14.68	39.93	0.52 O(2p) + 0.76 C(2p) + 0.58 N(2p) + 0.12 H(1s)
8	14.81	42.58	1.32 C(2p) + 0.22 O(2p) + 0.12 N(2p) + 0.08 C(2s) + 0.14 H(1s)
9	15.57	29.70	1.18 C(2p) + 0.48 H(1s) + 0.24 O(2p) + 0.08 N(2p)
10	15.99	54.43	0.84 O(2p) + 0.14 O(2s) + 0.68 C(2p) + 0.18 H(1s) + 0.08 N(2p)
11	16.36	61.11	0.96 O(2p) + 0.26 O(2s) + 0.56 C(2p) + 0.02 C(2s) + 0.06 H(1s) + 0.06 N(2p)
12	17.44	54.55	0.58 O(2p) + 0.48 C(2p) + 0.34 N(2p) + 0.20 O(2s) + 0.24 H(1s) + 0.10 C(2s)
13	17.62	33.84	0.90 C(2p) + 0.82 N(2p) + 0.26 O(2p)
14	18.59	39.11	0.76 N(2p) + 0.52 C(2p) + 0.54 H(1s) + 0.06 C(2s) + 0.02 O(2p)
15	20.28	42.22	0.88 N(2p) + 0.40 C(2p) + 0.34 H(1s) + 0.26 C(2s) + 0.08 O(2p) + 0.04 O(2s)
16	20.38	42.51	0.62 N(2p) + 1.06 C(2p) + 0.16 O(2p) + 0.04 C(2s)
17	23.51	49.98	0.90 N(2p) + 0.38 C(2s) + 0.30 C(2p) + 0.12 H(1s) + 0.12 O(2s) + 0.06 N(2s) + 0.06 O(2p)
18	24.08	41.29	0.50 N(2p) + 0.64 C(2s) + 0.46 C(2p) + 0.22 H(1s) + 0.06 N(2s) + 0.04 O(2s) + 0.02 O(2p)
19	25.53	41.80	1.24 C(2s) + 0.24 N(2p) + 0.20 C(2p) + 0.22 H(1s) + 0.04 O(2s)
20	29.23	45.68	1.44 C(2s) + 0.12 N(2s) + 0.22 C(2p) + 0.04 N(2p) + 0.06 O(2s)
21	32.65	57.70	1.52 N(2s) + 0.12 O(2s) + 0.12 C(2s) + 0.12 C(2p) + 0.10 H(1s)
22	34.46	59.36	1.04 N(2s) + 0.52 O(2s) + 0.20 C(2s) + 0.12 C(2p) + 0.08 N(2p) + 0.04 H(1s)
23	37.09	71.37	1.40 O(2s) + 0.34 C(2s) + 0.18 O(2p) + 0.04 N(2p) + 0.02 N(2s)
24	37.85	63.70	0.92 O(2s) + 0.38 C(2s) + 0.46 N(2s) + 0.14 O(2p) + 0.02 N(2p) + 0.02 C(2p)
25	293.56	432.00	1.98 C(1s)
26	294.27	431.97	1.98 C(1s)
27	296.03	431.87	1.98 C(1s)
28	297.42	431.87	2.00 C(1s)
29	298.44	431.76	2.00 C(1s)
30	408.28	596.45	1.98 N(1s)
31	408.68	596.44	1.98 N(1s)
32	536.74	787.21	2.00 O(1s)
33	536.87	787.23	1.98 O(1s)

Table B.2 Population, ionization potentials and average kinetic energies of the MOs of **thymine** [140].

MO	Ionization potential (eV)	Average kinetic energy (eV)	Population
1	8.94	45.65	0.70 C(2p) + 0.72 N(2p)+ 0.56 O(2p)
2	10.05	43.52	1.58 N(2p) + 0.38 C(2p)+ 0.04 O(2p)
3	10.67	53.81	1.22 N(2p) + 0.38 O(2p)+ 0.26 C(2p)+ 0.08 N(2s)
4	11.42	62.20	1.24 O(2p) + 0.40 N(2p)+ 0.18 N(2s)+ 0.14 C(2p)
5	13.15	40.75	0.62 O(2p) + 0.98 C(2p)+ 0.42 N(2p)
6	14.53	37.89	1.24 N(2p) + 0.62 C(2p)+ 0.12 O(2p)
7	15.61	61.94	0.92 O(2p) + 0.44 C(2p)+ 0.24 O(2s)+ 0.26 N(2p)+ 0.08 H(1s)
8	16.47	42.04	1.14 C(2p) + 0.38 N(2p)+ 0.34 H(1s)+ 0.04 N(2s)+ 0.04 C(2s)
9	16.80	42.76	0.88 C(2p) + 0.44 H(1s)+ 0.22 O(2p)+ 0.26 N(2p)+ 0.08 O(2s) + 0.02 C(2s)
10	17.02	32.48	0.86 N(2p) + 0.96 C(2p)+ 0.16 O(2p)
11	18.31	40.34	0.86 N(2p) + 0.52 H(1s)+ 0.40 C(2p)+ 0.08 O(2p)+ 0.12 C(2s)
12	19.47	45.80	0.90 N(2p) + 0.52 C(2p)+ 0.32 H(1s)+ 0.04 O(2p)+ 0.04 O(2s) + 0.12 C(2s)
13	20.63	39.94	0.94 N(2p) + 0.78 C(2p)+ 0.20 H(1s)+ 0.06 O(2p)
14	20.74	36.54	0.76 N(2p) + 0.54 C(2p)+ 0.46 H(1s)+ 0.10 C(2s)+ 0.06N(2s) + 0.02 O(2s)
15	23.79	48.17	0.90 N(2p) + 0.48 C(2s)+ 0.28 C(2p)+ 0.16 H(1s)+ 0.06 O(2s) + 0.04 N(2s)
16	24.28	44.22	0.02 O(2p) + 0.20 H(1s)+ 0.68 C(2s)+ 0.46 N(2p)+ 0.42 C(2p) + 0.18 N(2s)
17	28.93	47.66	1.20 C(2s) + 0.26 N(2s)+ 0.32 C(2p)+ 0.06 N(2p)+ 0.10 H(1s) + 0.04 O(2s)
18	31.79	55.82	1.58 N(2s) + 0.12 C(2p)+ 0.08 N(2p)+ 0.06 C(2s)+ 0.10 H(1s) + 0.02 O(2s)
19	34.14	54.77	1.38 N(2s) + 0.34 C(2s) + 0.08 O(2s) + 0.06 C(2p) + 0.08 H(1s) + 0.06 N(2p)
20	35.33	56.82	0.44 O(2s) + 0.92 N(2s) + 0.40 C(2s) + 0.16 N(2p) + 0.04 O(2p) + 0.02 C(2p)
21	37.70	63.70	0.92 O(2s) + 0.38 C(2s)+ 0.48 N(2s)+ 0.14 O(2p)+ 0.06 N(2p) + 0.08 C(2p)
22	302.18	431.91	1.98 C(1s)
23	304.47	431.86	2.00 C(1s)
24	305.09	431.88	2.00 C(1s)
25	305.69	431.78	2.00 C(1s)
26	417.42	596.64	1.98 N(1s)
27	418.83	596.37	1.98 N(1s)
28	419.80	596.44	1.98 N(1s)
29	550.88	787.20	2.00 O(1s)

Table B.3 Population, ionization potentials and average kinetic energies of the MOs of **cytosine** [140]. © Institute of Physics and Engineering in Medicine. Adapted with permission of IOP Publishing.

MO	Ionization potential (eV)	Average kinetic energy (eV)	Population
1	8.24	41.51	1.20 C(2p) + 0.56 N(2p) + 0.22 O(2p)
2	11.14	43.18	0.40 C(2p) + 1.48 N(2p) + 0.10 O(2p)
3	11.36	54.64	0.26 C(2p) + 1.24 N(2p) + 0.20 O(2p) + 0.02 H(1s) + 0.16 N(2s)
4	11.80	48.31	1.28 N(2p) + 0.46 O(2p) + 0.24 C(2p)
5	11.83	62.69	1.28 O(2p) + 0.38 N(2p) + 0.18 C(2p) + 0.04 C(2s) + 0.02 N(2s)
6	12.39	41.01	1.52 N(2p) + 0.42 C(2p) + 0.02 O(2p)
7	13.08	51.41	0.16 C(2p) + 1.40 N(2p) + 0.30 N(2s) + 0.02 H(1s)
8	15.34	40.51	0.78 C(2p) + 0.62 N(2p) + 0.58 O(2p)
9	16.62	64.92	1.08 O(2p) + 0.44 C(2p) + 0.10 N(2p) + 0.26 O(2s)
10	16.76	34.40	1.22 N(2p) + 0.74 C(2p)
11	16.93	44.59	0.96 C(2p) + 0.64 N(2p) + 0.28 H(1s) + 0.08 O(2p)
12	17.62	48.12	0.94 N(2p) + 0.76 C(2p) + 0.22 H(1s) + 0.04 O(2p)
13	18.51	31.22	0.98 N(2p) + 0.96 C(2p) + 0.06 O(2p)
14	18.87	45.54	0.68 N(2p) + 0.80 C(2p) + 0.18 O(2p) + 0.22 H(1s) + 0.04 C(2s) + 0.02 O(2s)
15	19.71	43.51	0.98 N(2p) + 0.54 H(1s) + 0.20 C(2p) + 0.06 O(2p) + 0.10 C(2s) + 0.04 O(2s) + 0.02 N(2s)
16	20.60	46.82	1.12 N(2p) + 0.46 C(2p) + 0.18 H(1s) + 0.16 C(2s)
17	20.88	42.53	0.98 N(2p) + 0.30 H(1s) + 0.10 C(2s) + 0.50 C(2p)
18	22.66	39.42	1.08 N(2p) + 0.58 C(2p) + 0.22 H(1s) + 0.04 C(2s) + 0.04 O(2p)
19	23.30	44.78	0.70 N(2p) + 0.30 C(2s) + 0.28 N(2s) + 0.38 C(2p) + 0.26 H(1s)
20	24.80	48.74	0.46 C(2s) + 0.22 C(2p) + 0.18 N(2s) + 0.88 N(2p) + 0.16 H(1s) + 0.02 O(2p)
21	25.30	45.42	0.74 N(2p) + 0.58 C(2s) + 0.42 C(2p) + 0.06 O(2s) + 0.12 H(1s) + 0.04 N(2s)
22	28.98	50.54	1.10 C(2s) + 0.30 C(2p) + 0.28 N(2p) + 0.18 N(2s) + 0.02 O(2s) + 0.02 H(1s)
23	32.88	57.55	1.68 N(2s) + 0.12 C(2s) + 0.08 H(1s) + 0.06 N(2p) + 0.22 C(2p)
24	34.05	58.22	1.52 N(2s) + 0.14 O(2s) + 0.10 C(2p) + 0.10 C(2s) + 0.06 H(1s)
25	34.24	53.24	1.48 N(2s) + 0.14 C(2s) + 0.14 H(1s) + 0.12 N(2p) + 0.04 C(2p)
26	37.55	53.76	1.18 N(2s) + 0.32 C(2s) + 0.18 O(2s) + 0.12 C(2p) + 0.20 N(2p)
27	38.28	56.64	0.46 O(2s) + 0.06 C(2p) + 0.02 H(1s) + 0.14 N(2p) + 0.42 C(2s) + 0.94 N(2s) + 0.04 O(2p)
28	39.20	60.43	0.74 O(2s) + 0.62 N(2s) + 0.46 C(2s) + 0.10 O(2p) + 0.02 N(2p)
29	311.53	431.85	1.98 C(1s)
30	313.15	431.78	2.00 C(1s)
31	313.79	431.86	2.00 C(1s)
32	314.93	431.94	2.00 C(1s)
33	315.93	431.80	2.00 C(1s)
34	431.02	596.71	1.98 N(1s)
35	431.10	596.78	1.98 N(1s)
36	432.32	596.36	1.98 N(1s)
37	432.91	596.48	2.00 N(1s)
38	432.94	596.50	2.00 N(1s)
39	568.45	787.24	1.98 O(1s)

Table B.4 Population, ionization potentials and average kinetic energies of the MOs of **guanine** [140].

MO	Ionization potential (eV)	Average kinetic energy (eV)	Population
1	10.53	56.47	1.20 O(2p) + 0.32 H(1s) + 0.38 C(2p)
2	10.64	62.65	1.88 O(2p) + 0.06 P(3p)
3	10.88	61.46	1.98 O(2p)
4	11.65	57.87	1.66 O(2p) + 0.08 P(3p) + 0.04 H(1s) + 0.06 C(2p)
5	11.73	48.20	0.72 O(2p) + 1.04 C(2p) + 0.10 H(1s) + 0.04 O(2s)
6	11.97	55.82	1.62 O(2p) + 0.08 P(3p) + 0.14 C(2p) + 0.02 H(1s)
7	12.27	50.03	0.92 O(2p) + 0.60 C(2p) + 0.26 H(1s) + 0.02 P(3p)
8	12.41	56.80	1.48 O(2p) + 0.12 H(1s) + 0.12 C(2p) + 0.12 P(3p)
9	12.73	37.04	0.88 C(2p) + 0.38 H(1s) + 0.42 O(2p) + 0.04 P(3p)
10	12.70	40.98	1.22 C(2p) + 0.20 H(1s) + 0.46 O(2p)
11	13.06	45.52	0.96 C(2p) + 0.64 O(2p) + 0.20 H(1s) + 0.04 P(3p)
12	13.69	57.27	1.40 O(2p) + 0.16 P(3p) + 0.22 C(2p) + 0.04 H(1s)
13	14.31	52.19	1.16 O(2p) + 0.50 C(2p) + 0.10 H(1s) + 0.06 P(3p) + 0.02 O(2s)
14	14.91	33.24	1.02 C(2p) + 0.32 O(2p) + 0.42 H(1s)
15	15.13	52.97	1.20 O(2p) + 0.38 C(2p) + 0.12 H(1s) + 0.06 O(2s) + 0.12 P(3p)
16	15.56	47.78	0.82 O(2p) + 0.60 C(2p) + 0.16 P(3p) + 0.08 O(2s) + 0.06 H(1s) + 0.02 P(3s)
17	15.84	46.70	0.88 O(2p) + 0.58 C(2p) + 0.16 P(3p) + 0.26 H(1s) + 0.04 O(2s)
18	16.54	53.18	0.92 O(2p) + 0.16 H(1s) + 0.20 O(2s) + 0.34 C(2p) + 0.10 P(3s) + 0.18 P(3p)
19	17.39	39.91	0.78 C(2p) + 0.70 O(2p) + 0.32 H(1s) + 0.06 P(3p) + 0.02 O(2s)
20	17.52	35.65	0.98 C(2p) + 0.48 O(2p) + 0.24 H(1s) + 0.04 C(2s) + 0.02 P(3p) + 0.02 O(2s)
21	17.96	34.81	1.02 C(2p) + 0.48 O(2p) + 0.20 H(1s) + 0.04 P(3s) + 0.04 P(3p) + 0.02 O(2s)
22	18.86	44.01	0.86 O(2p) + 0.48 C(2p) + 0.18 P(3p) + 0.16 H(1s) + 0.08 C(2s)
23	20.84	47.27	0.58 O(2p) + 0.48 C(2s) + 0.22 H(1s) + 0.28 C(2p) + 0.08 P(3s) + 0.08 P(3p) + 0.10 O(2s)
24	21.69	47.23	0.54 O(2p) + 0.50 C(2s) + 0.06 O(2s) + 0.20 H(1s) + 0.30 C(2p) + 0.04 P(3p) + 0.16 P(3s)
25	21.80	42.96	0.80 C(2s) + 0.28 H(1s) + 0.26 O(2p) + 0.34 C(2p) + 0.06 O(2s) + 0.08 P(3s)
26	24.76	42.81	1.24 C(2s) + 0.20 O(2p) + 0.14 C(2p) + 0.20 H(1s) + 0.02 P(3s) + 0.02 O(2s) + 0.02 P(3p)
27	27.84	40.27	1.52 C(2s) + 0.12 O(2p) + 0.10 H(1s) + 0.06 C(2p) + 0.04 O(2s)
28	28.33	43.53	1.48 C(2s) + 0.18 O(2s) + 0.14 C(2p) + 0.04 O(2p) + 0.02 H(1s)
29	33.17	78.82	1.78 O(2s) + 0.14 P(3p) + 0.08 O(2p)
30	34.67	75.49	1.64 O(2s) + 0.10 P(3s) + 0.06 P(3p) + 0.10 O(2p) + 0.02 C(2s)
31	36.35	72.13	1.66 O(2s) + 0.16 C(2s) + 0.02 P(3p) + 0.02 O(2p)
32	36.76	67.49	1.54 O(2s) + 0.30 C(2s) + 0.04 O(2p)
33	38.18	68.68	1.52 O(2s) + 0.22 P(3s) + 0.06 C(2s) + 0.08 O(2p)
34	149.58	396.15	2.00 P(2p)
35	149.61	396.01	2.00 P(2p)
36	149.61	395.56	2.00 P(2p)
37	207.08	440.68	2.00 P(2s)
38	303.73	432.14	1.98 C(1s)
39	304.55	432.29	1.98 C(1s)
40	304.90	432.10	1.98 C(1s)
41	305.23	432.27	1.98 C(1s)
42	305.48	432.16	1.98 C(1s)
43	554.24	787.18	2.00 O(1s)
44	554.24	787.19	2.00 O(1s)
45	555.91	787.17	2.00 O(1s)
46	556.77	787.07	2.00 O(1s)
47	556.80	787.06	2.00 O(1s)
48	2165.16	2867.87	2.00 P(1s)

Table B.5 Population, ionization potentials and average kinetic energies of the MOs of the **sugar-phosphate backbone** [140].